Measurement of photon-induced ZZ production at the ATLAS Experiment using AFP

Adrien Auriol

Thesis submitted for the degree of
Doctor of Philosophy

Particle Physics Group,
School of Physics and Astronomy,
University of Birmingham.

June 7, 2024

Abstract

This thesis presents a measurement of photon-induced ZZ production using proton-proton collision data at a centre-of-mass energy of 13 TeV and with an integrated luminosity of 14.6 fb^{-1}, recorded by the ATLAS experiment at the LHC. The scattered protons are detected by the ATLAS Forward Proton (AFP) detector. Only the four muon final state is considered, which is measured by the central ATLAS detector. The observed measured cross-section using a novel data-blinding method is :

$$\sigma_{\text{fid.}}^{\text{meas.}}(\text{fb}) = -0.595 \pm 0.250 \text{ (stat.)} \pm 0.283 \text{ (syst.)} \pm 0.014 \text{ (lumi.)}$$

This measurement is compatible with the SM-only hypothesis and the results are interpreted as an upper-limit on the cross-section for the process, computed to be of 1.967 fb at the 95% confidence level. The results are also interpreted as an upper-limit on Wilson coefficients of 15 dimension 8 Effective Field Theory (EFT) operators. The upper-limits on the EFT Wilson coefficients are given considering the fully simulated proton-elastic component of the operators only and also by using an estimation of their proton dissociative components. The statistical uncertainties remain dominant in this measurement. The AFP-related systematic uncertainties are dominant but are probably overestimated.

A tuning of the fast simulation of AFP as well as the implementation of a data-driven proton pile-up overlay is also described.

Declaration of authors contribution

This thesis covers the work I have done during my PhD studies. All of the work described here was done within the ATLAS collaboration, and none of it would have been possible without all the combined work from all of its members.

Chapter 1 is an introduction to the thesis. Chapter 2 describes the theoretical framework needed to understand the experimental work presented in the thesis and its motivations. Chapter 3 describes the experimental setup used in the research work presented in this thesis with a focus in Chapter 4 on AFP, the subdetector that is crucial to these studies. None of the information presented in these three chapters originates from my own work, but has been referenced all along. Two particular resources were a major source of informations: Ref. [1] for the deep theoretical description of particle physics and Ref. [2] for its detailed and referenced description of the AFP detector. Ref. [2–5] were all used together as a starting point for the description of the ATLAS detector. Chapter 5 describes the work done in the framework of the ATLAS qualification task and was all of my own. Chapter 6 describes the biggest part of the work that I have done during my PhD: an analysis of the ATLAS data aiming to measure the photon-induced ZZ production using AFP. I was the main analyser of this analysis and participated actively in all the steps described in this chapter. The results presented are obviously not the result of my work alone, as I was supervised and worked together with other researchers and PhD students during this analysis. Chapter 7 finally concludes and summarize the studies presented in this thesis.

Additionally to the work presented in this thesis, a significant part of my PhD involved my contributions during my long-term attachment at CERN. My involvement started as a Calo/Forward shifter in the ATLAS control room, where I undertook several shifts. Later on, I assumed the role of AFP on-call during a substantial portion of the end-of-2022 data-taking period. My responsibilities included participation in numerous interventions within the tunnel on the detector, as well as engagement in test beam operations. I also took responsibilities in coordinating efforts to proactively operate the detector.

Acknowledgements

I have taken the liberty of writing these thanks in two languages, as not all the people mentioned in this text are bilingual.
Je prends la liberté d'écrire ces remerciements dans deux langues, étant donné que les personnes mentionnées dans ce texte ne sont pas toutes bilingues.

English version

Just over three and a half years ago, I began the great adventure that is a PhD. Many people have told me that it was a marathon, the experience of a lifetime. The purpose of this paragraph is not to feel sorry for me, but to pay tribute to all the people who have accompanied me through this stage of my life, and who have turned this marathon into an (almost) healthy stroll.

First of all, I would like to thank the STFC, and by extension the British taxpayer, for supporting me financially during this period. I was lucky to start my thesis before Brexit, and to be welcomed into a country as if it were my own. But I'll come back to that.

This thesis is the result of work that was carried out of passion, and this passion began with a vocation. It was given to me (as I believe all vocations should be) by a teacher. Etienne Bascou, my high school physics teacher, pushed me towards this goal, told me it was possible and made me believe in myself. He gave me a taste for research and pushed me in the direction that resonates with me today. I was then lucky enough to be surrounded by other mentors during my studies, and three of them deserve special mention. Paul Newman was my thesis supervisor and I was the luckiest PhD student on earth to have someone like him direct my thesis. He trusted me, taught me a lot and often calmed my fears. His phlegm, his distance and his wisdom will always be an inspiration to me. Rafał Staszewski was my technical director during my ATLAS qualification task. He was then a colleague in my analysis group, but also and above all a devoted mentor. Rafał is a brilliant person, whose instinct, analytical skills and creativity inspired me every day. He welcomed me

to his home town of Kraków and I hope to have the opportunity to return very soon. Marko Milovanovic was a great support during my stay at CERN in 2022. He guided me in taking data and thus helped me to become a better experimenter in my opinion. He was my mentor during my stay at CERN and became a friend. The trust he placed in me very quickly made me very proud. If one day I get the chance to supervise a thesis, I hope to do at least half as well as these three people.

I've been lucky enough to meet so many caring colleagues in Birmingham and in the AFP community. I'm thinking in particular of Andy Kirk, Dave Charlton, Aleksandra Dimitrievska and Maciej Trzebinski who, each in their own way, have given me so much of their time, energy and attention. Thank you for answering my questions and making so many tasks easier. Thanks also to my friends at CapCowork for changing my mind every lunchtime while I was writing this thesis.

When you're running a marathon, it helps to have friends who are running the same marathon and suffering with you. Not out of sadistic pleasure, but because you feel less alone and push each other towards the finish line. I have too many memories with each of you to recount here, but thanks in particular to Mihaela Marinescu, Dan Thompson, Jon Mulvey, Josh Lomas, Júlia Silva, Rob Ward, António Costa, Miloš Vojinovic, Marc Granado, Ferhat Öztürk and Maura Barros. As I write all these names, what strikes me most is the variety of nationalities (even if dominated by Portugal!). Thank you all for teaching me about your culture too, especially the Brummies: thank you for making me feel at home in this city. Ryan Mayes, I didn't meet you at university, but these last words and thanks obviously apply to you too.

A race like the marathon is finished first and foremost thanks to the supporters. My friends have been my support, my pillars in the adventure, the ones who have prevented me from giving up. It would take too long to name them all here without encroaching on the scientific work that I am presenting in this thesis, which is why I'd like to include them under names that I know they'll recognise. Nor do I hide my pleasure at the idea that some of these words will be printed on paper that will remain in an old English university. Thanks to We All Love Ro, Cool, Oopsie, CCP's Neurchi, the Xenopoulos team and the Pie team.

Some people deserve special attention, I think, because they have each played a very central role in my journey. These people have all heard me doubt, cry, exult, shout, and have each guided me in their own way. Some of them have been with me longer than others. some haven't had the same role before and during this PhD, but each has been essential in their own way. It would take too long (and I wouldn't be able) to write down all the love and gratitude I have for you individually, so I'll just mention you: Thank you to Sebastien Calas, Romane Schnell, Anaé Balssa, Daniel Ardouin, Nolwenn Massaria, Chloé Maury, Nicolas Gaudy and Lucien Dupuy.

All my life, I've been surrounded by a loving family, who have always given me everything I needed to fulfil my dreams. During my PhD, they were unfailingly supportive, each and every one of them. Dad, Mum, my Auntie Claire, my brother Clem, I'm infinitely grateful for everything you do and have done. The love you

have always given me has given me Herculean strength. Three of my grandparents were there at the beginning of this stage of my life, but none of them were there at the end. My thoughts are with them as I write this, and I know they would all have been proud.

I'm going to end this paragraph very quickly, I know it's very long, but I still have two very important people to thank, the first is Minou, even though you're a cat and you can't read (too bad for you). You came into my life at the same time as the most important person in my life today. Maéva, thank you. You're the one who stood firm, who was with me every step of the way in what seemed like a never-ending race. I always thought I was alone on another planet, until I realised that you were on the same one as me. I love you, and I want you to be there for every other stage of my life, without exception.

At last, here is the finish line.

Version française

Il y a un peu plus de trois ans et demi, je commençais cette grande aventure qu'est le doctorat. Beaucoup m'ont dit que c'était un marathon, l'experience d'une vie. Ce paragraphe n'a pas pour vocation de me plaindre, mais bien de rendre hommage à toutes les personnes qui m'ont accompagné dans cette étape de ma vie, et qui ont transformé ce marathon en balade de santée (presque).

Tout d'abord, il convient de remercier la STFC, et par extension le contribuable anglais, qui m'a soutenu financièrement pendant cette periode. J'ai eu de la chance de commencer ma thèse avant le Brexit, et d'être accueilli dans un pays comme si c'était le mien. Mais j'y reviendrai.

Cette thèse est le résultat d'un travail qui a été mené par passion, et cette passion a commencé par une vocation. Elle m'a été donné (comme toute vocation doit l'être selon moi) par un enseignant. Etienne Bascou, mon professeur de physique du lycée, m'a poussé vers cet objectif, m'a dit que c'était possible et m'a fait croire en moi. Il m'a donné goût à la recherche et m'a poussé dans cette direction qui aujourd'hui résone autant en moi. J'ai eu la chance par la suite d'être entouré d'autres mentors pendant mes études, et trois d'entre eux méritent une attention toute particulière. Paul Newman a été mon directeur de thèse et j'ai été le doctorant le plus chanceux de la terre d'avoir une personne comme lui pour diriger ma thèse. Il m'a fait confiance, m'a énormément appris, et a souvent calmé mes angoisses. Son flegme, son recul, et sa sagesse resteront toujours très inspirants pour moi. Rafał Staszewski quant à lui a été mon directeur technique lors de ma tâche de qualification ATLAS. Il a ensuite été un collègue dans mon groupe d'analyse, mais aussi et surtout un mentor dévoué. Rafał est une personne brillante, dont l'instinct, la capacité d'analyse et la créativité m'ont chaque jour inspiré. Il m'a acceuilli dans sa ville Kraków et

j'espère avoir l'occasion d'y retourner très vite. Marko Milovanovic a été d'un grand soutien lors de mon séjour au CERN en 2022, il m'a guidé dans la prise de données et donc aidé à devenir selon moi un meilleur experimentateur. Il a été mon mentor pendant mon séjour au CERN et est devenu un ami. La confiance qu'il m'a très vite accordé m'a énormément touché et rendu fier. Si un jour la chance m'est donnée d'encadrer une thèse, j'espère réussir à faire au moins à moitié aussi bien que ces trois personnes.

J'ai eu la chance de rencontrer énormément de collègues bienveillant à Birmingham et dans la communauté d'AFP. Je pense en particulier à Andy Kirk, Dave Charlton, Aleksandra Dimitrievska et Maciej Trzebinski qui m'ont, chacun à leur manière, donné beaucoup de leur temps, de leur énergie et de leur attention. Merci d'avoir répondu à mes questions, et de m'avoir simplifié beaucoup de tâches. Merci également à mes ami·es de CapCowork de m'avoir changé les idées tous les midis pendant l'écriture de cette thèse.

Lorsque l'on court un marathon, ce qui aide, c'est aussi d'avoir des ami·es qui courrent le même marathon et souffrent avec nous. Non pas dans un plaisir sadique, mais bien car on se sent moins seul, et que l'on se pousse mutuellement vers la ligne d'arrivée. J'ai trop de souvenirs avec chacun d'entre vous pour les raconter ici, mais merci en particulier à Mihaela Marinescu, Dan Thompson, Jon Mulvey, Josh Lomas, Júlia Silva, Rob Ward, António Costa, Miloš Vojinovic, Marc Granado, Ferhat Öztürk et Maura Barros. En écrivant tous ces noms, ce qui me frappe le plus est la variété de nationalité (même si dominée par le Portugal!). Merci à tous·tes de m'avoir aussi appris votre culture, en particulier les Brummies : merci de m'avoir fait me sentir chez moi dans cette ville. Ryan Mayes, je ne t'ai pas rencontré à l'université, mais ces derniers mots et ces remerciements te concernent bien évidemment toi aussi.

Une course comme le marathon se finit avant tout grâce aux supporters. Mes ami·es ont été mes soutiens, mes piliers dans l'aventure, ceux qui m'ont empeché de lâcher. Il serait trop long de tous les nommer ici sans empiéter sur le travail scientifique que je présente dans cette thèse, c'est pourquoi j'aimerai les englober dans des appellations dans lequelles je sais qu'iels se reconnaîtront. Je ne cache pas non plus mon plaisir à l'idée que certains de ces mots seront imprimés sur du papier qui restera dans une vieille université anglaise. Merci à On Aime Tous Ro, à Cool, à Oupsi, au Neurchi de CCP, à la team Xenopoulos ainsi qu'à la team Galette.

Certaines personnes méritent une attention particulière je pense, car elles ont pris une place chacun très centrale dans mon parcours. Ces personnes m'ont toutes entendu douter, pleurer, exulter, crier, et m'ont chacune à leur manière guidé. Certain·es sont là depuis plus longtemps que d'autres, certain·es n'ont pas eu le même rôle avant et pendant ce doctorat, mais chacun·e a été essentiel·le à sa façon. Il serait trop long (et j'en serai incapable) de vous écrire tout l'amour et la reconnaissance que j'ai pour vous individuellement, alors je vais juste vous citer : merci à Sebastien Calas, à Romane Schnell, à Anaé Balssa, à Daniel Ardouin, à Nolwenn

Massaria, à Chloé Maury, à Nicolas Gaudy et à Lucien Dupuy.

Toute ma vie, j'ai été entouré d'une famille aimante, qui m'a toujours donné tout ce dont j'avais besoin pour réaliser mes rêves. Pendant mon doctorat, ils ont été d'un soutien sans failles, chacun·e d'entre eux. Papa, Maman, ma tante Claire, mon frère Clem, je vous suis infiniment reconnaissant de tout ce que vous faites et avez fait. L'amour que vous m'avez toujours donné m'a donné une force herculéenne. Trois de mes grands parents ont assisté au début de cette étape de ma vie mais aucun n'a pu assister à la fin. J'ai une forte pensée pour eux en écrivant ce texte, et je sais qu'ils auraient tous été fiers.

Je vais conclure très vite ce paragraphe, je sais qu'il est très long, mais il me reste deux personnes très importantes à remercier, la première c'est Minou, même si t'es un chat et que tu sais pas lire (dommage pour toi). Tu es entré dans ma vie en même temps que la personne la plus importante de ma vie aujourd'hui. Maéva, merci. Tu es celle qui a tenu bon, qui m'a acommpagné à chaque instant de cette course qui parraissait sans fin. J'ai toujours cru que j'étais seul sur une autre planète, jusqu'à me rendre compte que tu étais sur la même que moi. Je t'aime, et je veux que tu soies là pour toutes les autres étapes de ma vie sans exception.

Enfin, voilà la ligne d'arrivée.

C'est quoi ce bordel ??? - Daniel Bosson

Contents

List of Tables

List of Figures

Definitions of acronyms

AFP ATLAS Forward Proton

ALFA Absolute Luminosity For ATLAS

ALICE A Large Ion Collider Experiment

ALP Axion-like Particle

AOD Analysis Object Data

ATLAS A Large Torroidal AppartuS

aQGC Anomalous Quartic Gauge Couplings

aTGC Anomalous Triple Gauge Couplings

BBA Beam Based Alignment

BEH Brout-Englert-Higgs

BLM Beam Loss Monitor

BPM Beam Position Monitor

BSM Beyond the Standard Model

CERN Centre Européen pour la Recherche Nucléaire
European Center for Nuclear Research

CFD Constant Fraction Discriminator

CMS Compact Muon Solenoid

CP Combined Performance

CR Control Region

CSC Cathode Strip Chambers

CTP Central Trigger Processor

DAOD Derived Analysis Object Data

DD Double Dissociation

ECal Electromagnetic Calorimeter

EFT Effective Field Theory

EPA Equivalent Photon Approximation

FCal Forward Calorimeter

GRL Good Run List

HCal Hadronic Calorimeter

HEC Hadronic End Cap

HL-LHC High Luminosity LHC

HLT High-Level Trigger

HPTDC High-Performance Time-to-Digital Converter

IBL Insertable B-Layer

ID Inner Detector

IP Interaction Point

LAr Liquid Argon

LHC Large Hadron Collider

LHCb Large Hadron Collider beauty

LINAC2 Linear Accelerator 2

LO Leading Order

LS Long Shutdown

LUCID Luminosity Cherenkov Integrating Detector

MC Monte-Carlo

MCP-PMT Microchannnel Plate Photomultiplier Tube

MDT Monitored Drift Tubes

NLO Next to Leading Order

PDF Parton Distribution Function

PMG Physics Modelling Group

PPS Precision Proton Spectrometer

PS Proton Synchrotron

PV Primary Vertex

QCD Quantum Chromodynamics

QED Quantum Electrodynamics

QFT Quantum Field Theory

QGC Quartic Gauge Coupling

RoI Region of Interest

RP Roman Pot

RPC Resistive-Plate Chambers

SCT Semi-conductor Tracker

SD Single Dissociation

SiT Silicon Tracker

SM Standard Model

SPS Super Proton Synchrotron

SR Signal Region

SUSY Super Symmetry

TCP Three Primary Collimators

TDAQ Trigger and Data Acquisition

TDR Technical Design Report

TGC Thin-Gap chambers

ToF Time-of-Flight

TRT Transition Radiation Tracker

WLCG Worldwide LHC Computing Grid

ZDC Zero Degree Calorimeter

Chapter 1

Introduction

One of the most challenging questions the human race has ever faced is to understand how Nature works; in other words what is the set of rules that governs our universe and its components. After many centuries of experimental and theoretical research, the combined work of thousands of physicists led to the Standard Model of particle physics: an elegant mathematical description of the components of our universe and how they interact. This model, described in Chapter 2, tells us that our entire universe is made of a small set of fundamental components that we call elementary particles. Unfortunately, but very interestingly, astronomical and cosmological observations lead to a contradiction with the model and to a brutal conclusion: the model does not describe everything we see, and therefore must be incomplete. This suggests the existence of a new more fundamental pattern: numerous extensions of the Standard Model (such as supersymmetry, for example) have emerged in an attempt to explain these phenomena.

This is why the experimental study of phenomena predicted by the Standard Model is of critical importance: it tests the model's predictions and tests its limits. Despite the robustness of the Standard Model, measurements made at accelerators such as the Large Hadron Collider (LHC), the highest energy accelerator ever constructed by man, are key to deeper confirmation of the model and provide a potential opening

to new physics if deviations are observed. The theoretical background in high energy physics will be later described in Chapter 2.

This thesis presents a study of real data as well as simulations of collisions passing through the ATLAS detector - one of the general-purpose LHC experiments, described in Chapter 3. The goal of this analysis is to perform a measurement of one of the very rare processes happening in a proton-proton collision: this process is so rare that no collisions of this type are expected to be observed in the studied dataset corresponding to a full year of data-taking. For reasons that will be explained in this thesis, this process is also interesting because of the fact that not only can it test the model's prediction, but it can also set constraints on extensions of the Standard Model. These extensions, called Effective Field Theories, are parametric extensions of the model in its most general form and have phenomenological implications in an energy regime beyond the reach of the LHC.

This study makes use of one of the subsystems of ATLAS: the ATLAS Forward Proton (AFP) system. This subsystem, which will be described in its own dedicated Chapter 4, detects and measures protons that barely interact at the collision point. These protons, after their interaction through photon emission, therefore losing only a small fraction of their energy, do not smash but continue their way into the accelerator system, and are then detected by AFP. This type of collision changes the paradigm that we usually adopt when considering a "hard" collision, where the protons are destroyed during their collision. In a collision where the protons do not remain intact, the experimentalist can only access the final state of the quark or gluon interaction, *i.e.* what was produced after the collision, and must make assumptions (that rely on knowledge of the proton structure) to properly consider what was in the initial state. AFP, by measuring kinematic properties of the intact protons, gives access to additional initial state information by constraining the kinematics of the collision. In some ways, the AFP system transforms the LHC from a proton-proton collider into a photon-photon collider.

A key component of the experimentalist's toolbox is a deep knowledge of the detector

they use. This involves performance studies, hardware testing, but also computational simulation of the detector and how it interacts with the particles produced in the accelerator. This thesis also presents the work done by the author in the simulation of the AFP sub-detector in Chapter 5.

Chapter 2

Theoretical background of High Energy Physics

This chapter will present an overview of the different elements of theory in high energy physics relevant to the studies presented in this thesis. The Standard Model of particle physics will be described in Section 2.1 as well as its limitations. An approach to overcome these boundaries of applicability called Effective Field Theory (EFT) will be described in Section 2.2. Some elements of high energy physics in the context of hadron colliders will then be discussed in Section 2.3, with a specific focus on photon fusion physics. This chapter will then end with a brief description in Section 2.4 of the methods and computational tools used to simulate particle physics processes.

2.1 The standard model

The Standard Model (SM) of particle physics[1] is a combination of different theories providing the most complete description of the fundamental particles of our universe

[1]Other fields such as cosmology and solar physics also have a Standard Model. "SM" will only refer to the particle physics' standard model in this thesis.

and their interactions[2] [1, 7–9]. The SM is formulated as a Quantum Field Theory (QFT), meaning that the elementary particles that we observe are described as quanta of the quantum fields bathing our universe. The model is fully described by its Lagrangian $\mathcal{L}_{\text{SM}}$, a mathematical object on which Euler-Lagrange equations and the principle of least action are applied in order to predict physical quantities such as the cross-section of a process through its matrix element. Further details of these theoretical calculations can be found in Ref. [1].

The particles described by the SM can be split into two main categories, fermions with spin-1/2 describing matter, and bosons whose spin has an integer value acting as force carriers[3]. They obey different statistics, Fermi-Dirac for fermions and Bose-Einstein for bosons.

Fermions are further subdivided into quarks and leptons, each carrying different quantum numbers, sometimes called charges. Only quarks carry color charges C, while both quarks and leptons carry the other charges: the third component of weak isospin charge I_3 and electric charge Q, that can be combined into hypercharge $Y = 2(Q - I_3)$. The fermions are often split into three generations which differ in mass, and all fermions have a complementary anti-particle having the same properties as their counterpart but with flipped charges. The different types of quarks are called flavours, as are the different types of leptons.

The SM is symmetric under locally gauge invariant transformations of the $\text{SU}(3)_C \times \text{SU}(2)_L \times \text{U}(1)_Y$ group. The $\text{SU}(3)_C$ group describes the strong interaction, mediated by the gluon.[4] The $\text{U}(1)_Y \times \text{SU}(2)_L$ group describes the unification of the electromagnetic and the weak forces, mediated respectively by the photon γ and the Z^0 and $W^\pm$ bosons: the electroweak force. The spontaneous breaking of symmetry of this group give rises to the Higgs field, mediated by the Higgs boson, a spin-0 particle explaining the origin of the mass of the Z^0 and $W^\pm$ bosons [10–13]. All

[2] With the exception of gravity as discussed in Section 2.1.5.

[3] The Higgs boson contributes to the phenomenon of mass but is not strictly a force carrier.

[4] There are in fact eight gluonic fields carrying different color charges. As they cannot be distinguished experimentally, one generally refers to the excitation of all the gluonic fields as the gluon.

of these symmetries will be broken apart and detailed in the following sections. A detailed review of group theory applied to particle physics can be found in Ref. [14].

The properties of the particles constituting the SM are summarized in Figure 2.1.

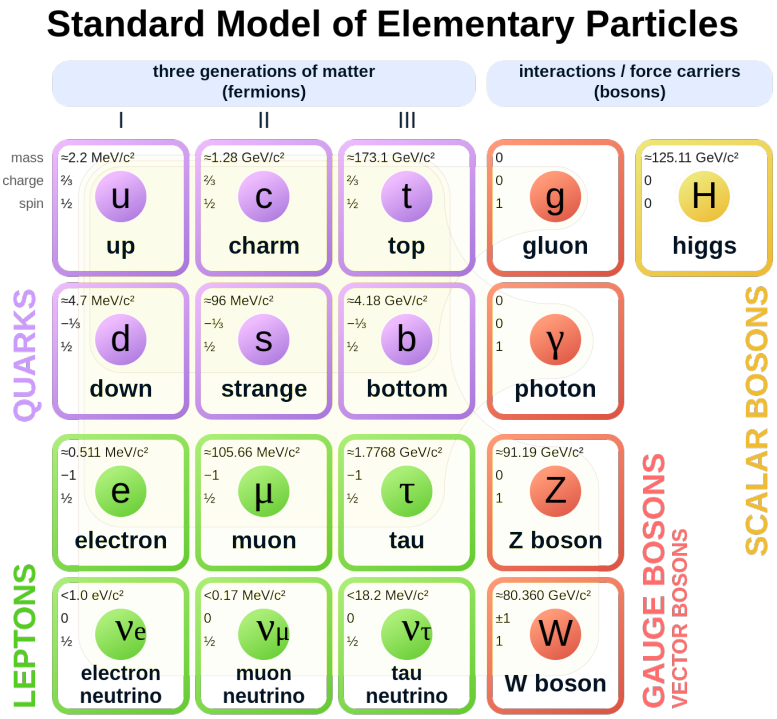

Figure 2.1: Overview of the elementary particles constituting the SM and their properties. Taken from Ref. [15].

2.1.1 Quantum Electrodynamics

Quantum Electrodynamics (QED) is the QFT extension of classical electromagnetism. It describes the interactions between charged fermions mediated by the massless spin-1 photon γ. It is represented by the abelian - meaning that the generators of the group commute, resulting in the photon not self-interacting - $U(1)_{EM}$ group at low energies. Electromagnetism is responsible for keeping negative and positive charged particles bound together (*e.g.* electrons and protons in atoms).

2.1.2 Weak force and Electroweak unification

The weak force is an interaction between all fermions mediated by the $W^{\pm}$ and Z^0 bosons. The weak charged-current interaction violates quark flavour conservation, and is the only interaction in the SM capable of that. The $W^{\pm}$ bosons and the weak force are responsible for β-decays, including the neutron decay into a proton, an electron and a neutrino.

In a letter addressed to the participants of a nuclear conference in Tübingen in 1930, Pauli postulated the existence of the neutrino in order to explain the electron spectrum in β-decay [16], and four years later, a weak force theory analogous to the electromagnetic one followed [17]. This will be later discussed in Section 2.2.1. The unification at high energy scales of the weak and electromagnetic forces was proposed by Glashow in 1961 [7] leading to the prediction of the existence of the Z^0 boson[5]. He proposed a description in terms of the $\mathrm{U}(1)_Y \times \mathrm{SU}(2)_L$ group. This group is non-abelian, resulting in the fact that the force carriers interact with each other. L refers to the left-handed fermions (the handedness of a fermion, also called helicity, is defined as the projection of the spin vector onto the momentum vector: left is negative, right is positive) to which the weak force applies, which have a weak isospin $I = 1/2$. The weak force does not couple to right-handed fermions.

Four gauge bosons, the B singlet for $\mathrm{U}(1)_Y$ and the $\vec{W} = (W_1, W_2, W_3)$ triplet for $\mathrm{SU}(2)_L$ arise from the local gauge invariance in the group's transformations. These bosons then mix to produce the physical state bosons Z^0, $W^{\pm}$ and γ through:

$$\begin{pmatrix} \gamma \\ Z^0 \end{pmatrix} = \begin{pmatrix} \cos(\theta_W) & \sin(\theta_W) \\ -\sin(\theta_W) & \cos(\theta_W) \end{pmatrix} \cdot \begin{pmatrix} B \\ W_3 \end{pmatrix} \tag{2.1}$$

where θ_W is the weak mixing angle, and :

[5]The weak neutral current interaction was observed more than 10 years later in 1973! [18]

$$W^{\pm} = \frac{1}{\sqrt{2}}(W_1 \mp iW_2) \tag{2.2}$$

The observation of the $W^{\pm}$ and Z^0 bosons in the beginning of the 1980's [19, 20] confirmed their existence but also showed them to have a large mass, even though they are predicted to be massless with the electroweak theory alone in order not to break gauge symmetry. The mechanism through which the symmetry is broken (and thus how they acquire mass) will be described in Section 2.1.4.

2.1.3 Quantum Chromodynamics

The strong force describes the interaction between quarks and is mediated by the gluons. It is responsible for the integrity of atom nuclei, binding together protons and neutrons, and is significantly stronger than the electromagnetic force (at the scale of a nuclei) repulsing the protons between each other. The strong interaction conserves colour charge, which can have six possible values (red, green and blue, and their three anti-colours). The quarks (anti-quarks) carry a colour (resp. anti-colour) charge while the leptons are colourless.

The strong force is described at the QFT level by Quantum Chromodynamics (QCD) through the $\mathrm{SU}(3)_C$ group. Similarly to the weak force, it is non-abelian, resulting in the eight gluons interacting with each other and carrying a 2-colour (one colour and one anti-colour) charge. As a consequence, at some point it becomes energetically favourable to form a new quark-antiquark pair from an intermediate gluon when separating two quarks. Therefore, quarks experience colour confinement and cannot be observed in isolation, only in bound colourless states. These states are known as hadrons and are formed in a process called hadronisation. The two major ways to form colourless states are to form quark-antiquark pairs known as mesons, or triple quark or triple antiquark combinations known as baryons or antibaryons. Other arrangements of four or five quarks (tetraquarks and pentaquarks) are also possible and have been observed recently [21, 22].

2.1.4 Spontaneous Symmetry Breaking: the Brout-Englert-Higgs mechanism

As stated in Section 2.1.2, with the electroweak theory alone, there is no mechanism through which the gauge bosons or fermions can acquire mass without explicitly breaking the gauge symmetries upon which the theory is built. The proposed solution is to spontaneously break the symmetry instead, meaning that while the Lagrangian of the theory is invariant under the group transformation, the vacuum of the theory (*i.e.* the state that minimizes the Hamiltonian) is not.

In order to achieve this, the Brout-Englert-Higgs (BEH) mechanism [10–13, 23, 24] introduces a new $\mathrm{SU}(2)_L$ doublet complex scalar field ϕ with a non-zero vacuum expectation value (*vev*), breaking the symmetry of the $\mathrm{SU}(2)_L$ group while keeping overall gauge invariance. An additional term is added to the Lagrangian:

$$\begin{aligned} \mathcal{L}_{\text{Higgs}} &= (\partial_\mu \phi)^\dagger (\partial^\mu \phi) - V(\phi) \\ \mathcal{L}_{\text{Higgs}} &= (\partial_\mu \phi)^\dagger (\partial^\mu \phi) - (-\mu^2 \phi^\dagger \phi + \frac{\lambda}{4}(\phi^\dagger \phi)^2) \end{aligned} \tag{2.3}$$

where the first term describes the interaction of the Higgs field with the electroweak bosons in terms of the covariant derivative ∂_μ, and the second term $V(\phi)$ is the potential. μ^2, the mass parameter can be of any sign, and λ, the self-interaction parameter must be a positive coefficient to achieve stability of the potential.

This potential, pictured in Figure 2.2 and usually referred to as "mexican-hat potential" due to its shape, has an unstable maximum at $V(\phi) = 0$ and a stable (but degenerate) set of non-zero minima. These minima satisfy :

$$\phi^\dagger \phi = -\frac{\mu^2}{2\lambda} = \frac{v^2}{2} \tag{2.4}$$

where $v = \sqrt{\frac{-\mu^2}{\lambda}}$ the vacuum expectation value. The symmetry is spontaneously broken when a physical state is chosen (*i.e.* when the degeneracy is removed). In order to keep the photon massless while giving a mass to the other two vector bosons, the corresponding vacuum state must be:

$$\phi = \frac{1}{\sqrt{2}} \begin{pmatrix} 0 \\ v + h \end{pmatrix} \tag{2.5}$$

with h the SM scalar Higgs field whose excitation is the spin-0 Higgs boson.

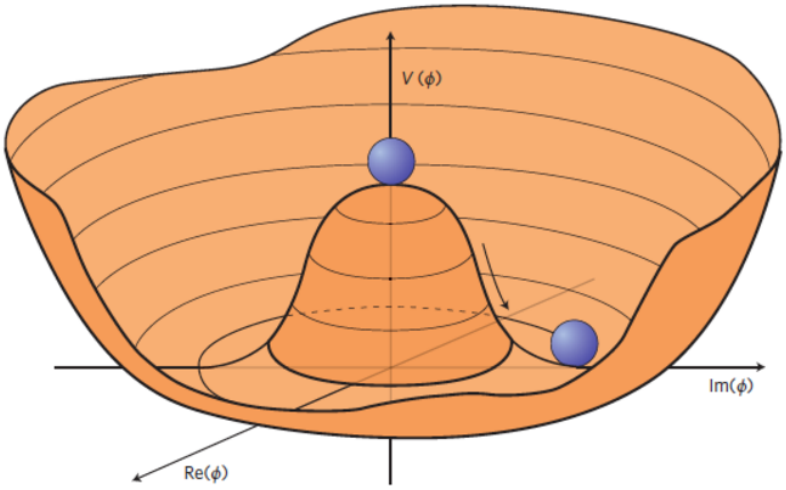

Figure 2.2: Schematic drawing of the Higgs potential in the case $\mu^2 < 0$. Taken from Ref. [25].

With this mechanism, the vacuum expectation value v and the self-interaction parameter λ, *i.e.* the free parameters of the model, dictate the masses of both the intermediate vector bosons $W^{\pm}$ and Z^0 and also the mass of the Higgs boson:

$$m_{W^{\pm}} = \frac{1}{2} v g \quad ; \quad m_{Z^0} = \frac{1}{2} v \sqrt{g^2 + g'^2} \quad \text{and} \quad m_H = v\sqrt{2\lambda} \tag{2.6}$$

where g and g' are $SU(2)$ and $U(1)$ gauge couplings, respectively.

The values of the masses of the intermediate vector bosons are also related to the

weak mixing angle θ_W via the relation :

$$\frac{m_{W^\pm}}{m_{Z^0}} = \cos(\theta_W) \tag{2.7}$$

The vacuum expectation value of the Higgs field is determined experimentally to be $v = 246\,\text{GeV}$ [26]. The current world average measurement for the masses of the intermediate vector bosons and the Higgs bosons are $m_{W^\pm} = (80.377 \pm 0.012)$ GeV, $m_{Z^0} = (91.1876 \pm 0.0021)$ GeV and $m_H = (125.25 \pm 0.17)$ GeV [26]. The mass of the $W^\pm$ in particular is a subject of interest at the time of writing because of the recent publication by the CDF collaboration [27] of a measurement of the $W^\pm$ mass, in significant disagreement (7σ) with the SM prediction.

The introduction of the Higgs field allows the construction of gauge invariant mass terms for the fermions, in the form of terms introducing new couplings g_f called Yukawa couplings, such that the mass of the fermion m_f is proportional to the coupling via the relation $g_f = \sqrt{2}\frac{m_f}{v}$.

2.1.5 Limitations of the standard model

The SM is a successful theory that has been widely tested by generations of physicists, with example measurements for the Large Hadron Collider (LHC) shown in Figure 2.3. This figure shows the comparison between the SM-predicted cross-sections of a variety of processes and their measurements by the ATLAS experiment. The cross section measurements agree well with the theory over many orders of magnitude.

However, this model has some restrictions that will be summarized here, either by considering observed phenomena that are not explained by the model, or by measurements clearly contradicting the model. These are :

- Gravity, one of the four fundamental forces, is not described by the model.

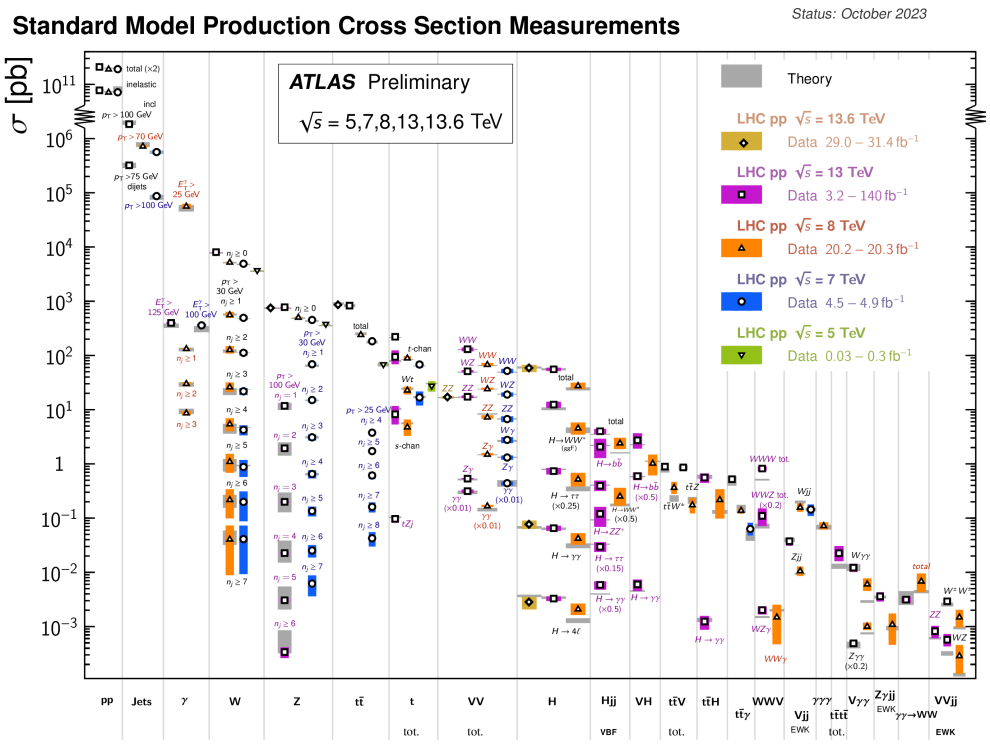

Figure 2.3: Summary of different Standard Model total and fiducial cross-section measurements made by ATLAS compared with their corresponding theoretical expectations. Taken from Ref. [28].

Similarly to the other forces, one could expect the existence of a QFT of gravity with a mediator boson, the graviton. However there is as yet no evidence for this.

- The SM describes the neutrinos as strictly massless particles. However, neutrino oscillations were observed from the sun's emission spectrum and also in atmospheric neutrinos, which are now a well studied phenomenon [29, 30], and can only be explained with non-zero masses.

- Cosmological observations such as the cosmic microwave background studies [31] or the galactic rotation curves combined with the current best description of gravity, General Relativity, lead to other contradictions. These observations imply that the SM only accounts for $\sim 5\%$ of the content of the universe, with the remainder made of $\sim 27\%$ dark matter and $\sim 68\%$ dark energy. Attempts to explain the origin of dark energy within the SM lead to discrepancies with

observations of dozens of order of magnitude [32].

- The observed CP violation in the universe, corresponding to the excess of matter over antimatter is many order of magnitude larger than can be obtained through known SM mechanisms.

- The large number of free parameters (19) makes the SM considered by some to be *ad-hoc*. Moreover, severe fine-tuning of these parameters is needed in order to explain why some forces are much stronger than others.

The different solutions that physicists have proposed to overcome all or part of these problems are described as Beyond the Standard Model (BSM) theories.

2.2 Beyond the Standard Model: Effective Field Theory

One of the common approaches used in experimental high energy physics is to make use of Effective Field Theory (EFT) operators. As an EFT interpretation will be used in the analysis presented in Chapter 6, this section will explain the theoretical framework needed. An EFT is an approximation for an underlying theory at a chosen energy scale.

2.2.1 The Fermi theory

One of the first examples of EFT in high energy physics is the theory proposed by Fermi to explain β decay ($n \rightarrow p + e^- + \bar{\nu}_e$) at the earliest stage of the weak interaction theory development [33]. This theory explains this reaction via a point-like interaction between the four fermions, coupled through Fermi's effective coupling constant G_F.

Fermi theory describes the weak interaction well, but its calculated cross-sections grow as the square of the energy ($\sigma = \frac{G_F^2}{\pi} s$, with s the Mandelstam variable defined as the square of the sum of the incoming particles' momenta), eventually violating unitarity and therefore describing an unphysical behaviour. The theory remains valid for energies below 100 GeV.

Later developments (as described in Section 2.1.2) determined the correct tensor structure of the weak interaction and predicted the existence of the two massive intermediate vector bosons.

2.2.2 Effective Lagrangian

Similarly to the Fermi theory, which is an effective low-energy approximation of the electroweak theory, the state of the art SM can be interpreted as a low-energy approximation of another model. This new theory would also be described by a Lagrangian, which would include the SM Lagrangian. One way to parametrize this new Lagrangian in the most general form is:

$$\mathcal{L} = \mathcal{L}_{\text{SM}} + \sum_{d=5}^{\infty} \sum_{i} \frac{c_{i,d}}{\Lambda^{d-4}} \mathcal{O}_i^{(d)} \tag{2.8}$$

where for a given dimension d, the $\mathcal{O}_i$ are the higher dimension operators[6] and c_i their associated dimensionless coefficients. Λ is the scale of the new physics described by this model, assumed to be at least $\mathcal{O}(10^{15})$ GeV. The ratio c_i/Λ^{d-4} is commonly referred to as Wilson coefficient. The underlying assumption is that new physics has to be at a higher energy scale than the SM. Each order of the expansion is more and more suppressed[7], leading to the fact that the biggest deviation from 0 should be dominant in the lowest-dimension operators. Odd-dimension operators are usually not considered as they violate lepton and baryon number conservation [34]. There

[6] In natural units, the SM Lagrangian has a [mass]^4 dimension.
[7] Each order of dimension d is suppressed by a factor $1/\Lambda^{d-4}$.

are eight dimension-6 operators in the Warsaw basis [35] and thirteen dimension-8 operators described by the Eboli model [36].

The EFTs effects are constrained by experimental data since they lead to changes in the predicted cross sections. Most of the differences are expected to be seen way beyond our current experimental energy reach, but some deviations might be seen (or at least constrained) in some well-chosen kinematic distributions in current data.

All coefficients are expected to be tiny: current analyses (including the one presented in Chapter 6) only constrains them with upper limits.

2.2.3 Anomalous gauge couplings

The different bosons introduced in Section 2.1.2 can only interact in certain configurations allowed by the SM at tree-level (*i.e.* without loops, with only one vertex) due to its abelian structure. Dimension-6 operators can introduce charged anomalous Triple Gauge Couplings (aTGC) while dimension-8 operators are the lowest order which can induce the anomalous Quartic Gauge Coupling vertices (aQGC). Examples include the vertex formed by four Z^0 bosons, or by four photons. As the analysis presented in Chapter 6 aims to provide an EFT interpretation of the $\gamma\gamma ZZ$ vertex (not allowed by the SM), only dimension-8 operators will be considered. The vertices allowed by the different operators of the Eboli model are summarized in Table 2.1.

Table 2.1: Summary of the dimension-8 operators and the corresponding QGC vertices allowed by them. The last row shows the vertices allowed by the SM for comparison.

	$WWWW$	$WWZZ$	$ZZZZ$	$WW\gamma Z$	$WW\gamma\gamma$	$ZZZ\gamma$	$ZZ\gamma\gamma$	$Z\gamma\gamma\gamma$	$\gamma\gamma\gamma\gamma$
$\mathcal{L}_{S,0}$, $\mathcal{L}_{S,1}$	✓	✓	✓	×	×	×	×	×	×
$\mathcal{L}_{M,0}$, $\mathcal{L}_{M,1}$, $\mathcal{L}_{M,6}$, $\mathcal{L}_{M,7}$	✓	✓	✓	✓	✓	✓	✓	×	×
$\mathcal{L}_{M,2}$, $\mathcal{L}_{M,3}$, $\mathcal{L}_{M,4}$, $\mathcal{L}_{M,5}$	×	✓	✓	✓	✓	✓	✓	×	×
$\mathcal{L}_{T,0}$, $\mathcal{L}_{T,1}$, $\mathcal{L}_{T,2}$	✓	✓	✓	✓	✓	✓	✓	✓	✓
$\mathcal{L}_{T,5}$, $\mathcal{L}_{T,6}$, $\mathcal{L}_{T,7}$	×	✓	✓	✓	✓	✓	✓	✓	✓
$\mathcal{L}_{T,8}$, $\mathcal{L}_{T,9}$	×	×	✓	×	×	✓	✓	✓	✓
$\mathcal{L}_{SM}$	✓	✓	×	✓	✓	×	×	×	×

The matrix element of a subprocess can be written as:

$$A = A_{\mathrm{SM}} + \sum_j f_j A_j \tag{2.9}$$

where A_{SM} is the SM amplitude corresponding to the SM cross-section and A_j are the contributions of the different additional operators with their associated Wilson coefficients f_j. In case of only one non-zero Wilson coefficient at a time (an assumption commonly made in analyses), the squared amplitude (proportional to the cross-section) is then:

$$|A|^2 = |A_{\mathrm{SM}} + f_j A_j|^2 = |A_{\mathrm{SM}}|^2 + f_j 2\mathfrak{Re}(A_{\mathrm{SM}} A_j) + f_j^2 |A_j|^2 . \tag{2.10}$$

One can see three terms appearing. $|A_{\mathrm{SM}}|^2$ corresponds to the pure SM contribution, and $f_j^2 |A_j|^2$ to the pure EFT operator contribution. The middle cross-term represents the interference between these two amplitudes, where f_j also appears. Modern generators (examples of such will be given in Section 2.4) are able to simulate the different contributions separately.

Unfortunately these simulations come with the drawback of breaking the gauge structure of the model and therefore violating unitarity at high energy. One of the chosen solutions to this issue is called "clipping". It consists of applying a step-function cutoff to the events generated with an energy greater than a chosen value E_c. It it common to compute limits with several values of E_c: this procedure is called a "clipping scan". The results are then compared with theoretical unitarity bounds [37, 38]. A procedure of this type is applied in Chapter 6.

2.3 High energy physics at hadron colliders

2.3.1 Cross-section calculation

It is possible to measure many features of the SM experimentally. A way of doing this is to make use of a hadron collider, such as the LHC colliding protons at the TeV energy scale. A description of the accelerator as well as the detectors used to measure the products of the collisions will be given in the next chapter.

Protons are hadrons made of a combination of three valence quarks, *uud*, referred to as partons. The internal structure of a proton consists of three valence quarks as well as the gluons that bind them together and also quark-antiquark pairs called sea quarks, any of which can be involved in the hard scatter process during a collision.

The cross-section of a process is closely related to the probability for this process to occur during a $pp \to X$ collision and can be calculated perturbatively (making use of the factorisation theorem [39]) by summing over all incoming partons (taking into account the internal structure of the proton via a so-function called Parton Distribution Function (PDF)) and integrating over the allowed momentum phase-space. It can be written as:

$$\sigma_{pp\to X} = \int dx_i dx_j \sum_{i,j} f_i(x_i, \mu_F^2) f_j(x_j, \mu_F^2) \sigma_{ij\to X} \tag{2.11}$$

where i and j represent the incoming partons, $f(x, \mu_F^2)$ their respective PDFs with x, the Bjorken variable representing the fraction of the proton momentum interacting, and the factorisation scale μ_F, representing the (arbitrary) scale at which the perturbative regime ceases to be applicable. The partonic cross-section $\sigma_{ij\to X}$ is calculated from the matrix element amplitude by summing over the different possible subprocesses (represented by Feynman diagrams). The calculation of the partonic cross-section can be done perturbatively, developing over an expansion on the relevant coupling constant. A simulation considering only the lowest order of the matrix

element is called Leading Order (LO), one simulating the next order is called Next to Leading Order (NLO), and so on adding as many "N" as are needed. Each next order is added in the simulation by considering diagrams with more vertices via virtual loops and initial/final state radiation.

The CT [40] and NNPDF [41, 42] collaborations provide the PDF sets used to compute the hard scatter processes considered in this thesis.

QED corrections become important for the photon fusion physics studied here and one solution is to consider the photon as a parton and include its contribution into the PDF set. This constraint on the PDFs is done assuming incoherent emission from the individual quarks. Another contribution comes at low Bjorken x from coherent photon emission, where the photon can be treated as being emitted from the proton itself, and is usually treated separately.

The threshold where the photon-photon contribution starts to dominate the central production process $pp \to pXp$ is at a system X mass of around 150 GeV [43], well below the mass range considered in the studies presented in this thesis. This is illustrated in Figure 2.4 which compares the di-photon invariant mass distribution due to QCD and photon-initiated central production using the `Superchic` generator [44].

2.3.2 Equivalent photon approximation

In the case of photon fusion physics at low momentum transfer Q^2, instead of including the photon emission in the PDF set, it is usual to compute the photon-induced cross-section using the Equivalent Photon Approximation (EPA). This consists of a convolution of equivalent photon fluxes due to the electromagnetic field emitted by the ultra-relativistic proton. When brought to ultra-relativistic speed, the radial electric field of the proton at rest can be considered as a source of coherent photons travelling in the same direction as the proton. This can be justified by looking at the form of the electromagnetic field strength tensor under a Lorentz boost. A schematic

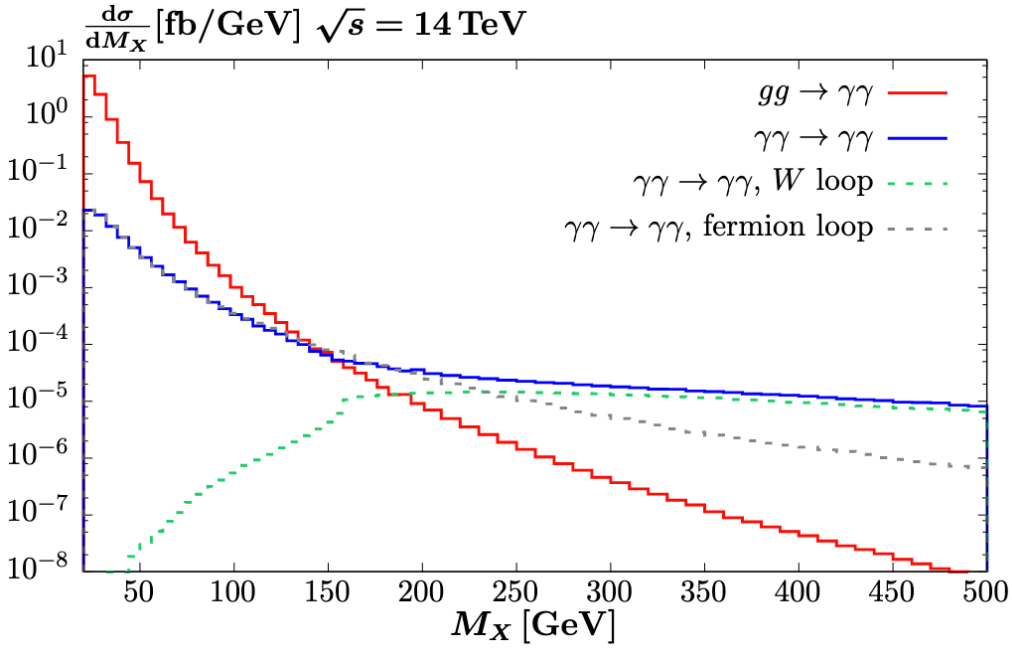

Figure 2.4: Di-photon invariant mass distribution due to QCD and photon-initiated central exclusive production in pp collisions at $\sqrt{s} = 14\,\text{TeV}$. The individual contributions from fermion and W loops to the photon-initiated process are also shown. Taken from Ref. [44].

representing this effect is shown in Figure 2.5. A review and a more detailed justification of this approximation can be found in Ref. [2, 45, 46]. The photon fluxes from the equivalent photon approximation can be included in Equation 2.11 in order to compute a cross-section.

In this procedure, there's a chance that the proton rescatters and produces secondary particles. For a measurement that requires intact final state protons, the dissociation of the proton due to this mechanism is taken into account via multiplying the predicted cross-section with the proton soft survival factor, which is unfortunately not well modelled by simulation (in fact it is reglected in many simulations). The analysis presented in Ref. [6] provides a measurement of this quantity.

Other processes yielding final states with intact protons will be introduced later in Section 4.2 when the physics goals of AFP, the forward subdetector of the ATLAS experiment, will be discussed.

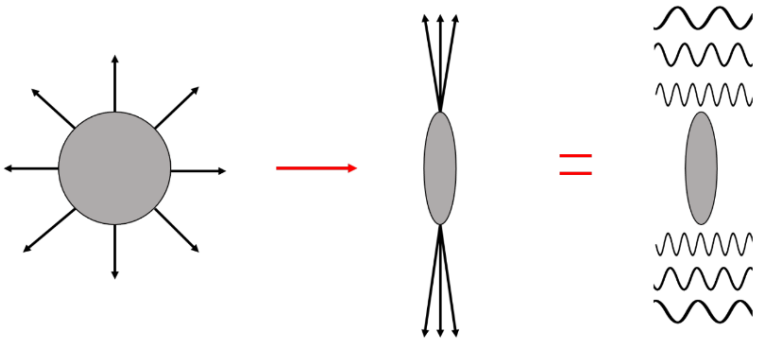

Figure 2.5: Schematic illustration of the EPA. The first image represents a proton at rest and its electromagnetic field lines. The second represents how the field lines are modified when travelling at ultra-relativistic speed. The last image shows how this situation is equivalent to a source of coherent photons. Taken from Ref. [2].

2.4 Monte-Carlo simulations

Monte-Carlo (MC) methods, taking their name from the famous casino located in Monaco, are a class of computational algorithms relying on repeated random sampling to obtain a numerical estimation of a quantity where the analytic answer cannot be easily found (or does not exist). The most basic example is to estimate the value of π by generating random pairs of values between 0 and 1. Each pair of values can be considered as the random coordinates of a point on a squared plane. One can then calculate the proportion of these points falling inside a circle centred in the bottom-left corner of the square (at coordinates (0,0)) with a radius of 1, *i.e.* points satisfying $\sqrt{x^2 + y^2} < 1$. The ratio of points satisfying this condition to the total number of points generated should tend to $\pi/4$ as the number of points generated grows.

MC methods are widely used in high energy physics to model the physics processes studied in hadron colliders [47].

2.4.1 From the matrix elements to the simulated truth particles

The generation of MC samples can be divided into four main distinct steps.

The fist step is to generate the matrix element of the hard-scatter at the desired accuracy (LO, NLO, ...). Thus, only the process of interest is generated. Cross-sections are calculated by summing the different Feynman diagrams together while taking into account the PDFs as described in the previous section. All contributions are then averaged over the different spin configurations of the initial particles. Selection cuts can already be defined at this stage, in order to ensure that the products of the hard scatter are within the kinematic range of interest (*e.g.* matching the detector acceptance).

The second step is to simulate the parton showers and the hadronisation. Parton showers corresponds to QCD radiative corrections to the particles emerging from the high-energy hard scatter. This step transforms the final state to the low-energy regime where quarks and gluons begin to cluster into hadrons. A hadronisation algorithm then groups the systems of partons to form hadrons. These steps both rely on phenomenological models tuned to experimental measurements. Depending on the generator, different models such as the Lund string model [48](*e.g.* `PYTHIA8` [49]) or the cluster model [50–52](*e.g.* `Herwig` [53, 54]) are used to model the hadronisation.

The third step is to simulate the decay of particles such as τ's and unstable hadrons - unstable is defined in practice to mean particles decaying before reaching the detector.

The last step is to overlay the effect of multi-parton interactions, originating both from spectator partons of the hard scatter but also from multiple parton-parton scattering in the same pp interaction.

The whole procedure is pictured in Figure 2.6, using a $t\bar{t}H$ event as an example.

At this stage, the produced samples only contain the kinematic information about the resulting particles after the collision, but before any interaction with the detector. This level of simulation is referred to as the "particle level", or equivalently the "truth level".

There are many existing MC generators, some capable of performing the matrix element computation, others the parton showering and hadronisation, and some both. As already mentioned in Section 2.3.2, some generators are specialised in photon-fusion physics. The samples used in the analyses described in Chapter 5 and Chapter 6 are generated (depending on the process) using `MadGraph` (MG5_aMC@NLO) [56, 57], `Sherpa` [55], `PYTHIA8` [49] and `Herwig7` [53, 54].

- `Herwig7` is used to model the elastic component of the signal process studied in the analysis (and its reproduction by the author) described in Chapter 5. `Herwig7` is a multi-purpose event generator, capable of performing all steps from matrix element generation to parton showering. It is capable of generating matrix elements at NLO accuracy in the QCD coupling, and LO in the QED coupling. It has been coupled with the `BudnevQED` [46] photon flux in order to model the photon-induced interactions described in Chapter 5.

- `MadGraph` is used to generate the elastic and dissociative component of the signal process studied in the analysis described in Chapter 6, but also all EFT samples. It is a matrix element generator that generates processes at LO and NLO accuracy. It is then interfaced with `PYTHIA8` for parton showering and hadronisation using the CT14qed [40] PDF.

- `Sherpa` is used to model the main background process in the analysis described in Chapter 6. Similarly to `Herwig7`, it is a multi-purpose event generator, capable of performing all steps from matrix element generation to parton showering. One of the major differences from `Herwig7` is the different model used for hadronisation.

2.4.2 Detector simulation

Once generated, the truth level particles have to pass through a simulation of the detector to simulate its response. This thesis focuses on the ATLAS detector, which will be described in detail in Chapter 3. The most general simulation of the detector (`FullSim`) fully simulates the geometry of each part of the detector using `Geant4` [58]. Fast simulations are often used to save computational time by using a parametrised version of the subsystems' response. An example is the AFP `FastSim`, which will be detailed in Chapter 4. Chapter 5 describes the author's work on the tuning of this simulation.

The information is then stored in Analysis Object Data (AOD) format, the exact same format that is used to save measured data. A second processing, called a derivation, is often done to skim the sample by reducing the information stored to what is actually needed in a given analysis, resulting in a Derived Analysis Object Data (DAOD) format, smaller in size and therefore easier to work with. These objects are then often transformed to other standard `ROOT` [59] object ntuples. An event skimming is often done at this step based on the analysis event selection requirement. Corrections are also applied at this step, typically in the form of weights applied to the events in order to simulate better the detector performance.

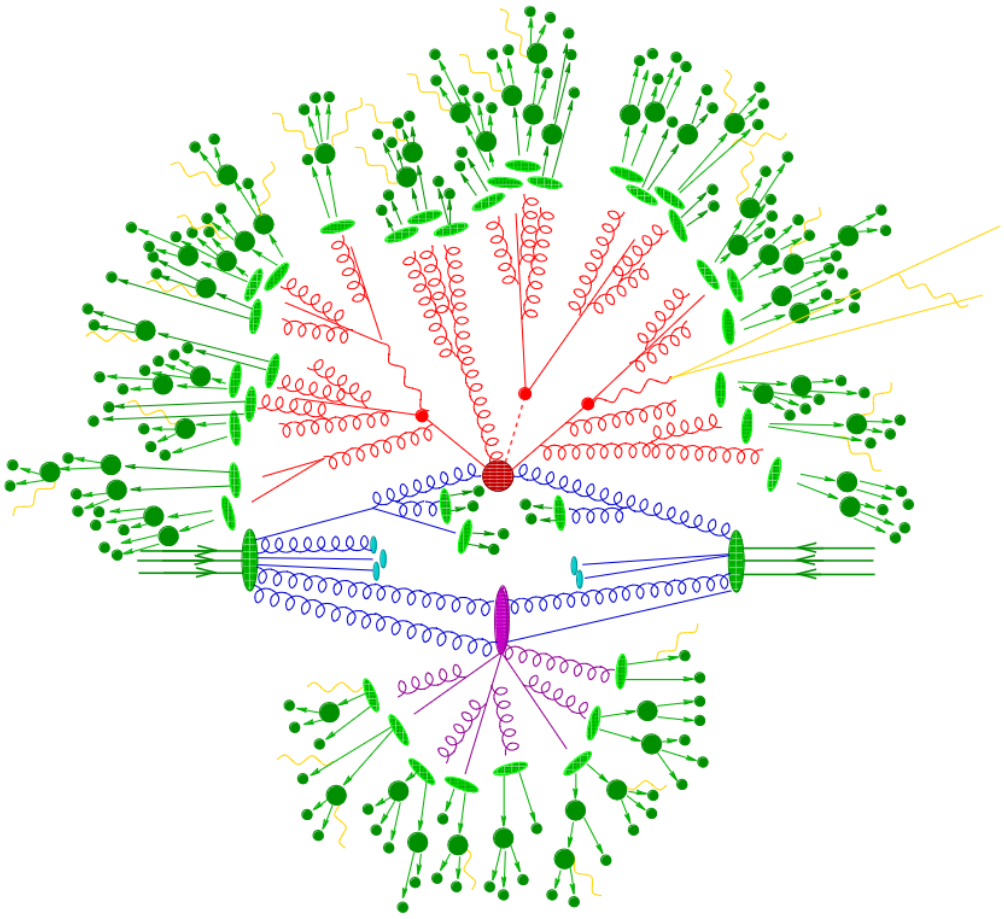

Figure 2.6: Representation of the full simulation procedure for the case of an example $t\bar{t}H$ event. The hard interaction is represented by the big red blob. It is followed by the decay of the two top quarks and the Higgs boson, represented by the small red blobs. Additional hard QCD radiation is produced (red) while a secondary partonic interaction takes place (represented by the purple blob) before the final state partons hadronise (light green blobs) and the hadrons decay (dark green blobs). The photon radiation occuring at multiple stages is represented in yellow. Taken from Ref. [55].

Chapter 3

Experimental setup

This chapter will present an overview of the experimental setup needed to perform the measurements described in later chapters. The particle accelerator needed to perform the collisions which will be studied will first be described in Section 3.1. The ATLAS detector, together with its reconstruction principle, will be presented in the rest of this chapter. As the studied dataset of this thesis was recorded in 2017, the detector will be described as it was at that time.

3.1 Large Hadron Collider

3.1.1 General presentation of the accelerator

The Large Hadron Collider (LHC) [60] is, with a circumference of 26.7 km, the largest accelerator and particle collider in the world. It is located in Geneva at CERN (Centre Européen pour la Recherche Nucléaire) about 100 metres below the surface. Protons (also Pb ions) collide at centre of mass energies up to $\sqrt{s} = 14$ TeV.

The beams of the LHC cross at four points and produce collisions. Each of the

four collision points (Interaction Points (IP)) hosts one experiment. The ATLAS (A Large Torroidal AppartuS) [61] and CMS (Compact Muon Solenoid) [62] experiments are general-purpose detectors. The LHCb (Large Hadron Collider beauty) experiment [63] specialises in the study of flavour physics and the measurement of CP violation and the ALICE (A Large Ion Collider Experiment) experiment [64] studies heavy ion collisions.

In the LHC, two proton beams are sent in two opposite directions at near-light speed. To bend such energetic beams, a magnetic field of 8.3 T is required. Such an intense magnetic field can be generated by electromagnets, at the cost of a high electric current (of the order of 12000 A). Such large currents can only be reached, without Joules losses, using superconductivity. 1232 superconducting electromagnets, 15 meters long, weighing 34 tons each, consisting of niobium-titanium filaments, are cooled to 1.9 K ($-271.3°$C) with 94 tons of liquid helium to allow the bending of the beams. Quadrupole electromagnets are used to focus the beams. The magnet configuration and powering determines the amplitude function β of the beam. The settings are often quoted using β^*: the distance for which the amplitude function of the beam is twice as wide as at the Interaction Point (IP). Small values of β^* indicate highly focused beams. The LHC typically operates with $\beta^* = 0.55\,\mathrm{m}$.

Before arriving in the LHC the protons are accelerated using a series of pre-accelerators. They are first extracted from hydrogen atoms and accelerated in Linear Accelerator 2 (LINAC2) to 50 MeV. They are then injected into the four superimposed rings of the Proton Synchrotron Booster, where their energy reaches 1.4 GeV. They are then accelerated to 26 GeV in the Proton Synchrotron (PS), a synchrotron with a diameter of 628 m, then in the Super Proton Synchrotron (SPS), with a diameter of 7 km, to finally be injected into the LHC at an energy of 450 GeV (see Figure 3.1).

3.1.2 Collisions in the LHC

A key characteristic of a collider is its instantaneous luminosity $\mathcal{L}$:

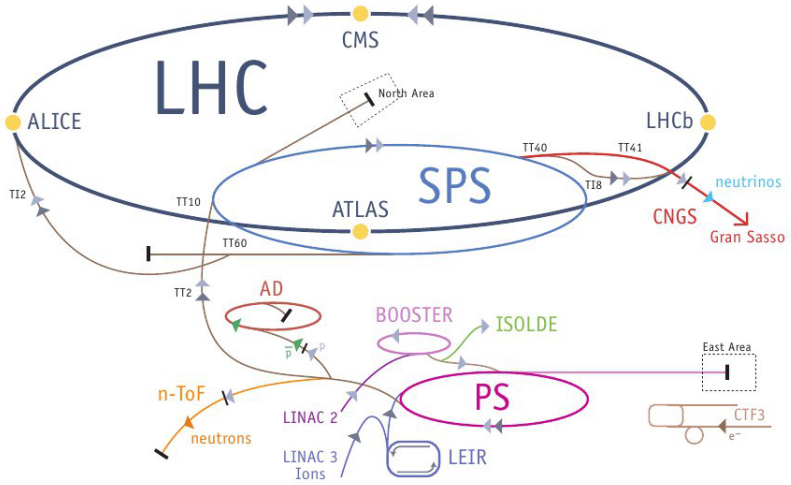

Figure 3.1: LHC accelerator and acceleration circuit. Taken from Ref. [65]

$$\frac{dN}{dt} = \sigma_{tot}\mathcal{L} \tag{3.1}$$

with $\frac{dN}{dt}$ the rate of collision and σ_{tot} the total cross-section for pp collisions. The luminosity measures the number of particle crossings per unit area per unit time [66]. It is given by:

$$\mathcal{L} = \frac{N_b N_p^2 f_{rev} F}{4\pi\sigma_x\sigma_y} \tag{3.2}$$

with N_b the number of bunches, N_p the number of protons within each bunch, f_{rev} the frequency of revolution of the beams, F a geometrical factor taking into account the angle of beam crossing (with $F = 1$ for parallel collisions) and $\sigma_{x,y}$ the transverse sizes of the beam at the IP.

The total integrated luminosity over a period of time is often used as a measure for the total amount of data collected. It is defined for a time T as:

$$\mathcal{L}_{int} = \int_0^T \mathcal{L}(t)dt \tag{3.3}$$

The collisions that take place in the LHC do not occur in isolation, because the protons travel in bunches, each bunch containing about 10^{11} protons. Two bunches cross every 25 ns, and typically several dozen collisions occur at each bunch crossing. Many of the interactions act as background to the collision of interest, because of their spatial proximity. This phenomenon is referred to as "pile-up".

The average number of interactions per bunch crossing is given by:

$$\langle \mu \rangle = \frac{\mathcal{L}\sigma_{inel}}{N_b f_{rev.}} \tag{3.4}$$

with σ_{inel} the inelastic cross-section in pp collision.

These characteristics permit the LHC to deliver pp collisions at a peak luminosity of $\mathcal{L} = 2 \times 10^{34}\,\mathrm{cm}^{-2}\mathrm{s}^{-1}$ today. The periods of data acquisition are called Runs and they are separated by periods without data capture called Long Shutdowns. (see Figure 3.2).

The LHC accelerator will be upgraded during the Long Shutdown 3 (LS3). This is expected to happen between 2026 and 2028. This shutdown will prepare the entrance into a new era of the LHC, the High Luminosity LHC (HL-LHC). Indeed, the luminosity of the accelerator will increase by a factor 3.5, leading to a peak luminosity of $\mathcal{L} = 7 \times 10^{34}\,\mathrm{cm}^{-2}\mathrm{s}^{-1}$ and collisions will occur at $\sqrt{s} = 14$ TeV (see Figure 3.2). During the HL-LHC phase, an integrated luminosity of $\mathcal{L}_{int} = 3000$ fb^{-1} is expected to be reached (in comparison, an integrated luminosity of 450 fb^{-1} is expected at the end of Run 3 in 2025). The number of protons per bunch crosses will increase, resulting in 200 inelastic collisions on average.

This phase will be essential to explore new horizons in physics. Several improvements to the detectors need to be implemented in order to fully exploit the LHC luminosity upgrade.

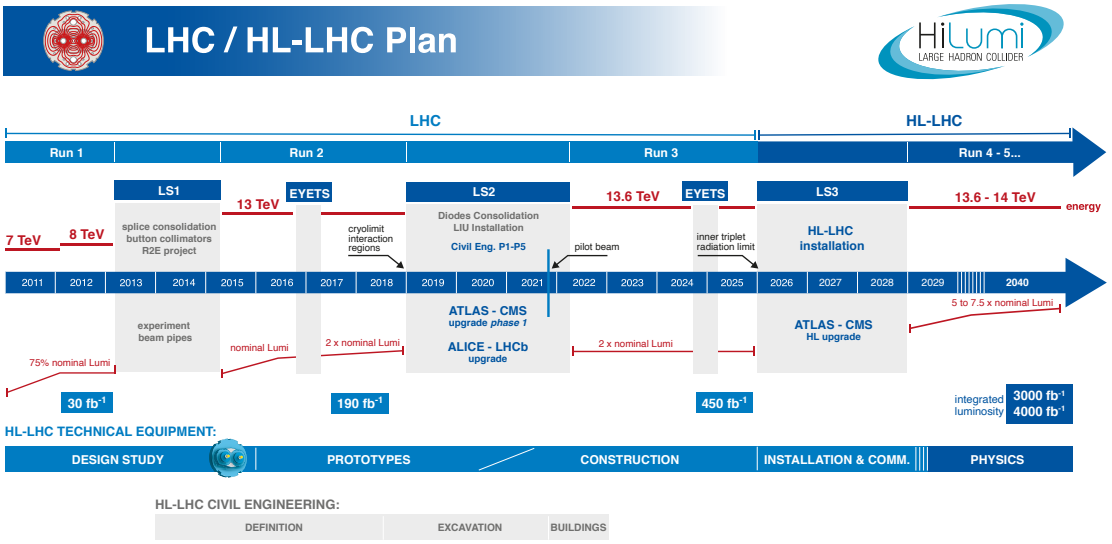

Figure 3.2: Time schedule of the LHC from 2011 to the end of HL-LHC phase accurate as of February 2024. Taken from Ref. [67]

3.2 ATLAS detector

ATLAS is a general-purpose detector designed to perform precision measurements on standard model processes and to search for new physics. The detector makes it possible to measure the energies and momenta of particles and jets produced in the collision. The presence of undetected particles can be inferred from the reconstruction using conservation of four-momentum in the plane transverse to the beam axis. ATLAS has a length of 44 m and a diameter of 25 m. The detector is forward and backward symmetric, and covers almost the entire solid angle around the collision point.

ATLAS is divided into three main concentric sub-systems that will be later described in subsections of this chapter.

- The inner detector, which detects tracks due to charged particles.
- Electromagnetic and Hadronic Calorimeters, mainly responsible for the energy measurement.

- The muon detector.

A system of toroidal (giving its name to the detector) and solenoidal magnets is also present in the detector.

A schematic of the detector is shown on Figure 3.3.

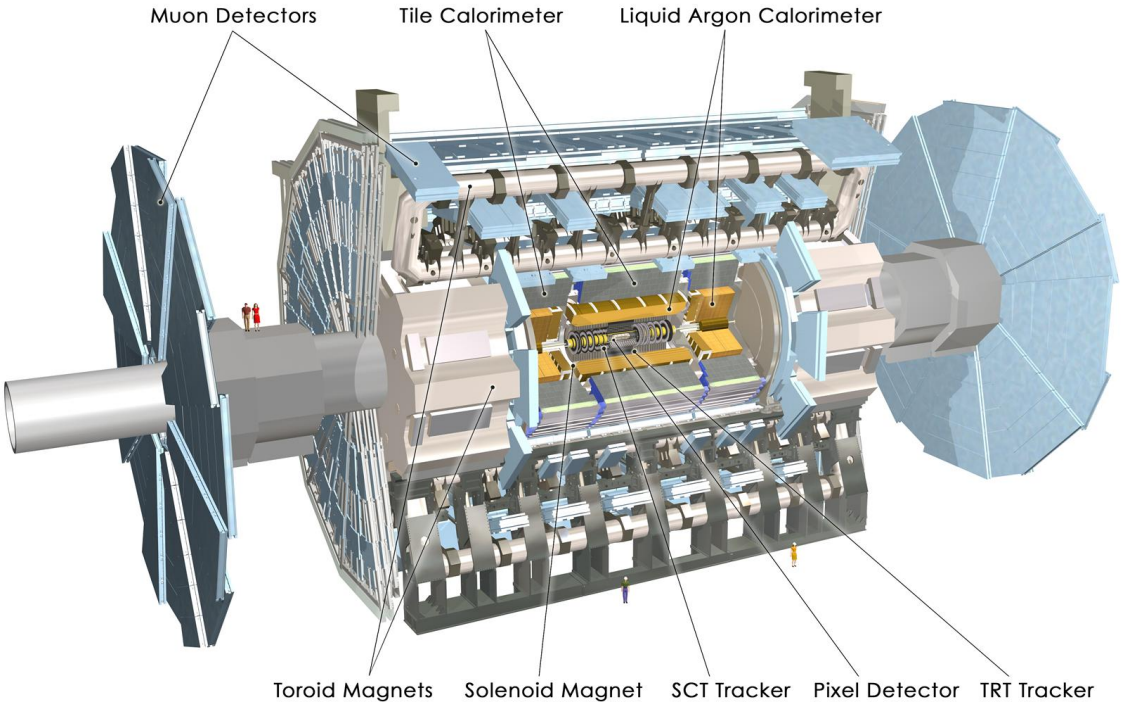

Figure 3.3: Schematic of the ATLAS detector. Taken from Ref. [68]

3.2.1 ATLAS coordinate system

The coordinate system of ATLAS is shown in Figure 3.4.

The ATLAS coordinate system origin is centred at the nominal interaction point. The x-axis points from the collision point to the centre of the LHC, and the y-axis points up vertically. The z-axis is parallel to the beam axis and forms a right-handed coordinate system.

Since the detector is approximately cylindrical in shape, it is useful to introduce a

cylindrical coordinate system. The azimuthal angle ϕ is defined as the angle around the z axis. It measures an angle in the $x - y$ plane, the transverse plane. The polar angle θ is the angle with respect to the beam axis. In practice, the pseudo-rapidity η is used and is defined as $\eta = -\ln(\tan(\frac{\theta}{2}))$. For massive objects, we also use the rapidity defined as $y = \frac{1}{2}\ln(\frac{E+p_z}{E-p_z})$ where E represents the energy and p_z the longitudinal projection of the momentum of the particle. The angular distance (forming a cone) ΔR between two objects can be given as a function of ϕ and η by $\Delta R = \sqrt{\Delta\eta^2 + \Delta\phi^2}$

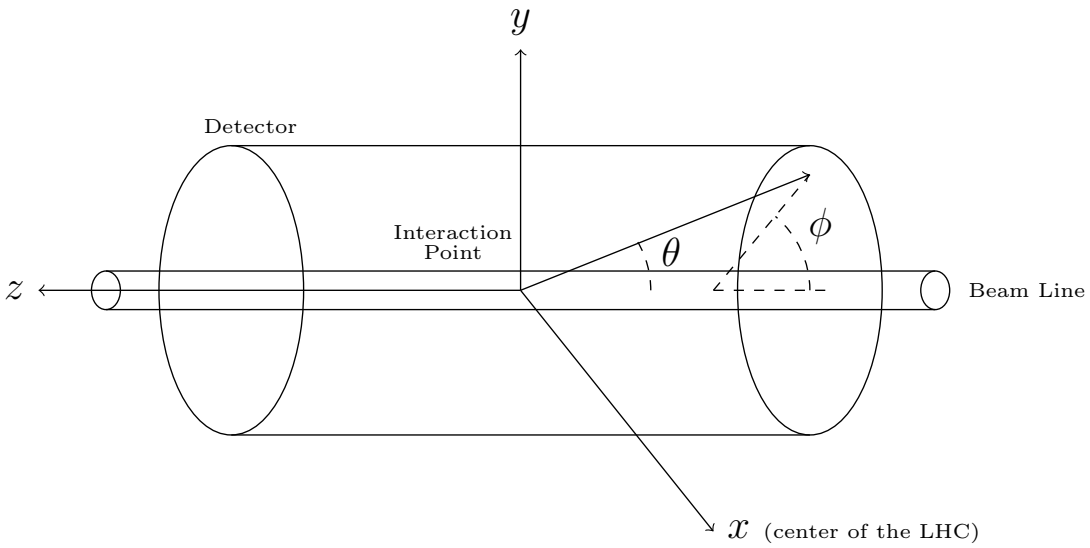

Figure 3.4: The ATLAS coordinate system.

3.2.2 Inner detectors and solenoidal magnets

The Inner Detector (ID), is the ATLAS sub-system located closest to the collision in the central region of the detector (therefore requiring a high radiation hardness). It is a cylinder-shape of 7 m in length and 115 cm in outer (33 mm in inner) radius. The very dense interaction environment requires a high granularity in order to perform track and vertex reconstruction with precision. The ID is composed of three concentric sub-systems, from the closest to the furthest away from the beam: the pixel detector, the Semi-conductor Tracker (SCT) and the Transition Radiation Tracker (TRT). These detectors surround the beam in the central part of the

ATLAS detector and cover a pseudo-rapidity region of $|\eta| < 2.5$. Figure 3.5 shows the structure of the barrel of the ID.

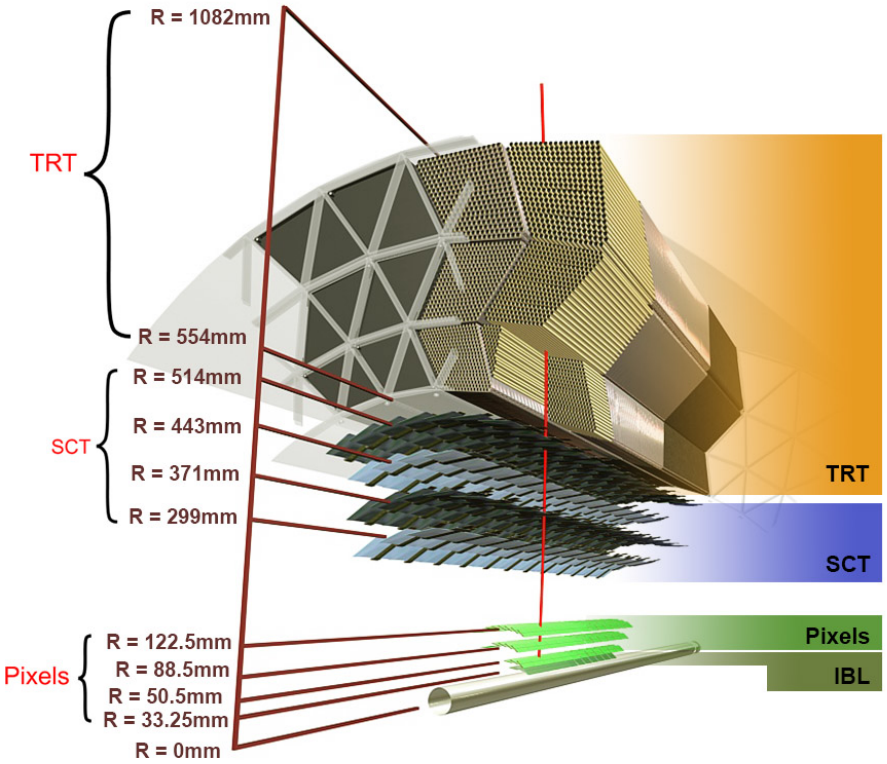

Figure 3.5: 3D visualisation of the structure of the barrel of the ID. Taken from Ref. [69].

Silicon technology is used in the ID but also in a variety of tracking detectors (and also in some parts of the AFP detector later described in Chapter 4) for its radiation hardness, precision and short response time. Silicon is a semiconductor in which there is a small gap (3.6 eV) between the the valence band (highest filled energy level) and the conduction band (next available energy level). Ionising particles passing through the material create an electron-hole pair, drifting to the electrodes under the influence of a bias voltage and creating an electronic signal. However, pure unbiased silicon has more free charge-carriers than those produced by the ionization caused by a charged particle, and the electron-hole pair quickly recombine: the solution is to dope the material and apply a reverse-bias. In "n-type" semiconductors, donor ions from Group V of the periodic table are added, introducing energy levels close to

the lower end of the conduction band, creating a surplus of electrons in the material. In the same way, "p-type" semiconductors are doped with donors ions from Group III, creating a surplus of holes. When the two types are brought together in what is called a "p-n junction", it results in a region free of charge carriers called a "depletion region". The width of this region can be increased by the application of a reverse-bias voltage [70].

The innermost part of the ID is the pixel detector, consisting of three barrel layers and two end caps with three disks each for a total of 1744 silicon sensors. Each sensor is constituted of roughly 46000 pixels with an area of 50×400 µm^2. They are segmented in $R\phi$ and z to provide the 3D position of each hit. The barrel layers have a resolution of $\sigma_{R\phi} = 12$ µm and $\sigma_z = 66$ µm while the end-caps have a resolution of $\sigma_{R\phi} = 12$ µm and $\sigma_R = 77$ µm [71]. These are typical values as the actual resolution depends on η.

The Insertable B-Layer (IBL) is an additional layer installed within the pixel detector for Run 2 to improve the vertex resolution and the identification of short-lived particles, in particular for B-hadron decays. It uses a 3D silicon technology and front-end electronics also used in the AFP detector for its radiation hardness (later described in Chapter 4). Details on the impact on b tagging performance can be found in Ref. [72]. Each charged particle passing through the ID is expected to leave one hit in the IBL and three hits in the pixel detector [73].

The SCT is the next component radially outwards of the ID. It consists of 4088 modules arranged in 4 barrels and two end-caps of nine disks each. Each module is made of silicon microstrips to provide precision points in the $R\phi$ and z coordinates. Two pairs of single-sided strip sensors are glued back-to-back together with a 40 mrad angle between them in order to provide a 2D measurement. The strip sensors have an area of 128 mm × 80 µm and a resolution of $\sigma_z = 580$ µm for the barrel and $\sigma_R = 580$ µm for the end-caps. The resolution of $\sigma_{R\phi} = 16$ µm is identical for both. The system contributes to the measurement of momentum, impact parameter and vertex position [71, 74].

The last part of the ID is the TRT system, consisting of about 50000 gas-filled[1] tubes in the barrel region (and 32000 in the two end-caps regions combined), called straws arranged parallel to the beam in the central region and perpendicularly on the sides. The principle of this technology is similar to silicon tracking: when a charged particle passes through a straw, it ionizes the gas and charges are collected by an anode wire at the centre and converted into an electronic signal. The maximal straw length is 150 cm and the resolution is $\sigma = 170\,\mu m$ per straw. Each particle is expected to hit the TRT system 36 times. The poor resolution of individual straws is counterbalanced by the large number of straws and in total is equivalent to a single point with a resolution smaller than $\sigma \leq 50\,\mu m$ [71, 75–77].

A solenoid magnet encloses the ID generating a 2 T magnetic field. It deflects charged particles via the Lorentz force[2] to enable the calculation of their momenta and determination of the sign of their charge. The solenoid is 44 mm thick and designed to be as thin as possible in order not to deteriorate the later energy measurement in the calorimeters [78]. The chosen technology for the magnets uses an indirectly-cooled aluminum-stabilised superconductor and a vacuum vessel wall is shared with the Liquid Argon (LAr) calorimeter.

3.2.3 Calorimeters

The calorimetry system of the ATLAS detector is designed to measure accurately the energies and position of particles interacting electromagnetically (electrons and photons), particles interacting through strong force (hadrons), to provide some particle identification and to reconstruct the missing transverse energy E_T^{miss} in an event over the available η acceptance.

One can distinguish two subsystems, the Electromagnetic Calorimeter (ECal) and the Hadronic Calorimeter (HCal), designed to reconstruct electron and photon en-

[1] Xe, CO_2, O_2, Ar.

[2] A particle with a charge q moving with a velocity $\vec{v}$ in an electric field $\vec{E}$ and a magnetic field $\vec{B}$ experiences a force of $\vec{F} = q(\vec{E} + \vec{v} \times \vec{B})$.

ergies (ECal) and hadronic particles (HCal), each making use of the different technologies available in ATLAS: LAr and tile scintillators respectively. Additionally, a Forward Calorimeter (FCal) covers the forward region ($|\eta| \in [3.1, 4.9]$).

The calorimeters also serve as part of the Level-1 trigger system later described in Section 3.2.6.

Both subsystems use the same technique, known as sampling calorimetry, where passive and active layers alternate. The passive layers induce electromagnetic or hadronic showers such that the incoming particle is stopped within the volume of the calorimeter. A fraction of such showers (that were not absorbed in the passive layers) are then sampled in the active layers.

3.2.3.1 Electromagnetic Calorimeter

The ECal is designed to stop and measure the energy of the electrons and the photons. It consists of a barrel, inner and outer end-cap, and a FCal. The ECal covers the region $|\eta| < 3.2$. Table 3.1 indicates the detailed $|\eta|$ coverage of each part. The ECal is constructed from Pb absorber and uses LAr as a sampler. The electrodes are accordion-shaped and arranged in four sampling layers, with the highest granularity layer being closest to the beam axis. An additional layer called the presampler in the central region $|\eta| < 1.8$, thinner than the others, takes into account the energy losses in the ID. This layout was adopted to optimize the acceptance while shortening electronic cables for fast readout and limiting dead space [79]. The FCal consists of a LAr module with a Cu absorber optimised for electromagnetic calorimetry.

Table 3.1: $|\eta|$ coverage of each part of the ECal [79].

Section of the ECal	$\|\eta\|$ coverage
Barrel Presampler	$\|\eta\| < 1.52$
Barrel	$\|\eta\| < 1.475$
Endcap Presampler	$1.5 < \|\eta\| < 1.8$
Inner endcap	$1.375 < \|\eta\| < 2.5$
Outer endcap	$2.5 < \|\eta\| < 3.2$
FCal	$3.0 < \|\eta\| < 4.9$

Electrons will interact electromagnetically with the passive layers and emit a bremsstrahlung photon, which will then interact with the field of a nucleus and create an electron-positron pair. The initial electron and the created electron-positron pair will undergo further bremsstrahlung and emit more photons in a chain reaction, up to the point where the energy of the photon reaches $2m_e$ and the pair production will not be possible any more. After, ionization becomes the main contribution to energy loss, creating pairs drifting toward the electrodes. The amount of collected signal is then calibrated to the particle energy.

The ECal is $25X_0$ thick, with X_0 being the radiation length, a property of the material (depending on Z and A the atomic number and atomic mass of the material), defined as the average distance an electron travels through this material before its energy is reduced by a factor $1/e = 1/2.71828...$ via bremsstrahlung [80]. Table 3.2 gives the thickness and granularity separately for each sampling layer. Figure 3.6 shows the barrel ECal structure. The barrel of the ECal is contained within a cryostat cooling the calorimeter to a temperature of 89 K in order to keep the Argon in a liquid state.

Table 3.2: Thickness and granularity of each sampling layer of the ECal[79].

Sampling layer	Thickness	Granularity ($\Delta\eta \times \Delta\phi$)
1^{st} sampling layer	$6X_0$	0.003×0.1
2^{nd} sampling layer	$16X_0$	0.025×0.025
3^{rd} sampling layer	$3X_0$	0.05×0.025

The fractional energy resolution varies thought the ECal but has a typical value of $\frac{\sigma_E}{E} = \frac{10\%}{\sqrt{(E)}} \oplus 7\%$[3] (barrel resolution) [82]. Details about the performance of the LAr calorimeter during the LHC Run 1 and Run 2 are extensively discussed in Ref. [83, 84]. The barrel to end-cap transition region (often referred to as "crack region"), where service pipes and electronics go through, is an area with reduced performance and is often excluded from analyses.

[3]The symbol $\oplus$ indicates a quadratic sum. The first term is called the stochastic term and includes the shower intrinsic fluctuation. The second term is called the constant term and accounts for instrumental effects that cause variations of the calorimeter impact which do not depend on the energy of the particle [81].

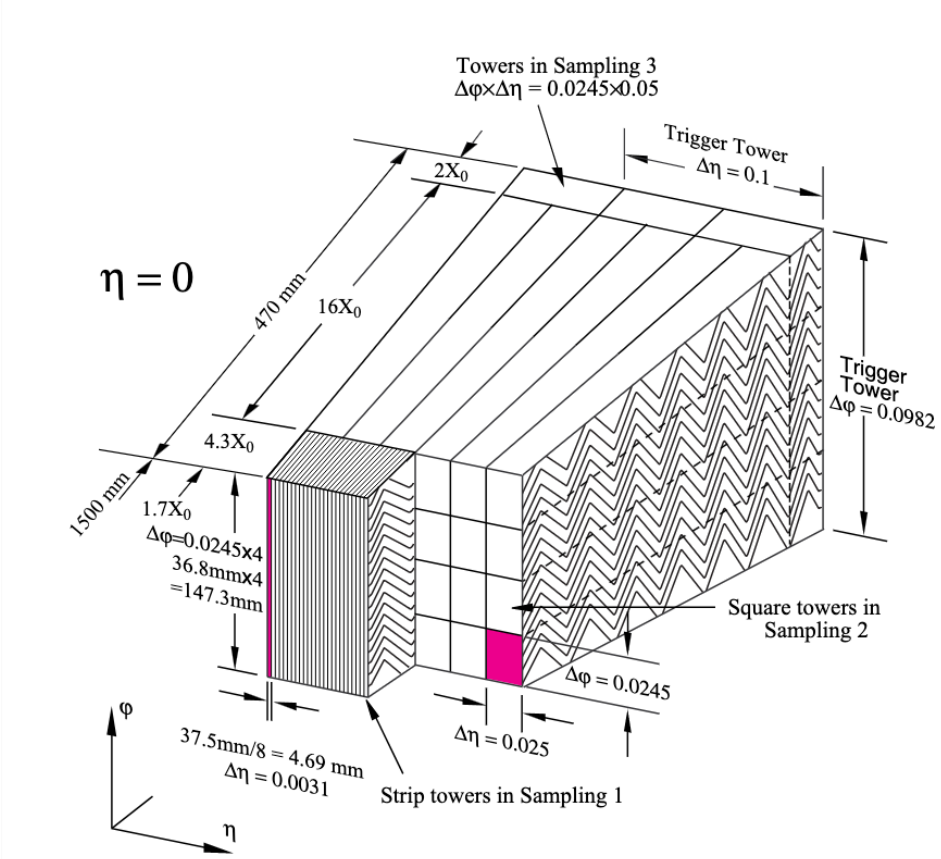

Figure 3.6: Schematic representing the structure of a module of the barrel of the ECal. Taken from Ref. [79].

The ECal, coupled with the information from the ID, can distinguish photons and electrons. Both particles will interact in the same way with the calorimeter, but only the electron, carrying a charge, will give tracks in the ID.

3.2.3.2 Hadronic Calorimeter

The HCal is designed to stop and measure the energy of neutral and charged hadrons (such as pions, kaons, neutrons, protons). It consists of the Tile Calorimeter (barrel and extended barrel), the Hadronic End Cap (HEC) and two Forward Calorimeters (FCal). The Tile Calorimeter covers the region $|\eta| < 1.7$. The detailed coverage of each part of the calorimeter is shown in Table 3.3. The Tile Calorimeter uses modules made of alternating steel (as absorber material) and scintillating tiles (as

active material). An example of a module is shown on Figure 3.7. The HEC and FCal use the same LAr sampling technology as the ECal, with the difference that the absorber is made of Tungsten, optimised for hadronic calorimetry.

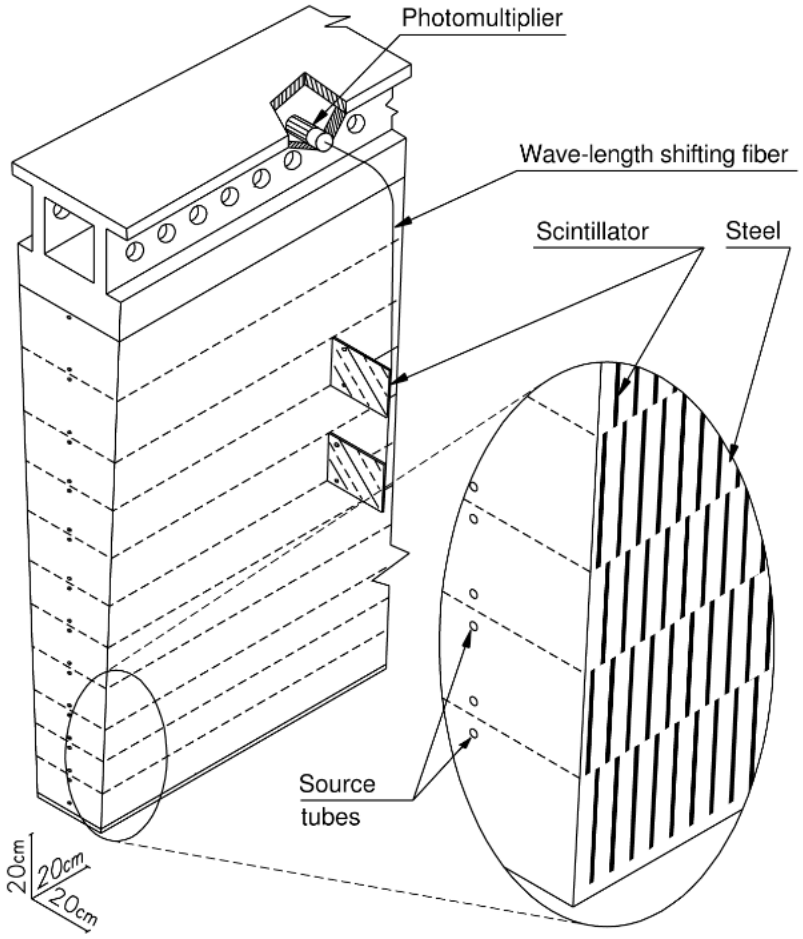

Figure 3.7: Schematic representing the structure of a module the barrel of the HCal. Taken from Ref. [85].

Table 3.3: $|\eta|$ coverage of each part of the HCal [85].

Section of the HCal	$\|\eta\|$ coverage
Central barrel	$\|\eta\| < 1.0$
Extended barrels	$0.8 < \|\eta\| < 1.7$
HEC	$1.5 < \|\eta\| < 3.2$
FCal	$3.1 < \|\eta\| < 4.9$

When particles hit the steel they cause hadronic or electromagnetic showers, producing UV photons in the scintillating materiel. The photons are then collected by

wavelength-shifting optical fibres, converted into visible light, and sent to photomultiplier tubes in order to be converted into electrical signal.

The Tile Calorimeter consists of three concentric longitudinal layers. The detailed thickness and granularity of each layer is given in Table 3.4. Distances are given in terms of λ, the nuclear interaction length, a property of a material, proportional to $A^{-2/3}$, characteristic scale of hadronic cascades, corresponding to the mean distance travelled by a hadronic particle in this material before an inelastic nuclear collision occurs [80].

Table 3.4: Thickness and granularity of each sampling layer of the HCal and FCal.

Sampling layer	Thickness	Granularity ($\Delta\eta \times \Delta\phi$)
Barrel 1$^{\text{st}}$ sampling layer	1.4λ	0.1×0.1
Barrel 2$^{\text{nd}}$ sampling layer	4.1λ	0.1×0.1
Barrel 3$^{\text{rd}}$ sampling layer	1.8λ	0.2×0.1
Extended Barrel 1$^{\text{st}}$ sampling layer	1.5λ	0.1×0.1
Extended Barrel 2$^{\text{nd}}$ sampling layer	2.6λ	0.1×0.1
Extended Barrel 3$^{\text{rd}}$ sampling layer	3.3λ	0.2×0.1
HEC ($\lvert\eta\rvert < 2.5$)	-	0.1×0.1
HEC ($\lvert\eta\rvert > 2.5$)	-	0.2×0.2

The HCal is designed to have a fractional energy resolution for jets better than $\frac{\sigma_E}{E} = \frac{50\%}{\sqrt{(E)}} \oplus 3\%$ within $|\eta| < 3$. Similarly to the ECal, the barrel to end-cap transition region ("crack region" at $|\eta| = 1$) is an area with reduced performance.

3.2.4 Toroid magnets and muon spectrometer

After the calorimeters, only a few particles remain unstopped in the detector. Among them are muons, with a mass two hundred times larger than the electrons, and thus less subject to bremsstrahlung radiation. The outermost component of the ATLAS detector is a spectrometer designed to measure these highly penetrating muons up to $|\eta| = 2.7$ with a resolution of up to 10% for muons with $p_T \simeq 1\,\text{TeV}$. It measures their deflection (using the same principle as the solenoid magnet system described above) by the magnetic field generated by eight flat superconducting coils assembled radially around the beam axis (for muons with $|\eta| < 1.0$) [86] and an end

cap (for muons with $1.4 < |\eta| < 2.7$) [87]. For the transition region (muons with $1.0 < |\eta| < 1.4$), a combination of both bend the muons. The toroids provide an orthogonal field to the muon trajectories.

The superconducting toroid magnet system extends over a length of 25 m with an inner "hole" of 9.4 m and an outer diameter of 20.1 m. The end-caps occupy the radial space between 7.63 m and 12.63 m with a radial span from 1.2 m to 5 m. Each coil is contained within its own cryostat, operating at a temperature of 4.5 K. Figure 3.8 shows a photograph of a prototype of one of the toroid magnets and a schematic of the whole magnet system. Its shape is designed to limit losses in resolution due to multiple scattering. During operation, the end-caps experience an axial force of 320 tonnes toward the center of the detector, and each coil a radial force of 1100 tonnes, thus requiring strong mechanical support.

(a) (b)

Figure 3.8: (a) Photograph of a final prototype of a toroid magnet at $\simeq \frac{1}{3}$ scale. The prototype is displayed in front of the entrance of the ATLAS control room at CERN. A person is standing in front of the magnet for scale. (b) Schematic of the ATLAS magnet system. Both solenoid and toroidal systems are shown. Taken from Ref. [88].

The muon spectrometer is separated into four subsystems: Thin-Gap chambers (TGC), Resistive-Plate Chambers (RPC), Monitored Drift Tubes (MDT) and Cathode Strip Chambers (CSC). The layout of the muons spectrometer is shown on Figure 3.9.

The MDTs and CSCs are designed for precision tracking and they cover a central

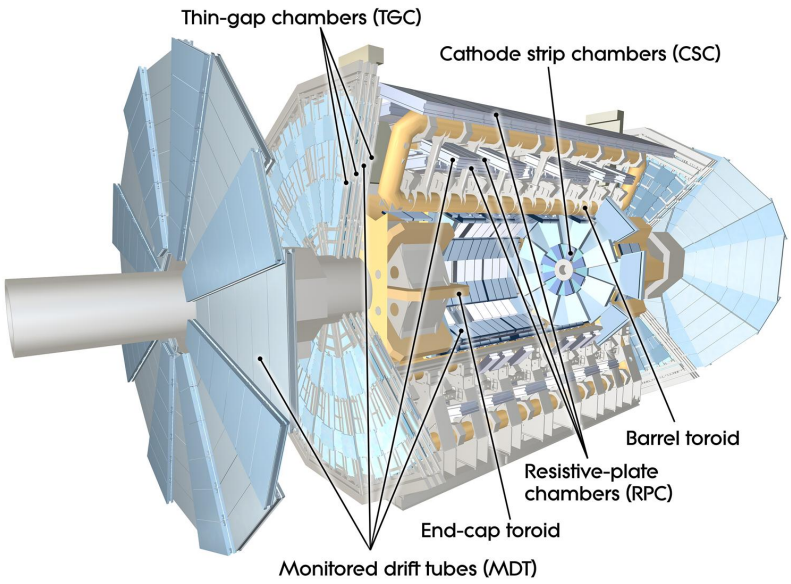

Figure 3.9: Schematic of the ATLAS muon spectrometer. Taken from Ref. [89]

barrel region of $|\eta| < 2.7$, arranged in three layers around to the beam axis but also perpendicular to it in the end-cap regions. The MDTs provide measurement of the track coordinates in the principle bending direction of the toroid magnet system field while the CSCs are used in forward regions close to the beam pipe. The MDTs are made of 1150 chambers arranged in three layers and filled with a mix of CO_2 and Argon at a pressure of 3 bar. They use the same gas-ionisation working principle as the TRT straws presented above. Each chamber consists of three to eight layers of drift tubes, achieving a resolution of 35 µm per chamber (80 µm per tube). The CSC works similarly using the same gas mixture, with cathodes segmented into strips in the orthogonal direction. There are 31000 channels per end-cap spread across 32 chambers each, achieving a resolution of 40 µm (resp. 5 mm) in the bending (resp. transverse) plane. The CSC performance is however better than the MDT at the higher rates expected in the forward regions. They have a fast response time (with drift times $\leq$ 30 ns), time resolution of $\simeq$ 7 ns and good radiation hardness (low neutron sensitivity) [90].

Since the maximum drift time of the MDTs is larger than the LHC bunch-crossing period (25 ns), RPCs and TGCs are needed, forming the muon triggering system.

The RPC is a gaseous detector (filled mostly with $C_2H_2F_4$) with excellent timing resolution ($\simeq 1\,\text{ns}$). The RPC system is made of 373000 channels arranged in 606 chambers. A chamber is made from two rectangular detector layers, each being read out by two series of pick-up strips arranged orthogonally, providing η and ϕ measurements. The TGCs have a similar design to the CSCs, being filled with a CO_2 and n-pentane gas mixture, consisting of layers of wires held at high voltage and surrounded by two cathode planes. The TGC system is made of 318000 channels spread across 3588 chambers. The muon trigger system (RPCs and TGCs) covers a range of $|\eta| < 2.4$ with the barrel coverage ($|\eta| < 1.05$) provided by the RPCs and the end-cap coverage ($1.05 < |\eta| < 2.4$) by the TGCs [90].

The muon spectrometer has an overall momentum resolution of $2-3\%$ across most of the kinematic range, increasing to $\simeq 10\%$ for high momentum muons of $p_T = 1\,\text{TeV}$ [90].

3.2.5 Forward detectors

The ATLAS detector also uses a number of forward detectors to reconstruct particles with very high η that fall outside of the coverage of the other subsystems described above. A brief description of these will be given in this section.

Luminosity Cherenkov Integrating Detector (LUCID) Located 17 m away from the IP on both sides and covering a range of $5.6 \leq |\eta| \leq 5.9$, LUCID [91] is a detector aiming to measure both the integrated and per-bunch instantaneous luminosity. It is made of quartz photo-multipliers. It provides the main online and offline luminosity measurement for ATLAS .

Zero Degree Calorimeter (ZDC) Located 140 m away from the IP on both sides and covering a range of $|\eta| \geq 8.3$, the ZDC [92] provides measurements of neutral particles. As neutral particles are not being affected by the LHC magnets,

the detector is positioned past the point the beam pipes are split into two after being merged for collisions to occur. The detector is used only during heavy ion runs.

Absolute Luminosity For ATLAS (ALFA) ALFA [93] is a Roman Pot (RP)-based detector (see Section 4.1 for explanation about RP) located 237 m and 245 m away from the IP on both sides. It is designed to provide an absolute measurement of the luminosity by measuring intact protons scattered through tiny angles. It has also been used for elastic and soft diffractive cross section measurements.

ATLAS Forward Proton (AFP) AFP is the detector used in most of the work described in this thesis. Therefore Chapter 4 is entirely dedicated to its description.

The position of all ATLAS forward detectors is shown on Figure 3.10.

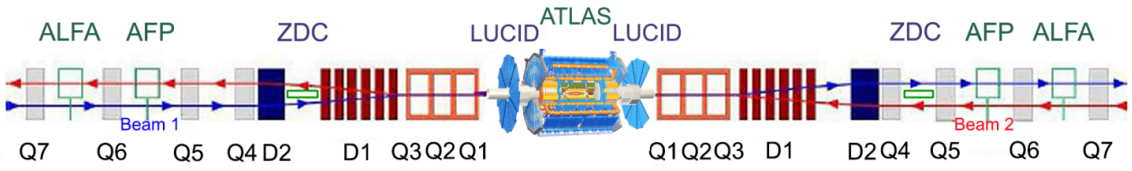

Figure 3.10: Layout of the four forward ATLAS detectors. LHC dipoles and quadrupoles are also shown. In order from the IP toward downstream: LUCID, ZDC, AFP, ALFA. Taken from Ref. [94].

3.2.6 Trigger and Data Acquisition

Proton bunches collide in the LHC at a rate of 40 MHz (every 25 ns) with an average number of interactions per bunch crossing around $\langle\mu\rangle = 35$ at IP1 for Run 2. This corresponds to approximately 1.4 billion collisions per second, corresponding to a data volume of approximately 60 TB per second. One can easily imagine the challenging task to record this quantity of data. However it is not needed, as only a small fraction of these collisions contain information that is ultimately used in further physics analysis. The majority of these collisions are indeed soft processes, usually not considered interesting for physics analyses which tend to study hard-scatter

and/or high mass interactions. Therefore, ATLAS uses a two level Trigger and Data Acquisition (TDAQ) system to decide which events to store and process based on combined information from individual subsystems giving fast measurements of the kinematic properties of objects, discarding the event if no characteristics are above certain predefined thresholds. Figure 3.11 shows a flowchart of the ATLAS trigger and data acquisition system operating throughout Run 2.

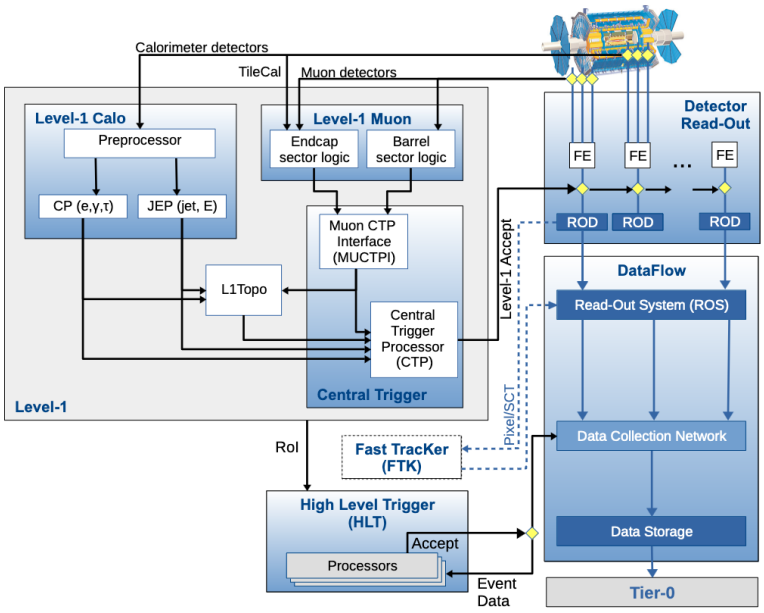

Figure 3.11: Flowchart representing the ATLAS TDAQ system in Run 2. Relevant components for triggering are shown as well as the detector read-out flow. Taken from Ref. [95].

The first level trigger (referred to as L1) [96] is a hardware-based trigger processing a subset of information coming from the calorimeters (L1Calo) and the muon spectrometer (L1Muon). It operates with a latency of 2.5 µs, reducing the data rate from 40 MHz to 100 kHz. It delivers geometric information on where a signal is detected (called Region of Interest (RoI)) as well as the candidate object nature and energy threshold passed. If the event passes the selection, it get passed to the Central Trigger Processor (CTP) which applies a pre-scaling, reducing the trigger-rates of common signatures by processing a set fraction (the prescale) of that signature.

The second level trigger (referred to as the High-Level Trigger (HLT)) [97] is a software-based trigger using the full information provided by the different parts of

ATLAS. It operates with a latency of 200 µs, filtering the data rate coming from the L1 trigger from 100 kHz to more than 2 kHz for permanent storage on the Worldwide LHC Computing Grid (WLCG)[4] and also on tape at CERN. It uses fast versions of object reconstruction algorithms, referred to as online reconstruction, as it is done in real time while new data is being processed by the detector. These reconstruction algorithms are divided into several steps to form trigger chains. Groups of chains are collected into groups of related signatures called trigger menus. Approximately 1500 individual event selections were available in the trigger menu throughout Run 2.

The ATLAS trigger menu reflects the physics strategy of the experiment, aiming for triggers that are as inclusive as possible in order to maximise the physics coverage while remaining open for potential new physics signatures. The trigger configuration is designed to be as flexible as possible, allowing for the possibility of a parametrization of thresholds and prescale on a (close to) run-by-run basis.

3.3 Reconstruction

Information (electrical signals) originating from all subsystems described above needs to be combined together in order to reconstruct physics objects later used in physics analysis. Various techniques are used and will be described in this section. Standard ATLAS objects are tracks, photons, electrons, muons, taus, jets and missing transverse energy E_t^{miss} interpreted as particles not interacting with the detector (neutrinos or BSM particles).

[4]The WLCG provides global computing resources for the storage, distribution and analysis of the data generated by the LHC. It combines 1.4 million computer cores and 1.5 exabytes of storage distributed over 170 sites around the world. All data recorded from ATLAS is stored with redundancy on the grid. [98]

3.3.1 Tracks, Vertices and Beamspot

The reconstruction of charged particle tracks is mainly performed by the ID and must be able to cope with a high number of tracks per event ($\mathcal{O}(1000)$ particles pass simultaneously through the ID during high-pile-up run). Charged particles which do not decay inside the beam pipe and reach the detector are electrons, muons, protons, kaons and pions. Track reconstruction is performed following a series of algorithms and produces tracks with $p_T > 400\,\text{MeV}$ and $|\eta| < 2.5$. Reconstructed tracks are described using a reference point (usually chosen to be the average position of the interactions in the bunch crossing - the beamspot position) and five parameters:

- d_0 is the transverse impact parameter, defined as the transverse distance of the point of closest approach to the reference point.
- z_0 is the longitudinal impact parameter, defined as the longitudinal distance of the point of closest approach to the reference point.
- ϕ is the azimuthal angle of the track momentum at the reference point.
- θ is the polar angle of the track momentum at the reference point.
- q/p is the ratio of the charge of the reconstructed track to the magnitude of its momentum.

The geometric description of these parameters is shown in Figure 3.12.

The first type of algorithm used to reconstruct the tracks is the inside-out algorithm. This algorithm first finds track candidates in the layers of the ID using a combinatorial Kalman filter [100]. Then ambiguities between fake and overlapping track candidates found during the pattern recognition is done, before finally extending them into the TRT. A complementary outside-in pattern recognition algorithm is also used, starting from the TRT and moving inwards to the ID, helping to resolve secondary particles such as photon conversions ($\gamma \to e^+e^-$) which don't always have hits in the silicon detectors. The quality working points are based on kinematic

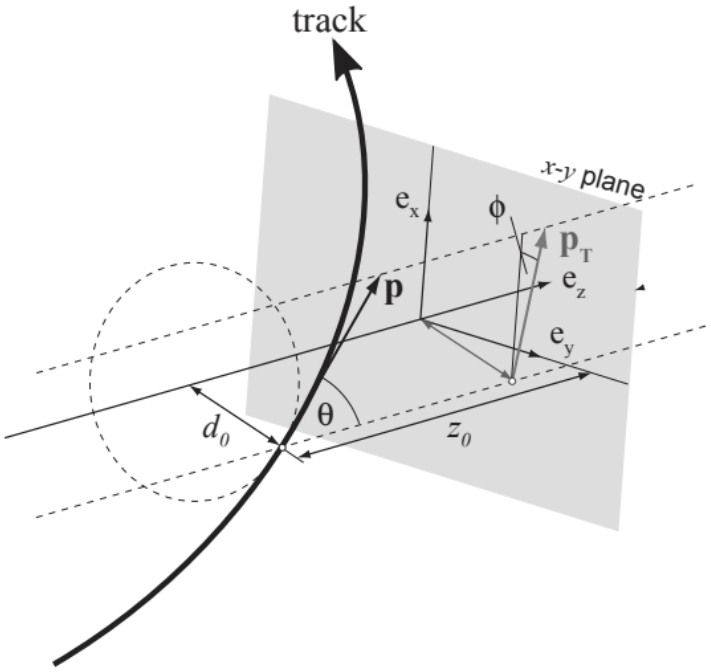

Figure 3.12: Global track parameters in the perigee representation. Taken from Ref. [99].

requirements and the number of hits and missing hits of the tracks. An extensive description of these algorithms and the associated reconstruction qualities is given in Ref. [2, 99, 101]. Figure 3.13 shows the ID track reconstruction efficiency as a function of track p_T and η using minimum bias events.

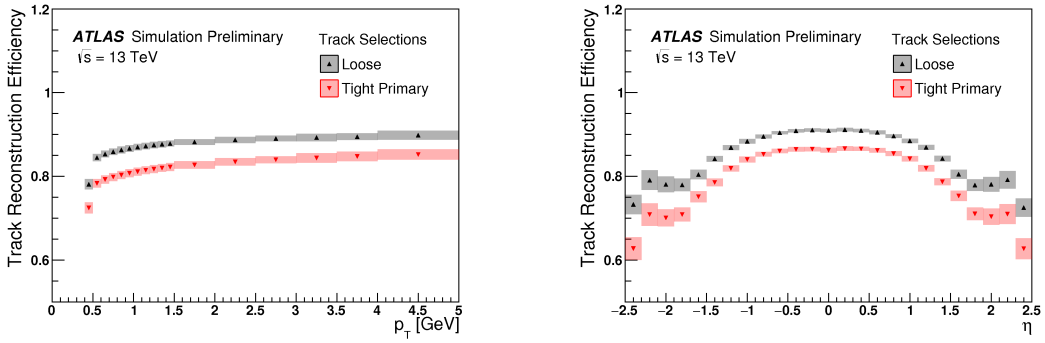

(a) (b)

Figure 3.13: Track reconstruction efficiency as a function of (a) p_T and (b) η for muons at different quality requirements (Loose, Tight Primary). Details of the selection can be found in Ref. [102].

The set of reconstructed tracks in an event is used to reconstruct primary and secondary interaction vertices using an iterative vertex finding algorithm [103], where the Primary Vertex (PV) is defined as the point where the interaction took place, and a secondary vertex where an unstable particle decayed. The vertex reconstruction efficiency as a function of the number of tracks in the event is shown in Figure 3.14.

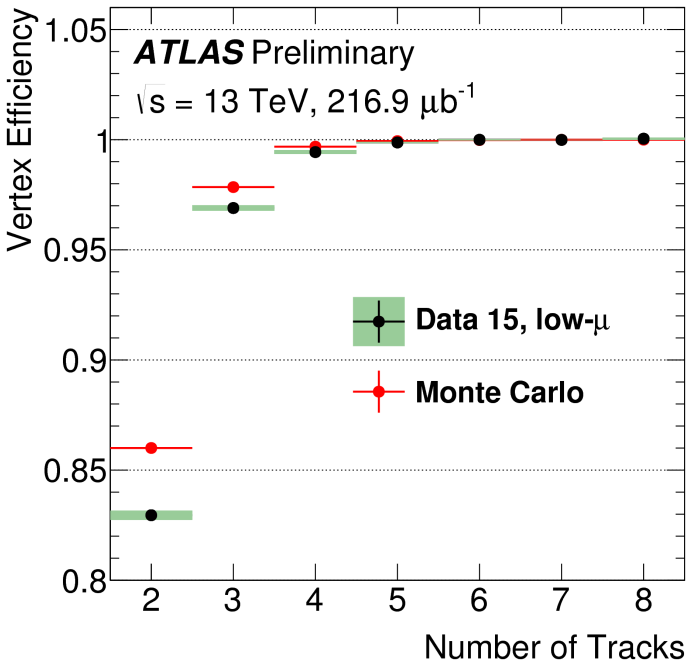

Figure 3.14: Reconstruction efficiency of the primary vertex as a function of the number of tracks of the event in low pile-up (low-μ data). Taken from Ref. [104].

The beamspot is assumed to follow a 3D Gaussian distribution with a longitudinal length of 40 mm and a width of 8 µm. It is reconstructed from an unbinned maximum likelihood fit to the distribution of the PV over thousands of vertices originating from events in intervals of about 10 minutes of data-taking.

3.3.2 Photons and Electrons

Both electrons and photons form showers in the ECal. They are therefore reconstructed in a similar way, the difference being that electrons leave tracks in the ID. Photons can be converted, *i.e.* they interact in the ID forming a e^+e^- pair or unconverted where they just leave a deposit in the ECal.

Energy deposits in the ECal are clustered using a topo-cluster algorithm [105], which clusters together neighboring cells, as long as the signal in the cell is significant (ratio greater than 4) compared to noise. These clusters are then (if possible) matched to a track reconstructed in the ID if they are to be classified as electrons. When there is no track to match, they are classified as unconverted photons. When they are matched with a single track reconstructed in the ID consistent with a photon conversion or a two track vertex fulfilling requirements on the number of hits in the pixel detector layers and in the TRT they are classified as converted photons [106].

Several identification criteria are defined to qualify the reconstructed photons and electrons, based on calorimeter-based and track-based isolation variables for electrons and on shapes of the showers in the calorimeters and isolation for photons. These criteria are then used in physics analysis to better select the signal. Details about the quality requirements can be found in Ref. [107, 108]. Reconstruction efficiencies for electrons as a function of E_T and η are shown on Figure 3.15 while the reconstruction efficiency for unconverted and converted photons as a function of E_T are shown in Figure 3.16.

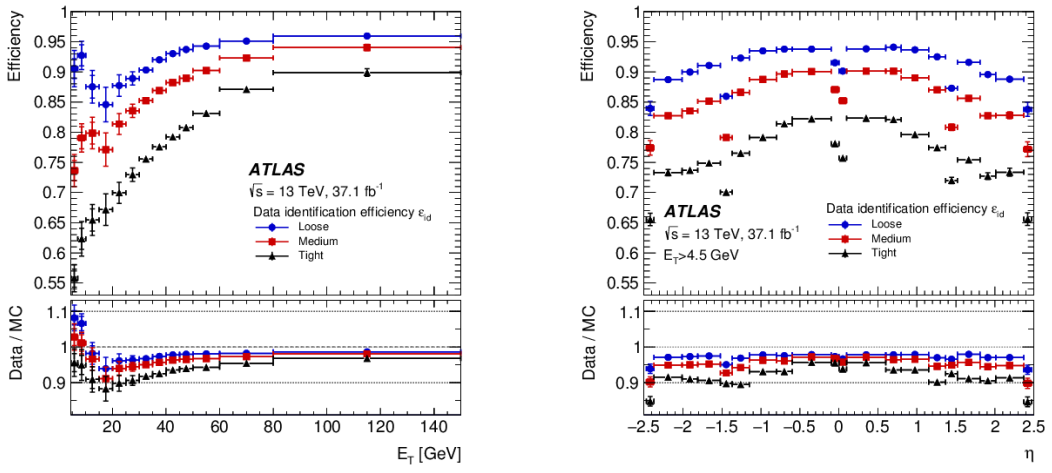

(a) (b)

Figure 3.15: Electron reconstruction efficiency as a function of (a) track E_T and (b) η for several identification criteria. The looser the requirements are, the better is the efficiency. Taken from Ref. [107]

Isolation criteria are also defined based on the amount of hadronic activity in the

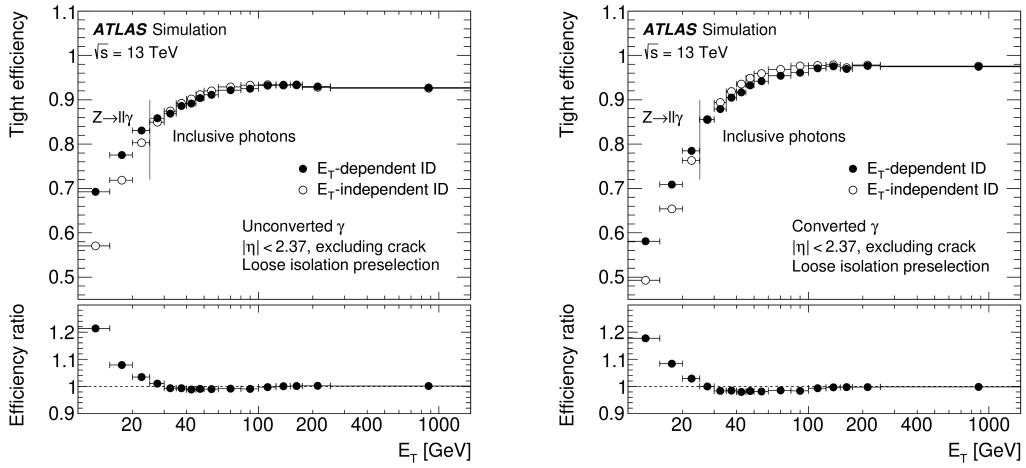

(a) (b)

Figure 3.16: Reconstruction efficiency for unconverted (a) and converted (b) "tight" photons as a function of photon E_T. The description of the event selection can be found in Ref. [109]. The bottom-panel shows the ratios between the E_T-dependent and independent selection efficiencies.

vicinity, more precisely on the transverse energy measured in a ΔR cone around the particle divided by the particle p_T.

3.3.3 Muons

Apart from neutrinos, muons are the only SM particle that reaches the muon spectrometer. Their reconstruction is based on ID, calorimeter and muon spectrometer information. Several types of muons object are defined depending on the subsystem information used for their reconstruction [110]. The first and preferred type is called a combined muon. Tracks are first reconstructed independently in the ID (as described above) and in the muon spectrometer before matching them. Reconstruction in the muon spectrometer is done by searching for hit patterns (using what is called Hough transforms [111]) in each muon chamber to form track segments. Track matching is then done via inside-out (extrapolating ID tracks) or outside-in (extrapolating muon spectrometer tracks, most commonly used) fitting; muon spectrometer hits can either be added or removed from the fit. Another type of reconstructed muon is called a segment-tagged muon, aiming to recover efficiency

losses for low-p_T muons which might not reach all layers of the muon spectrometer. Segment-tagged muons are reconstructed from a single ID track with at least one associated segment hit in the MDT or CSC chambers when extrapolated. Therefore only the ID information is used for the determination of the track parameters. This class has lower purity than a combined muon. The third muon type is called a calorimeter-tagged muon: similar to the previous type but the ID track is matched to a deposit in the calorimeter corresponding to an isolated minimally ionising particle (*i.e.* a muon). This type of muon is optimised for the region of $|\eta| < 0.1$ where the muon spectrometer is only partially instrumented, resulting in it being the type of muon with the lowest purity. The last muon type is the extrapolated (or standalone) muon, where the muon spectrometer track has not matched an ID track but is still compatible with originating from the IP. It is most commonly used in the region $|\eta| \in [2.5; 2.7]$ where the muon spectrometer has acceptance but the ID doesn't. Any overlap between the different types of reconstructed muons is resolved by analysing the track hit content and selecting the track with the better fit quality and larger number of hits [110].

As for the other ATLAS objects, muons are classified with different identification and isolation criteria. A detailed overview of the different quality requirements is given in Ref. [110]. The default identification criteria (*"Medium"*) minimise the systematic uncertainties associated with muon reconstruction and calibration by using only combined and extrapolated tracks.

Figure 3.17 shows the muon reconstruction efficiency as a function of p_T and η for the different identification criteria.

3.3.4 Other objects

The ATLAS detector can also reconstruct other objects, such as taus, jets and neutrinos.

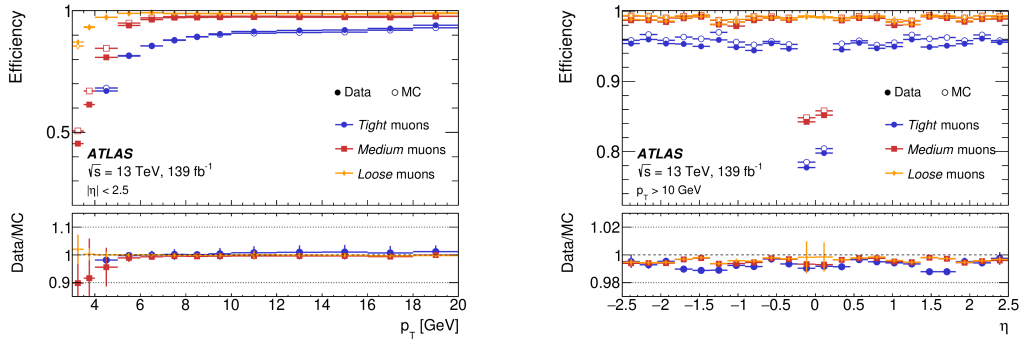

(a) (b)

Figure 3.17: Muon reconstruction efficiency as a function of p_T (a) and η (b) at different quality requirements (Tight, Medium, Loose). Taken from Ref. [112].

- Taus typically decay before reaching the detector: they are therefore reconstructed via their leptonic decay products ($\Gamma_i/\Gamma \simeq 35\%$) or hadronic decay products ($\Gamma_i/\Gamma \simeq 65\%$) [26]. Leptonic taus cannot be distinguished from prompt electrons or muons, therefore only hadronic taus are reconstructed on their own.

- Jets are formed by QCD showers, single quarks hadronising because of QCD confinement, which allows only for colorless states. Jets are reconstructed from ID tracks and calorimeter deposits.

- The presence of neutrinos is inferred from E_T^{miss}. By summing the vector p_T contributions of all reconstructed objects (all objects discussed above in this section) and requiring it to be zero (the total p_T of the event must be conserved), one can indirectly reconstruct neutrinos and other non-interacting particles.

None of these objects are used in the analysis presented in this thesis. They will therefore not be further discussed. Details of the reconstruction and performance of these objects can be found in Ref. [113–115].

Chapter 4

The ATLAS Forward Proton detector

The ATLAS Forward Proton (AFP) detector will be described in this chapter. After describing the physics program, a technical presentation will be made. Then, the different steps of the workflow to go from collisions to usable data will be described. The chapter will end with a description of the performance of the detector evaluated by the Combined Performance (CP) group during Run 2 data-taking.

4.1 General introduction

The AFP system is a Roman Pot (RP)-based spectrometer that reconstructs protons scattered through tiny angles ($\mathcal{O}(\mu\text{rad})$) in elastic and diffractive processes. Roman pots, named after their implementation by the CERN Rome group in the early 1970's, are vacuum-sealed insertions to the beampipe as close to the beam line as possible that host detectors allowing precise measurements. A proton scattered at the IP is deflected outside the beam profile by the lattice of dipole and quadrupole magnets of the LHC. Figure 4.1 shows the AFP system in relation to LHC IP1 where the central ATLAS detector is located. The AFP Roman Pots are located

on both sides of the IP denoted side A ($+z$ direction) and side C ($-z$ direction). Each side (A or C) is also referred to as an arm. Each arm has two Roman pot units, referred to as the NEAR and FAR stations, which are located at longitudinal distances of approximately $z = 205$ m and $z = 217$ m, respectively, from the IP.

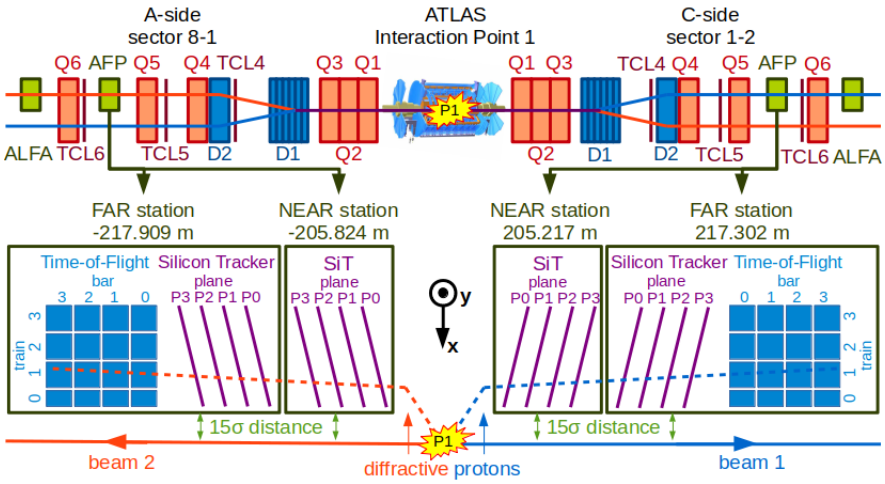

Figure 4.1: Schematic view of AFP in the relation to ATLAS central detector. Taken from Ref. [116].

4.2 Physics goals

The AFP program for LHC Run 2 aimed to perform measurements of soft and hard diffractive processes in standard runs as well as in dedicated runs with a low pile-up (low μ) environment. It also aims to measure photon-induced processes with intact protons.

Due to the QCD factorisation theorem, which applies in the case of hard events with the presence of high-p_T jets or electroweak bosons, the use of perturbative calculations is allowed and these processes are thus quite well understood. In contrast, soft processes are poorly known theoretically because their nature does not permit the use of a perturbative approach. In the absence of a full theoretical understanding, these processes need to be well measured because of their presence as background or pile-up processes to hard processes. Some of these soft processes can be measured

by AFP .

Two kinds of processes can happen in a soft proton interaction: diffractive and non-diffractive processes. Non-diffractive processes involve the exchange of coloured objects, leading to the break-up of both interacting protons and particle production in the central and mid-rapidity regions. On the other hand, diffractive processes involve a colourless strongly interacting object (sometimes referred to as a Pomeron as described by Regge theory) in order for one or both of the protons to remain intact. If the two protons remain intact, the process is referred to as elastic scattering. Also, one or both protons can not remain intact and be dissociated into a multi-particle state. These processes are referred to as Single Dissociation (SD) and Double Dissociation (DD), respectively.

Figure 4.2 shows diagrams displaying the different processes mentioned above.

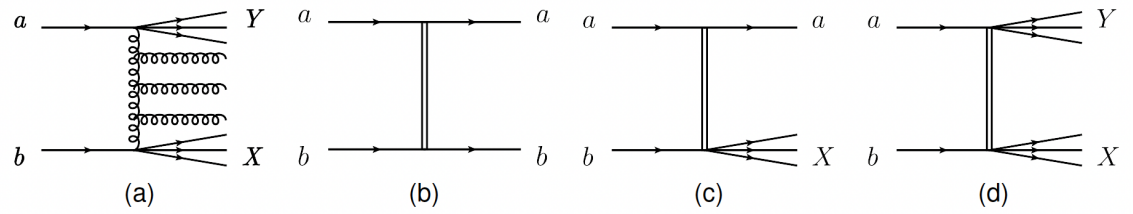

Figure 4.2: Diagrams of soft processes in hadron-hadron collisions: (a) non-diffractive interaction, (b) elastic scattering, (c) single diffractive dissociation, (d) double diffractive dissociation. Taken from [117].

One can also find forward intact protons in events containing a hard scale. Two possible mechanisms can explain such types of interaction for the exchange of strongly interacting particles: Pomeron exchange (as in soft diffraction but where the partons in the pomeron are resolved) and soft colour interactions. The latter suggests that the diffractive signature does not originate from the hard process itself, but rather emerges during the formation of the final state due to exchange of soft gluons. The hard systems considered for AFP measurements in Run 2 are jets (narrow cone of hadrons and other particles produced by the hadronization of a quark or gluon), photon+jet, pairs of photons, and electroweak bosons. A more detailed overview of

hard processes studied with AFP can be found in Ref. [117].

Processes initiated by photon-photon collisions (where one or more protons remains intact) can be studied in AFP as well. So far, two analyses studying photon-induced processes have been published by ATLAS : the observation and measurement of forward proton scattering in association with lepton pairs [6] and the search for an axion-like particle with forward proton scattering in association with photon pairs in the channel $\gamma\gamma \to \gamma\gamma$ [118]. The lepton pair analysis will be described in more detail in Chapter 5 as it is the basis for some of the work presented in that chapter. In Chapter 6, a measurement of forward proton scattering in association with two lepton pairs will be presented.

4.3 Technical description of the AFP detector

4.3.1 Silicon Tracking system

The AFP silicon tracking system (combined with the LHC magnet system) provides detection and momentum measurement of scattered protons in the forward region. Each AFP station houses four pixel sensor layers, each one being a 336×80 pixel grid with a pixel size of 50×250 µm^2 resulting in a total area of 1.68×2.00 cm^2. The planes have a depth of 230 µm in the z-direction (direction of the beam) and are separated by a distance of 9 mm.

A picture of Silicon Tracker (SiT) planes mounted on the heat exchanger is shown in Figure 4.3.

The silicon technology used in AFP is similar to the pixel modules used in ATLAS IBL [119] being based on 3D pixels sensors. The only difference is that the slim edges (inactive regions) of the planes were kept to a minimum on the side of the beam in order to maximise detector acceptance.

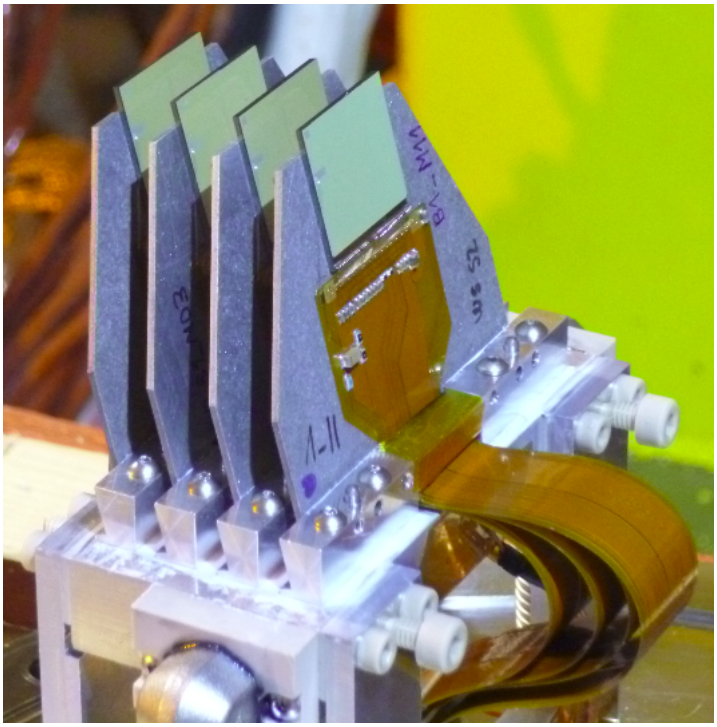

Figure 4.3: Picture of AFP SiT sensor mounted on the heat exchanger. Taken from Ref. [116].

The major difference between the 3D sensor technology and the more standard planar approach is that the n- and p-type electrodes penetrate the substrate in the shape of columns, defining the pixel configuration. This technology requires less bias voltage and cooling to operate than standard planar technology. Also, the reduced drift path induced by this geometry makes these devices more radiation-hard, addressing one of the major challenges of AFP as the detector is regularly placed at a few mm distance from the beam.

The electrodes are 10 µm wide and are doped from both wafer sides. Each pixel consists of 2 n^+-junction columns and 6 surrounding p^+-ohmic columns. A schematic view of the 3D sensor layout is shown on Figure 4.4.

The electrodes are connected through bump-bonding to a pixel readout electronic chip (FE-I4 [120]). This chip and its performance has been studied for the ATLAS IBL detector [121] and has a high radiation hardness, surpassing AFP requirements. The FE-I4 is glued and wire-bonded to a flexible printed circuit to read out the

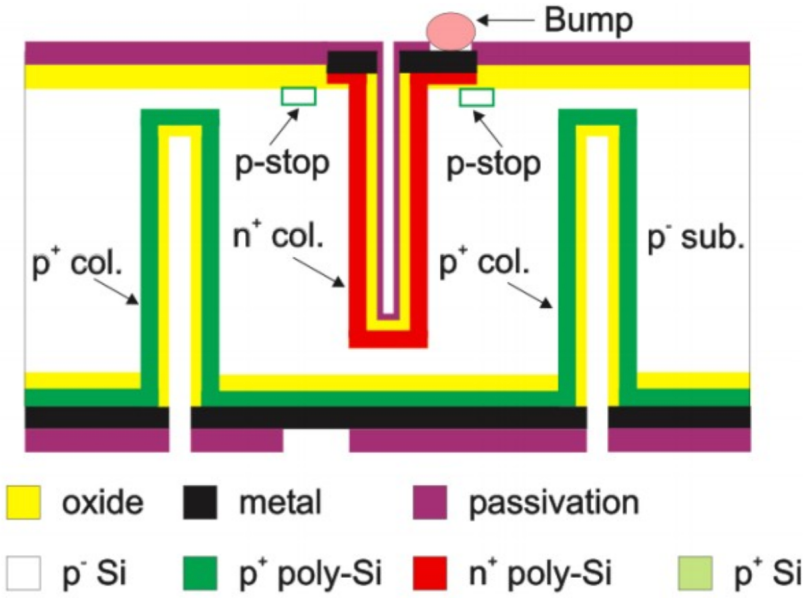

Figure 4.4: Schematic view of AFP SiT sensor. Taken from Ref. [117].

signals.

A more detailed explanation of Silicon tracking techniques, electronics and performance falls beyond the scope of this thesis. More technical details about how this technology was used in the context of AFP and its performance can be found in Ref. [122].

The pixels do not have a square shape: they are shorter in the x direction to maximize the resolution in the direction which the protons are deflected. The deflection in the y direction primarily arises from the non-zero crossing angle at the IP. This results in each plane having a resolution of 14×72 µm in, respectively, the x and y directions. All four SiT planes are also tilted by an angle of 14° about the y axis to maximize the number of pixel hits and thus further improve the resolution in the x direction to about 6 µm by allowing interpolation between neighbouring pixels.

4.3.2 Time of Flight system

The FAR stations also house a high-resolution Time-of-Flight (ToF) detector. The ToF is important in high-luminosity data-taking to provide high pile-up background rejection.

In processes where both protons remain intact and are detected in AFP , the arrival time of the protons can be measured, and thus so can the difference in time of flight from the IP to the detector. This allows a reconstruction of the z position of the interaction vertex z_{vertex} using the following equation: $z_{\text{vertex}} = \frac{c\Delta t}{2} = \frac{c(t_{\text{RightArm}} - t_{\text{LeftArm}})}{2}$ with c the speed of light and $t_{\text{Right(Left)Arm}}$ the time of arrival of the proton in the right (respectively left) arm station. z_{vertex} can then be compared with the vertex reconstructed in the ATLAS central detector with central objects (such as tracks, calorimeter deposits or muon tracks - as discussed in Section 3.3). This allows a high discrimination power between central pile-up events and the events of interest in the case of an analysis. This principle is illustrated in Figure 4.5.

For this, several conditions need to be fulfilled :

- Both detected protons must originate from the same interaction.
- A ToF detector timing resolution of $\mathcal{O}(10)$ ps - resulting in a spatial resolution in the z direction of $\mathcal{O}(1)$ mm and a background rejection power around 20.
- A radiation hard detector to be able to operate at the high dose required.
- Acceptance that matches that of the SiT detectors.
- High efficiency.
- High rate capability of $\mathcal{O}(5)$ MHz.

The design adopted was a quartz Cherenkov detector coupled with a Microchannnel Plate Photomultiplier Tube (MCP-PMT).

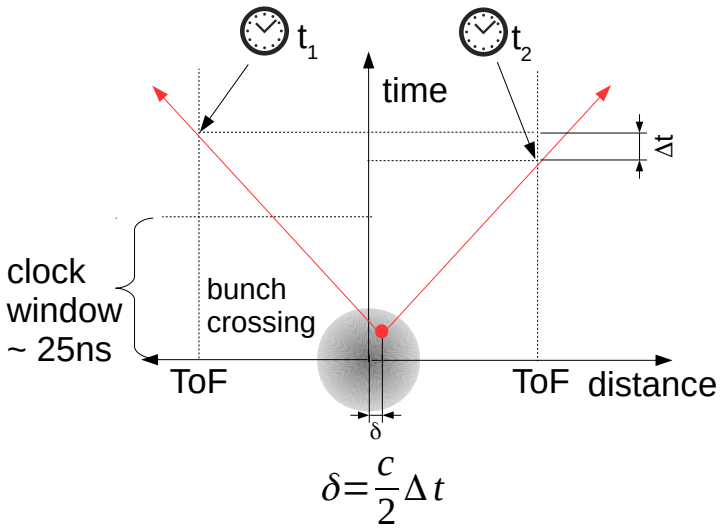

Figure 4.5: Schematic representing the principle of ToF vertex reconstruction. The vertex is represented by the red dot and is located at a distance δ in the z direction from the origin. Protons travel toward both ToF stations and are detected at time t_1 and t_2, separated by a Δt duration. Taken from Ref. [116].

The quartz Cherenkov detector is made of 16 L-shaped quartz bars arranged in a 4×4 layout. Each bar consists of two arms glued together, a radiator arm (tilted though the Cherenkov angle of 48° with respect to the beam axis, optimizing the time needed for light propagation through the bar) exposed to the proton beam, and a light guide arm. The Cherenkov photons are emitted at the Cherenkov angle to the proton trajectory, then propagate to the light guide arm finally to the end of the bars which are attached to the MCP-PMT. A schematic view of a single ToF bar and a photo of the whole set of ToF bars is shown on Figure 4.6

Each set of four bars placed one next to the other is referred to as a train. Each train has a decreasing length to achieve synchronicity of the signals, regardless of the position of the proton with respect to the ToF detector.

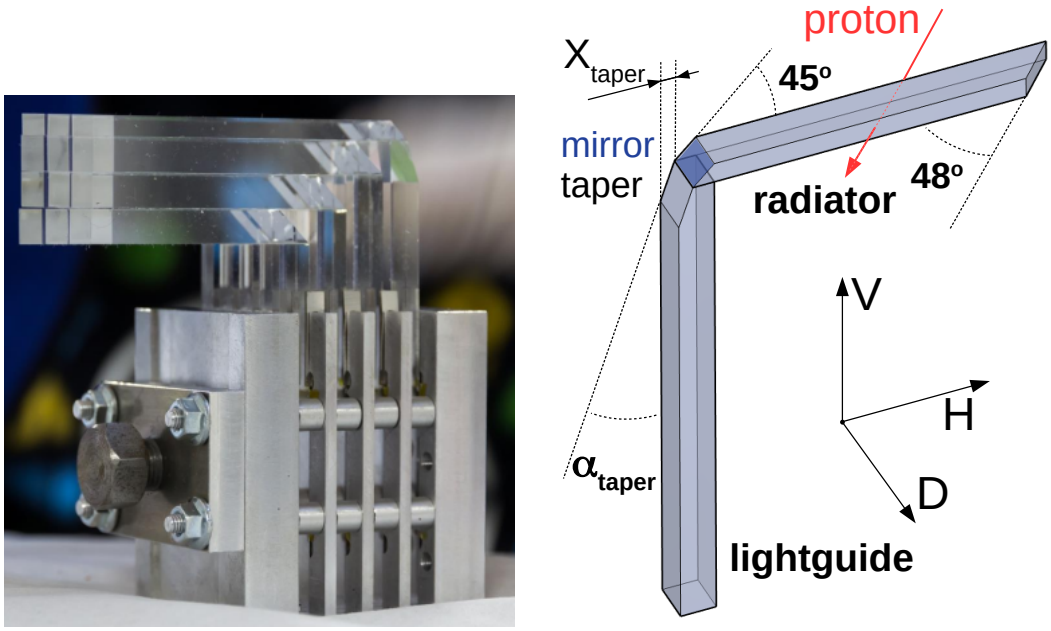

(a) (b)

Figure 4.6: (a) Photography of the ToF detector. (b) Schematic view of a single quartz Cherenkov bar. Taken from Ref. [116].

The Cherenkov photon statistics determine the quantity of photo-electrons through the quantum efficiency of the MCP-PMT. The amplified number of photo-electrons results from the high voltage applied to the micro-channel plates of the MCP-PMT. These voltage pulses from the MCP-PMT anodes undergo amplification and processing through a Constant Fraction Discriminator (CFD), generating a square signal for a High-Performance Time-to-Digital Converter (HPTDC). Sampling occurs in 1024 bins, each of approximately 25 picoseconds, corresponding to the interval between LHC bunch crossings.

The ToF system also has trigger capability, even though the SiT system is used for triggering in normal data-taking conditions.

The ToF detector was not fully operational during Run 2 due to low efficiency of the MCP-PMT. The main work presented in this thesis in Chapter 6 uses a dataset recorded in 2017 during Run 2. The ToF was not used in this analysis thus it will not be further described apart from a short discussion of time resolution in Section 4.8.2. A more detailed review of the ToF detector can be found in Ref. [117, 123].

4.3.3 Trigger

Even though many physics processes that are studied with AFP have a distinctive signature in the central ATLAS detector, for which the ATLAS trigger menu is sufficient, AFP L1 triggers are needed in several cases:

- Processes with forward protons without a clear central signature
- Processes with high central background
- Processes with highly prescaled triggers in other menus

AFP is a detector with a *"high spatial spread"*, meaning here that the two furthest parts are more than 400 metres apart (stations A and C Far). Both are located far away from USA15 where the ATLAS CTP is located, where trigger signals are processed. For this reason, a very fast AFP L1 trigger is needed to take into account the propagation delay, while remaining within the ATLAS L1 trigger latency of around 2.15 µs.

The AFP trigger is made of both SiT and ToF signals and the decision on which one to use is made at the CTP level via a radio frequency switch.

4.4 Reconstruction

AFP provides a proton object to ATLAS inferred from a reconstruction chain that begins with SiT hits. These hits are first clustered, then reconstructed into tracks using a linear regression. Depending on quality parameters set by the user, tracks are reconstructed into a proton object that can be used for physics analysis. The implementation of the reconstruction (and the simulation) in the analysis software is explained in Section 5.4.1.

SiT hits are first clustered within each plane of each station independently. The clustering starts with a first pixel hit which is not (yet) associated with others. This pixel hit is called the cluster seed. A search for other hits is then performed in the x direction (along the long edge direction). If a hit is found adjacently it is added to the cluster and the operation then continues by looking at the next pixel in line. The cluster position is defined as the position in local coordinates of the charge-weighted average position of the pixel centres for the hits constituting the cluster. The geometry of the pixels indicates that it is likely for a proton track to hit multiple pixels in the long-edge direction. The situation is pictured in Figure 4.7. The hit multiplicity is expected to be between one and three [124]. This can be seen by looking at the hit multiplicity distribution of an ATLAS run, shown on Figure 4.8, corresponding to approximately two hours of data-taking.

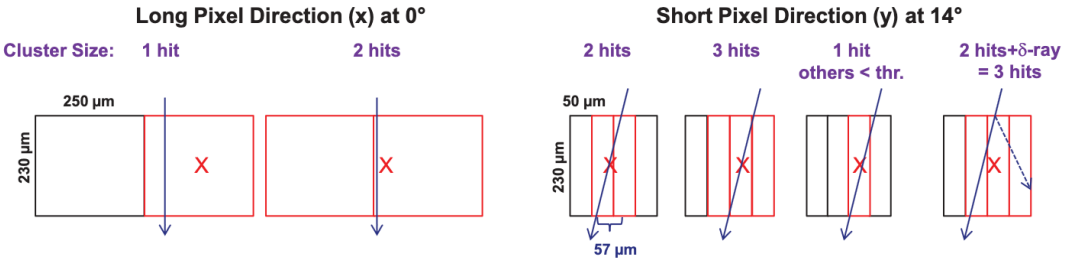

Figure 4.7: Sketch of pixel hits and clusters for the long pixel direction x and the short pixel direction y. The red cross indicates the reconstructed cluster center. Taken from Ref. [124].

The local coordinates of the clusters are corrected for inter-plane misalignment before the track reconstruction. This procedure will be discussed in Section 4.6. The clusters formed in all SiT layers of a given station are next clustered together into super-clusters called "track candidates". Clusters have to be separated by a user-defined maximal distance in the $x - y$ plane. The default value is set at $\sqrt{(\Delta x)^2 + (\Delta y)^2} < 0.05$ mm. The fact that protons travel almost parallel to the beam line permits the track finding algorithm to be simple. Each track candidate is required to have clusters in at least two SiT planes. This avoids reconstructing

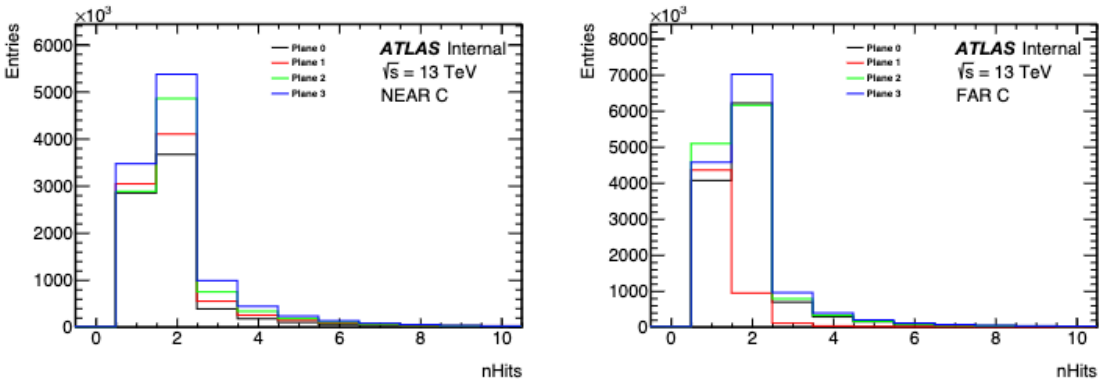

Figure 4.8: Hit multiplicity in AFP clusters for the NEAR (left) and FAR (right) station on side C for a Run. Taken from Ref. [5].

tracks from a single cluster. A linear regression is performed to fit the best track passing through the clusters. The χ^2 test statistic is used to measure the goodness of the fit using the cluster position uncertainties dictated by the pixel resolutions. Figure 4.9 shows a comparison between the pixel hit distribution and the reconstructed cluster distribution in a given plane of AFP , in a given ATLAS run.

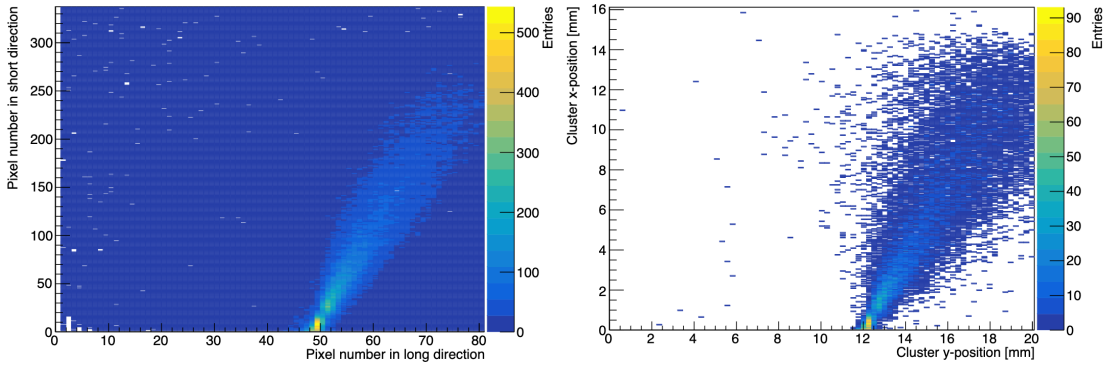

(a) (b)

Figure 4.9: Comparison of pixel hits (a), reconstructed clusters (b) coordinates distributions in plane 0 of the A-FAR station in run 336506. Taken from Ref. [2].

Forward AFP proton candidates are reconstructed from the tracks passing quality requirements. The user can chose the quality of the reconstructed proton from a list of three working points:

- Loose: At least 2 clusters in a track.

- Medium (default): At least 2 clusters in a track, at least 2 planes.
- Tight: At least 2 clusters in a track, at least 2 planes but no more than one cluster per plane.

It is possible to reconstruct protons from one or two Roman Pot stations. This is a user defined option. By default double-station reconstruction is used, and to form a proton, the tracks need to have a separation in the $x - y$ plane smaller than 2 mm. This distance is defined similarly to the distance used for the clustering as: $r = \sqrt{(x_{\text{FAR}} - x_{\text{NEAR}})^2 + (y_{\text{FAR}} - y_{\text{NEAR}})^2}$. If the two tracks fail this requirement, only the track in the FAR station is used for the proton candidate.

4.5 Proton kinematics reconstruction

The kinematic properties of the scattered protons falling in the AFP acceptance are inferred from the track(s) used to reconstruct the proton candidate. The kinematics of the proton are usually expressed in terms of ξ, the proton energy loss given by $\xi_{\text{AFP}} = 1 - \frac{E_{p'}}{E_p}$ with $E_{p'}$ and E_p the energy of the scattered and incoming proton, respectively, and in terms of p_T, the proton transverse momentum.

AFP has a geometric acceptance of protons for $\xi_{\text{AFP}} \in [0.02; 0.12]$. The geometric acceptance in the $\xi_{\text{AFP}} - p_T$ plane is shown on Figure 4.10. It is defined as the ratio of protons with a given (ξ_{AFP};p_T) that reached the detector to the total number of scattered protons having a given (ξ_{AFP};p_T) according to simulations.

The protons are assumed to remain ultra-relativistic (*i.e.* $E/M >> 1$) with tiny scattering angles $p_T/p_z << 1$. Thus, we have $E \sim p_z$.

First, the knowledge of the machine optics is needed to convert the $(x; y)$ coordinates of the proton in AFP to $(\xi; p_T)$, by computing the transport of the proton from the IP to the AFP stations. The more the proton loses energy, the more it will be deflected by the LHC magnets. The strongest correlation with ξ is with x, due to

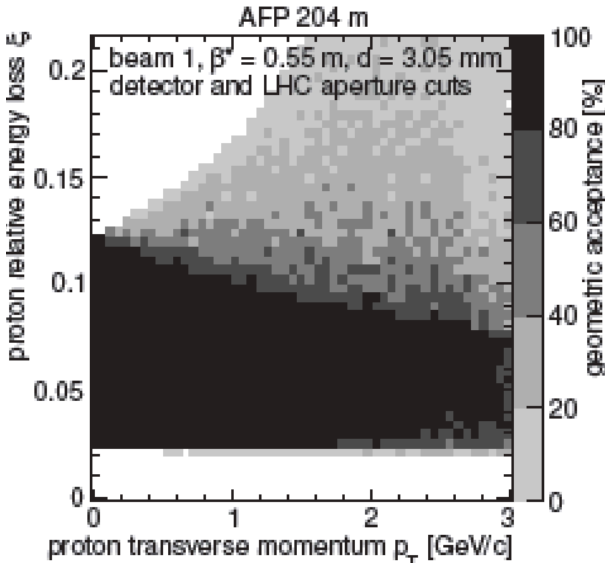

Figure 4.10: Geometric acceptance (grey scale) of the AFP detector in the $\xi_{\mathrm{AFP}} - p_T$ plane, in nominal data taking conditions ($\beta^* = 0.55\,\mathrm{m}$ and $3.05\,\mathrm{mm}$ (15σ) distance from the beam).

the D1 and D2 dipole magnets. The non-zero crossing angle in the vertical direction also leads to deviations in y [125].

A file stores the coefficients and the orders of the polynomials used for the parametrization of the transport function relating the proton position in AFP to its ξ value. Additional information is also saved such as the distance for which it was calculated or the crossing angle [126].

Each p_T value gives rise to an elliptical pattern in the $x; y$ plane, for which the position is determined by the azimuthal degree of freedom (see Figure 4.11 (a)). At large ξ, this dependence leads to ambiguities that can be resolved by the use of the information from the two stations within an arm. This exploits the separation in z of the stations. Figure 4.11 (b) shows for different (p_T, ξ) values the corresponding $(x; y)$ coordinates.

As the y component of the proton momentum p_y is in practice difficult to reconstruct due to its dependence on the crossing angle which changes constantly during the period of data-taking, only the x component is reconstructed in practice.

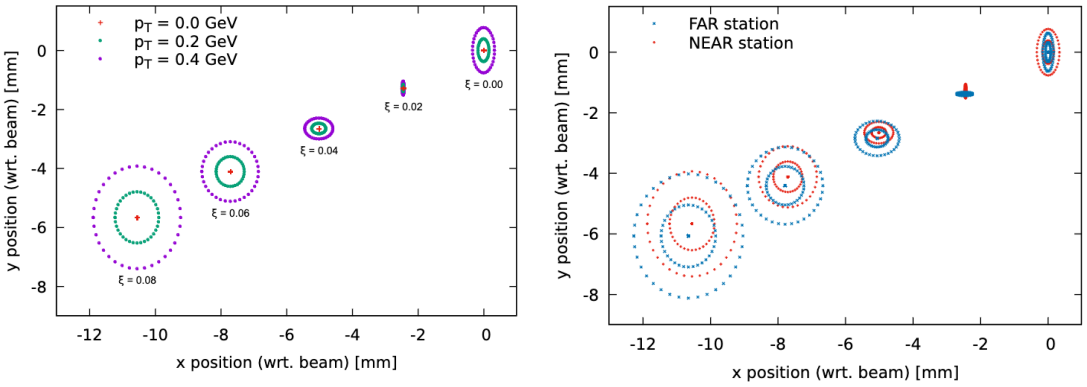

(a) (b)

Figure 4.11: The x and y position of the proton in the AFP planes for various values of p_T and ξ determined from simulation. (a) Values for the A-NEAR stations with equally spaced values of azimuthal scattering angles. (b) Comparison between the NEAR and FAR stations for the same ξ and p_T combinations as in the (a) plot. Taken from Ref. [125].

When information from two stations of an arm is available, the slope of the proton trajectory with respect to the x, z plane, expressed as the difference Δx between the x positions of the two stations, together with the x position in the NEAR station, are used to reconstruct the proton kinematics. The unique mapping between $(x, \Delta x)$ and (p_T, ξ) is shown on Figure 4.12, illustrating how the reconstruction works.

4.6 Local alignment

As mentioned in the previous sections, an important part of the AFP reconstruction procedure is the knowledge of the local alignment, also referred to as the inter-plane alignment; in other words how well the planes are aligned with respect to each other within a station. This has a smaller effect than the global alignment (presented in Section 4.7) on the reconstruction but still needs to be taken into account. An extensive description of this procedure can be found in Ref. [2], which was used as the main reference for this section.

Each plane has six degrees of freedom, three translational (δx, δy and δz) and three

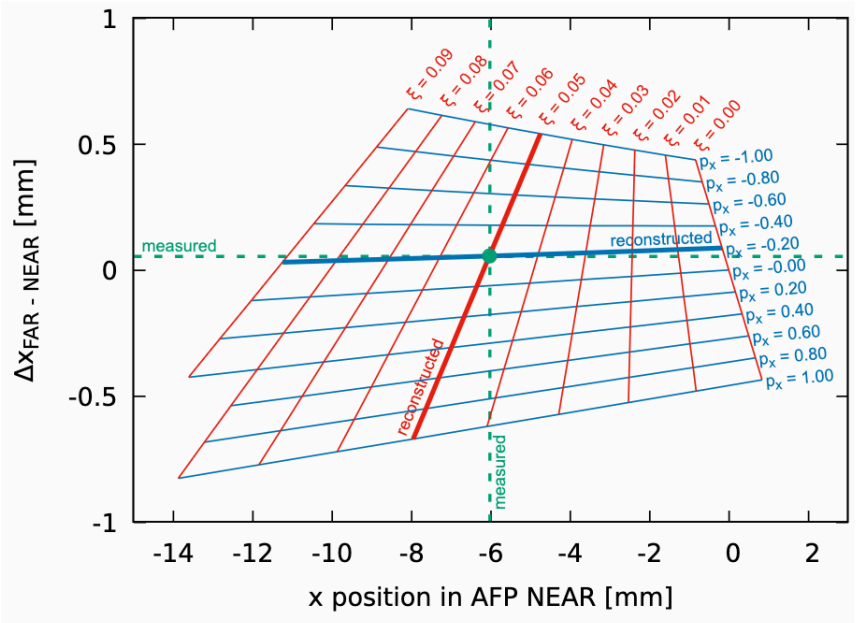

Figure 4.12: Unique mapping between $(x, \Delta x)$ and (p_x, ξ). The green dashed lines indicate an example of measured values of x and Δx, while the solid blue (respectively red) line indicates the corresponding p_T (respectively ξ) reconstructed values. Taken from Ref. [125].

rotational (α, β and γ, the rotation angle about the z, y and x axis respectively). These degrees of freedom are pictured in Figure 4.13.

Each plane is expected to have an offset of the order of 100 μm relative to each other, and a rotation of the order of few mrad.

The measured position vector, denoted $\vec{r_m}$ in the following, can be expressed as the rotation, denoted $\mathcal{R}$ of a perfectly aligned detector, denoted $\vec{r}$ and a linear offset, denoted $\delta\vec{r}$. In the most general form we have:

$$\begin{aligned}\vec{r_m} &= \mathcal{R}\cdot\vec{r} + \delta\vec{r} \\ &= \underbrace{\begin{pmatrix}\cos(\alpha) & -\sin(\alpha) & 0\\ \sin(\alpha) & \cos(\alpha) & 0\\ 0 & 0 & 1\end{pmatrix}\cdot\begin{pmatrix}\cos(\beta) & 0 & \sin(\beta)\\ 0 & 1 & 0\\ -\sin(\beta) & 0 & \cos(\beta)\end{pmatrix}\cdot\begin{pmatrix}1 & 0 & 0\\ 0 & \cos(\gamma) & -\sin(\gamma)\\ 0 & \sin(\gamma) & \cos(\gamma)\end{pmatrix}}_{\mathcal{R}=\mathcal{R}_x\cdot\mathcal{R}_y\cdot\mathcal{R}_z}\cdot\underbrace{\begin{pmatrix}x\\ y\\ z\end{pmatrix}}_{\vec{r}} + \underbrace{\begin{pmatrix}\delta x\\ \delta y\\ \delta z\end{pmatrix}}_{\delta\vec{r}}\end{aligned} \tag{4.1}$$

Using the fact that $\alpha, \beta, \gamma << 1$, with the small approximation angles, equation

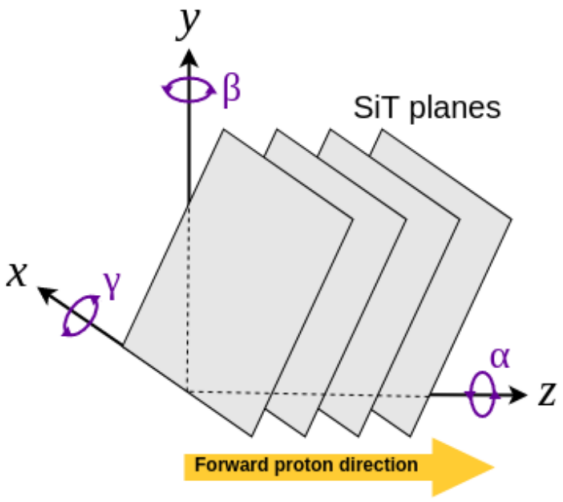

Figure 4.13: Sketch representing the six degrees of freedom of the AFP planes expressed in the local AFP coordinates, with the origin typically measured from the corner of the first plane of a given station. Taken from Ref. [2].

(4.1) becomes:

$$\vec{r_m} = \begin{pmatrix} 1 & -\alpha & \beta \\ \alpha & 1 & -\gamma \\ -\beta & \gamma & 1 \end{pmatrix} \cdot \begin{pmatrix} x \\ y \\ z \end{pmatrix} + \begin{pmatrix} \delta x \\ \delta y \\ \delta z \end{pmatrix} \tag{4.2}$$

As the true position of the proton is unknown, we start by considering the reconstructed track coordinates. The difference between the position of the measured clusters and the reconstructed track position in x and y is given by:

$$\begin{aligned} \Delta x &= x_m - x = -\alpha y + \beta z + \delta x \\ \Delta y &= y_m - y = \alpha x - \gamma z + \delta y \end{aligned} \tag{4.3}$$

with x_m and y_m being the x and y components of $\vec{r_m}$.

When differentiating these expressions with respect to the respective coordinates,

expressions for α, β and γ are obtained:

$$\begin{aligned} \frac{\partial \Delta x}{\partial y} &= -\alpha; \quad \frac{\partial \Delta x}{\partial z} = \beta \\ \frac{\partial \Delta y}{\partial x} &= \alpha; \quad \frac{\partial \Delta y}{\partial z} = -\gamma. \end{aligned} \tag{4.4}$$

An iterative algorithm is used to compute the alignment of the detector. One starts by assuming perfect alignment, *i.e.* $\alpha; \beta; \gamma; \delta x; \delta y; \delta z = 0$. Then, for many events in an ATLAS data-taking period, tracks are reconstructed from the SiT hits assuming these values, as presented in Section 4.4, with the difference that the tracks are required to have a zero slope. This is done by replacing the linear regression by taking the average position of the clusters in x and y as the track position. The allowed distance between the clusters in the track reconstruction is set to 0.5 mm, removing tracks at large angles, likely to originate from showering. Exactly one track per station per event is required.

Cluster-track residuals are then computed in x and y. For a perfectly aligned detector, this would result in a sharply peaked distribution centred around zero. The mean value of the residual distributions is used for the value of the offset in the respective direction. A linear fit is then performed on the plot of the residuals versus the respective coordinate axis. The slope of this fit is used as the value for the rotational correction (from Eq. (4.4)). Among the two possibilities available to compute α, the measurement of Δy versus x is chosen due to the better resolution in the y-direction. The values for the correction are updated and the same process is iterated until the parameters converge to a steady value. Tests were done in Ref. [2] and the chosen value ended up to be 10 iterations.

A reduced$-\chi^2$ selection, χ^2/NDF, with NDF the number of degree of freedom, is applied and the iteration is done again. This iterative process justifies further the use of the small angle approximation, each correction of higher order ending up to be smaller and even more negligible at each iteration.

Figure 4.14 shows a simplified version of the procedure in one dimension. In reality, all six parameters are corrected per plane. All stations are corrected independently, considering the first plane of the station as a reference. A degree of freedom is removed by assuming that the z positions of the planes are known exactly, an appropriate assumption as the differences in z will not affect the track reconstruction. A similar assumption stands by considering only rotation about the z axis, setting the two other angles β and γ to zero. This rotation is the most likely to result in adjacent pixels being hit and therefore biasing the reconstruction.

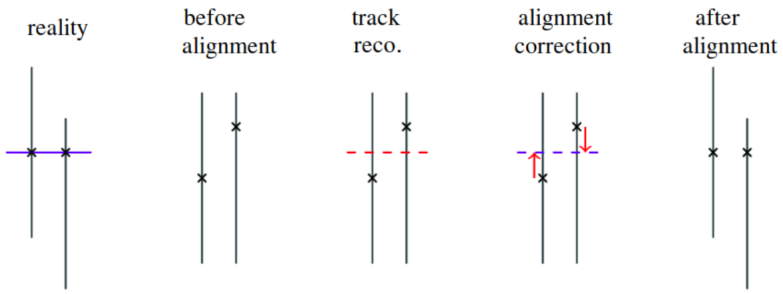

Figure 4.14: Sketch representing a one-dimensional simplified version of the alignment procedure. Taken from Ref. [2].

An example of the cluster-track residuals before and after alignment for plane 0 of the A-Near station for one ATLAS run is shown on Figure 4.15. The corrections for all the other planes of the station are computed relative to the alignment of plane 0.

The alignment was considered to be stable over the whole data-taking period used for the analysis presented in this thesis as there was no intervention on the SiT detector. An exhaustive discussion and study of the stability of the alignment, as well as the convergence of the alignment parameters across iterations, can be found in Ref [2].

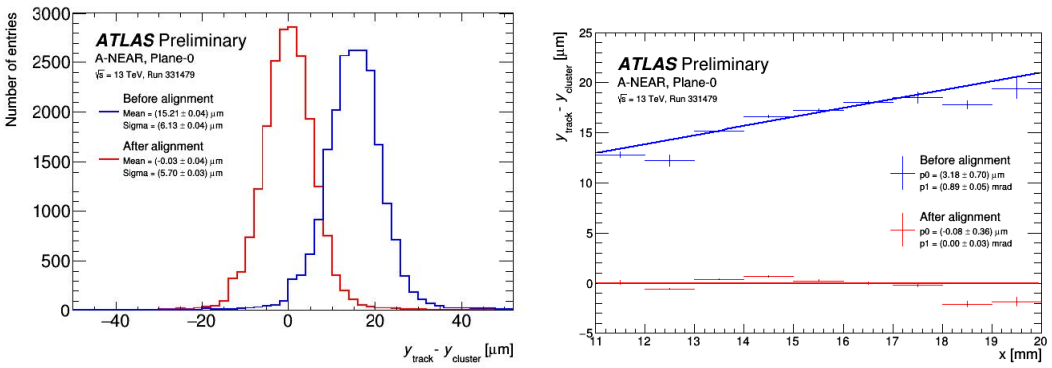

(a) (b)

Figure 4.15: Corrections to the alignment parameters for the offset in x (a) and the rotation about the z axis (b) for the first plane of the A-NEAR station in one ATLAS run. Residuals in x_{AFP} (a) and residuals in x_{AFP} against y_{AFP} distributions are shown before (blue) and after (red) alignment. The coordinate system used in this plot is the ATLAS coordinate system (x and y coordinates are inverted compared to the AFP coordinates). The uncertainties are only statistical. Taken from Ref. [125]

4.7 Global alignment

The alignment of the stations with respect to the beam, referred to as the AFP global alignment is a key element of the AFP precision. The precision on the reconstructed proton kinematics depends strongly on the precision of the alignment. It is also more challenging and must be monitored over time due to the constant change of the AFP stations position relative to the beam.

The RP are restricted not to approach the beam by more than $12 - 15\sigma$[1] of the beam transverse width in order to protect the integrity and the quality of the beam for other experiments. Before stable beams are declared by the machine operators, the AFP stations remain away from the beam (~ 40 mm), in a garage position.

The position of a proton track in a given station s can be described over runs r (and thus, time) by the following relation:

[1] Corresponding to approx. 1 mm.

$$x(s,r) = x_{\text{pre-align}} + x_{\text{tracker}} - x_{\text{beam}}(s) + x_{\text{RP}}(r,s) + \delta x_{corr.}(s) \tag{4.5}$$

$x_{\text{pre-align}}$ corresponds to the track coordinate before the alignment correction presented in Section 4.6 is done. This quantity is corrected by adding x_{tracker}, an estimate of the distance between the edge of the active SiT region and the outer side of the floor of the RP. It is assumed that it is independent of the station and time and has a value of -0.5 mm.

$x_{\text{beam}}(s)$ is subtracted, corresponding to the nominal beam position. It is determined in dedicated runs at the beginning of the data-taking period using a procedure called Beam Based Alignment (BBA) [127]. The principle for this procedure is to inject into the LHC a low intensity beam that is trimmed by the horizontal and vertical primary collimators (Three Primary Collimators (TCP)), scraping the beam halo, defining a well-defined beam edge. RP are then slowly (in steps of 10 µm), one by one, moved towards the beam. The movement stops when the signal peaks in the closest Beam Loss Monitor (BLM) installed after the RP, indicating that the beam was touched. This procedure is done each time RP are significantly touched[2] or when the beam optics are changed. It is cross-checked regularly using Beam Position Monitor (BPM) measurements [128]. The distance $x_{\text{beam}}(s)$ is different for each station but has a typical order of magnitude of 1 mm. This position is also stable to better than 100µm throughout the year [125].

$x_{\text{RP}}(r,s)$ is the RP position, corresponding to the distance between the beam and the edge of the stations during data-taking (when the stations are inserted). This nominal distance was changed twice during 2017 data taking, following agreements between ATLAS and the LHC Machine Protection Panel. The three settings were $12\sigma + 0.8$ mm, $12\sigma + 0.3$ mm and $11.5\sigma + 0.3$ mm, corresponding to typical distances of $3.6 - 4.3$ mm for the NEAR stations and $2.2 - 3.1$ mm for the FAR stations [125].

$\delta x_{corr.}(s)$ are the in-situ corrections, accounting for remaining misalignments. They

[2]Meaning any intervention more severe than connecting/disconnecting the cables.

are based on event-by-event comparisons between the central ATLAS kinematics and forward protons using an exclusive dimuon sample, with tight requirements making sure of the fact that the lepton pair and the scattered protons are coming from the same process [6]. The proton energy loss computed from the dimuon system $\xi_{\mu\mu}$ can be used to predict the x coordinate of the proton track in AFP , $x_{\mu\mu}$[3]. Residuals between this quantity and the measured track x_{AFP} are then formed for each station, leading to a peak corresponding to true correlations. After subtracting background as described in [6, 125], the mean value of the Gaussian fit is taken to be the correction. Figure 4.16 shows an example of such distributions before and after corrections, before and after background subtraction. Typical values of $\delta x_{corr.}(s)$ range from 0.22 to 0.43 mm. The uncertainties from these corrections are conservatively taken to be 300 µm in Ref. [6][4].

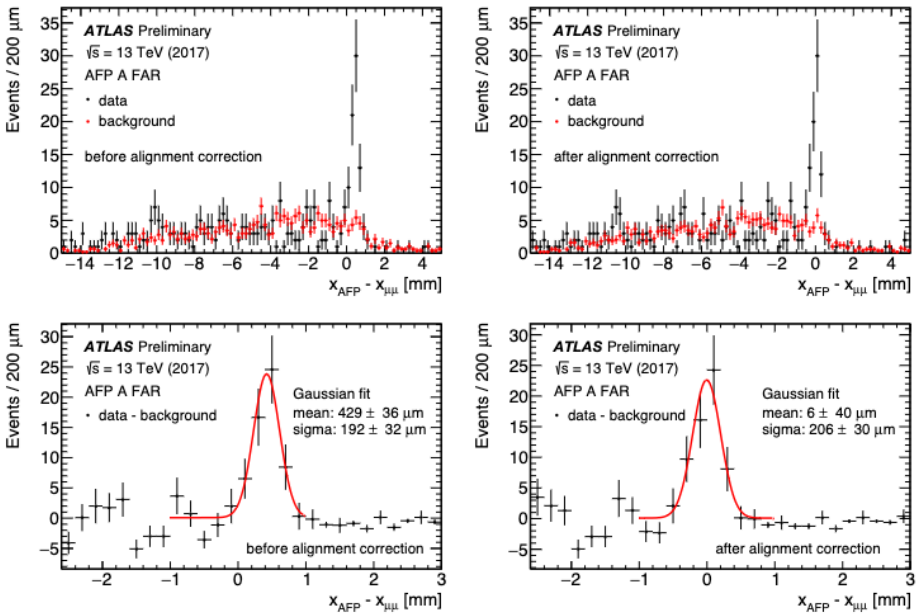

Figure 4.16: Data-driven AFP global alignment procedure based on exclusive dimuons events for A FAR station. Top-left(right) plot shows the raw $\Delta x = x_{\mathrm{AFP}} - x_{\mu\mu}$ distribution for both data and background model before (respectively after) the correction was applied. Bottom-left(right) plot shows the $\Delta x = x_{\mathrm{AFP}} - x_{\mu\mu}$ distribution with a Gaussian fit displayed on top after the background was subtracted before (respectively after) the correction was applied. Taken from [125].

[3]This is true because p_x is tiny and has a mean value of zero.

[4]Considering that the region $\xi \in [0; 0.1]$ corresponds to approximately 15 mm, this corresponds to approximately 0.002 in terms of ξ.

4.8 Performance during Run 2

In 2017, during the LHC Run-2, AFP recorded 32 fb^{-1} of integrated luminosity as shown in Figure 4.17. This section will discuss some of the performance monitoring during 2017 data taking.

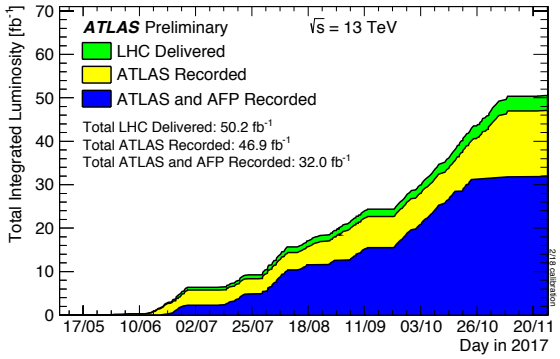

Figure 4.17: Cumulative AFP integrated luminosity recorded during 2017 (blue). Total delivered integrated luminosity by the LHC and ATLAS recorded are also shown in green and respectively yellow. Taken from Ref. [129].

4.8.1 Proton reconstruction efficiency

Proton reconstruction efficiencies need to be evaluated to perform a measurement with AFP . This efficiency corresponds to how often a proton object is reconstructed in AFP if a scattered proton falls into the AFP acceptance. The nominal approach for this is a "*tag-and-probe*" method using an exclusive di-lepton sample (described in Section 5.2.2). The principle is to use one station of an arm to select events with exactly one proton track (*tag*) and the other station on the same arm to calculate the probability to find a corresponding track satisfying $|r_{tag} - r_{probe}| < 2$ mm (*probe*). The track position in the tag station is also required to fall in the overlap acceptance region between the NEAR and FAR stations ($-12 < x < -5$ mm). The tag and probe stations of the same arm are then inverted to compute the efficiency of the other station of the same arm.

Figure 4.18 shows the results of this procedure as a function of time throughout

2017 ATLAS runs. The probabilities are stable around 99% throughout the year for the NEAR stations. The probabilities for the FAR stations are lower, of the order of 96%. These differences are expected due to the showering taking place between the two stations. The showering effect arises from the station windows and SiT planes. A more detailed study of this effect for Run 2 data-taking can be found in Ref. [125].

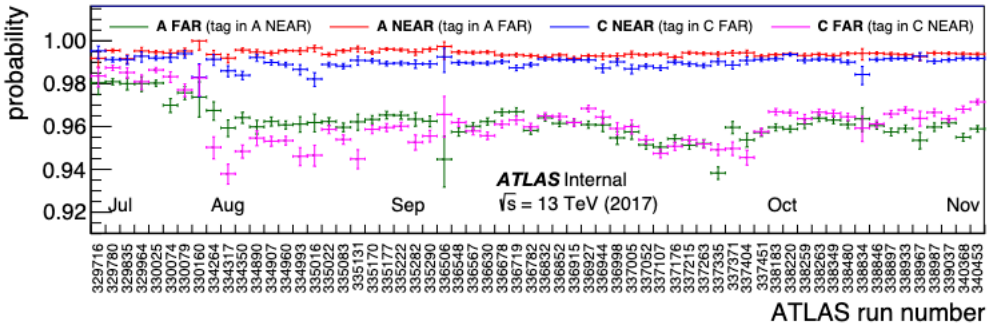

Figure 4.18: Results of the tag and probe study throughout 2017 ATLAS runs. The x axis indicates the different ATLAS runs, the y axis the associated efficiencies for the different stations. The uncertainties are statistical. Taken from Ref. [125].

A cross-checking efficiency evaluation method was also used, consisting of calculation of the efficiency of each SiT plane per station to reconstruct a cluster of hits if a proton was reconstructed in the station. It was found to be consistent with the nominal method, up to some asymmetries observed between A and C sides. An extensive description of this method can be found in Ref. [2], where the authors discuss the pros and cons of this method in comparison to the nominal one.

The NEAR and FAR combined efficiencies give an overall proton reconstruction efficiency of 0.92 ± 0.02.

4.8.2 Time-of-flight system performance

Figure 4.19 shows the time resolution of each channel (ToF bars) for a chosen run. The time resolutions are typically 30 ps for single channels and shrink to 20 ps when integrated over a train (set of 4 bars). This corresponds to a vertex resolution of $\simeq 6 \pm 1$ mm. Figure 4.20 shows the distribution of the difference between the vertex

position measured by the central ATLAS detector and that measured with the ToF system on double-tagged events in a chosen ATLAS run. The data excess over the random coincidence background model are the double tagged events.

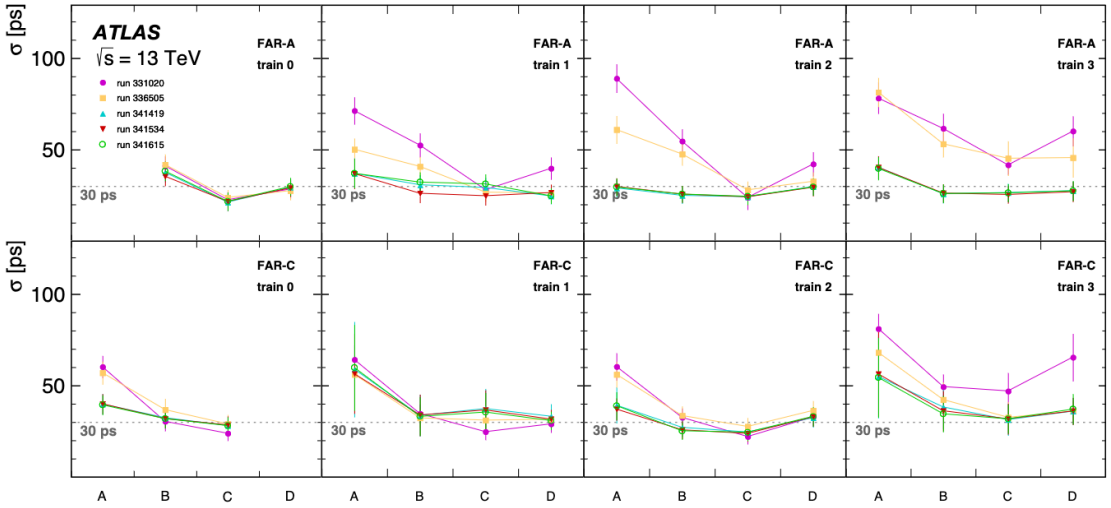

Figure 4.19: Time resolution of each channel (ToF bars) for different chosen runs. The upper row shows the time resolution measured for station FAR-A while the bottom row for station FAR-C. The total error bars indicate the statistical and systematic uncertainties added in quadrature, where the systematic uncertainties dominate. Taken from Ref. [123].

While the resolutions were evaluated to be very good, fulfilling the design requirements, the efficiency was poor. It was quoted to be at a $1-9\%$ level in single channels, raising to $5-10\%$ when integrated over a train. This was partly due to the MCP-PMT which degraded fast. For this reason, ToF data was not used in Run 2 AFP physics analyses.

4.8.3 Silicon tracker system performances

Figure 4.21 shows the hit reconstruction efficiency in A-NEAR SiT plane 0 as a function of bias voltage. It is fairly stable, with an efficiency of $\simeq 98\%$ for bias voltages $> 20\,\mathrm{V}$. The efficiency drops at low bias voltages for regions with highest occupancy (closest to the beam), indicating evidence of ageing.

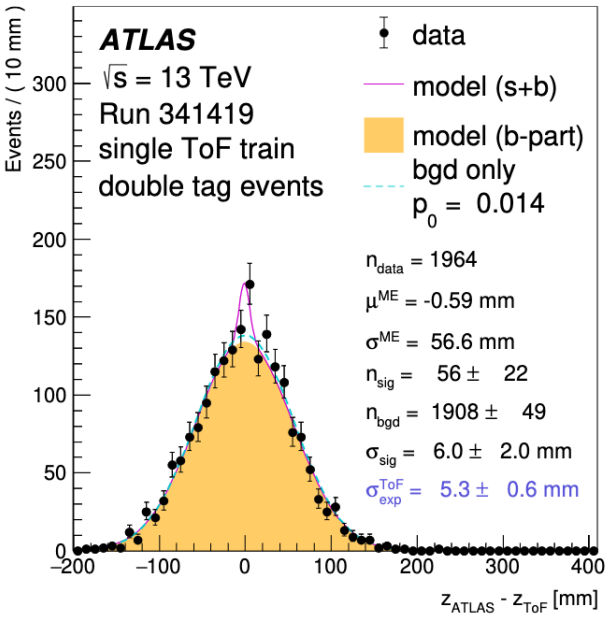

Figure 4.20: Distribution of the difference between the vertex position measured by the central ATLAS detector and the one measured with the ToF system on double-tagged events of a chosen ATLAS run. The filled area represents the background expectation, evaluated from an event-mixing technique, blue solid line represents the signal (double tagged events) together with the expected background fit. Dashed lines represent the background-only fit. Black points represents the data. Taken from Ref. [123].

Figure 4.22 shows the the trigger rate (set as a 2 out of 3 coincidence of selected SiT planes) together with the pile-up rate over the luminosity blocks of a chosen ATLAS run. The strong correlation between the two quantities indicates that the beam-induced background is small.

Figure 4.23 shows the mean number of tracks reconstructed in each station per *pp* collision during ATLAS runs. The occupancy stays stable over the course of 2017, with a value of approximately 0.02 per proton-proton collision. The observed difference between the NEAR and FAR stations is due to the showering happening in between the two stations.

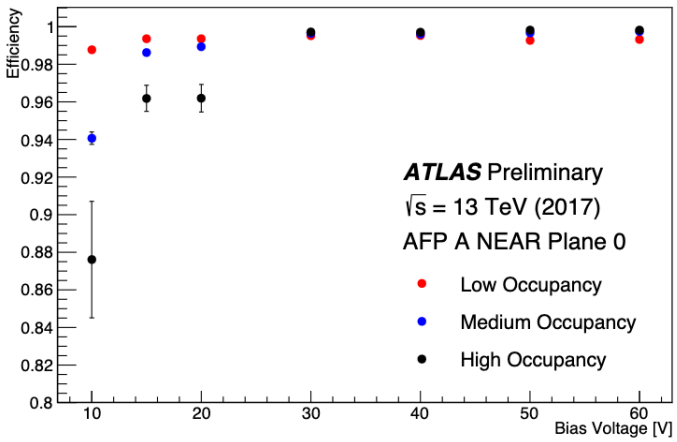

Figure 4.21: Efficiency of hit finding as a function of bias voltage for a given plane (A-NEAR SiT plane 0). Red (respectively blue, black) dots represents the regions of the detector with low (respectively medium, high) occupancy. The regions with higher occupancy are located closer to the beam, resulting in more radiation damage. Taken from Ref. [125]

4.8.4 Systematic uncertainties

During the whole reconstruction workflow, uncertainties arise from different sources. As quoted in the previous section, all AFP analysis, including the one presented in Chapter 6 of this document, should include a proton reconstruction efficiency uncertainty of 2%. The other systematic uncertainties comes from the sources described in the previous sections of the present chapter:

- Global alignment. This is the dominant source of uncertainty at low ξ_{AFP}. The associated systematic uncertainty is 300μm. The imperfect knowledge of AFP station positions with respect to the beam leads to a global shift of the measured x positions of the SiT planes from their true value.

- Local alignment. This value is known quite precisely. The associated systematic uncertainty ranges from 30μm at $\xi = 0.02$ to 120μm at $\xi = 0.1$. It is estimated from the residual differences between the NEAR and FAR station x positions, reflecting the imprecise knowledge of the alignment of each plane relative to the other.

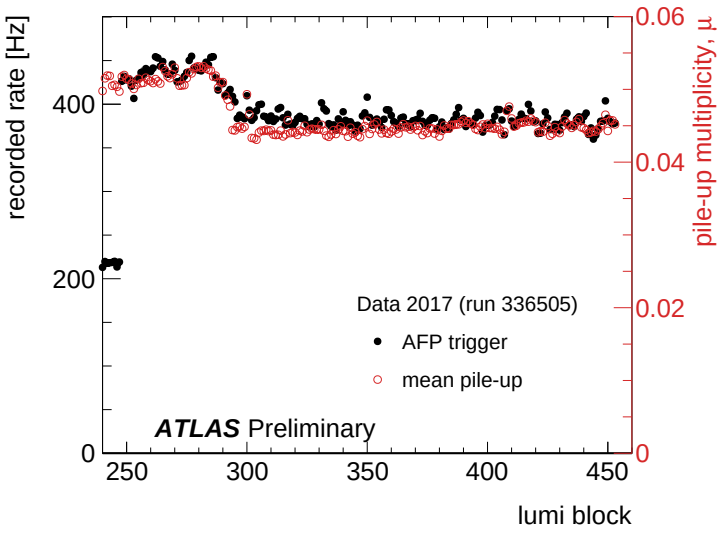

Figure 4.22: AFP trigger rate (black) together with the pile-up rate (red) over the luminosity blocks of a chosen ATLAS run. Taken from Ref. [130].

- Optics. This is the dominant source of uncertainty at high ξ_{AFP}. It mainly comes from the variation of the crossing angle over a LHC run.
- Spatial resolution of tracks. The associated systematic uncertainty is quite small compared to the others. It is fundamentally limited by the size of the pixels of the SiT planes, but it is improved by the tilting of the planes and the presence of two stations within an arm.

Some other effects were not taken into account and were assumed to be minor, such as the changes of the beam spot position and the RP thermal expansion.

4.8.5 2018 data-taking

Even though AFP was operational in 2018, data taken during this year are unfortunately not usable for physics purposes.

Detector timing and bunch-crossing identification issues, decorrelating the data from the ATLAS central detector made impossible the use of AFP data for physics analysis.

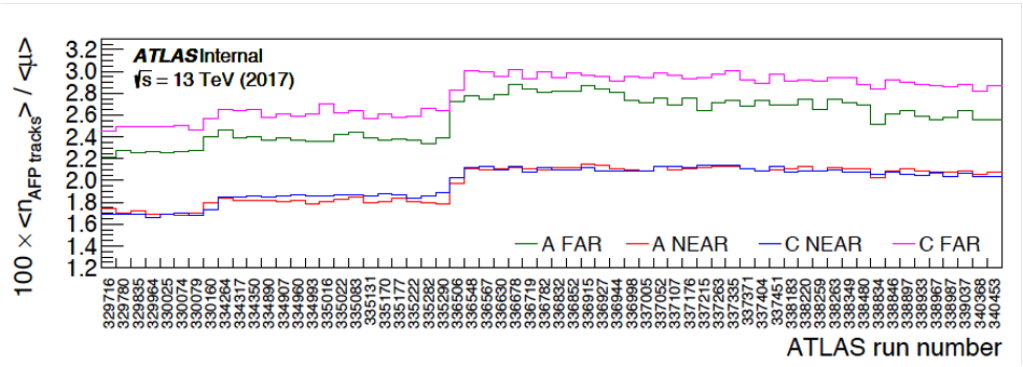

Figure 4.23: Mean number of tracks reconstructed in each station normalized by the average pile-up multiplicity in different ATLAS runs. This quantity is multiplied by 100. The observed step is due to a change of data-taking conditions over the course of 2017.

However, these data were used in a luminosity determination analysis that lead to consistent results with LUCID luminosity measurements at a better than 1% level [131].

Chapter 5

AFP Fast simulation tuning

This chapter will focus on the work done by the author in the framework of the ATLAS Qualification Task. The main focus was the tuning of `FastSim` (the AFP fast simulation) smearing parameters, but also the addition of new features in `FastSim` such as the pile-up proton simulation, together with the implementation of the simulation from the SiT hit clusters.

5.1 State of the art

In 2020, the first AFP physics paper was published [6]. This analysis used AFP to observe forward proton scattering in association with lepton pairs ($e^+e^- + p$ or $\mu^+\mu^- + p$; with p being the only proton reconstructed) assumed to be produced via photon fusion. Proton-tagging techniques were used for cross-section measurements of these processes. The idea of the analysis was to measure the proton energy loss ξ both from AFP and from the central detector using the two leptons and then to establish the signal from the correlation. This strategy is now a standard in all AFP analyses (see also the Axion-like Particle (ALP) search [118], the $\gamma\gamma \to ZZ \to 4\ell$ analysis described in Chapter 6, and other ongoing analyses).

The expected proton energy loss based on di-lepton kinematics, $\xi_{\ell\ell}$ is determined using the following relation:

$$\xi_{\ell\ell} = \frac{m_{\ell\ell}}{\sqrt{s}} e^{\pm y_{\ell\ell}} \tag{5.1}$$

with $m_{\ell\ell}$ being the invariant di-lepton mass, $y_{\ell\ell}$ the di-lepton rapidity and +(-) corresponding to the proton on side A(C).

As will be explained later, since the same dataset as that used in Ref. [6] is used for the FastSim calibration, the first step was to perform a reproduction of di-lepton analysis.

5.2 $\gamma\gamma \to 2\ell$ process

As mentioned before, the goal of the analysis was to measure forward proton scattering in association with lepton pairs ($e^+e^- + p$ or $\mu^+\mu^- + p$) produced via photon fusion. The underlying process of interest is represented by the Feynman diagram shown on Figure 5.1.

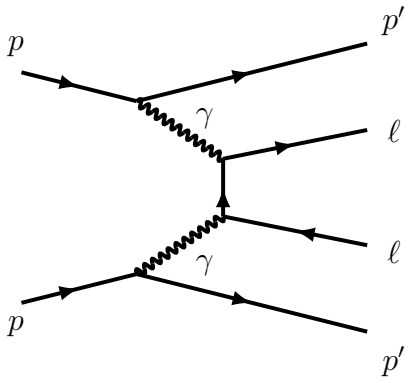

Figure 5.1: Feynman diagram of forward proton scattering in association with lepton pairs ($e^+e^- + p$ or $\mu^+\mu^- + p$) produced via photon fusion.

This process has the highest $\gamma\gamma$ cross-section among the observable channels, which is why it is used for calibration (for instance global alignment as detailed in Sec-

tion 4.7). Still, the cross-section of this process remains very small compared to other background processes producing the same final state (see Section 5.2.1). The cross-section measured in Ref. [6] was $\sigma_{ee+p} = 11.0 \pm 2.6$ (stat) ± 1.2 (syst) ± 0.3 (lumi) fb and $\sigma_{\mu\mu+p} = 7.2 \pm 1.6$ (stat) ± 0.9 (syst) ± 0.2 (lumi) fb.

5.2.1 Estimation of background

The main background comes from uncorrelated protons in the AFP due to pile-up - *i.e.* the central di-lepton is a real signal but it comes from a process that doesn't yield forward protons and the background is due "other" protons in AFP . A schematic illustration of the difference between signal and pile-up events is shown on Figure 5.2.

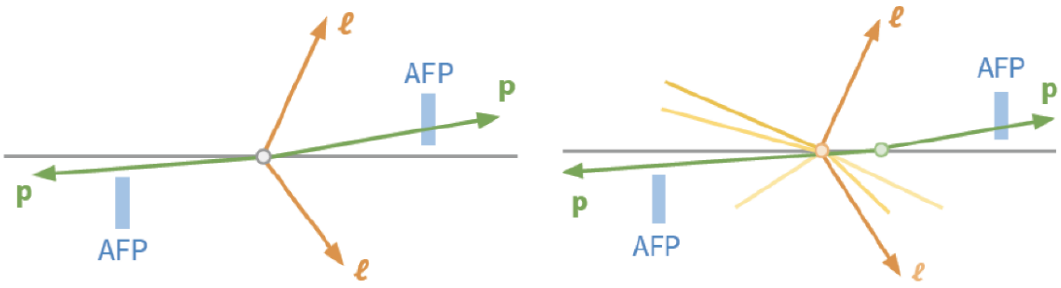

(a) (b)

Figure 5.2: AFP signatures of signal and background processes. In a signal event (a), The two protons and the two leptons come from the same process. In a background event (b), they do **not**.

After the event selection described in Section 5.2.2, the dominant source of background in the central detector arises from di-lepton production via the Drell-Yan mechanism (a quark from a proton and an antiquark from another proton annihilating into a virtual photon which then decays into a pair of oppositely-charged leptons) overlaid with a SD process giving an AFP proton (see Figure 4.2). A secondary background arises from $\gamma\gamma \to \ell\ell$ processes in which any outgoing protons are outside the AFP acceptance or are not reconstructed due to detector inefficiency.

5.2.2 Event selection

In order to remove the largest amount of events resulting from background possible, requirements were imposed both to the di-lepton system and to the scattered protons.

- Events must have been produced in a run contained in the Good Run List (GRL). This list, produced by Data Preparation group, corresponds to 44.3 fb^{-1}, with a total uncertainty of ± 1.0 fb^{-1}. It corresponds to Runs when the central detector and AFP fulfil a range of quality requirements such as fully operational detectors.

- Exactly 2 leptons (electrons or muons) were required. They had to be of opposite charge and the same flavour. Other requirements were made on their reconstruction quality. These leptons also have to match the di-lepton triggers. More technical details are given in Appendix A, in Ref. [6] or in the associated ATLAS note.

- $m_{\ell\ell} > 20$ GeV, $m_{\ell\ell}$ being the invariant mass of the di-lepton system, in order to avoid low mass quarkonia resonances such as J/ψ and Υ and to be within the AFP ξ acceptance.

- $m_{\ell\ell} \notin [70, 105]$ GeV, in order to avoid the Z boson resonance.

- $p_T^{\ell\ell} < 5$ GeV, to suppress Drell-Yan relative to the $\gamma\gamma$ production mechanism, which typically generates only very little transverse momentum.

- $A_\phi^{\ell\ell} = 1 - |\Delta\phi_{\ell\ell}|/\pi < 0.01$, with $\Delta\phi_{\ell\ell}$ being the difference in the ϕ coordinate between the two leptons. $A_\phi^{\ell\ell}$ is known as the acoplanarity. This means the leptons must be emitted back-to-back.

- $N_{\text{tracks}}^{0.5\text{mm}}$, the events must have no inner-detector tracks that satisfy $\Delta R(\text{track}, \ell) > 0.01$ for both leptons and $|z_0^{\text{track}} - z_0^{\ell\ell}| < 0.5$ mm, where $\Delta R(\text{track}, \ell)$ is the angular distance between the track and the lepton, z_0^{track} is the track z_0 position

and $z_0^{\ell\ell} = (z_0^{\ell_1} + z_0^{\ell_2})/2$ with $\ell_{1,2}$ denoting the two leptons. This cut removes pile-up events, that have a displaced vertex.

- Both ξ_{AFP} and $\xi_{\ell\ell} \in [0.02, 0.12]$ for at least one AFP side. This requirement selects events with one or more proton candidate. If there is more than one proton candidate on the same AFP side, which occurs in 35% of the selected events, the proton with ξ_{AFP} closest to $\xi_{\ell\ell}$ is chosen.

- $|\xi_{\mathrm{AFP}} - \xi_{\ell\ell}| < 0.005$. Proton tagged di-lepton candidates are selected by requiring kinematic matching. This retains more than 95% of the signal and rejects more than 85% of the background [6].

Technical details on how the selection is done using Athena [132] are given in Appendix A. Kinematic distributions in the variables used in the selection are also shown, after all cuts are done. A cut-flow analysis and an event yield are given in Section 5.2.4.

5.2.3 Comparison with published analysis

In this section, some of the kinematic distributions after all cuts used in Ref. [6] are compared to those presented in that report.

Figure 5.3 shows $A_\phi^{\ell\ell}$ distributions. More events are observed at high acoplanarity in this analysis than in the published results, which may indicate the presence of background events.

Figure 5.4 shows $m_{\ell\ell}$ distributions. A correct agreement is reached when comparing this analysis to the published results.

Figure 5.5 shows $\Delta\xi$ distributions. The two distributions are in reasonable agreement.

The event yield is higher in this analysis than in Ref. [6]. After comparing each sample event by event, we observe that every single event selected in the published

analysis is also selected here. The difference in the yield after selection will be considered as satisfactory for the rest of the study as the peak in $\Delta\xi$ distribution is clearly distinguishable. The differences is the selections might arise from the different versions of the tools used.

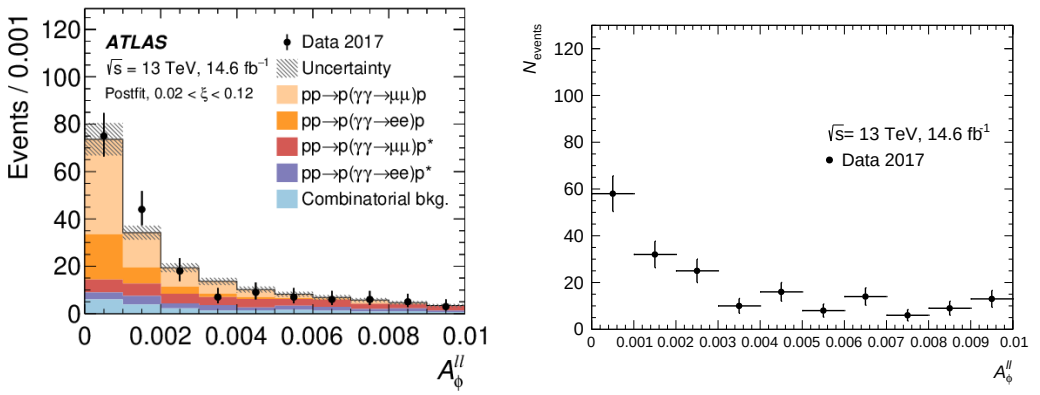

(a) (b)

Figure 5.3: Comparison of $A_\phi^{\ell\ell}$ distributions between Ref. [6] (a) and this analysis (b).

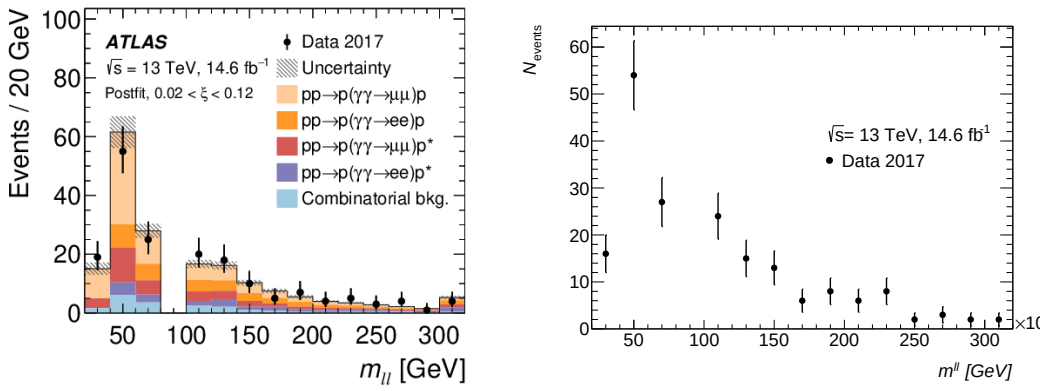

(a) (b)

Figure 5.4: Comparison of $m_{\ell\ell}$ distributions between Ref. [6] (a) and this analysis (b).

5.2.4 Cutflow and event yield

Table 5.1 shows the number of events and the relative change in sample size after each cut. The track veto has the largest impact, providing an indication of the high background rejection rate.

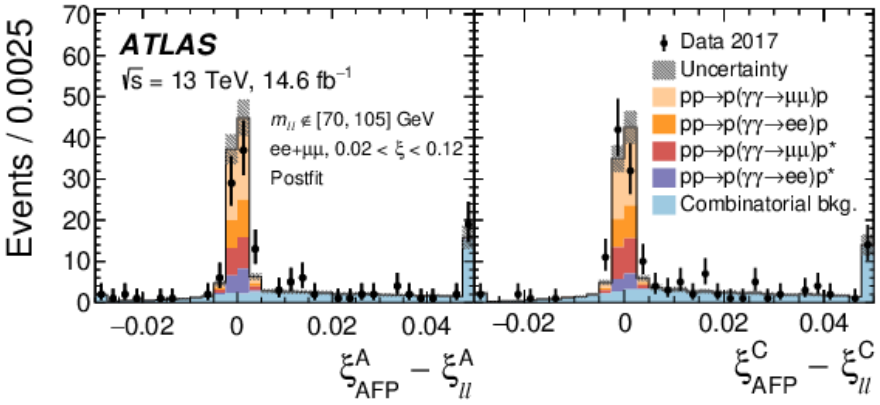

(a)

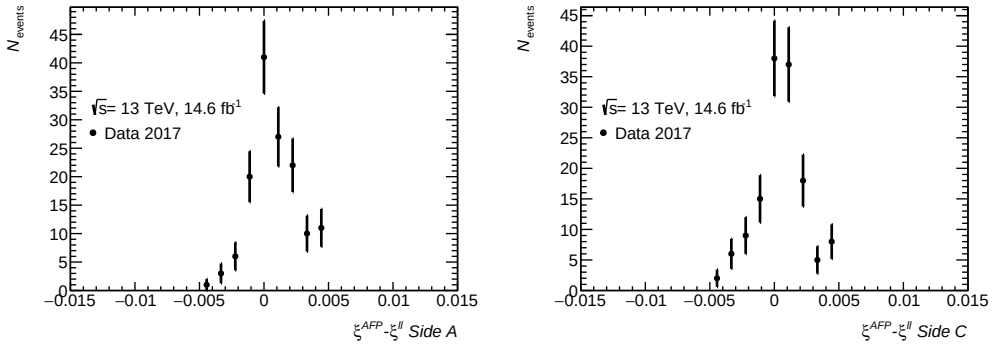

(b)

Figure 5.5: Comparison of $\Delta\xi$ distributions between Ref. [6] (a) and this analysis (b).

5.3 Determination of FastSim smearing parameters

5.3.1 Discrepancy comparing data to Monte-Carlo

The selection presented in Section 5.2.2 is applied both to data and to MC simulation (signal process only). Events are simulated using the `Herwig7` event generator [53, 54]. First, the $pp \to \gamma\gamma + pp$ process is simulated, then the $\gamma\gamma \to \ell\ell$ process, as described in Section 2.4. The AFP response is simulated after the main ATLAS simulation (see next paragraph). The samples used for comparison with data are events within a mass range of $m_{\ell\ell} > 20(45)$ GeV for the electron (muon) channel.

Table 5.1: Cutflow of yields after each requirement applied sequentially.

Requirement	Yield	Change
GRL	8.62839×10^7	-
Trigger	2.8821×10^7	-66.6%
2 leptons	1.3619×10^7	-52.7%
$p_T^{\ell\ell} < 5$ GeV	2.43335×10^6	-82.1%
$m_{\ell\ell} > 20$ GeV	2.43335×10^6	-0%
$A_\phi^{\ell\ell} < 0.01$	841663	-65.4%
$N_{\text{tracks}}^{0.5\text{mm}} = 0$	6674	-99.2%
$m_{\ell\ell} \notin [70, 105]$ GeV	2420	-63.7%
At least one AFP proton	1850	-23.6%
$\xi_{\text{AFP}}^A \in [0.02, 0.12]$	934	-49.5%
$\xi_{\ell\ell}^A \in [0.02, 0.12]$	201	-78.5%
$\lvert\xi_{\text{AFP}}^A - \xi_{\ell\ell}^A\rvert < 0.005$	128	-36.3%
$\xi_{\text{AFP}}^C \in [0.02, 0.12]$	197	-89.4%
$\xi_{\ell\ell}^C \in [0.02, 0.12]$	104	-47.2%
$\lvert\xi_{\text{AFP}}^C - \xi_{\ell\ell}^C\rvert < 0.005$	63	-39.4%

The response of the AFP spectrometer is modelled by an offline fast simulation (`FastSim`), where a Gaussian smearing is applied to truth-level track element positions at each AFP plane (see Section 5.3.2) to take into account and simulate the detector resolution.

Figure 5.6 shows the $\Delta\xi = \xi_{\text{AFP}} - \xi_{\ell\ell}$ distribution on side A and side C after the selection has been applied both to data and MC. A Gaussian fit is then applied. The data peak seems to be slightly shifted towards positive $\Delta\xi$ values on side A. Figure 5.7 shows the distributions on side A separately for electrons and muons. The shift seems to mainly come from the electron channel, though statistics are low. This shift has been previously observed in the muon channel and seemed to be systematic [125, 133]. This shifts still needs to be investigated in the future.

The width of the Gaussian fit for MC is smaller on both sides in comparison with the width of the Gaussian fit for data. For example, on side A, the width of the Gaussian fit to MC is $\sigma_{\text{MC}} = (1.30 \pm 0.02) \times 10^{-3}$ while it is $\sigma_{\text{data}} = (1.85 \pm 0.18) \times 10^{-3}$ for data. A similar observation applies on side C.

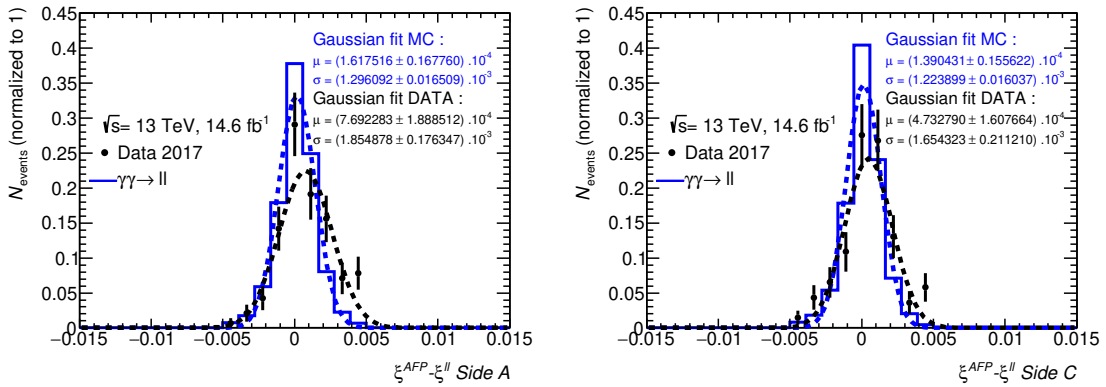

Figure 5.6: $\xi_{\mathrm{AFP}} - \xi_{\ell\ell}$ distribution for data (black) and MC (blue) in both the electron and muon channels. All distributions are normalized to 1. The default parameters of FastSim are applied.

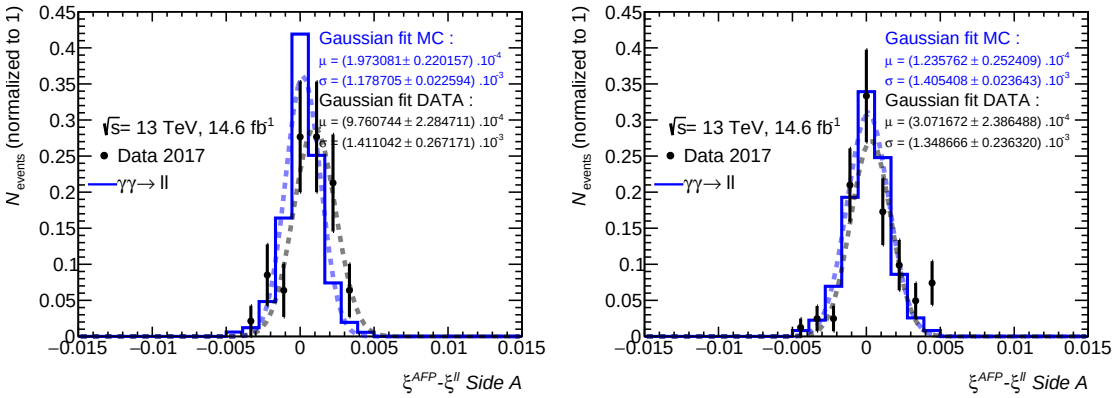

(a) (b)

Figure 5.7: $\xi_{\mathrm{AFP}} - \xi_{\ell\ell}$ distribution for data on Side A in each channel. (a) is the di-electron channel, (b) is the di-muon channel.

Using the default parameters of `FastSim` thus leads to a poor description of the data. This has been observed already in Ref. [6]. The smearing needs to be enhanced if the data distributions are to be well described.

5.3.2 Description of the smearing parameters

The detailed reconstruction and simulation flow has already been described in Section 4.4. AFP `FastSim` applies a Gaussian smearing in order to simulate AFP

detector effects. Two pairs of smearing parameters are used to produce the simulation:

- `smearPosition` (x, y) [mm]: This is the detector resolution. The same value is used for both NEAR and FAR stations. In reality, there is an additional multiple Coulomb scattering in the NEAR station which is expected to make the smearing in the FAR station slightly larger than in the NEAR station, but that is not considered here.
  - The default values were taken from the AFP Technical Design Report (TDR) [117]: $(x, y) = (10 \times 10^{-3}, 30 \times 10^{-3})$ mm
- `smearAngle` (x, y) [µrad]: This takes into account the angular spread of the beam.
  - The default value is based on the LHC design parameters (emittance and β^* value): $(x, y) = (30, 30)$ μrad

In addition, a smearing of the vertex position should also be taken into account. However, this is relevant for the whole ATLAS simulation and is already included in the sample before it is processed by `FastSim`. In the future, this smearing needs to be investigated as well.

5.3.3 Linear fit of smearing parameters: method and results

Figure 5.8 shows the $\xi_{\text{AFP}} - \xi_{\ell\ell}$ distributions after each of the 4 smearing parameters has been increased by a factor of 10. The value for this increase factor was chosen arbitrarily, so as to be bigger than the quoted resolution in order to see a clear effect. It is clear that the smearing of the x position is the most sensitive variable. The increases of width of the Gaussian fit after changing the smearing parameters are summarised in Table 5.2. Both Figure 5.8 and Table 5.2 show results for side A for readability, but similar results are obtained for side C.

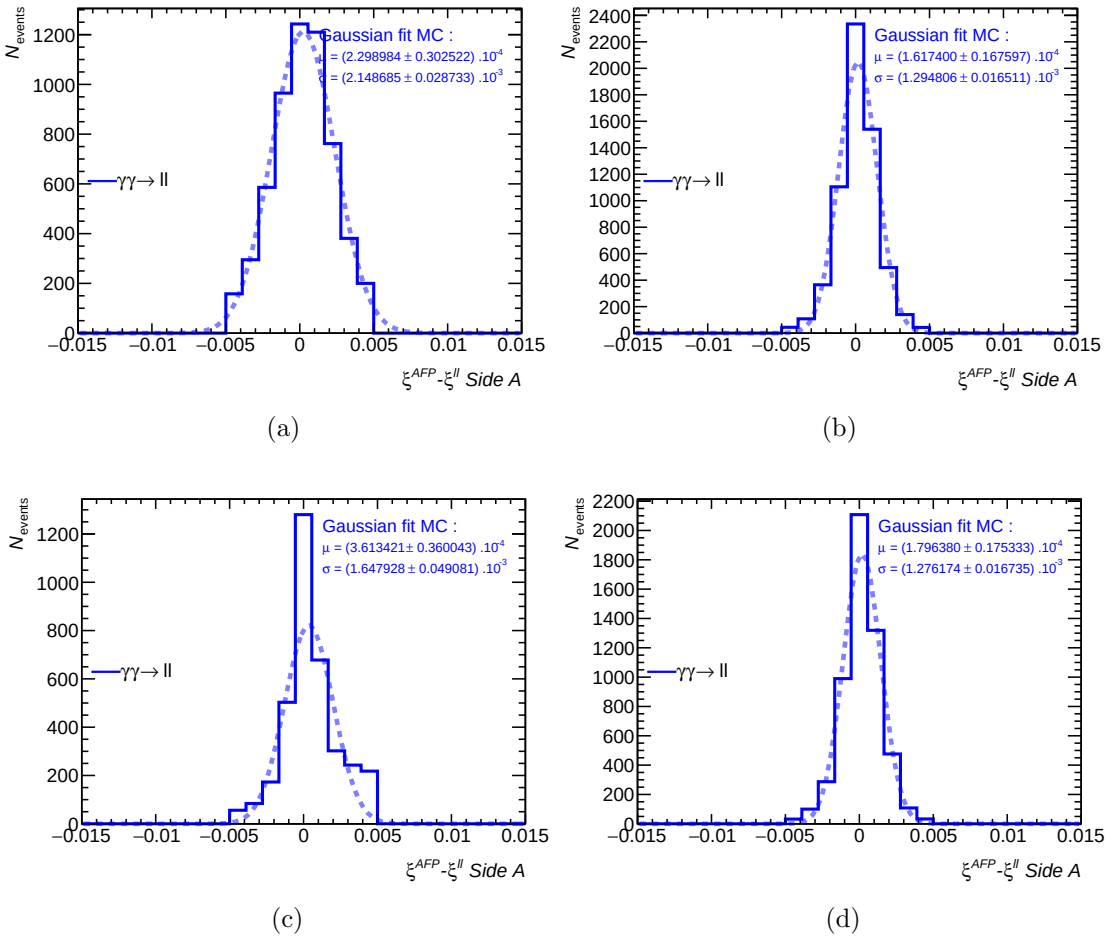

Figure 5.8: $\xi_{\mathrm{AFP}} - \xi_{\ell\ell}$ distribution on side A after each parameter has been increased by a factor 10. Smearing in x position has been increased in (a), in y position in (b), in x angle in (c), in y angle in (d).

Table 5.2: Increases of the width of the Gaussian fit to the $\xi_{\mathrm{AFP}} - \xi_{\ell\ell}$ distribution on side A after each parameter has been increased by a factor of 10.

Smearing parameter	Width of the Gaussian fit	Increase comparing to default parameters
Smearing in x position	2.15×10^{-3}	+65 %
Smearing in y position	1.29×10^{-3}	-1 %
Smearing in x angle	1.65×10^{-3}	+27 %
Smearing in y angle	1.28×10^{-3}	-2 %

As a first approximation, we only tune the most sensitive parameter (*i.e.* the x position) and leave the other parameters unchanged at their default values. To perform this tuning, we run the simulation several times while changing the value of the x position smearing parameter each time. We then extract the revised width of a Gaussian fit. We then perform a linear fit of the different values of the x position

smearing parameter to the width of the Gaussian fit and find an optimal value for this parameter by comparing it with the width of the Gaussian fit to the data. This process is done on each side independently. The results are shown in Figure 5.9.

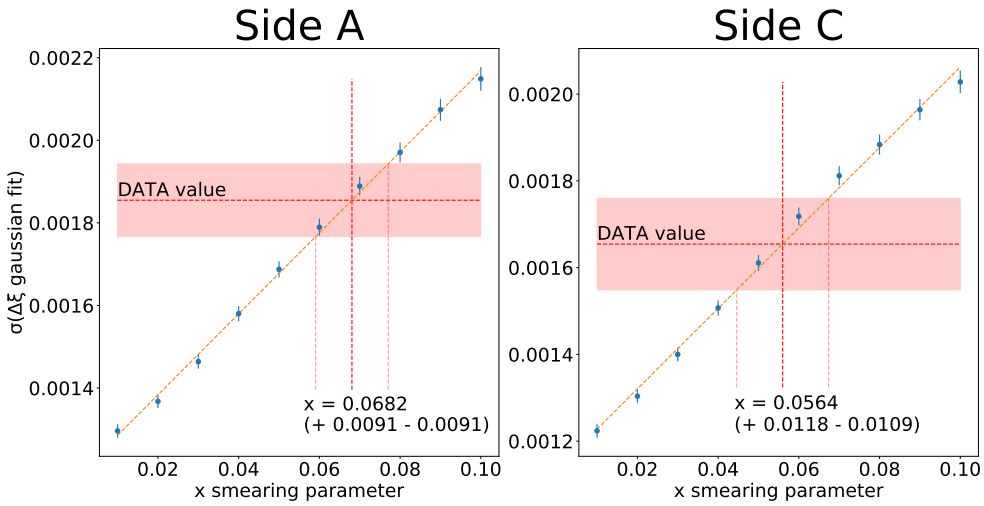

Figure 5.9: Width of Gaussian fits plotted against the value of the x position smearing parameter it as been generated with. The red dashed line represents the width of the Gaussian fit to the $\Delta\xi$ distribution in the data. The red box represents the associated uncertainty.

With this method, we obtain an optimal value for the smearing in the x position parameter for each side: $x^{A}_{\text{position}} = (6.82 \pm 0.91) \times 10^{-2}$ mm and $x^{C}_{\text{position}} = (5.64^{+1.18}_{-1.09}) \times 10^{-2}$ mm. As `FastSim` only allows a single global smearing parameter for both sides, we take the mean of the two $x^{\text{opt.}}_{\text{position}} = 6.23 \times 10^{-2}$ mm. Taking the mean between the two values can be justified using two arguments. One is that we can reasonably assume symmetry between the event sources on the two sides, at least to first approximation. The other is that this parameter represents the actual detector resolution, which is supposed to be the same on both sides as the same detector technology is used.

Figure 5.10 shows the $\xi_{\text{AFP}} - \xi_{\ell\ell}$ distribution both in data and MC using this new optimal smearing parameter. We now observe a much better agreement between data and MC compared to the default values used to produce Figure 5.6. The optimal value for the width of the Gaussian fit to the MC is now compatible with

the observed value in data.

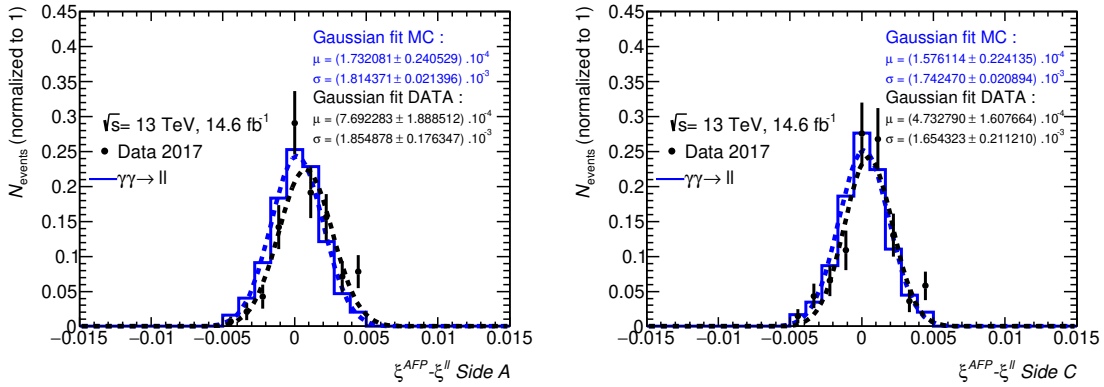

Figure 5.10: $\xi_{\mathrm{AFP}} - \xi_{\ell\ell}$ distribution for data (black) and MC (blue) in both electron and muon channel. All distributions are normalized to 1. Default parameters of FastSim are applied except for smearing in x position where the optimal parameter is applied.

5.4 Proton pile-up simulation

The AFP full-simulation is not enabled by default in the production of MC samples. Most of the time, its simulation relies on a fast simulation (`FastSim`), which takes place at runtime - meaning the AFP response is simulated for each event when the analysis code is run. The simulation flow is the following:

1. Protons are generated by the MC generator.

2. When the analysis is running, for each event, the AFP fast-simulation reads the proton information at the generator level.

3. Using knowledge of the optics and alignment constants, the fast simulation simulates track components in the AFP SiT detectors. A maximum of two track segments per proton can be simulated (one for each station). If only one track is simulated, then this track will always be in the FAR station, by construction.

4. As discussed in Section 4.4, the track(s) will then be reconstructed as proton objects exploitable at the analysis level (*i.e.* accessing their kinematics).

So far, it was assumed that reconstructing AFP protons from simulated tracks in AFP stations (instead of starting the simulation earlier in the reconstruction chain) is a correct description of the reality, but one can imagine a possible loss of signal efficiency due to pile-up SiT hit clusters that happen to be close to the signal track biasing the reconstructed position of the signal track. In order to quantify this effect, the implementation of a proton pile-up simulation was needed at the hits cluster level and at the track segment level, together with the implementation of the simulation at the hits cluster level (as it was already implemented at tracks level).

5.4.1 Cluster-level simulation

The changes to AFP `FastSim` needed in order to implement the simulation at the cluster level will be described here. The detailed code can be found in commit `57a3fc0d` (authored on the 8$^{\text{th}}$of November, 2021) on the Gitlab project `AfpAnalysisToolbox` [134].

- A switch was implemented for the user to decide the type of simulation wanted. Default is `FromTracks`, the other options are `Full` and `FromClusters`. This decides where to start the simulation in the simulation chain.
- A method `simulateClusters` was implemented. This method:
    1. Retrieves all appropriate containers. Containers are base objects of the Athena framework [132], acting as a storage for various physics objects. In this case, the truth particles container and the cluster containers are retrieved to be able to modify them.
    2. Retrieves the global alignment (see Section 4.7) constants based on a unique simulated run alignment ID. The part of the code returning the

alignment constants is used in various places in the well established AFP toolkit.

3. Uses the proton truth information to compute the position of the proton in AFP . This is where the smearing described in Section 5.3.2 is applied. This method was also already implemented before the developments described here.

4. Adds a cluster in the corresponding container at the position computed by the method `addSiHitsClusters` called for each plane of each station of the appropriate side.
   The method first checks if the proton trajectory passes through the plane geometry, taking into account the global alignment correction of the x coordinate of the detector. If it is the case, the coordinates of the cluster for a given plane p (ranging from 0 to 3 in the plane coordinate system) are set as:

$$\begin{bmatrix} x_{\text{cluster}} = \pm y_{\text{proton}} \\ y_{\text{cluster}} = -x_{\text{proton}} + x_{\text{GlobalAlignment}} \\ z_{\text{cluster}} = y_{\text{proton}} \times \sin(14^\circ) + 9 \times p \end{bmatrix}$$

   This changes the coordinates of the proton from the ATLAS coordinate system to the local plane coordinate system, taking into account the fact that the planes are tilted by 14° and applying the global alignment correction. The 9 in the z coordinate corresponds to the distance between each plane p. In the plane coordinate system, the z origin is set at the first plane ($p = 0$).

5. Saves all simulated cluster objects in the clusters container.

6. Adds a pile-up simulation (detailed in next section) if requested by the user.

5.4.2 Data-driven proton overlay

As already discussed in Section 5.2.1, the main background contribution in AFP analyses usually arises from a similar final state to the one studied in the central detector with further protons coming from pile-up. This effect was estimated in previous AFP analyses [6, 118] by the use of a fully data-driven method called event mixing. This technique will be described in Chapter 6 as it was used together with a MC-based method for background estimation in the analysis presented in this thesis. In the case of a simulated process not containing intact protons in the final state, one must take into account this effect. A proposed method developed by the author is to overlay a real (real meaning here coming from data) proton taken from a separately created database on top of each existing MC event.

This overlay can be done regardless of the fact that the sample contains diffractive information. For example, MC samples of non-diffractive processes that do not have intact protons in the final state do not contain a proton container, but the proton overlay will still work by creating the appropriate container.

First a database must be created. A simple program based on AnalysisBase (ATLAS official analysis framework based on `Athena` [132]) and `AfpAnalysisToolbox` [134] was developed to read ATLAS data (containing AFP information) and record hit-clusters and track segments in containers, for each event: an entry in the database can be an empty container, coming from an event with no AFP protons. The code is public to the ATLAS collaboration and can be found in the ATLAS GitLab repository [135]. This code produces a ROOT [59] file containing a `TTree` (a generic ROOT data structure containing event-by-event information).

Similarly to what was presented in Section 5.4.1, modifications were made to the `AfpAnalysisToolbox` project.

- A switch was implemented for the user to decide if they want to use the proton pile-up overlay together with options to define the name of the database file

and the name of the `TTree` that were saved.

- If the switch is activated by the user and the options are correctly set up, the overlay takes place in the `simulateClusters` method (see step 6 of the bullet list in Section 5.4.1). For each MC event, an entry from the source database (the content of the hit-cluster container of an event) is read and copied to the appropriate container in the MC event. Then the reconstruction chain continues with these new indistinguishable hit-clusters stored in the container.

- The type of pile-up overlay used is tied to the simulation type property chosen by the user (see first bullet point of Section 5.4.1). By default its value is set to `FromTracks` and can be changed to `FromClusters` to perform transport and pile-up simulation starting from cluster level. The code works in the exact same way if the `FromTracks` option is chosen, except that the overlay takes place in the similar `simulateTracks` method.

A straightforward illustration of the effect of this code is to look at the proton multiplicity with the pile-up simulation on and off. The sample used to do this test is the MC simulation of the signal process used in the analysis [6] presented in Section 5.2: photon-induced lepton pair production in association with intact protons. The proton database produced for this test uses period C of 2017 data, corresponding in the AFP GRL to 8 ATLAS runs and 0.734454 fb^{-1}. Figure 5.11 shows the proton multiplicity distribution in this sample, after requiring at least one AFP proton. A tail appears in the distribution, indicating that the overlay is correctly implemented. Starting the simulation and doing the overlay at the hit-cluster level leads to the same distribution.

One can now look at other distributions, such as ξ_{AFP} and $\Delta\xi$ and compare the two simulation and overlay modes to investigate the effect of the proton pile-up.

Figure 5.12 compares the ξ_{AFP} distributions (only on side A for readability, but the behaviour is the same on both sides) with the simulation and overlay done at track level with and without the pile-up simulation. One can see a secondary peak

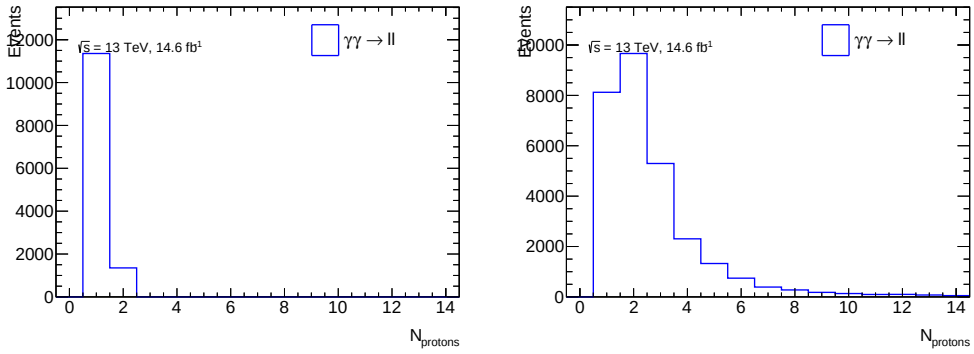

(a) (b)

Figure 5.11: Proton multiplicity distribution of the $\gamma\gamma \to \ell\ell$ sample with the requirement of having at least one AFP proton, with the proton pile-up overlay off (a) and on (b).

appearing, due to the fact that the pile-up tracks come from real data, where the acceptance of the detector is lower than the ideal acceptance simulated (primary peak). This indicates that this feature must be used with caution, matching the data-taking conditions between the data being analysed and that in the pile-up database.

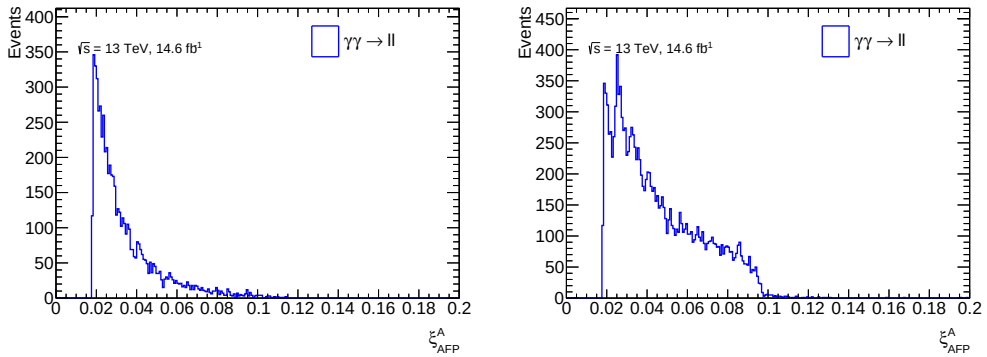

(a) (b)

Figure 5.12: ξ^{A}_{AFP} distribution of the $\gamma\gamma \to \ell\ell$ sample with the requirement of having at least one AFP proton, with the proton pile-up overlay off (a) and on (b).

In the same way, Figure 5.13 compares the $\Delta\xi$ distributions (only on side A for readability but the behaviour is the same on both sides) with the simulation and overlay done at track level with and without the pile-up simulation. A similar selection to the one presented in Section 5.2.2 is applied, but with the cuts on ξ_{AFP} and $\xi^{\pm}_{\ell\ell}$ relaxed. We can see a tail appearing due to the pile-up events that can be

easily removed by requiring kinematic matching (the standard cut in AFP analyses is $|\Delta\xi| < 0.005$).

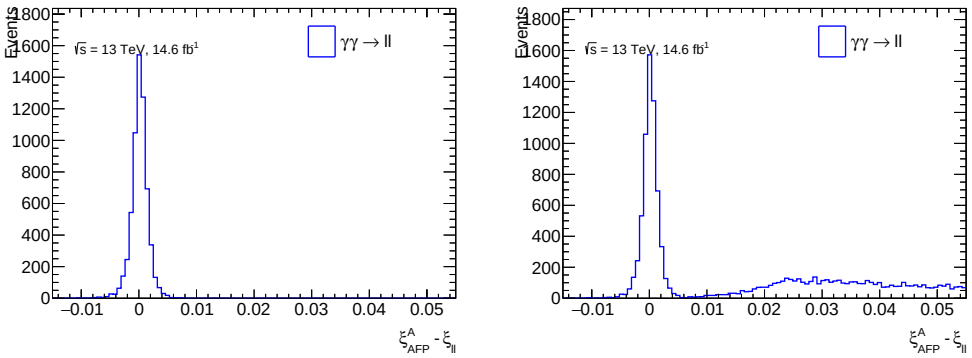

(a) (b)

Figure 5.13: $\xi^A_{\text{AFP}} - \xi_{\ell\ell}$ distribution of the $\gamma\gamma \to \ell\ell$ sample with the requirement of having at least one AFP proton and cuts on the di-lepton system kinematics (presented in Section 5.2.2), with the proton pile-up overlay off (a) and on (b).

As already said, the difference between the two hit-cluster and the track overlay levels is tiny or non-existent. For this reason, a special hit-clusters database was created (by tweaking the code creating the database) in order to enhance artificially the effect: only events with at least 100 clusters were selected to enter into the database. Figure 5.14 compares the $\Delta\xi$ distributions (only on side A for readability but the behaviour is the same on both sides) at track and at cluster level (with an enhanced database for hits clusters). The effect is negligible at the peak. As explained before, the tails will be cut in any case in a physics analysis.

These observations lead to the conclusion that simulating the AFP response from the hit-cluster level does not improve the quality of the reconstruction. Pile-up clusters cannot bias the track reconstruction in these data taking conditions. This addition in the simulation framework makes possible the test of this assumption with later data. One can also imagine considering other effects to simulate properly the detector's inefficiency:

- Consider noisy pixels. Some individual pixels are known to be noisy resulting in fake activations that can be identified as hits and thus bias the clusters

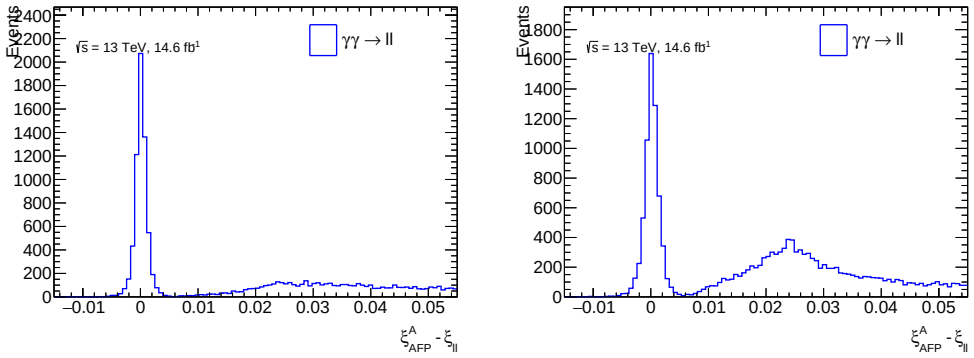

(a) (b)

Figure 5.14: $\xi^{A}_{\mathrm{AFP}} - \xi_{\ell\ell}$ distribution of the $\gamma\gamma \to \ell\ell$ sample with the requirement of having at least one AFP proton and cuts on the di-lepton system kinematics (presented in Section 5.2.2), with the proton pile-up overlay and simulation done at tracks level (a) and at clusters level (b). The (b) distribution is done using an enhanced proton pile-up database, with events containing at least 100 clusters in order to see the effect more clearly.

reconstruction. Regularly during data taking, checks are done to identify and map them. One could imagine linking these maps to the simulation.

- Consider the per-plane efficiency. All planes do not have the same efficiency and one could take this into account as a correction factor.

- Choose randomly from the proton pile-up database. For now, the proton pile-up database is read from top to bottom and looped over if more entries are needed than its length (which never happens in practice due to the difference in size between the database and the typical order of magnitude of selected events in an AFP anaalysis). Another approach would be to read the database randomly. It was assumed during the development of this tool that the benefit would be minor in comparison with the difficulty of technical implementation. It is considered that the process is already random enough to not introduce any bias.

This tool will be used in the next chapter for the background estimation of the studied process.

Chapter 6

Measurement of the photon-induced ZZ production process

This chapter will describe the author's work in the ongoing of $\gamma\gamma \to ZZ \to 4\ell$ analysis. As the analysis is not finalized at the time of writing, only preliminary results will be exposed and should not be considered as final: many optimizations and corrections are still ongoing. The limitations of this simplified analysis in comparison with the future final analysis will be presented and discussed.

6.1 Analysis strategy

This analysis aims to measure the cross section of the $\gamma\gamma \to ZZ \to 4\ell$ process in association with at least one intact proton. The leptons are reconstructed within the central ATLAS detector while AFP detects one of the intact protons. Only one decay channel of the Z boson pair, the four muon final state, was studied and will thus be discussed in this chapter, even though the other channels (four electrons and two muons plus two electrons) will be considered in the final analysis. The goal

is also to set limits on Wilson coefficient of dimension 8 EFT operators from the Eboli model [136], which describes Anomalous Quartic Gauge Couplings (aQGC)s. The origin of these operators has already been discussed in Section 2.2.

Figure 6.1 shows the Feynman diagram of the process. This process is not predicted by the SM at tree-level (see Table 2.1). The only valid SM diagrams contain loops and are therefore heavily suppressed. In the studied dataset (Run 2 2017 AFP dataset corresponding to $14.6\,\mathrm{fb}^{-1}$), no events originating from this process are expected (details will be given later in Section 6.2). Any observation of signal events would be a sign of new physics.

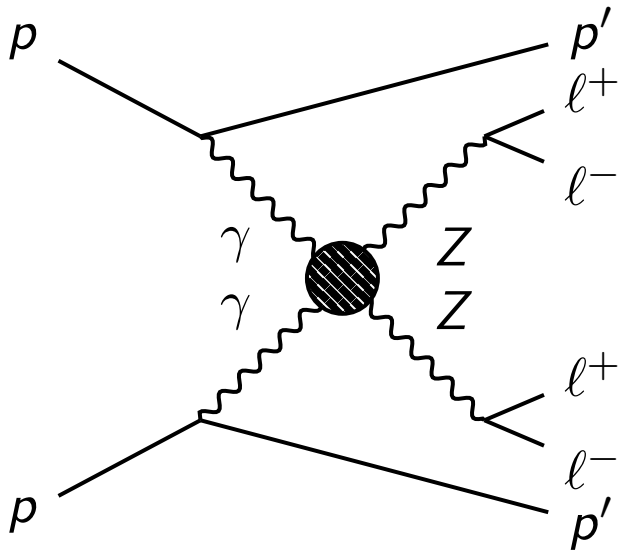

Figure 6.1: Feynman diagram of forward proton scattering in association with 2 lepton pairs ($e^+e^-e^+e^- + p$, $\mu^+\mu^-\mu^+\mu^- + p$, or $e^+e^-\mu^+\mu^- + p$) produced from Z decay via photon fusion. The dotted circle represents any SM or BSM vertex or interaction. This diagrams represent the elastic case only but diagrams in which one of the protons dissociate are also considered.

This analysis is based on a "cut-and-count" strategy. Different Signal Regions (SRs) were designed in the phase space in order to accept as many signal events as possible while rejecting as many background events as possible.

The blinding strategy used in the analysis was different from the one usually used in ATLAS analysis (consisting of explicitly blinding the SR): the principle was

to create a blinded sample by decorrelating the protons from the central detector information. The details of this procedure will be explained later in Section 6.3.

An EFT interpretation is done by fitting a likelihood function of the Wilson Coefficients of certain EFT operators in which aQGCs appear to the data.

Since this analysis does not require two protons to be detected, one must consider the different soft processes in hadron-hadron collisions, where protons can dissociate (see Section 4.2 for more details). The elastic scattering (where both protons remain intact) and the single diffractive dissociation (where only one proton remains intact while the other dissociates) cases will be considered.

6.2 Data and simulated samples

6.2.1 Analysis software

This analysis has been developed using two different computational frameworks: one was developed from scratch by the author and was used as the main source for the results shown in this chapter; the second is a standard ATLAS analysis framework actively used for many analyses in the Super Symmetry (SUSY) group, `SusySkimAna` [137]. It was used mainly for cross-checks during the development of the analysis. Unless stated otherwise, all plots presented in this chapter originate from the standalone framework and were produced by the author.

The DAOD to ntuple step is performed using code based on `Athena` [132], the official ATLAS analysis base framework presented in Chapter 5. During this step, standard CP tools are applied to take into account detector performance. These corrections will be detailed in Section 6.2.3. No event selection is done at this step, but all relevant information about the reconstructed objects in each event (and therefore if they meet the selection criteria or not) are recorded after corrections. The selection code was developed using `PyROOT`, a `Python` [138] interface to `ROOT` [59], specifically

using the `RDataFrame` class [139]. It is then completed by a semi-automatic plotting macro developed using `PyROOT` and the `atlasplots` package [140].

The limit setting procedure on the cross-section compared with the SM that will be presented in Section 6.8.1 is done using the `pyhf` framework [141, 142]. The EFT interpretation and corresponding limits that will be presented in Section 6.8.2 is done using the `EFTfun` framework [143].

6.2.2 Data

The analysis uses proton-proton collision data recorded with the ATLAS detector during the Run 2 data-taking period at $\sqrt{s} = 13\,\text{TeV}$. The data are first "cleaned" to remove events recorded with a non-functional detector [144]. The average number of interactions per bunch-crossing was 36 [145]. During Run 2, AFP was fully operational and instrumented in 2017 only. Data are selected using the lowest unprescaled di-lepton trigger (`HLT_2mu14`, firing if two muons with a p_T of at least 14 GeV are detected). Other unprescaled di-lepton triggers exist but require asymmetric p_T thresholds. The choice of not using these triggers was motivated by the selection of this analysis which requires the leptons to have a very low combined lepton p_T, $p_T^{4\ell}$, thus the lepton p_T will be almost balanced. The offline selection recommended by the muon trigger group is the trigger p_T cut $\times 1.05$ so the chosen value in the offline analysis was $p_T(\mu) > 15\,\text{GeV}$ only for the leading and sub-leading[1] muons.

The selected events are required to pass the AFP GRL selection. This list is a subset of the GRL for the nominal 2017 data produced by the Data Preparation group, for which AFP was inserted and recorded data with tolerable data quality as defined by the Forward CP group. After the central 2017 GRL is applied, the total integrated luminosity with AFP inserted is $26\,\text{fb}^{-1}$. Several requirements need to be fulfilled for a luminosity block[2] to be in the nominal AFP GRL:

[1] Muons are sorted based on their p_T value.
[2] A subdivision of a run, typically one minute long.

- All the AFP stations need to be in physics position.
- At least three[3] planes with a correct High Voltage ($< -5\,\mathrm{V}$) in every station.
- No problems with the readout on side A and C.
- No problems with the data processing modules on side A and C.

The total integrated luminosity of runs fulfilling AFP data quality requirements is $14.6\,\mathrm{fb}^{-1}$.

6.2.3 Simulated samples

Signal and background processes were modelled using MC event generators. Background was also modelled using a data-mixing technique, detailed in Section 6.3. Only MC samples will be discussed here. EFT samples were also produced using MC event generators. All of the MC samples undergo the same selection process where different corrections recommended by the various CP groups are applied and the subsequent weights are applied. The simulations use the knowledge of the detector to calculate a weight to be applied to the data as follows :

- Cross-section normalization: this scale factor renormalizes the event sample to the target cross-section $\mathcal{L}_{int.}$. It is done by accessing the sum of the MC event weights (attributed by the generator to each event - which can be negative) from the AOD (where the DAOD originates from), $\sum w_{\mathrm{AOD}}$. The cross-section normalization w_{xsec} is applied to each event and is obtained using $w_{\mathrm{xsec}} = \frac{\mathcal{L}_{int.} \times \sigma}{\sum w_{\mathrm{AOD}}}$ where σ is the cross-section of the simulated process.
- Lepton weights and corrections: this scale factor is provided by the Muon CP group and takes into account the detector efficiencies, correcting the reconstruction (*e.g.* track-to-vertex association, identification, isolation) of these

[3]Another *Loose* GRL is defined, requiring only two instead of three planes working. Due to some serious efficiency drops observed in some runs having fewer than 3 planes working in station A-NEAR , the requirement was changed from two to three, vetoing 25 runs. The *Loose* GRL corresponds to $19\,\mathrm{fb}^{-1}$.

objects. A correction tool is also used to correct for the imperfect reconstruction of the leptons.

- Pile up weights: this scale-factor reweights the MC to Data in terms of the average pile-up distribution.

- Trigger scale-factor: this event-level weight takes into account the trigger efficiencies.

Detailed information on the different tools used in the analysis can be found in the appropriate documentation pages provided by the various ATLAS CP groups, summarized in Ref. [146].

6.2.3.1 SM samples

The $\gamma\gamma ZZ$ vertex isn't allowed by the SM. The only way of producing a Z boson pair via photon fusion is through a loop (an example is shown on Figure 6.2) and is therefore highly suppressed. Table 6.1 summarizes the information of the different MC samples originating from SM processes used in this analysis. All the different diffractive contributions (elastic and single-dissociative) were generated independently and constitute together the signal of the analysis. It uses the `MG5_aMCNLO` generator [56, 57] for the matrix element together with `Pythia8` for modelling the underlying event and parton shower with the `CT14qed` [40] PDF set. Only the main background MC sample was considered and will be detailed in Section 6.3. It is simulated using `Sherpa 2.2.2` [55] with the `NNPDF3.0 NNLO` [41, 42] PDF. Each sample is generated with the generation filter indicated in Table 6.1 in order to reduce the size of the sample by rejecting events that will for sure fail the selection, due to the kinematics of their generated leptons falling outside of the detector acceptance or their lepton multiplicity.

Table 6.1: Overview of the simulation tools used to simulate the various MC samples originating from SM processes. The first four rows give information about the signal processes considered. EE corresponds to the elastic component, SD (DS) to the single diffractive dissociation on side A (C) component. The last row gives information about the main background process.

Process	Generator	Filter
$\gamma\gamma \to 4\ell$ (EE)	`MG5_aMCNLO` + `Pythia8` + `CT14qed`	$p_T^{4\ell} > 2.5\,\text{GeV}$; $\lvert\eta\rvert < 2.7$; $N_{leptons} = 4$
$\gamma\gamma \to 4\ell$ (SD)	`MG5_aMCNLO` + `Pythia8` + `CT14qed`	$p_T^{4\ell} > 2.5\,\text{GeV}$; $\lvert\eta\rvert < 2.7$; $N_{leptons} = 4$
$\gamma\gamma \to 4\ell$ (DS)	`MG5_aMCNLO` + `Pythia8` + `CT14qed`	$p_T^{4\ell} > 2.5\,\text{GeV}$; $\lvert\eta\rvert < 2.7$; $N_{leptons} = 4$
di-boson VV	`Sherpa 2.2.2` + `NNPDF3.0 NNLO`	1 to 4ℓ

6.2.3.2 EFT samples

The different MC samples contributing to the $\gamma\gamma \to ZZ$ process originating from EFT operators were all produced using the same generator and the same filter. Similarly to the SM signal sample, a combination of `MG5_aMCNLO` and `Pythia8` together with the `CT14qed` PDF were used to generate the different samples. The generator level filter applied was similar although not identical: $p_T^{4\ell} > 3.5\,\text{GeV}$; $|\eta| < 2.5$; $N_{leptons} = 4$. These small differences are reflected in the choices made for the selection thresholds presented in the following sections. The operators considered in the analysis are the dimension 8 Eboli operators that give rise to aQGCs (see Table 2.1): $\mathcal{O}_{M0}$, $\mathcal{O}_{M1}$, $\mathcal{O}_{M2}$, $\mathcal{O}_{M3}$, $\mathcal{O}_{M4}$, $\mathcal{O}_{M5}$, $\mathcal{O}_{M7}$, $\mathcal{O}_{T0}$, $\mathcal{O}_{T1}$, $\mathcal{O}_{T2}$, $\mathcal{O}_{T5}$, $\mathcal{O}_{T6}$, $\mathcal{O}_{T7}$, $\mathcal{O}_{T8}$ and $\mathcal{O}_{T9}$.

Each sample was generated by setting the corresponding Wilson coefficient to $f_{\mathcal{X}i} = 10^{-8}\,\text{GeV}^{-4}$, leaving all the other parameters to zero. This is the usual assumption made in analyses with EFT interpretations. The linear (*i.e.* the SM interference term in the amplitude) and the quadratic (*i.e.* the the purely new physics term in the amplitude) terms are generated independently in two different samples, leaving us with 30 samples (15 operators $\times$ 2 terms).

Only the elastic components of these samples were generated, with the exception of the $\mathcal{O}_{T5}$ sample, where all contributions were generated. The procedure used to estimate the dissociative components of the other operators consists of applying corrections to the elastic sample and will be explained in Section 6.6. The simulated

dissociative components of the $\mathcal{O}_{T5}$ samples are used to derive the corrections and for the closure test of this procedure.

6.3 Background modelling

The main source of background arises from processes with four leptons in the final-state combined with intact protons originating from pile-up interactions. Feynman diagrams of such processes are shown in Figure 6.2. One can also refer to Figure 5.2, showing the signatures of a background process. The only difference with this schematic is that in the analysis presented in this chapter, we must consider events with four leptons instead of two (as in the analysis presented in Chapter 5).

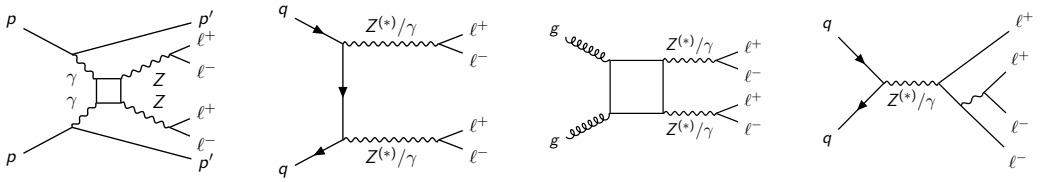

(a) (b) (c) (d)

Figure 6.2: Feynman diagrams of SM signal and main background processes. Fig. (a) shows a possible SM signal, introducing a fermionic loop. Fig (b-d) show different background processes with four leptons in the final state and proton arising independently due to pile-up. (b) shows the di-boson production of a Z boson pair originating from quarks, (c) shows the di-boson production of a Z boson pair originating from gluon fusion, (d) shows four lepton production via QED radiation in a Drell-Yan process.

Two methods were considered in order to evaluate the background in this analysis. The first one, commonly used in ATLAS analyses, is MC-based, where the background is simulated using MC generators. Unfortunately, most ATLAS MC samples do not contain diffractive information, *i.e.* the scattered (or dissociated) proton information is not simulated. The pile-up proton overlay presented in Section 5.4.2 was developed (among other reasons) for this purpose. The resulting background samples contain simulated particles (for the central detector part) overlaid with proton information coming from real data.

The second background modelling method is referred to as "combinatorial background" and uses a data-driven technique called event mixing. It consists in combining the central detector information from a real data event and the proton information from a different data event which is shifted by some number of position in the event record i. It mimics the combination with pile-up protons occurring in the combinatorial background. Many orthogonal mixed samples are generated (16 in this analysis), using a different value of shifting i (here, from $i = 2$ to $i = 17$) and combined together (assigning each event a weight of 1/16) to provide a large sample size for the background model, reducing the statistical uncertainty on the background prediction. As the protons and the central lepton system are decorrelated using this method, it is also used for the blinding strategy of this analysis by generating a mixed sample with $i = 1$. This means that the blinded data sample is obtained from the central detector information and the proton information coming from the next event present in the sample, thus ignoring the proton information from the considered event[4]. The value for the shifting $i = 1$ is chosen arbitrarily and could be any other value.

This method was also used in Ref. [6]. A schematic representing the event mixing procedure for a given value of $i = 2$ is shown in Figure 6.3. It will be used as the primary background modelling technique in this analysis. The MC-based technique will be used for cross-checks and uncertainty estimates.

An alternative method for the background estimation is also used in a similar ongoing ATLAS analysis measuring photon-induced WW production in the semileptonic channel with AFP. This method is MC-based and also consists on overlaying AFP proton information onto background MC samples. The overlay is however done in a different way from that presented in this thesis: it consists of randomly sampling the number of protons on each side from a real Data event, before sampling proton energy loss values based on the number of protons in the event. These information (the number of protons and their energy) are then overlaid to the background MC

[4]This proton information will be used and combined with the central detector information coming from the previous event

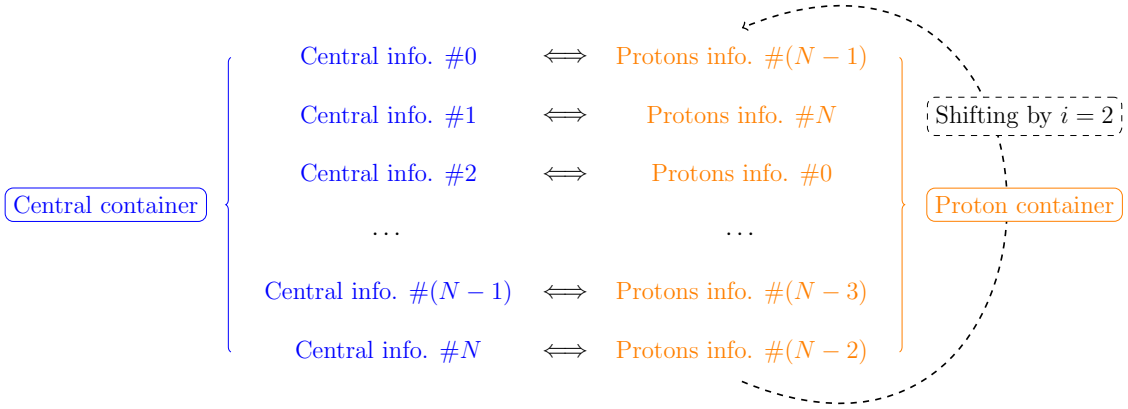

Figure 6.3: Event mixing procedure used to produce the data-driven model of the combinatorial background, with an event shifting value of $i = 2$. A given ATLAS event $\#n$ in a sample of size N is composed of central detector information (blue) coming from the central containers and proton information (orange) coming from the proton container. After shifting, the proton information is matched with the central information of the next-to-next event in the sample.

samples. The procedure is repeated multiple times over the full background MC samples and averaged to reduce statistical fluctuations. It is not clear yet within the AFP community which solution will ultimately be chosen, even though they lead to similar results.

6.4 Event selection

In order to remove the largest possible amount of background, several requirements were imposed both to the leptons system and to the scattered protons detected in AFP. Some of the requirements for the selection are similar to the ones presented for the di-lepton analysis in Section 5.2.2. This is understandable as the two processes share similarities that will be explained below. First, a preselection is done, categorizing the individual leptons in two classes: “baseline” and “signal”. Table 6.2

summarizes the requirements that a muon needs to fulfil for both categories. The baseline selection was only defined for control purposes but was quickly abandoned in the analysis as the signal preselection showed a much better agreement between data and MC.

Table 6.2: Definition of baseline and signal muon objects.

	Baseline Muon	Signal Muon
Kinematics	$p_T > 3.0\,\text{GeV}$, $\lvert\eta\rvert < 2.47$	$p_T > 3.0\,\text{GeV}$, $\lvert\eta\rvert < 2.40$
Identification	Medium	Medium
Isolation	-	Loose_VarRad
Impact parameters	$\lvert z_0 \sin\theta\rvert < 0.5\,\text{mm}$	$\lvert\frac{d_0}{\sigma_{d_0}}\rvert < 3$, $\lvert z_0 \sin\theta\rvert < 0.5\,\text{mm}$

We will refer to the following selection as the "preselection" in the following. This preselection was already partly presented and explained in Section 6.2 but the full preselection is:

- For data, the event must be part of the AFP GRL. As detailed in Section 6.2, this list corresponds to Runs when the central detector and AFP fulfil several quality requirements.
- At least 4 signal muons are required. Two pairs of muon-antimuon are required, by summing the charge of the leptons and requiring it to be equal to zero.
- The event must pass the lowest unprescaled di-lepton trigger `HLT_2mu14`, firing when two muons with a p_T of at least 14 GeV are detected.
- The leading and subleading muons, sorted in p_T order, must satisfy $p_T^\ell > 15\,\text{GeV}$ and $\lvert\eta\rvert < 2.4$.

Some chosen kinematic distributions are shown after preselection for data and compared with the main background MC sample in Figure 6.4. Additional distributions can be found in Appendix B. The same distributions are shown both for the standalone analysis and the `SusySkimAna`-based framework, including all the background

processes discussed in Section 6.3 and the signal sample. The agreement between the two frameworks is satisfactory for this analysis, the differences arise due to the versions of the underlying CP tools used for the corrections and weights. The combinatorial background is not shown at this stage as it is exactly the same as data by design (as there is no AFP selection yet at this stage).

6.5 Definition of the signal

Different event regions were designed in order to characterise the signal and reject the largest amount of events resulting from background. There are two Signal Regions (SRs), defined as follows:

- The event must pass the preselection criteria. Exactly 4 leptons must be identified as signal muons, as described in Section 6.4.
- $p_{T,\text{norm.}} = p_T^{4\ell} / \sum p_T^{\ell} < 0.06$, where is $\sum p_T^{\ell}$ the scalar sum of the four individual leptons p_T, to suppress diboson background relative to the $\gamma\gamma$ production mechanism, which typically generates only very little transverse momentum. This cut chosen in preference to to a cut on the $p_T^{4\ell}$ variable. The choice of balancing $p_T^{4\ell}$ by the sum of the individual p_T^{ℓ} was motivated by resolution effects observed in the EFT samples. A discussion about the motivation and the optimization of this cut can be found later in this section.
- $\xi_{4\ell}, \xi_{\text{AFP}} \in [0.02; 0.12]$ for at least one AFP side. This requirement selects events with one or more proton candidate. If there is more than one proton candidate on the same AFP side, which occurs in 35% of the selected events, the proton with ξ_{AFP} closest to $\xi_{4\ell}$ is chosen.
- $|\Delta\xi| = |\xi_{\text{AFP}} - \xi_{4\ell}| < 0.005$. Proton tagged four lepton candidates are selected by requiring kinematic matching.

This selection defines two SRs, one per side, SRA and SRC, depending on which side

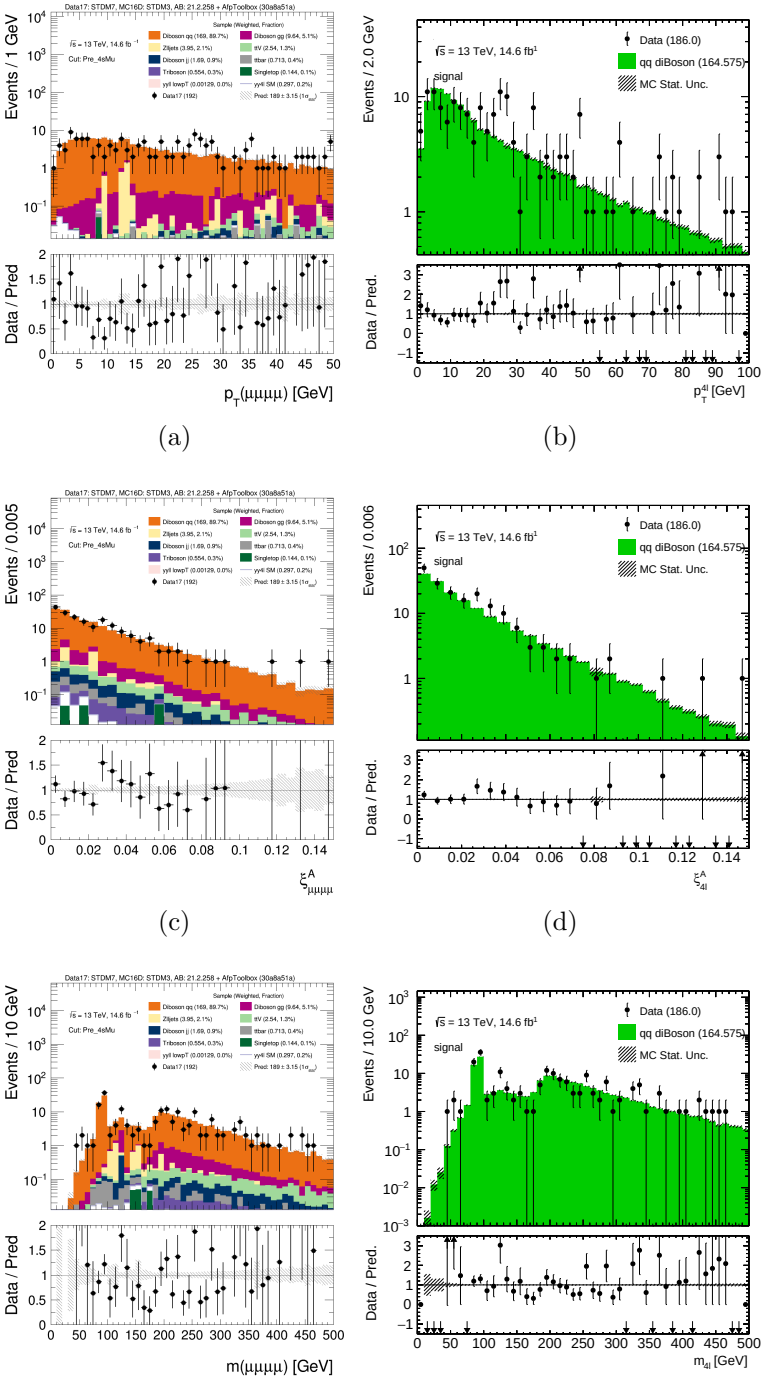

Figure 6.4: Distributions of the transverse momentum (a-b), the proton energy loss (c-d) and the invariant mass (e-f) of the four leptons system in the case where 4 signal muons are required. The left column (a-c-e) shows the distributions produced by the `SusySkimAna` framework and includes all MC samples (signal and background) and Data. The right column (b-d-f) only includes the main $q\bar{q}$ diboson background MC sample and Data. The plots in the left column were not produced by the author.

the proton is tagged. Several Control Regions (CRs) are also defined, by inverting each cut individually. The event yield in the two SRs is given in Table 6.3 for the blinded data sample, the main background (diboson) sample, combinatorial background obtained by the event-mixing method, and the signal process for all diffractive components. No events are expected in the SRC (resp. SRA) for the DS (resp. SD) sample, as all protons on side C (resp. A) dissociate in this sample. The uncertainties are only statistical and are taken as the square root of sum of the squared weights.

Table 6.3: Comparison of the event yield in the two Signal Regions between the blinded data sample, the two background modelling methods, the main MC background sample and the combinatorial background, and the signal model, the $\gamma\gamma \to 4\ell$ signal MC sample for all different diffractive components. The uncertainties are only statistical.

Sample	SRA yield	SRC yield
Data	1	1
MC Diboson	0.838 ± 0.05	0.932 ± 0.04
Combinatorial background	1.9 ± 0.3	1.4 ± 0.3
MC $\gamma\gamma \to 4\ell$ (EE)	0.010 ± 0.003	0.014 ± 0.003
MC $\gamma\gamma \to 4\ell$ (SD)	0.007 ± 0.002	0
MC $\gamma\gamma \to 4\ell$ (DS)	0	0.010 ± 0.003

6.5.1 Background modelling controls

The quality of the modelling of the combinatorial background simulated by the event-mixing method can be checked in the following Control Region (CR)s:

- CRA-$p_T^{4\ell}$, CRC-$p_T^{4\ell}$, defined as their corresponding SR with an opposite $p_{T,\text{norm.}}$ cut, *i.e.* $p_{T,\text{norm.}} > 0.06$.
- CRA-match, CRC-match, defined as their corresponding Signal Region (SR) with an opposite $|\Delta\xi|$ cut, *i.e.* $|\Delta\xi| > 0.005$.
- CRA-$p_T^{4\ell}$,match, CRC-$p_T^{4\ell}$,match, defined as their corresponding SR with an opposite $|\Delta\xi|$ and $p_{T,\text{norm.}}$ cut, *i.e.* $|\Delta\xi| > 0.005$, $p_{T,\text{norm.}} > 0.06$.

Table 6.4 compares the event yield in each of these CRs between the blinded data sample and the combinatorial background. Some corresponding kinematic plots are shown in Figure 6.5. The good agreement between data and the mixed-event background sample in these background-dominated regions of the phase-space gives confidence in using the event-mixing technique to estimate the background yield. Since this sample is hybrid and made of non-independent sub-samples, the statistical uncertainties can't be estimated as the square root of the squared weights and a more refined statistical treatment is needed to estimate properly the associated uncertainties: a bootstrap method consisting of creating many replicas of the mixed-event sample. Then, for each event in each replica, we assign a random event weight generated from a Poisson distribution with mean of 1. For any observable (for example the expected background in a given bin), the statistical uncertainty will be given by the standard deviation among the replicas. A toy study of the estimation of these uncertainties can be found in Ref. [147]. As a first estimate, the uncertainties will, however, be taken as the square-root of the sum of the squared weights, therefore over-estimating them.

Table 6.4: Comparison of the event yield in each of the Control Regions between the blinded data sample and the combinatorial background. The uncertainties are only statistical.

Region	Data yield	Combinatorial background yield
CRA-$p_T^{4\ell}$	2	4.4 ± 0.5
CRC-$p_T^{4\ell}$	5	4.3 ± 0.5
CRA-match	6	7.3 ± 0.7
CRC-match	7	7.6 ± 0.7
CRA-$p_T^{4\ell}$,match	26	23.1 ± 1.2
CRC-$p_T^{4\ell}$,match	21	27.2 ± 1.3

6.5.2 Motivation and optimization of the normalized transverse momentum of the four leptons system selection

When looking at the preselected events for the different samples, non-negligible resolution effects were observed in the transverse momentum of the four lepton

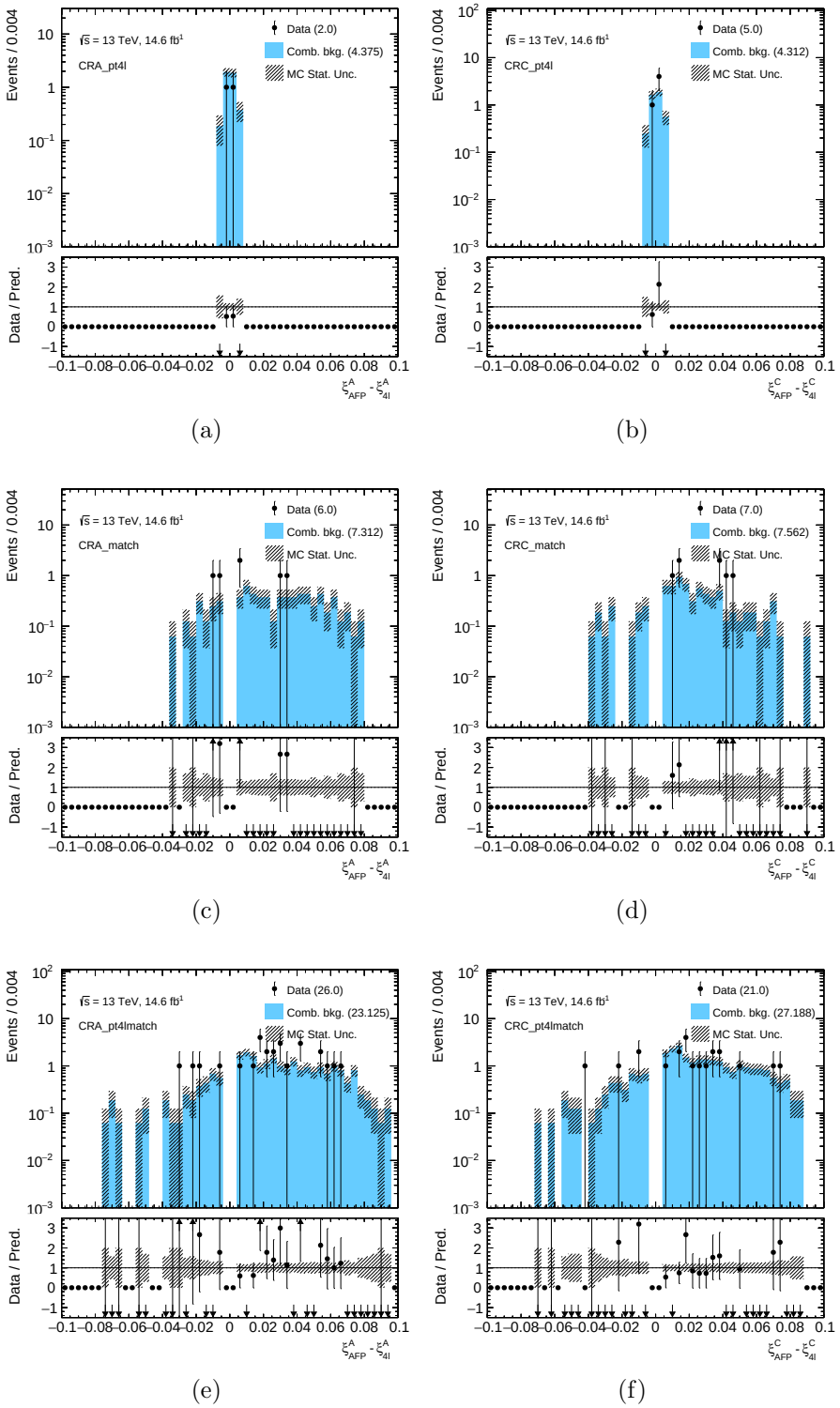

Figure 6.5: Comparison of the distribution in the difference in proton-energy loss for the CR-$p_T^{4\ell}$ (a-b), CR-match (c-d) and the CR-$p_T^{4\ell}$,match (e-f) control regions between the blinded data sample and the combinatorial background sample.

system distribution. Figure 6.6 shows this distribution at the reconstructed and the truth level for two MC signal samples: one describing the SM contribution for the signal and the other the signal model coming from the quadratic contribution of the EFT operator $\mathcal{O}_{T5}$. This effect was observed in all EFT samples.

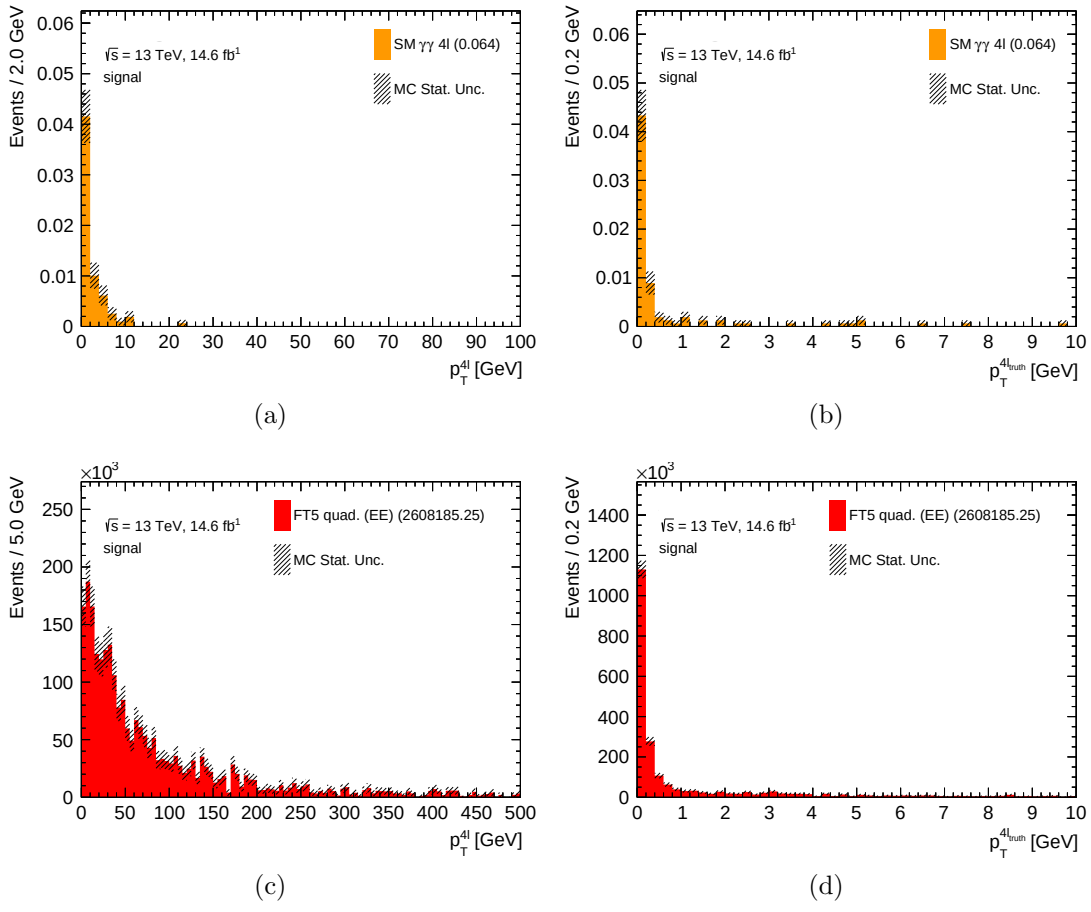

Figure 6.6: Distribution of the transverse momentum of the four leptons system for preselected events (requiring four signal muons) at the reconstructed (left column) and the truth (right column) level for the signal SM sample (upper row) and the quadratic component of the EFT $\mathcal{O}_{T5}$ sample. Only the elastic component of each sample are shown here.

A different behaviour can be observed between the two samples. As expected, both truth distributions are peaked at 0, but the spread of the reconstructed distribution (which we can access experimentally and therefore cut on) becomes large for the the EFT $\mathcal{O}_{T5}$ sample. Cutting on this variable (*e.g.* at 5 GeV like the analysis described in Chapter 5) would result in a massive loss of efficiency.

The reason for the large growth in $p_T^{4\ell}$ between truth and reconstructed level in the EFT sample is that this variable is subject to high cancellation: muons in the EFT samples have in general larger individual p_T, leading to larger uncertainty when summing as vectors to obtain $p_T^{4\ell}$. This hypothesis can be checked by looking at the dependence of the $p_T^{4\ell}$ resolution with $p_x^{\ell 1,truth}$ and $p_y^{\ell 1,truth}$, the p_x and p_y values of the leading muon momentum. The resolution on $p_T^{4\ell}$ is estimated by looking at the distribution of the difference between the reconstructed and truth value of $p_T^{4\ell}$, and taking the resolution as the width of the Gaussian fit. This is done in a range of $p_x^{\ell 1,truth}$ and $p_y^{\ell 1,truth}$ bins. The resulting plot is fitted with a linear and a quadratic function and shown in Figure 6.7 for the the EFT samples (for the example of $p_x^{\ell 1,truth}$) together with the fractional resolution dependence (the resolution divided by the bin value of $p_x^{\ell 1,truth}$). As expected, we observe a dependence of the $p_T^{4\ell}$ resolution with $p_x^{\ell 1,truth}$. This effect becomes even more visible in the fractional resolution fit being flat.

The easiest solution was to balance $p_T^{4\ell}$ by the scalar sum of the individual p_T^{ℓ}, resulting in the $p_{T,\text{norm.}} = p_T^{4\ell} / \sum p_T^{\ell}$ variable. Distributions for the elastic component of the signal SM sample, the diboson backgound MC sample (the main background), and the quadratic component of the elastic component of the EFT $\mathcal{O}_{M0}$ sample are shown on Figure 6.8. Selecting the signal on $p_{T,\text{norm.}}$ instead of $p_T^{4\ell}$ allows to use the same selection for both the SM and EFT samples. Another solution to overcome this problem would have been to propagate the reconstruction error of the individual muons to the 4-muon system reconstruction and cut on its consistency with zero (*e.g.* at 3σ). This solution was not chosen given the satisfactory results of the first solution which was easier to implement, but this more precise and elegant solution could be used for future improvements of the analysis.

Different values were tested for the cut on $p_{T,\text{norm.}}$ and the choice was made by looking at the distributions shown in Figure 6.8. The objective was to keep as much signal as possible while removing the most background events possible. The values tested for the cut were $p_{T,\text{norm.}} < \{0.04, 0.06, 0.1\}$. The metric used to choose the value were the computed limits for the associated Wilson coefficient. The procedure used

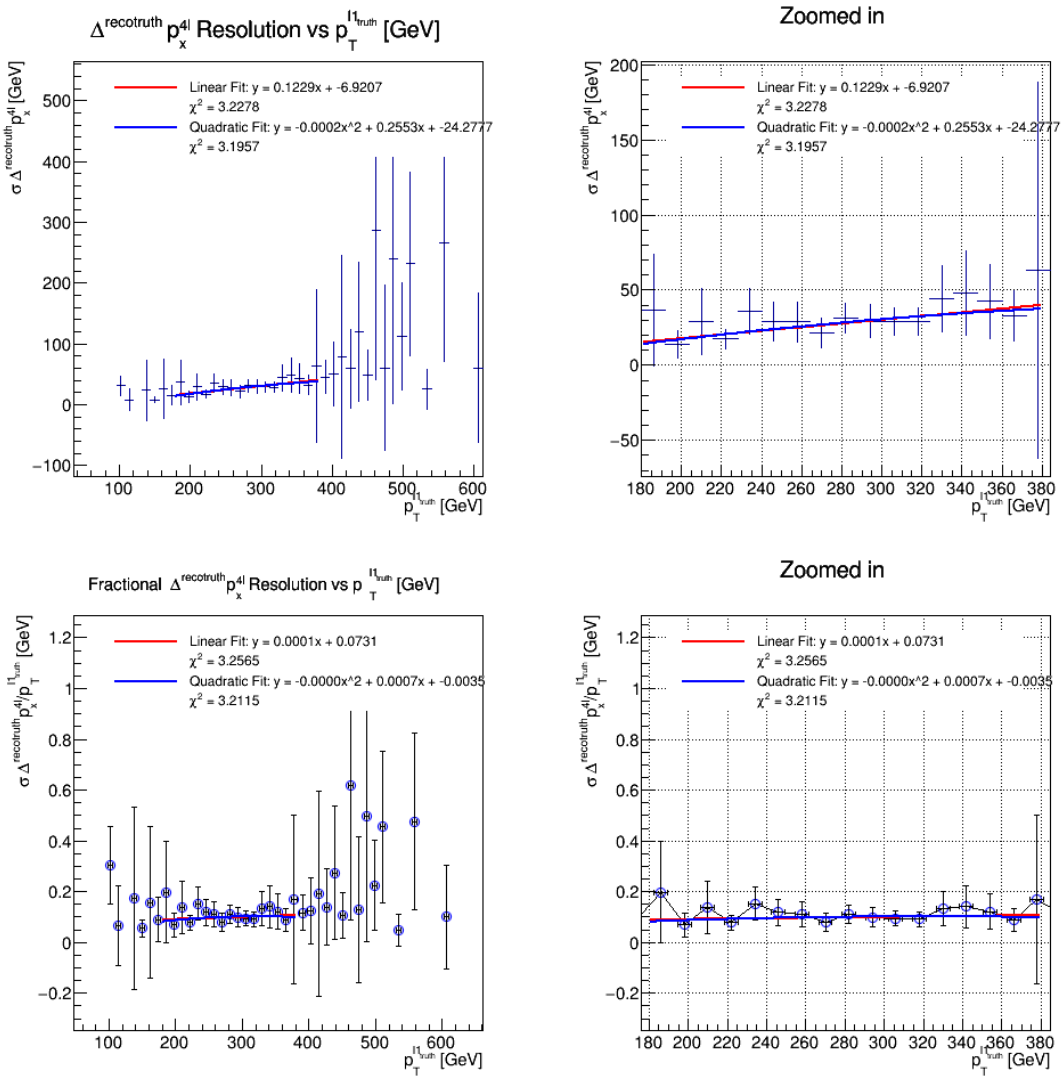

Figure 6.7: Linear and quadratic fits of the $p_T^{4\ell}$ resolution (top-left) and fractional $p_T^{4\ell}$ resolution (bottom-left) as a function of $p_x^{\ell 1,truth}$ (top-left). The plots on the right are zoomed versions of the plots on the left on the range of value where the fit is done. The samples are preselected events of the quadratic contribution of the EFT $\mathcal{O}_{M0}$ sample.

to obtain this limit will be explained later in Section 6.8.2. The cut at $p_{T,\text{norm.}} < 0.06$ gave the best results. A more refined study optimizing this cut could lead to slightly better results.

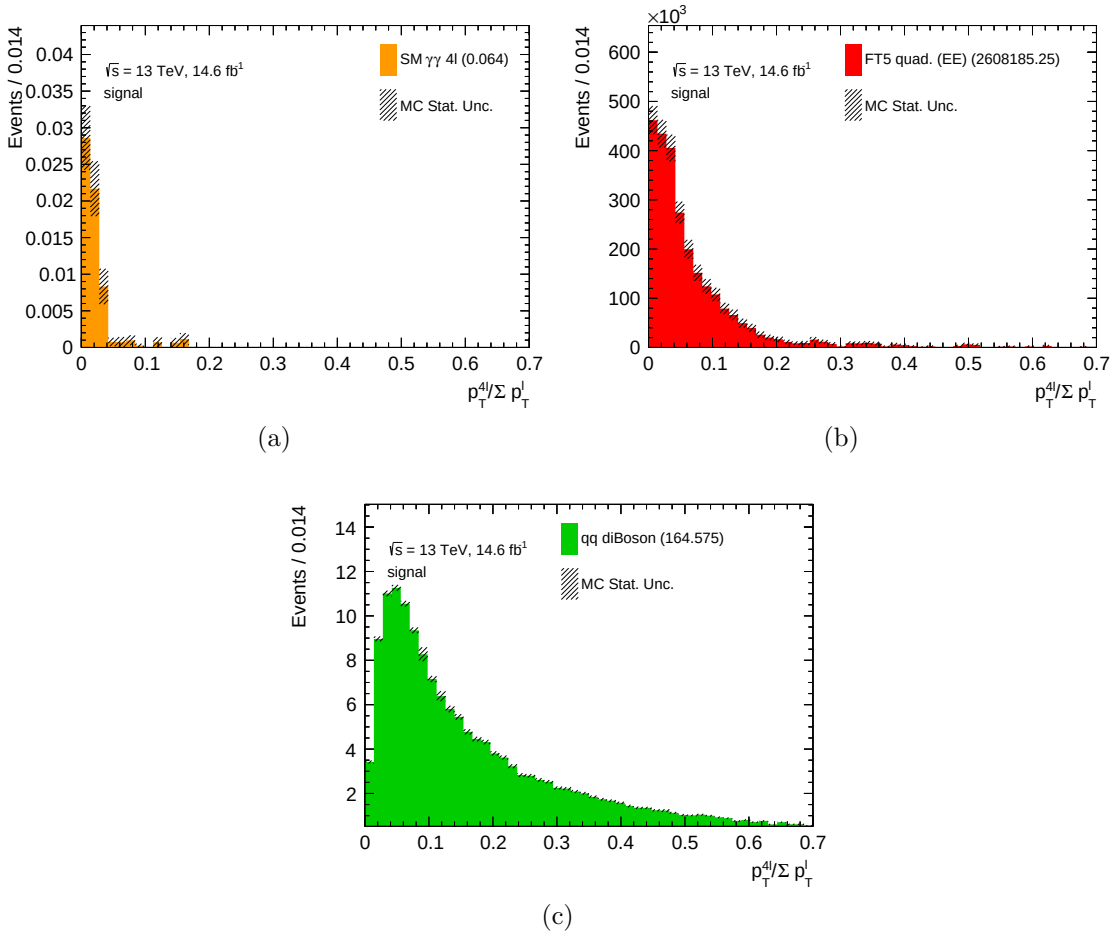

Figure 6.8: $p_{T,\text{norm.}} = p_T^{4\ell} / \sum p_T^{\ell}$ distribution of the preselected events (requiring four signal muons) for the signal SM sample (a), the quadratic component of the EFT $\mathcal{O}_{T5}$ sample (b) and the diboson MC sample (c). Only the elastic component of the first two samples is shown here.

6.5.3 Linear and quadratic contributions of the EFT samples

As already said in Section 6.2.3.2, the linear and the quadratic terms are generated independently for each EFT sample. Table 6.5 shows the cross-sections of each term for each operator considered in this analysis. Some of the cross-sections for the linear term are negative because these terms take into account for interferences between the EFT operator and the SM Lagrangian, which may be destructive. It is important to bear in mind that the cross-sections presented here are for a specific value of the Wilson coefficient for which the samples were created. The fact that linear

terms represent the interference between the EFT operator and the SM Lagrangian sometimes leads to negative cross-section. The linear contributions are negligible in comparison to the quadratic contributions, therefore they will not be considered further by default.

Table 6.5: Cross-sections of each term (linear and quadratic) for the 15 EFT operators considered in the analysis generated with a value of the respective Wilson coefficient of 10^{-8} GeV^{-4}. Only the elastic contributions are shown in this table.

Operator	Cross-section (linear term) [fb]	Cross-section (quadratic term) [fb]
$\mathcal{O}_{M0}$	-6.86 $\times 10^{-3}$	4.10 $\times 10^{3}$
$\mathcal{O}_{M1}$	4.62 $\times 10^{-3}$	2.69 $\times 10^{2}$
$\mathcal{O}_{M2}$	-4.32 $\times 10^{-2}$	1.76 $\times 10^{5}$
$\mathcal{O}_{M3}$	3.06 $\times 10^{-2}$	1.16 $\times 10^{4}$
$\mathcal{O}_{M4}$	1.24 $\times 10^{-2}$	1.34 $\times 10^{4}$
$\mathcal{O}_{M5}$	1.67 $\times 10^{-2}$	3.53 $\times 10^{3}$
$\mathcal{O}_{M7}$	-2.39 $\times 10^{-3}$	6.73 $\times 10^{1}$
$\mathcal{O}_{T0}$	6.13 $\times 10^{-1}$	5.82 $\times 10^{5}$
$\mathcal{O}_{T1}$	6.13 $\times 10^{-1}$	5.82 $\times 10^{5}$
$\mathcal{O}_{T2}$	4.64 $\times 10^{-1}$	1.33 $\times 10^{5}$
$\mathcal{O}_{T5}$	7.99 $\times 10^{-1}$	2.42 $\times 10^{6}$
$\mathcal{O}_{T6}$	-4.12 $\times 10^{-1}$	1.08 $\times 10^{6}$
$\mathcal{O}_{T7}$	1.85 $\times 10^{-2}$	1.44 $\times 10^{5}$
$\mathcal{O}_{T8}$	1.85	2.36 $\times 10^{7}$
$\mathcal{O}_{T9}$	1.34	5.42 $\times 10^{6}$

Table 6.6 compares the event yields in different phase-space regions of the linear and quadratic terms for each operator. Some kinematic plots for different chosen operators are shown in Appendix B. As expected when comparing the cross-sections of the processes for the Wilson coefficients, the quadratic contributions dominates heavily. The linear contributions are almost all consistent with zero.

6.6 Estimation of the dissociative components of the EFT samples

As already said in Section 6.2, in most cases only the elastic components of the EFT samples are simulated. However, the proton dissociative contributions are expected

Table 6.6: Event yield in the preselection and the two Signal Regions of the linear and quadratic terms for each operator. The uncertainties are only statistical.

Operator	**Preselection**	**SRA**	**SRC**
Linear term			
$\mathcal{O}_{M0}$	$(-1.30 \pm 0.50) \times 10^{-2}$	$(-5.00 \pm 3.00) \times 10^{-3}$	$(-6.00 \pm 3.00) \times 10^{-3}$
$\mathcal{O}_{M1}$	$(4.00 \pm 4.00) \times 10^{-3}$	$(-3.00 \pm 2.00) \times 10^{-3}$	$(2.00 \pm 2.00) \times 10^{-3}$
$\mathcal{O}_{M2}$	$(-8.20 \pm 4.90) \times 10^{-2}$	$(-5.90 \pm 3.20) \times 10^{-2}$	$(-6.60 \pm 3.30) \times 10^{-2}$
$\mathcal{O}_{M3}$	$(2.70 \pm 2.20) \times 10^{-2}$	$(1.20 \pm 1.40) \times 10^{-2}$	$(2.20 \pm 1.30) \times 10^{-2}$
$\mathcal{O}_{M4}$	$(2.90 \pm 1.20) \times 10^{-2}$	$(2.00 \pm 0.80) \times 10^{-2}$	$(5.00 \pm 8.00) \times 10^{-3}$
$\mathcal{O}_{M5}$	$(1.40 \pm 0.70) \times 10^{-2}$	$(5.00 \pm 4.00) \times 10^{-3}$	$(9.00 \pm 5.00) \times 10^{-3}$
$\mathcal{O}_{M7}$	$(-1.00 \pm 1.00) \times 10^{-3}$	$(-1.00 \pm 1.00) \times 10^{-3}$	$(-1.00 \pm 1.00) \times 10^{-3}$
$\mathcal{O}_{T0}$	$(7.32 \pm 0.53) \times 10^{-1}$	$(2.44 \pm 0.32) \times 10^{-1}$	$(2.61 \pm 0.33) \times 10^{-1}$
$\mathcal{O}_{T1}$	$(7.16 \pm 0.57) \times 10^{-1}$	$(2.51 \pm 0.33) \times 10^{-1}$	$(1.92 \pm 0.35) \times 10^{-1}$
$\mathcal{O}_{T2}$	$(5.45 \pm 0.38) \times 10^{-1}$	$(1.94 \pm 0.24) \times 10^{-1}$	$(2.32 \pm 0.24) \times 10^{-1}$
$\mathcal{O}_{T5}$	$(6.69 \pm 1.98) \times 10^{-1}$	$(2.47 \pm 1.19) \times 10^{-1}$	$(8.80 \pm 1.29) \times 10^{-2}$
$\mathcal{O}_{T6}$	$(-4.09 \pm 1.46) \times 10^{-1}$	$(-7.20 \pm 8.90) \times 10^{-2}$	$(-1.97 \pm 8.60) \times 10^{-2}$
$\mathcal{O}_{T7}$	$(-2.00 \pm 3.60) \times 10^{-3}$	$(1.00 \pm 2.00) \times 10^{-2}$	$(-2.10 \pm 2.10) \times 10^{-2}$
$\mathcal{O}_{T8}$	(1.34 ± 1.26)	(1.41 ± 0.74)	$(4.55 \pm 0.71) \times 10^{-1}$
$\mathcal{O}_{T9}$	(1.70 ± 0.48)	$(5.51 \pm 0.32) \times 10^{-1}$	$(5.05 \pm 0.32) \times 10^{-1}$
Quadratic term			
$\mathcal{O}_{M0}$	$(4.69 \pm 0.12) \times 10^{3}$	$(1.04 \pm 0.06) \times 10^{3}$	$(1.06 \pm 0.06) \times 10^{3}$
$\mathcal{O}_{M1}$	$(2.99 \pm 0.01) \times 10^{2}$	$(7.05 \pm 0.04) \times 10^{1}$	$(7.00 \pm 0.04) \times 10^{1}$
$\mathcal{O}_{M2}$	$(1.99 \pm 0.05) \times 10^{5}$	$(4.53 \pm 0.03) \times 10^{4}$	$(4.53 \pm 0.02) \times 10^{4}$
$\mathcal{O}_{M3}$	$(1.31 \pm 0.34) \times 10^{4}$	$(3.00 \pm 0.16) \times 10^{3}$	$(3.19 \pm 0.17) \times 10^{3}$
$\mathcal{O}_{M4}$	$(1.48 \pm 0.39) \times 10^{4}$	$(3.21 \pm 0.18) \times 10^{3}$	$(3.37 \pm 0.19) \times 10^{3}$
$\mathcal{O}_{M5}$	$(3.86 \pm 0.10) \times 10^{3}$	$(8.72 \pm 0.49) \times 10^{2}$	$(9.29 \pm 0.50) \times 10^{2}$
$\mathcal{O}_{M7}$	$(7.52 \pm 0.02) \times 10^{1}$	$(1.68 \pm 0.01) \times 10^{1}$	$(1.87 \pm 0.01) \times 10^{1}$
$\mathcal{O}_{T0}$	$(6.15 \pm 0.16) \times 10^{5}$	$(6.07 \pm 0.51) \times 10^{4}$	$(7.78 \pm 0.58) \times 10^{4}$
$\mathcal{O}_{T1}$	$(6.18 \pm 0.16) \times 10^{5}$	$(7.34 \pm 0.57) \times 10^{4}$	$(7.32 \pm 0.57) \times 10^{4}$
$\mathcal{O}_{T2}$	$(1.40 \pm 0.04) \times 10^{5}$	$(1.68 \pm 0.13) \times 10^{4}$	$(1.69 \pm 0.13) \times 10^{4}$
$\mathcal{O}_{T5}$	$(2.61 \pm 0.69) \times 10^{6}$	$(3.10 \pm 0.24) \times 10^{5}$	$(3.02 \pm 0.24) \times 10^{5}$
$\mathcal{O}_{T6}$	$(1.16 \pm 0.31) \times 10^{6}$	$(1.23 \pm 0.10) \times 10^{5}$	$(1.18 \pm 0.10) \times 10^{5}$
$\mathcal{O}_{T7}$	$(1.58 \pm 0.04) \times 10^{5}$	$(1.13 \pm 0.11) \times 10^{4}$	$(1.10 \pm 0.11) \times 10^{4}$
$\mathcal{O}_{T8}$	$(2.48 \pm 0.66) \times 10^{7}$	$(2.53 \pm 0.21) \times 10^{6}$	$(1.82 \pm 0.18) \times 10^{6}$
$\mathcal{O}_{T9}$	$(5.71 \pm 0.15) \times 10^{6}$	$(3.99 \pm 0.40) \times 10^{5}$	$(5.12 \pm 0.46) \times 10^{5}$

to be significant and is therefore necessary to take them into account. In order to estimate them, the dissociative contributions of the quadratic component of the $\mathcal{O}_{T5}$ sample were generated and compared with the elastic contribution. The cutflow data for the elastic and dissociative components, together with their ratio are compared in Table 6.7. These values are shown considering the SM signal sample and the quadratic component of the $\mathcal{O}_{T5}$ operator only. These ratios are summarized on Figure 6.9. The elastic-to-dissociative ratio increases after each cut but stays at a

comparable level. Since the cross section of the linear EFT term was much smaller than the quadratic one, it was ignored in this procedure. The elastic-to-dissociative ratio is about 1 : 1 for the SM signal sample, and about 1 : 5 for the quadratic component of the $\mathcal{O}_{T5}$ sample in the signal regions. This can be explained by the fact that the EFT samples tend to have larger momentum transfer at the proton vertices. As the transverse momentum of the four muon system is equal to the transverse momentum of the proton system, this can be seen by comparing the width of the $p_T^{4\ell}$ distribution at the truth level of the SM signal sample and the quadratic component of the $\mathcal{O}_{T5}$ sample. Figure 6.10 shows these distributions, together with a Gaussian fit on the peak of the distribution. It is unlikely that these small differences are the only explanation of this difference in the elastic-to-dissociative ratio between the two samples. Also, the choice of a Gaussian function for the fit might not be the best choice but was arbitrarily made to enable comparison.

Table 6.7: Event yield after each cut is applied sequentially in the elastic and dissociative components of the signal SM sample and the quadratic component of the $\mathcal{O}_{T5}$ sample. The uncertainties are only statistical.

$\gamma\gamma \to 4\ell$ **sample**	EE contribution	SD + DS contributions	Ratio EE/(SD+DS)
Preselection (≥ 4 signal muons)	$(6.40 \pm 0.60) \times 10^{-2}$	$(1.76 \pm 0.11) \times 10^{-1}$	0.36
$p_T^{4\ell} / \sum p_T^{\ell} < 0.06$	$(5.90 \pm 0.60) \times 10^{-2}$	$(9.80 \pm 0.80) \times 10^{-2}$	0.61
$\xi_{4\ell}^{A} \in [0.02; 0.12]$	$(1.70 \pm 0.30) \times 10^{-2}$	$(3.00 \pm 0.40) \times 10^{-2}$	0.55
$\xi_{\mathrm{AFP}}^{A} \in [0.02; 0.12]$	$(1.00 \pm 0.30) \times 10^{-2}$	$(7.00 \pm 2.00) \times 10^{-3}$	1.46
$\lvert\Delta\xi^{A}\rvert < 0.005$ (SRA)	$(1.00 \pm 0.30) \times 10^{-2}$	$(7.00 \pm 2.00) \times 10^{-3}$	1.46
$\xi_{4\ell}^{C} \in [0.02; 0.12]$	$(1.80 \pm 0.40) \times 10^{-2}$	$(3.80 \pm 0.60) \times 10^{-2}$	0.47
$\xi_{\mathrm{AFP}}^{C} \in [0.02; 0.12]$	$(1.40 \pm 0.30) \times 10^{-2}$	$(1.00 \pm 0.30) \times 10^{-2}$	1.34
$\lvert\Delta\xi^{C}\rvert < 0.005$ (SRC)	$(1.40 \pm 0.30) \times 10^{-2}$	$(1.00 \pm 0.30) \times 10^{-2}$	1.34

$\mathcal{O}_{T5}$ **quad. sample**	EE contribution	SD + DS contributions	Ratio EE/(SD+DS)
Preselection (≥ 4 signal muons)	$(2.61 \pm 0.07) \times 10^{6}$	$(4.82 \pm 0.93) \times 10^{7}$	0.05
$p_T^{4\ell} / \sum p_T^{\ell} < 0.06$	$(1.65 \pm 0.06) \times 10^{6}$	$(2.17 \pm 0.63) \times 10^{7}$	0.08
$\xi_{4\ell}^{A} \in [0.02; 0.12]$	$(4.61 \pm 0.03) \times 10^{5}$	$(4.39 \pm 0.28) \times 10^{6}$	0.11
$\xi_{\mathrm{AFP}}^{A} \in [0.02; 0.12]$	$(3.63 \pm 0.03) \times 10^{5}$	$(1.77 \pm 0.18) \times 10^{6}$	0.21
$\lvert\Delta\xi^{A}\rvert < 0.005$ (SRA)	$(3.10 \pm 0.02) \times 10^{5}$	$(1.55 \pm 0.17) \times 10^{6}$	0.20
$\xi_{4\ell}^{C} \in [0.02; 0.12]$	$(4.81 \pm 0.03) \times 10^{5}$	$(4.08 \pm 0.27) \times 10^{6}$	0.12
$\xi_{\mathrm{AFP}}^{C} \in [0.02; 0.12]$	$(3.59 \pm 0.03) \times 10^{5}$	$(1.84 \pm 0.18) \times 10^{6}$	0.20
$\lvert\Delta\xi^{C}\rvert < 0.005$ (SRC)	$(3.02 \pm 0.02) \times 10^{5}$	$(1.63 \pm 0.02) \times 10^{6}$	0.19

In order to avoid having to actually produce the dissociative components of all the EFT samples, therefore saving computation time and shrinking the analysis timescale, an alternative solution was chosen. The elastic-to-dissociative ratio in

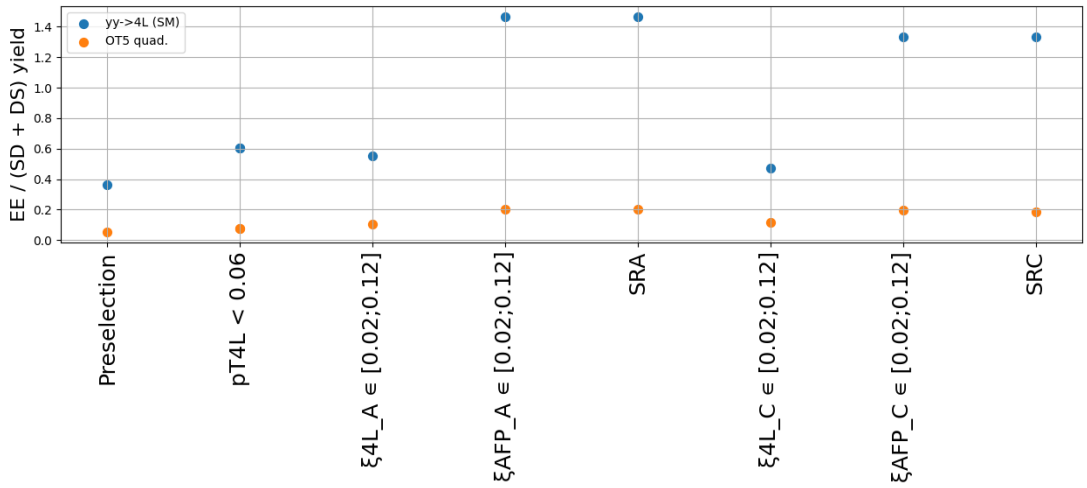

Figure 6.9: Elastic to dissociative event yield ratio after each cut is applied sequentially for the signal SM sample (blue) and the quadratic component of the $\mathcal{O}_{T5}$ sample (orange).

the SRs is taken as a global scale-factor such that the result from $\mathcal{O}_{T5}$ can be applied in all cases to the elastic sample to estimate the dissociative contributions. All the EFT samples share a similar phase-space in terms of kinematics and have a similar acceptance. Figure 6.11 shows selected kinematic distributions for the different quadratic components of the EFT samples in the SRA region, grouping together the $\mathcal{O}_T$ and the $\mathcal{O}_M$ operators. All of the distributions are normalized to 1 in order to compare the shapes of the distributions (the yields are indicated in the legend). The shapes of the $\mathcal{O}_T$ operators are compatible between themselves, the same stands for the $\mathcal{O}_M$ operators. The agreement between all of the operators of the two classes has been judged to be satisfactory at this stage of the analysis.

Figure 6.12 shows selected kinematic distributions of the quadratic component of the $\mathcal{O}_{T5}$ sample for three different subsamples: the elastic contribution, the MC-generated dissociative contribution, and the dissociative contribution obtained by scaling the elastic component by the elastic-to-dissociative ratio. $\mathcal{O}_{T5}$ is the only case for which this comparison is possible as it is the only operator for which the dissociative contributions are generated. The shapes of the distributions do not match well therefore the results presented in Section 6.8.2 will be given using this estimation but also the purely elastic case.

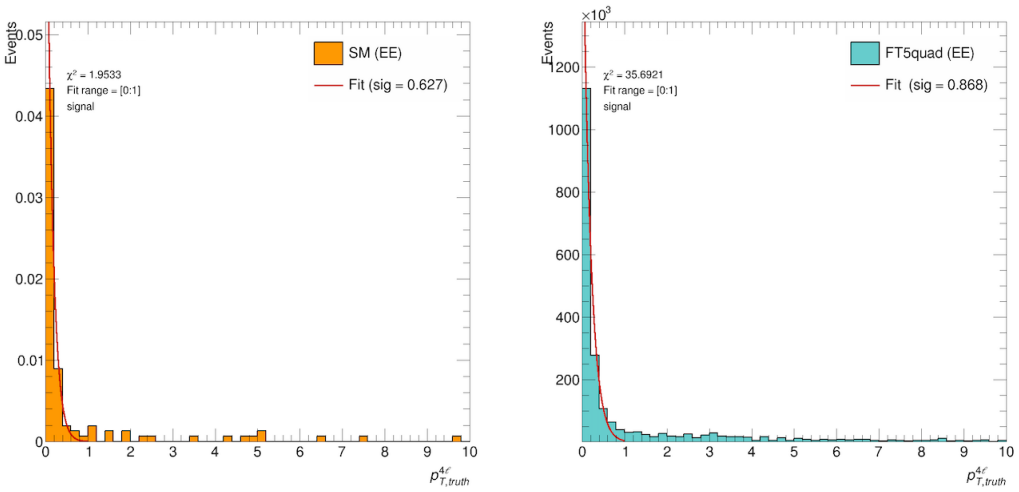

(a)

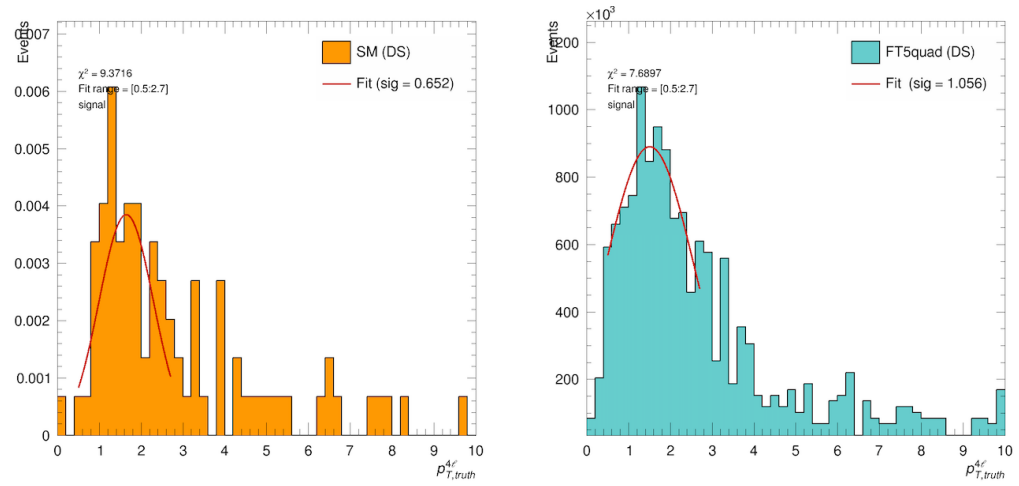

(b)

Figure 6.10: Comparison of the distributions of the $p_T^{4\ell}$ at truth level between the SM sample (left) and the quadratic component of the $\mathcal{O}_{T5}$ sample (right) for the elastic (a) and single-dissociative (b) components. The distributions are fitted with a Gaussian distribution. The range of the fit and the resulting χ^2 is indicated on the top left of each plot. The width of the fitted Gaussian distribution is indicated in the legend on the top-right of each plot.

Another more refined solution to obtain the elastic-to-dissociative ratio for the EFT samples was proposed by a similar ongoing ATLAS analysis (looking for photon-induced WW pair production using low-p_T tracking). The principle is to derive correction weights and apply them to the elastic sample in order to simulate the dissociative selection efficiencies. In order to do this, the SM elastic and dissociative contributions to the process of interest of the analysis ($\gamma\gamma \to WW$) were compared

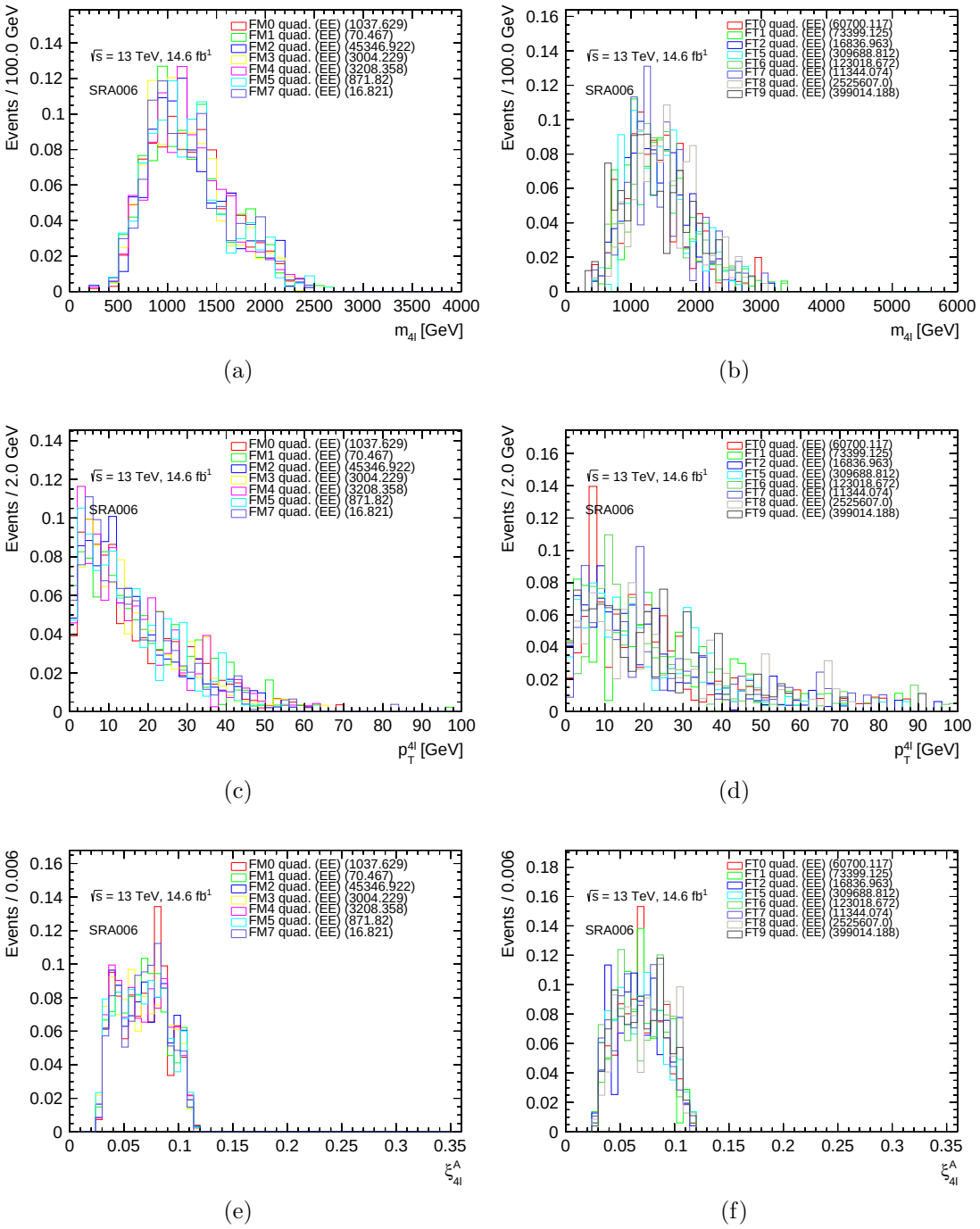

Figure 6.11: Invariant mass (a-b) transverse momentum (c-d) and proton energy loss (e-f) of the four lepton system compared between the $\mathcal{O}_M$ operator (a-c-e) and $\mathcal{O}_T$ operator (b-d-f) samples in the SRA region. All histograms are normalized to 1.

with generated $\mathcal{O}_{T5}$ elastic and dissociative contributions. Similarly to the present analysis, the linear EFT term was ignored in this procedure. The selection efficien-

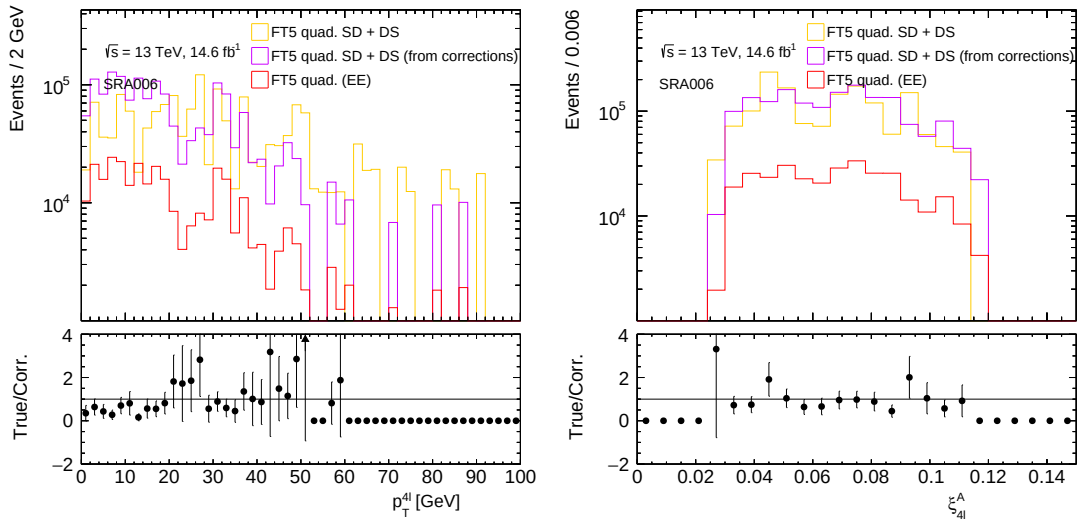

Figure 6.12: Distributions the transverse momentum of the four leptons system (a-c) and the proton energy loss measured from the four leptons (b-d) for the elastic (red), sum of single-dissociative (purple) and dissociative obtained from scaling the elastic contribution (orange) samples in both signal regions A (a-b) and C (c-d). The bottom panel shows the per-bin ratio of the true dissociative and dissociative obtain from correction samples.

cies, defined as the product of the acceptance of the signal region and the efficiency of all the different samples, was extracted in all samples, and the ratio of selection efficiencies of the single-dissociative component to the elastic component as a function of the truth-level di-boson mass was compared between the different samples.

It was observed that this quantity was consistent with being constant among the different samples, as seen in Figure 6.13. This ratio is extracted and applied as a weight dependent on the truth di-boson mass to the other EFT elastic samples where we don't have the samples for the dissociative components. These samples are then normalized to their respective cross-sections. As a closure test, the selection efficiencies were then compared between the privately generated dissociative samples and the corresponding elastic samples where the measured combined ratio is applied and worked as intended.

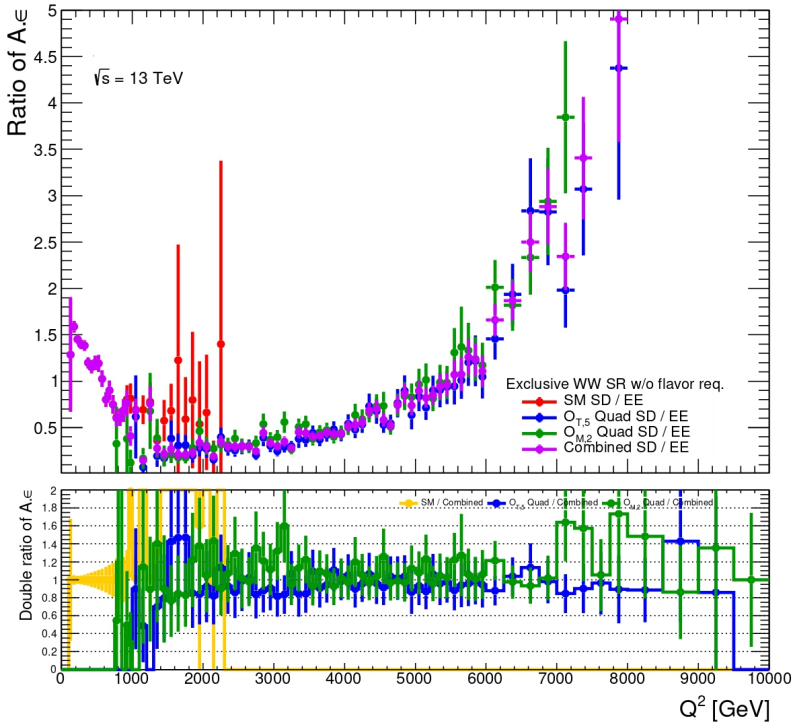

Figure 6.13: Ratio of selection efficiencies ($A \cdot \epsilon$) of the single-dissociative to the elastic component as a function of the truth di-boson mass (Q^2) for SM (red), $\mathcal{O}_{T5}$ quadratic component (blue), $\mathcal{O}_{M2}$ quadratic component (green) and combined (pink). This plot was produced by the $\gamma\gamma \to WW$ analysis team. Taken from Ref. [148].

One might reasonably assume that the same correction weights derived by the $\gamma\gamma \to WW$ analysis team could be used in the analysis described in this chapter. However, some additional checks will be needed in the future because the phase-space considered in the two analyses differ: the two main differences being that the

$\gamma\gamma \to WW$ analysis uses a track veto (*i.e.* no additional tracks in a small window of typically 1 mm around the vertex) and that there is no proton selection. Also, the application of the corrections is not straightforward as this analysis has two SRs. One should take into account the fact that the correction is applied to the elastic events which have protons on both sides (*i.e.* in both SRs) in order to avoid double counting. The following table and figures show the preliminary results. Table 6.8 shows the cutflow data for the elastic and dissociative samples but also for the corrected dissociative sample (obtained from the di-boson mass dependent weights applied to the elastic sample). The ratio between the two is also shown. A good agreement is obtained in the final SRs, while the agreement in the earlier steps of the cutflow remains poor. Figure 6.14 shows different kinematic distributions in the two SRs. The agreement in shape in the SRs is not perfect, especially in the invariant mass of the Z pair distributions. This could be explained by the limited statistics but also by the differences in phase-space of the two analyses. Some features of this correction require additional checks. This di-boson mass-based correction was therefore not deployed in the results presented in this thesis.

Table 6.8: Event yield after each cut is applied sequentially in the elastic, sum of MC-generated dissociative and dissociative obtained from di-boson mass dependent weighted components of the quadratic component of the $\mathcal{O}_{T5}$ sample. The uncertainties are only statistical.

$\mathcal{O}_{T5}$ **quad. sample**	EE	SD + DS	SD + DS (from weighted EE)
Preselection (≥ 4 signal muons)	$(2.78 \pm 0.07) \times 10^6$	$(5.19 \pm 0.94) \times 10^7$	$(1.33 \pm 0.38) \times 10^7$
$p_T^{4\ell} / \sum p_T^{\ell} < 0.06$	$(1.74 \pm 0.05) \times 10^6$	$(2.33 \pm 0.63) \times 10^7$	$(8.74 \pm 0.30) \times 10^6$
$\xi_{4\ell}^A \in [0.02; 0.12]$	$(4.86 \pm 0.03) \times 10^5$	$(4.58 \pm 0.28) \times 10^6$	$(2.50 \pm 0.14) \times 10^6$
$\xi_{\mathrm{AFP}}^A \in [0.02; 0.12]$	$(3.98 \pm 0.03) \times 10^5$	$(2.02 \pm 0.19) \times 10^6$	$(2.05 \pm 0.13) \times 10^6$
$\lvert\Delta\xi^A\rvert < 0.005$ (SRA)	$(3.42 \pm 0.02) \times 10^5$	$(1.70 \pm 0.17) \times 10^6$	$(1.83 \pm 0.13) \times 10^6$
$\xi_{4\ell}^C \in [0.02; 0.12]$	$(5.01 \pm 0.03) \times 10^5$	$(4.54 \pm 0.28) \times 10^6$	$(2.82 \pm 0.17) \times 10^6$
$\xi_{\mathrm{AFP}}^C \in [0.02; 0.12]$	$(3.89 \pm 0.03) \times 10^5$	$(2.17 \pm 0.19) \times 10^6$	$(2.12 \pm 0.14) \times 10^6$
$\lvert\Delta\xi^C\rvert < 0.005$ (SRC)	$(3.35 \pm 0.02) \times 10^5$	$(1.88 \pm 0.18) \times 10^6$	$(1.87 \pm 0.13) \times 10^6$

6.7 Study of systematics uncertainties

This section will present the different systematic uncertainties on the measurement presented in this chapter, and evaluated to what extent they impact the final result.

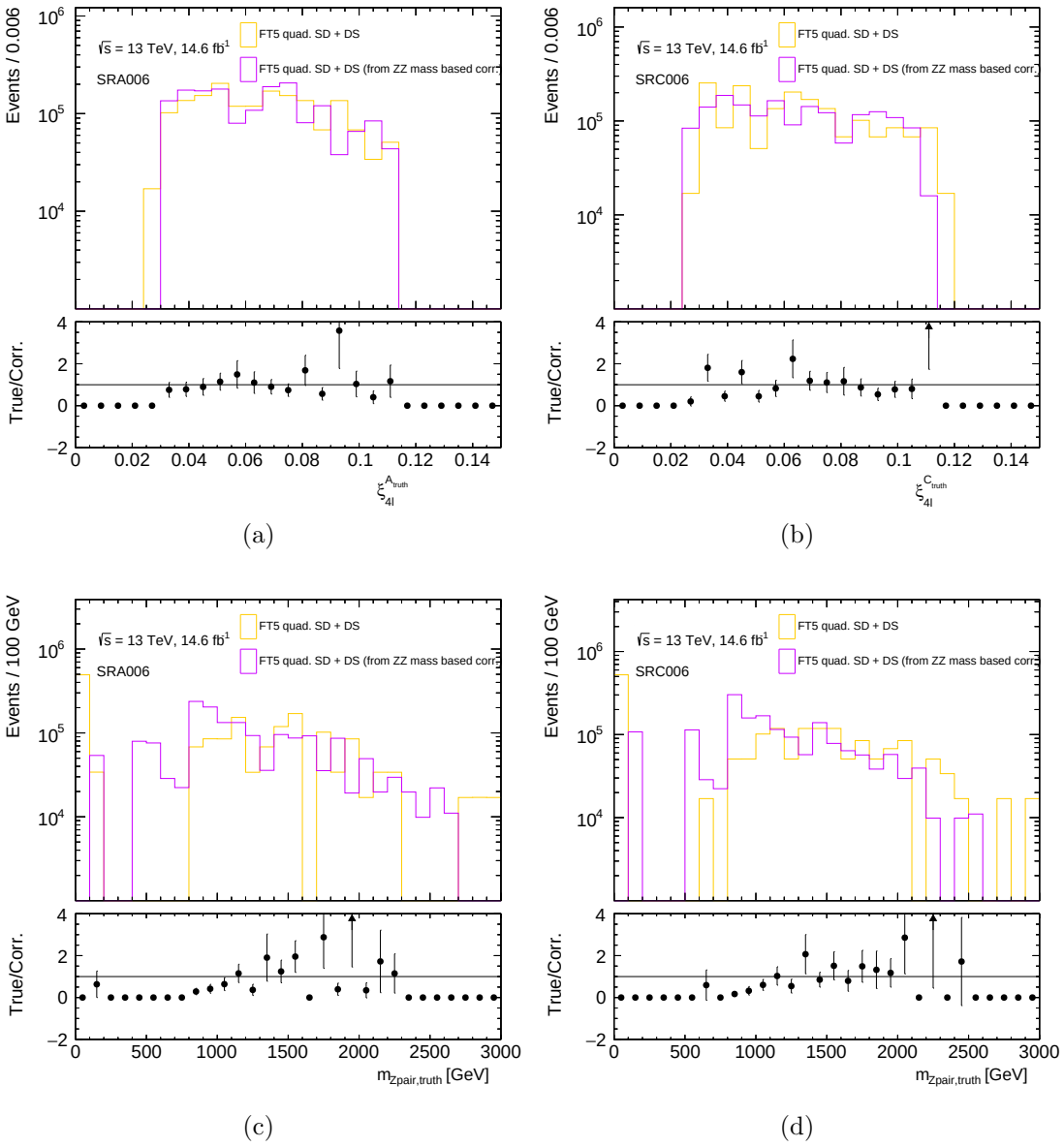

Figure 6.14: Distributions of the proton energy loss obtained from the four leptons system (a-b) and the invariant mass of the Z pair (c-d) in the SRA (a-c) and SRC (b-d). All distributions are shown at truth level.

6.7.1 Central detector uncertainties

The systematic uncertainties for the central detector are estimated by varying essential reconstruction parameters according to CP group recommendations. The following systematics will be taken into account for the C_{central} correction factor in the unfolding procedure to be described in Section 6.8.1 :

- Muon reconstruction: Two different types of systematic variations are applied. The first type affects the muon kinematics. They are variations of the inner detector track resolution, the muon spectrometer track resolution, the momentum scale of the muons, and two different type of charge-dependant momentum-scale. The latter correct independently for muons and anti-muons because of misalignment and magnetic field effects which impact differently on muons and anti-muons. The second type affects the data-to-MC scale-factors. It includes variations on the scale-factors for muon isolation, reconstruction and track-to-vertex association. All these variations are provided by the muon CP group.

- Pile-up reweighting: These systematic variations take into account uncertainties in the reweighting of the MC events to match the pileup profile in the data. They are provided by the ATLAS Physics Modelling Group (PMG).

- Trigger scale factor: These are systematic variations in the modelling of the inefficiencies of the di-muon triggers.

- Luminosity: The uncertainty on the luminosity measurement has been evaluated to be 2.4 % for the 2017 dataset [145].

Except for luminosity, which will be treated separately, the different systematic variations have been applied to the elastic and dissociative components of the MC signal sample and combined in Table 6.9. The uncertainties are quoted for the C_{central} correction factor, defined as the ratio of events passing the modified SR selection without AFP requirements at the detector level $N^{\text{SR-noAFP}}_{\text{detector-level}}$ to the number of events passing the equivalent selection at truth-level $N^{\text{SR-noAFP}}_{\text{particle-level}}$. This correction factor will be further described in Section 6.8.1. All sources of systematics are first symmetrised[5], which in some cases may lead to overestimating the uncertainties. Combining the different sources of systematic uncertainties in quadrature gives a total uncertainty of 3.6% for the central detector correction factor C_{central}. The

[5]The symmetrisation of uncertainties is a standard procedure where the average between the up and down parameter variation is taken instead.

dominant source of systematic uncertainty arises from pile-up reweighting, while momentum scale and track-to-vertex association systematic uncertainties are sub-dominant.

Table 6.9: Summary of systematic uncertainties for the central detector correction factor C_{central}. Each uncertainty is symmetrised and summed in quadrature to give the total.

Systematic	Uncertainty on C_{central}
Pileup reweighting	2.6 %
Isolation	1.5 %
Muon spectrometer	1.1 %
Trigger	1 %
Reconstruction	0.9 %
Inner detector	0.8 %
Scale	0.4 %
Track-to-vertex association	0.4 %
Total	3.6 %

6.7.2 AFP uncertainties

The systematic variations for the AFP detector are estimated by varying the parameters used during the reconstruction process in the data sample collected with lepton triggers in 2017 data. The different sources of uncertainties that have already been discussed in Section 4.8.4 arise mainly from clustering, track reconstruction and global alignment. They are standardized by the ATLAS proton CP group and provided through the `AfpAnalysisToolbox` tool. The following variations were taken into account:

- `CLUST_NEIGHBOUR`. The clusters are formed from the the short (default) or long edge.

- `TRK_FIND_DIST`. The allowed distance from the beampipe between clusters in forming a track segment within an AFP station is decreased from 1 mm (default) to 0.5 mm.

- `TRK_FIND_CLUST`. The minimum number for clusters in a track is increased from 2 (default) to 3.
- `TRK_SEL_MATCH`. The cut in the transverse distance between tracks in the NEAR and FAR stations used for proton reconstruction is varied, in both the x and y coordinate, by 1 mm.
- `ALIGN_GLOB_[MINUS/PLUS]`. The central value of the global alignment is shifted up and down by 1 mm. The envelope of these variations is taken as the uncertainty.
- `ALIGN_ROTATE`. The pots are rotated around the z axis by 4 mrad.
- `OPTICS_BEAMANGLE_[MINUS/PLUS]`. The beams optics are changed from their nominal set for the two beams. The most significant source of uncertainty arises from the dynamical variation of the crossing angle, which is at the level of 50 µrad over the course of a LHC run. The envelope of these variations is taken as the uncertainty.

The systematic uncertainties for the C_{AFP} correction factor in the unfolding procedure to be described in Section 6.8.1 are estimated by looking at these variations in the signal MC sample in the two SRs and evaluated separately for both sides. The envelope (*i.e.* the larger uncertainty of A and C side) is taken as the global uncertainty. The results are compiled in Table 6.10. An asymmetry between side A and side C can be observed in several of the systematic variations. This may be explained by considering the statistical uncertainties of the event yields in these regions, evaluated at around 30% for all MC signal samples. Taking the envelope as the uncertainty is therefore a conservative way of estimating the AFP uncertainties.

When comparing the systematic uncertainties to the uncertainties quoted in the AFP di-lepton analysis [6], the most striking difference is observed when comparing the optics beam angle uncertainties. For reference, the uncertainty was evaluated to be at a 5% level in the AFP di-lepton analysis. This can be explained by considering different effects. First, the method used in the di-lepton analysis differs from the

one used in this analysis: the systematic uncertainty is evaluated from the 2017 data sample in a kinematically close region to the SR of the analysis. The use of data instead of the signal MC is justified by the fact that the SR in the di-lepton analysis is dominated by signal. The modified region in which the di-lepton analysis evaluates the systematics uncertainties is a phase space region close to the one where the measurement is done, which is relaxed from some central detector cuts in order to enhance statistics. This choice is questionable because it results in background contamination in this region, leading to an underestimation of the overall AFP systematic uncertainties. Then, the second major difference is the proton energy loss range probed by the di-lepton analysis, which is much smaller than the one considered in the analysis presented in this chapter. The optics beam angle correction is proportional to the ξ_{AFP} value, as shown in Figure 6.15 and was designed to model accurately the uncertainties for low ξ_{AFP}, and may lead to an overestimation by a factor 3 of the uncertainty in this case.

Table 6.10: Summary of systematic uncertainties for the AFP correction factor C_{AFP}. Each uncertainty is categorised and symmetrised then summed in quadrature to give the total.

Systematic	Side A	Side C	Envelope
Optics beam angle	24.4 %	43.4 %	43.4 %
Track selection match	1.5 %	14.7 %	14.7 %
Global alignment	3.9 %	10.3 %	10.3 %
Cluster neighbourhood	3.2 %	2.1 %	3.2 %
Cluster neighbourhood	3.2 %	2.1 %	3.2 %
Track find distance	3.1 %	2.6 %	3.1 %
Track find cluster	2.3 %	0.5 %	2.3 %
Total			47.4%

6.8 Results

6.8.1 Cross-section measurement

The measured fiducial cross-section of the process $\sigma_{\text{fid.}}^{\text{meas.}}$ is defined as:

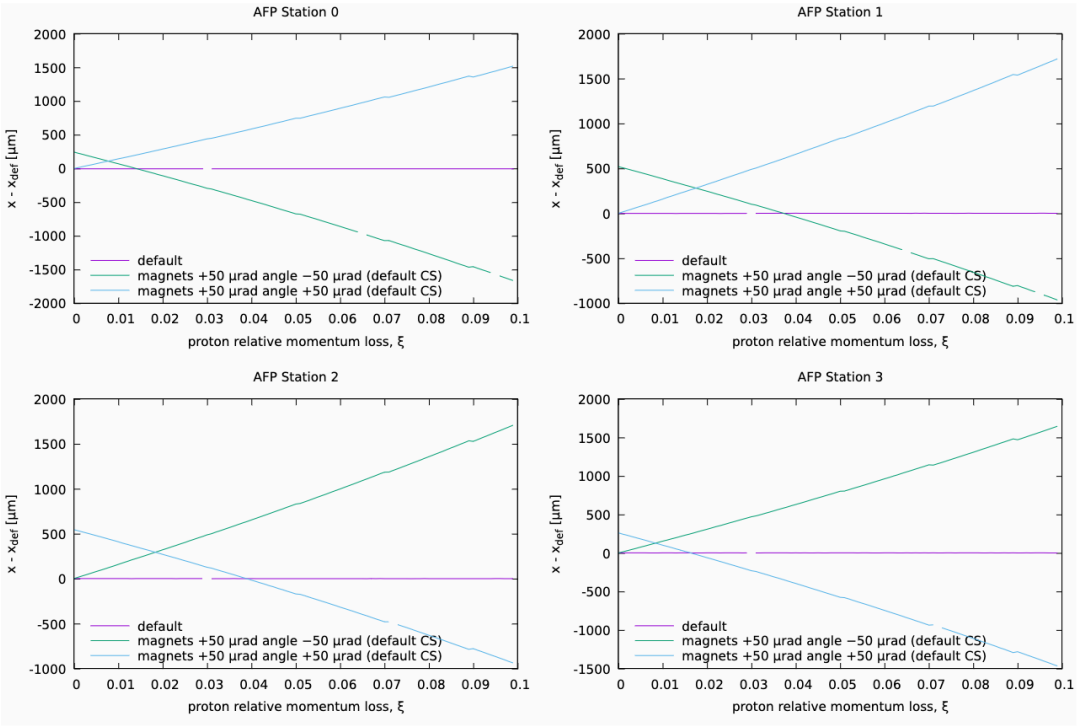

Figure 6.15: Systematic variations when varying beam optics, which affects ξ_{AFP} reconstruction. All stations are shown but only station 0 (Far A) is used to model the beam optics uncertainty for both sides. Taken from Ref. [149].

$$\sigma_{\text{fid.}}^{\text{meas.}} = \frac{N_{\text{data}} - N_{\text{bkg}}}{\mathcal{L} \cdot C_{\text{central}} \cdot C_{\text{AFP}}} \tag{6.1}$$

where N_{data} and N_{bkg} are, respectively, the number of measured data events in the SR and the number of expected background events in the SR, $\mathcal{L} = 14.6\,\text{fb}^{-1}$ is the integrated luminosity, C_{central} and C_{AFP} are correction factors taking into account the acceptance resolution and reconstruction efficiencies for the central detector and AFP, respectively.

C_{central} is defined as the ratio of events passing the modified SR selection without AFP requirements at the detector level $N_{\text{detector-level}}^{\text{SR-noAFP}}$ to the number of events passing the equivalent selection at truth-level $N_{\text{particle-level}}^{\text{SR-noAFP}}$. C_{AFP} is defined as the product of two terms, ϵ_{AFP} and ϵ_{match}. ϵ_{AFP} is the combined proton reconstruction efficiency (defined in Section 4.8.1) and was evaluated to be $\epsilon_{\text{AFP}} = 0.92 \pm 0.02$. ϵ_{match} is defined as the ratio of the number of events passing the SR selection at the detector

level $N^{\text{SR}}_{\text{detector-level}}$ to the number of events passing the modified SR selection without the ξ matching at the truth-level $N^{\text{SR-noMATCH}}_{\text{detector-level}}$. We therefore obtain:

$$C_{\text{central}} = \frac{N^{\text{SR-noAFP}}_{\text{detector-level}}}{N^{\text{SR-noAFP}}_{\text{particle-level}}}; \quad C_{\text{AFP}} = 0.92 \times \frac{N^{\text{SR}}_{\text{detector-level}}}{N^{\text{SR-noMATCH}}_{\text{detector-level}}} \tag{6.2}$$

The corresponding yields are given in Table 6.11. One can observe that the central efficiencies are worse in the dissociative samples. This may be caused by the fact that the system has more boost compared to the elastic case, and therefore in geometrical regions of the detector with lower efficiency.

Table 6.11: Event yields in all regions considered to compute the cross-section. The yields are given for both SRA and SRC. The uncertainties are only statistical. The total uncertainty is propagated using the sum in quadrature.

Region	EE	SD	DS	Tot.
N^{SR}_{data}	(1 + 1)			
N^{SR}_{bkg}	(1.9 + 1.4) ± 0.45			
$N^{\text{SR-noAFP}}_{\text{detector-level}}$	(0.017 + 0.018) ± 0.005	(0.016 + 0.021) ± 0.005	(0.015 + 0.017) ± 0.005	0.104 ± 0.009
$N^{\text{SR-noAFP}}_{\text{particle-level}}$	(0.086 + 0.075) ± 0.010	(0.148 + 0.110) ± 0.013	(0.113 + 0.131) ± 0.013	0.663 ± 0.021
$N^{\text{SR}}_{\text{detector-level}}$	(0.009 + 0.014) ± 0.003	(0.007) ± 0.002	(0.010) ± 0.003	0.040 ± 0.006
$N^{\text{SR-noMATCH}}_{\text{detector-level}}$	(0.009 + 0.014) ± 0.003	(0.007) ± 0.002	(0.010) ± 0.003	0.040 ± 0.006
$C_{central}$	0.156 ± 0.014			
C_{AFP}	0.92 ± 0.18			

Propagating the statistical uncertainties from Table 6.11, the systematic uncertainties on $C_{central}$ and C_{AFP} evaluated in Section 6.7 and the luminosity uncertainties evaluated by the ATLAS luminosity group results in the following fiducial cross section value for the blinded data:

$$\sigma^{\text{meas.}}_{\text{fid.}}(\text{fb}) = -0.595 \pm 0.250\ (\text{stat.}) \pm 0.283\ (\text{syst.}) \pm 0.014\ (\text{lumi.})$$

The measurement is dominated by the systematic uncertainties on C_{AFP}. As already discussed in Section 6.7, this source of uncertainty seems to be overestimated, in particular the optics beam angle uncertainty. Changing only this uncertainty from the conservative estimation of 43.4% to the mean of the the two sides (33.9%) reduces the systematic uncertainties on C_{AFP} to 38.8% and the systematic uncertainties on $\sigma^{\text{meas.}}_{\text{fid.}}$ to a sub-dominant value of 0.232 fb, even though 33.9% is still an overestimate

as discussed in Section 6.7.

The central value of the computed cross-section is negative, but the result is consistent with a positive cross-section. A statistical treatment is needed to estimate the upper-limit of the cross-section consistent with the data. The goal of the procedure is to determine, at a certain confidence level, what hypothesis is compatible with the observed data.

In order to do this, one needs to perform a hypothesis test for different values of the signal strength μ, defined as $\mu = \sigma_{\text{meas.}}/\sigma_{\text{SM}}$. Therefore, we equivalently have $N = \mu N_s + N_b$, with N the number of events in the SR, N_s (N_b) the number of SM signal (background) events in the SR. μ is an unconstrained normalization factor for the signal sample. The background sample carries an uncorrelated shape systematic constrained by a Poisson distribution with a mean of σ_b^{-2}, with σ_b defined as the absolute uncertainty for the background estimation. The relative uncertainties are taken as the relative difference between the two background estimations used in the analysis $\left|\frac{N_{\text{mxd}}^{\text{SR}} - N_{\text{MC}}^{\text{SR}}}{N_{\text{mxd}}^{\text{SR}} + N_{\text{MC}}^{\text{SR}}}\right|$.

The null-hypothesis, denoted H_0 is defined in this case as the assumption that only background contributes to the measurement. It is complemented with the alternative hypothesis H_1, defined as the assumption that additional signal processes contribute. We use the alternative asymptotic profile likelihood test statistic $\tilde{q}$ consisting of a ratio of the value of the likelihood for a value of μ, denoted $\mu_{\text{hypo.}}$, given the observation, to the maximum likelihood estimate (the best value for μ resulting from a global fit given the observations). A formal definition can be found in Eq. (16) of Ref. [150].

For different values of μ, we can then perform a hypothesis testing. Knowing the distributions of the test statistic under the two different hypotheses for a given value of $\mu_{\text{hypo.}}$, we can compute CL_s, the modified pseudo-frequentist p-value as:

$$\mathrm{CL_s} = \frac{\mathrm{CL_{s+b}}}{\mathrm{CL_b}} = \frac{\int_{\tilde{q}_{\mu_{\mathrm{hypo.}}}}^{\infty} g(\mu_{\mathrm{hypo.}}|\mu = \mu_{\mathrm{hypo.}})\mathrm{d}\tilde{q}_{\mu_{\mathrm{hypo.}}}}{\int_{\tilde{q}_{\mu_{\mathrm{hypo.}}}}^{\infty} g(\mu_{\mathrm{hypo.}}|\mu = 0)\mathrm{d}\tilde{q}_{\mu_{\mathrm{hypo.}}}} \tag{6.3}$$

where $g(\mu_{\mathrm{hypo.}}|\mu = \mu_{\mathrm{hypo.}})$ are the conditional probability density functions where $\mu = \mu_{\mathrm{hypo.}}$. The value of $\mu_{\mathrm{hypo.}}$ for which $\mathrm{CL_s}$=0.05 is the value for which the null hypothesis is rejected at the 95% confidence level. Figure 6.16 shows the expected and observed upper limit on the signal strength μ at the 95% confidence level.

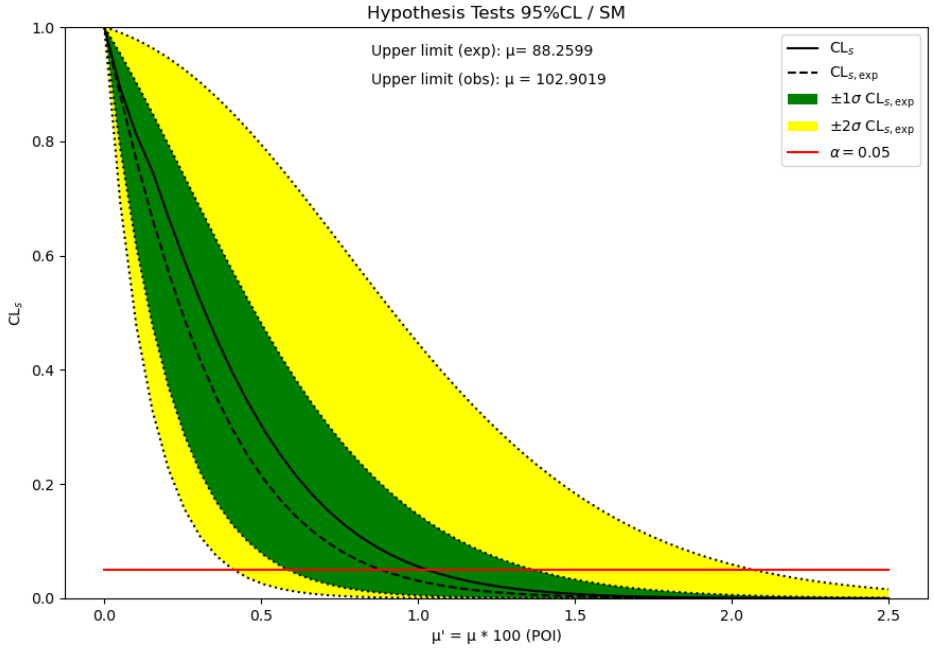

Figure 6.16: Expected (dashed line) and observed (solid line) CLs values as a function of the signal strength μ using blinded data. The expected and observed upper limits on the signal strength μ at 95% confidence level correspond to the values of μ for which CLs is equal to 0.05 (indicated by the red solid line). The signal yields have been multiplied by 100 to help with the convergence of the code used to generate this plot, so the signal strength on the x axis is 100 times bigger than the real signal strength. The green (yellow) envelope represents the CLs at a $\pm 1(2)\sigma$ variation.

The signal yields have been multiplied by 100 to help with the convergence of the code used to generate this plot, so the signal strength on the x axis is 100 times bigger than the real signal strength. Accounting for this yields the following results:

$$\mu_{95}^{exp.} = 88.3 \quad ; \quad \mu_{95}^{obs.} = 102.9$$

Given the measured data, we can therefore exclude signals 102.9 times stronger than the SM signal model we have with 95% confidence. In terms of cross-section, this corresponds to an upper-limit of :

$$\begin{aligned}\sigma_{\text{fid.}}^{\text{UL95}} &= \frac{\mu_{95}^{obs.} \times N_{\text{sig.}}}{\mathcal{L} \cdot C_{\text{central}} \cdot C_{\text{AFP}}} \\ &= 1.967 \text{ fb}\end{aligned}$$

at the 95 % confidence level. Clearly, the measured cross-section is compatible with the background-only hypothesis.

6.8.2 Upper limit on the EFT parameters

As already described in Section 6.2.3.2, each MC sample corresponding to a given operator is generated one term at the time (linear or quadratic). In order to obtain the corresponding event yield for a given value of the Wilson coefficient, the respective sample is multiplied by the appropriate amplitude term ($f_j, |f_j|^2$). A similar statistical treatment to the one presented in the cross-section measurement is then done in order to fit the value of these parameters to the observed yield[6] in both signal regions simultaneously using a likelihood ratio estimator. The floating parameter in this case is the coupling constant of each individual EFT operator.

As in the cross-section measurement, the uncertainties on the background modelling are taken as the relative difference in yield between the two different background modelling methods: $\left|\frac{N_{\text{mxd}}^{\text{SR}} - N_{\text{MC}}^{\text{SR}}}{N_{\text{mxd}}^{\text{SR}} + N_{\text{MC}}^{\text{SR}}}\right|$, with $N_{\text{mxd}}^{\text{SR}}$ (resp. $N_{\text{MC}}^{\text{SR}}$) the number of expected events in one of the SRs using the data-driven event-mixing technique (resp. the MC

[6] In the present case, to the yield of the blinded data sample.

estimation considering the main background). This leads to relative uncertainties of 38.2 % for SRA and 19.2 % for SRC.

As already discussed, the linear components are not taken into account in the limit setting process due to their negligible impact.

The confidence intervals are determined using Wilk's theorem [150], assuming that the profile likelihood test statistic is χ^2 distributed. This assumption is probably not valid due to low statistics. Hence the use of an asymptotic formula should be only taken as a preliminary estimation of the result and could be refined using a simulated representative data set, called "Asimov data set"[7] in which all observed quantities are set equal to their expected values.

The limits on each coefficient at the 95% confidence level are given in Table 6.12 in two cases: considering the elastic component only and considering all proton dissociative components. The dissociative components for each operator are obtained using the first method presented in Section 6.6 by scaling the elastic component by a factor $\simeq 5.195$, obtained from averaging the elastic-to-dissociative ratio of both signal regions in the $\mathcal{O}_{T5}$ sample. As expected, considering the dissociative components leads to lower limits, but both results are given as the method used to obtain the dissociative components are still under development, especially for the $\mathcal{O}_M$ operators.

As explained in Section 2.2, the amplitudes predicted by the EFT can break the gauge structure and violate unitarity at high energy scales. More physical limits can be obtained by setting the EFT contributions above a certain energy threshold E_c to zero. This is referred to as "clipping". By computing the limits at different values for E_c and comparing them to theoretical unitarity bounds for a given operator, one can chose the appropriate clipping energy E_c. The unitarity bounds are given as a function of the Mandelstam variable s in Ref. [38], considering one operator at a

[7] This method is named after the science-fiction short-story "Franchise" written by the author Isaac Asimov, in which a computer selects a single-person to answer a number of questions, whose answers are used to determine what the results of an election would be, without having to actually hold the election [151].

Table 6.12: Upper limit at the 95% confidence level of the $\mathcal{O}_M$ and $\mathcal{O}_T$ operators without clipping. The results are shown considering the elastic component only and the dissociative components using the elastic-to-dissociative ratio correction factor obtained from $\mathcal{O}_{T5}$.

Coupling	95% CL upper limit [TeV^{-4}] (EE only)	95% CL upper limit [TeV^{-4}] (all diss.)
$\lvert f_{M,0}/\Lambda^4\rvert$	4.13×10^2	1.65×10^2
$\lvert f_{M,1}/\Lambda^4\rvert$	3.93×10^3	6.69×10^2
$\lvert f_{M,2}/\Lambda^4\rvert$	6.57×10^1	2.51×10^1
$\lvert f_{M,3}/\Lambda^4\rvert$	2.41×10^2	9.58×10^1
$\lvert f_{M,4}/\Lambda^4\rvert$	2.33×10^2	9.30×10^1
$\lvert f_{M,5}/\Lambda^4\rvert$	4.46×10^2	1.78×10^2
$\lvert f_{M,7}/\Lambda^4\rvert$	1.70×10^4	2.39×10^3
$\lvert f_{T,0}/\Lambda^4\rvert$	5.09×10^1	2.03×10^1
$\lvert f_{T,1}/\Lambda^4\rvert$	4.94×10^1	1.97×10^1
$\lvert f_{T,2}/\Lambda^4\rvert$	1.03×10^2	4.11×10^1
$\lvert f_{T,5}/\Lambda^4\rvert$	9.52×10^1	1.36×10^1
$\lvert f_{T,6}/\Lambda^4\rvert$	4.06×10^1	1.54×10^1
$\lvert f_{T,7}/\Lambda^4\rvert$	1.27×10^2	5.05×10^1
$\lvert f_{T,8}/\Lambda^4\rvert$	9.00	3.61
$\lvert f_{T,9}/\Lambda^4\rvert$	4.34×10^1	9.65

time, or all at once. The results presented in this section will use the bounds for one operator at a time, as the limits are set individually considering all other operators' contributions to be zero. Figure 6.17 shows the results of the clipping scan for two examples operators, $\mathcal{O}_{M0}$ and $\mathcal{O}_{T8}$. The results of the clipping scan for all the other operators can be found in Appendix C. These two operators have been chosen to illustrate the two distinct cases observed in the clipping scans. The first case can be observed in the clipping scan of the $\mathcal{O}_{M0}$ operator. The upper (and lower) limit on the coefficient always remains bigger (smaller) than the theoretical unitarity bound. This means that the limits are set in an unphysical region, due to the fact that the analysis is not sensitive enough for this particular operator with the current data. On the other hand, there are several points in the clipping scan of the $\mathcal{O}_{T8}$ operator where the limits are within the unitarity bounds. The limit is then given by the value for the highest E_c for which the limit is within the unitarity bounds. Figure 6.17 also shows the results in the case where only the elastic components are taken into account. None of the considered operators have limits set within the unitarity bounds, showing how crucial it is to take the dissociation contributions into account.

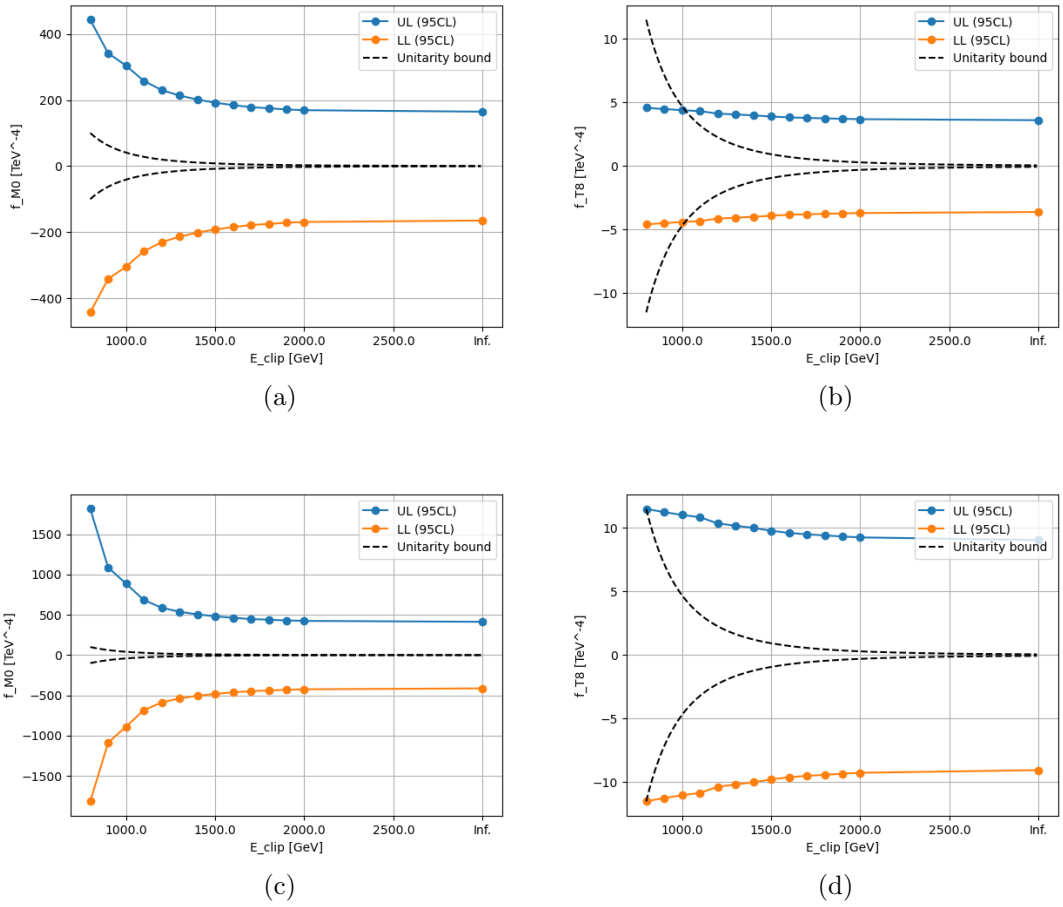

Figure 6.17: Clipping scan for the $\mathcal{O}_{M0}$ (a-c) and $\mathcal{O}_{T8}$ (b-d) operators. The results are shown considering all dissociative contributions (a-b) and only the elastic case (c-d). The blue (orange) points represent the upper (lower) limits at the 95 % confidence level as a function of the clipping energy. The black dashed line represents the theoretical unitarity bound for each operator.

Table 6.13 gives the upper limits of each EFT coefficient at the 95% confidence level with the highest clipping value for each operator. Only the operators for which the limit falls within the unitarity bound are shown.

For reasons that are not yet understood, this analysis seems to be more sensitive to certain operators such as $\mathcal{O}_{T8}$ or $\mathcal{O}_{T9}$ than it is to others. A phenomenological study of these operators would be an interesting follow-up to try to identify more generic behaviour.

Table 6.13: Upper limits at the 95% confidence level on dimension 8 operators for which the limit falls within the unitarity bound. The results are shown considering the dissociative components using the elastic-to-dissociative ratio correction factor obtained from $\mathcal{O}_{T5}$.

Coupling	95% CL upper limit [TeV^{-4}]	Clipping [TeV]
$\lvert f_{M,2}/\Lambda^4\rvert$	5.26×10^1	0.9
$\lvert f_{M,3}/\Lambda^4\rvert$	1.85×10^2	0.9
$\lvert f_{M,5}/\Lambda^4\rvert$	4.56×10^2	0.8
$\lvert f_{T,1}/\Lambda^4\rvert$	3.23×10^1	0.8
$\lvert f_{T,6}/\Lambda^4\rvert$	2.12×10^1	1
$\lvert f_{T,7}/\Lambda^4\rvert$	5.96×10^2	1
$\lvert f_{T,8}/\Lambda^4\rvert$	4.40	1
$\lvert f_{T,9}/\Lambda^4\rvert$	2.30×10^1	0.8

6.8.3 Comparison with CMS

The CMS collaboration published a similar analysis, searching for $\gamma\gamma \to ZZ$ and $\gamma\gamma \to WW$ exclusive final states with intact protons [152]. The major difference compared with the analysis described in this chapter is that the CMS analysis was focussed on hadronic final states, *i.e.* where both gauge bosons decay to boosted and merged jets. The branching ratio of Z decays into hadrons is of about 70% while it is of about 3% for two muons [26]. On the other hand, jet-based analysis are subject to significantly larger corrections and uncertainties than is the case for leptons. The proton spectrometer used is the Precision Proton Spectrometer (PPS) [153], the CMS equivalent to AFP. The studied dataset corresponds to 100 fb^{-1}. In the CMS analysis, aQGC limits were extracted for dimension 6 operators. Under certain assumptions (for example that the $WWZ\gamma$ vertex vanishes), the "LEP-like" dimension 6 operators can be translated into the same dimension 8 operators considered in this analysis [36]. The limits were extracted only for the $\mathcal{O}_M$ operators and were given for only one value of clipping at $E_c = 1.4$ TeV. The values are shown in Table 6.14, and can be compared with those presented in this chapter. Table 6.15 shows the limits for the $\mathcal{O}_{M0}$ operator without clipping (already given in Table 6.12) and with a clipping value of 1.4 TeV in order to compare with CMS. Both cases, considering the elastic case only and including the dissociative components are shown.

Table 6.14: Upper limits at the 95% confidence level on the f_M parameters with and without clipping at 1.4 TeV as obtained by CMS. Taken from Ref. [152].

Coupling	Observed (expected) 95% CL upper limit [TeV^{-4}]	Clipping
$\lvert f_{M,0}/\Lambda^4\rvert$	66.0 (60.0)	-
$\lvert f_{M,1}/\Lambda^4\rvert$	245.5 (214.8)	-
$\lvert f_{M,2}/\Lambda^4\rvert$	9.8 (9.0)	-
$\lvert f_{M,3}/\Lambda^4\rvert$	73.0 (64.6)	-
$\lvert f_{M,4}/\Lambda^4\rvert$	36.0 (32.9)	-
$\lvert f_{M,5}/\Lambda^4\rvert$	67.0 (58.9)	-
$\lvert f_{M,7}/\Lambda^4\rvert$	490.9 (429.6)	-
$\lvert f_{M,0}/\Lambda^4\rvert$	79.8 (78.2)	1.4 TeV
$\lvert f_{M,1}/\Lambda^4\rvert$	306.8 (306.8)	1.4 TeV
$\lvert f_{M,2}/\Lambda^4\rvert$	11.9 (11.8)	1.4 TeV
$\lvert f_{M,3}/\Lambda^4\rvert$	91.3 (92.3)	1.4 TeV
$\lvert f_{M,4}/\Lambda^4\rvert$	43.5 (42.9)	1.4 TeV
$\lvert f_{M,5}/\Lambda^4\rvert$	83.7 (84.1)	1.4 TeV
$\lvert f_{M,7}/\Lambda^4\rvert$	613.7 (613.7)	1.4 TeV

Table 6.15: Upper limits at the 95% confidence level on the f_M parameters with and without clipping at 1.4 TeV for the present analysis. The results are shown considering the elastic component only and also correcting for the dissociative components using the elastic-to-dissociative ratio correction factor obtained from $\mathcal{O}_{T5}$.

Coupling	95% CL upper limit [TeV^{-4}] (EE only)	95% CL upper limit [TeV^{-4}] (all diss.)
No clipping		
$\lvert f_{M,0}/\Lambda^4\rvert$	4.13×10^2	1.65×10^2
$\lvert f_{M,1}/\Lambda^4\rvert$	3.93×10^3	6.69×10^2
$\lvert f_{M,2}/\Lambda^4\rvert$	6.57×10^1	2.51×10^1
$\lvert f_{M,3}/\Lambda^4\rvert$	2.41×10^2	9.58×10^1
$\lvert f_{M,4}/\Lambda^4\rvert$	2.33×10^2	9.30×10^1
$\lvert f_{M,5}/\Lambda^4\rvert$	4.46×10^2	1.78×10^2
$\lvert f_{M,7}/\Lambda^4\rvert$	1.70×10^4	2.39×10^3
Clipping at 1.4 TeV		
$\lvert f_{M,0}/\Lambda^4\rvert$	5.05×10^2	2.01×10^2
$\lvert f_{M,1}/\Lambda^4\rvert$	5.58×10^3	8.58×10^2
$\lvert f_{M,2}/\Lambda^4\rvert$	8.88×10^1	3.05×10^1
$\lvert f_{M,3}/\Lambda^4\rvert$	2.83×10^2	1.13×10^2
$\lvert f_{M,4}/\Lambda^4\rvert$	2.79×10^2	1.11×10^2
$\lvert f_{M,5}/\Lambda^4\rvert$	5.31×10^2	2.11×10^2
$\lvert f_{M,7}/\Lambda^4\rvert$	2.44×10^4	3.47×10^3

The most direct comparison of results is between CMS with clipping at 1.4 TeV and this analysis with "all diss." and clipping at 1.4 TeV. None of the computed limits ended up being better than those computed by CMS, though several are similar and all are at the same order of magnitude. This result has to balanced with the

fact that only the four muon channel is taken into account, and the addition of the other channels in this analysis (four electrons and two muons plus two electrons) will surely improve the results and that dominant systematic uncertainty (on the AFP beam optics) is likely to reduce considerably with more work. It is therefore possible that the ATLAS results with leptonic final states may ultimately be more sensitive than those obtained by CMS.

Chapter 7

Conclusion and Future Prospects

The work presented in this thesis covered several aspects of the AFP detector and its exploitation.

The AFP detector offers an alternative way of measuring particle physics processes, has been used to measure photon-induced ZZ production in association with intact protons, and thus to set limits on a variety of EFT operators giving rise to aQGCs. Work on the fine-tuning of some of the AFP simulation parameters has also been discussed, together with the implementation of a new functionality, that is now used in a variety of other AFP analysis, such as the ongoing $\gamma\gamma \to Z +$ invisible analysis, and the recently published light-by-light scattering measurement interpreted as a search for ALPs [118].

At this stage of the analysis, the results shown in this thesis are not quite competitive with an already made public similar Compact Muon Solenoid (CMS) analysis. However, this analysis covers more EFT operators. Several improvements can be made to the analysis in the future, such as including the other leptonic final state channels, or improving the dissociative component modelling of the EFT samples. Statistics are also a limitation of this measurement: in comparison, the CMS analysis that this analysis is compared to makes use of almost seven times more data ($100\,\text{fb}^{-1}$). Another improvement that could be done would be to study the effect

of a track veto, *i.e.* removing additional tracks close to the vertex, synergising with AFP to improve the background rejection. This approach was taken in the di-lepton analysis with AFP discussed in Chapter 5 [6].

Unfortunately, the AFP detector was not approved for continuation of operations during Run 4. Some of the ongoing analyses, including this one, may motivate the reintroduction of AFP for later stages of the HL-LHC, since statistics are one of the main limitations of this analysis. However, for the time-being this analysis will be the best statement ATLAS can make on proton-tagged ZZ production.

Appendix A

Details about the reproduction of the AFP dilepton measurement analysis

A.1 Details about the event selection

All the selection is done using Athena [132] release 21.2.91 in addition with AfpAnalysisToolbox commit eba80e9c, the latest master version in date.

The leptons are selected using the lowest unprescaled dilepton triggers (HLT_2e17_lhvloose_nod0_L12EM15VH OR HLT_2e24_lhvloose_nod0 for electrons; HLT_2mu14 for muons).

Tracks The default *Loose* working point is used for tracks from the InDetTrackParticles track container which the same criteria as that used in reconstruction. Tracks are required to satisfy $p_T > 500$ MeV, $|\eta| < 2.5$. The inner detector requirements are $N_{\text{Si}} \geq 7$,$N_{\text{mod}}^{\text{sh}} \leq 1$,$N_{\text{Si}}^{\text{hole}} \leq 2$ and $N_{\text{pix}}^{\text{hole}} \leq 1$.

Electrons Electrons must satisfy $p_T > 18$ GeV, $|\eta| < 2.47$, where the crack region is included, and the *MediumLLH* identification working point is used. The longitudinal impact parameter projected perpendicular to the beam axis satisfies $|z_0 \sin\theta| < 0.5$ mm. The following configuration for isolation is used: *Gradient* isolation is applied for $p_T < 200$ GeV, while *FCHighPtCaloOnly* isolation is applied for high $p_T > 200$ GeV. Following standard track-to-vertex-association recommendations for electrons, the transverse impact parameter significance satisfies $|d_0/\sigma(d_0)| < 5$.

Muons Muons satisfy $p_T > 15$ GeV, $|\eta| < 2.4$ and *Medium* identification. Muons also satisfy *FCLoose* isolation. Standard lepton-to-vertex association recommendations for muons apply $|z_0 \sin\theta| < 0.5$ mm, $|d_0/\sigma(d_0)| < 3$.

Protons *Medium* quality criterion is used for proton reconstruction. Protons can be reconstructed with either both stations. The *allowSingleStationReco* is set to true in this analysis in order to allow a wider AFP acceptance range. This means if there is no track in the Near station, proton reconstruction with only the Far station is used.

A.2 Distributions of the main kinetic variables

This paragraph shows distributions of the main kinematic variables. All variables are defined in Section 5.2.2. Agreement between these distributions and the published ones is discussed in Section 5.2.3. Figure A.1 shows the $\xi_{\ell\ell}$ and ξ_{AFP} distribution for data, with all cuts described in Section 5.2.2 applied except for the kinematic matching requirement. Figure A.2, Figure A.3 and Figure A.4 show the remaining kinematic variables which not shown in the main text for data with all the cuts applied.

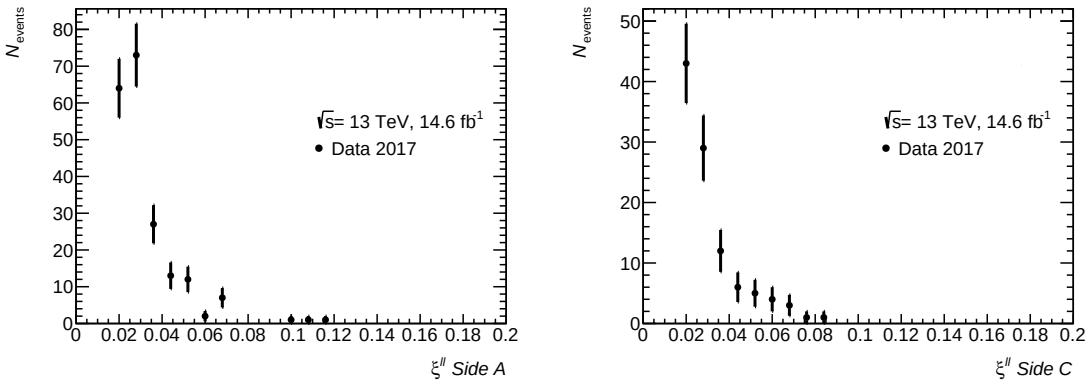

(a)

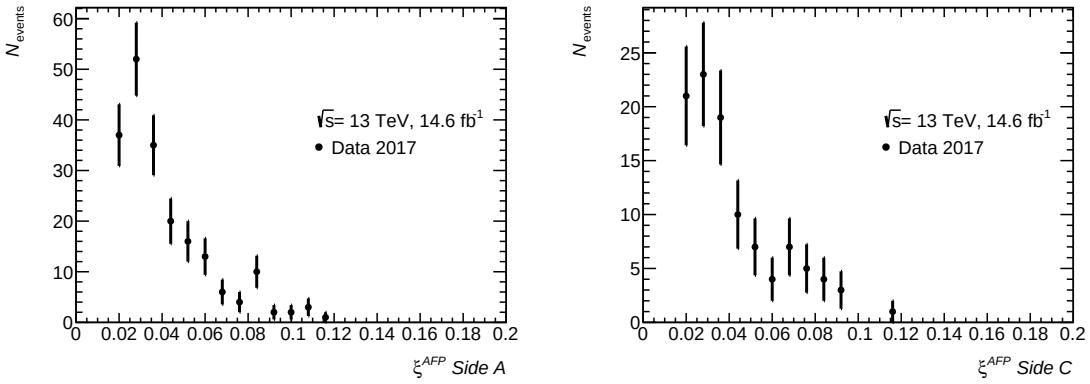

(b)

Figure A.1: Distributions of $\xi_{\ell\ell}$ (a) and ξ_{AFP} (b) shown separately for side A (left) and side C (right). Only data is shown and all cuts presented in Section 5.2.2 are applied except for the kinematic matching requirement.

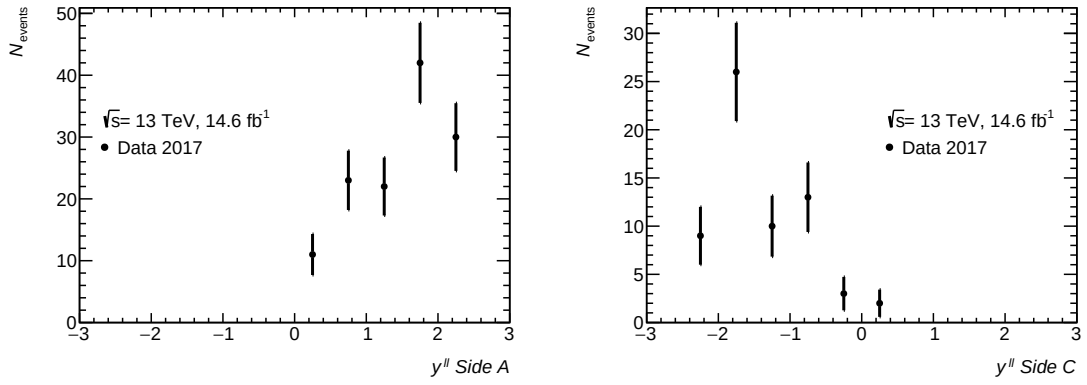

(a)

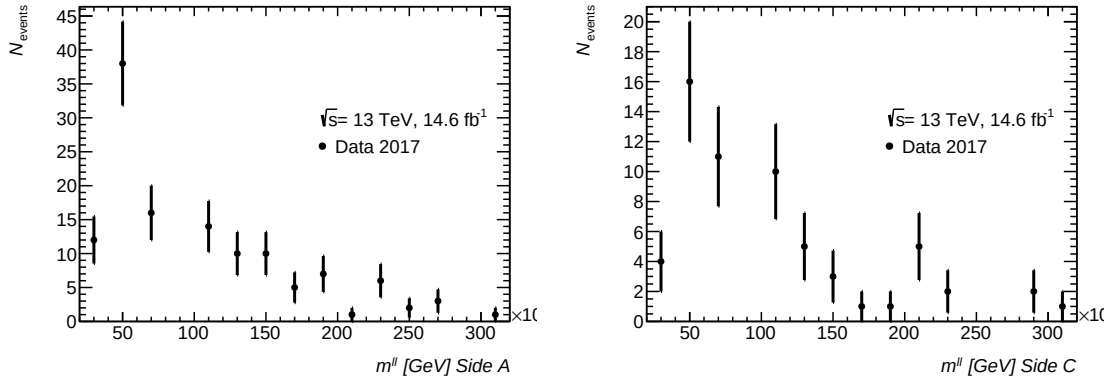

(b)

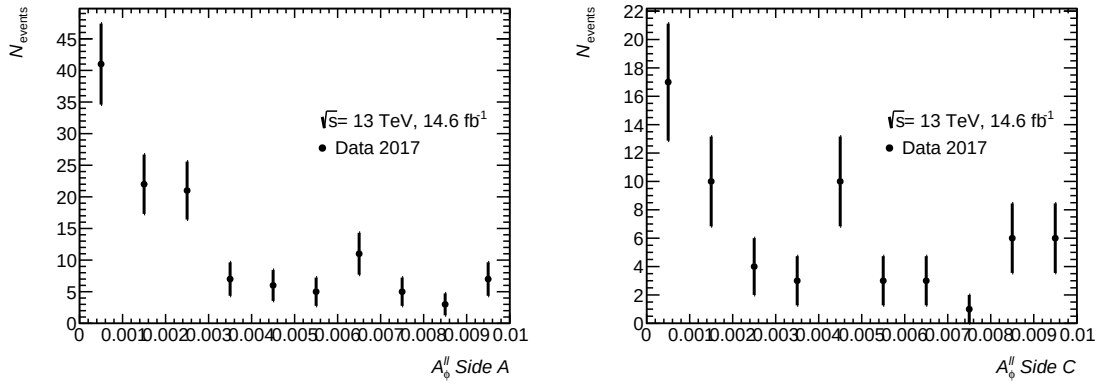

(c)

Figure A.2: Distributions of rapidity (a) invariant mass of the di-lepton system (b) and acoplanarity (c) shown separately for side A (left) and side C (right). Only data is shown and all cuts presented in Section 5.2.2 are applied.

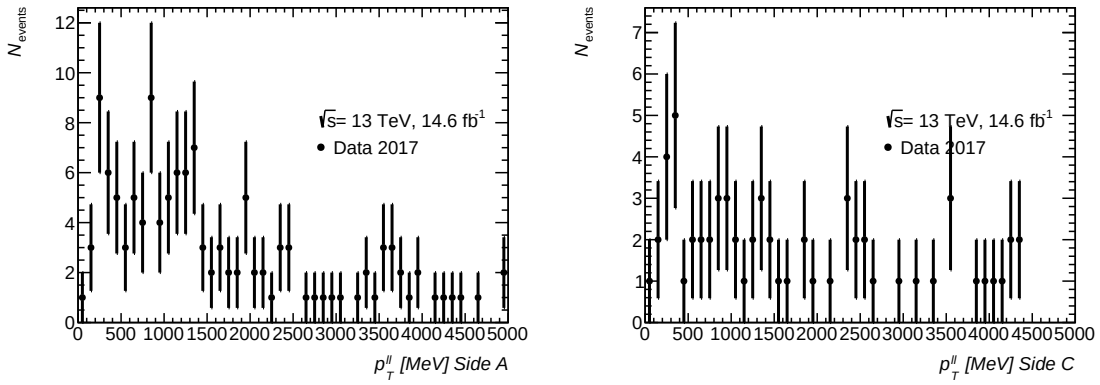

(a)

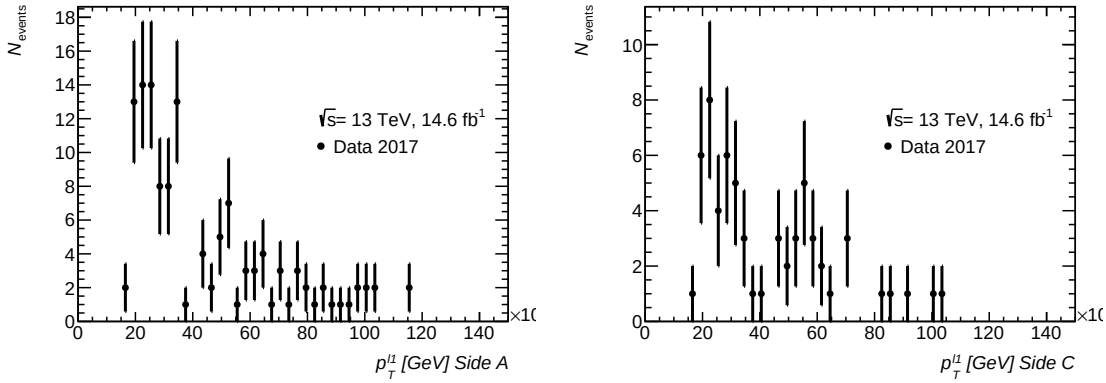

(b)

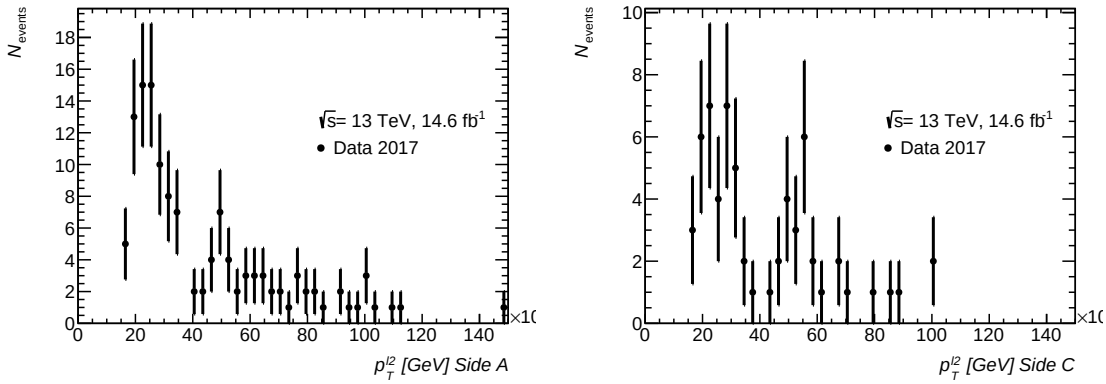

(c)

Figure A.3: Distributions of $p_T^{\ell\ell}$ (a), p_T of the leading (b) and subleading (c) lepton shown separately for side A (left) and side C (right). Only data is shown and all cuts presented in Section 5.2.2 are applied.

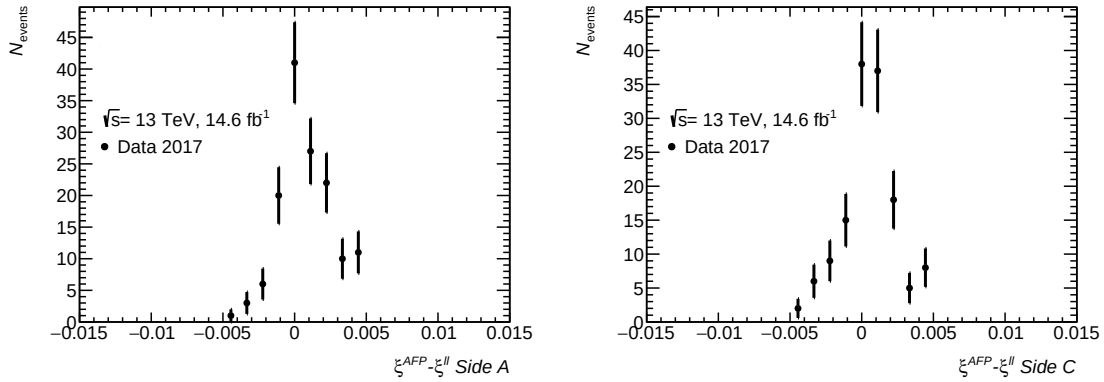

Figure A.4: Distribution of $\xi_{\mathrm{AFP}} - \xi^{\ell\ell}$ shown separately for side A (left) and side C (right). Only data is shown and all cuts presented in Section 5.2.2 are applied.

Appendix B

Additional plots for the photon-induced ZZ production with AFP analysis

B.1 Additional plots of data vs. diboson background

This section follows the discussion in Section 6.4 and presents some kinematic plots of the 2017 data and the MC sample modelling the main background considered in the analysis, as well as their ratio.

B.2 Additional plots of chosen kinematic variables of the linear terms of chosen operators

This section follows the discussion in Section 6.5.3 and presents some kinematic plots of the linear terms of some chosen operators, $\mathcal{O}_{M0}$ and $\mathcal{O}_{T5}$. Only two of them are shown for clarity, but all behave similarly.

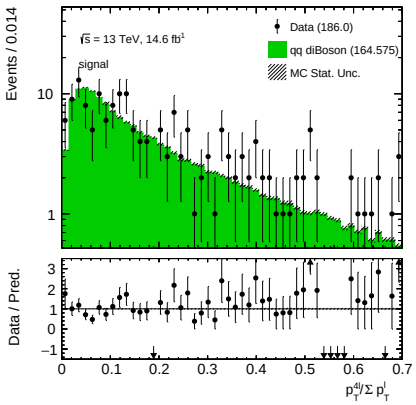

(a)

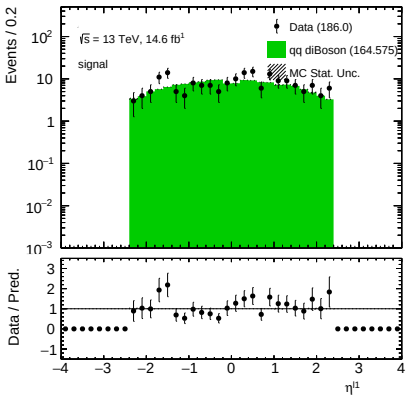

(b)

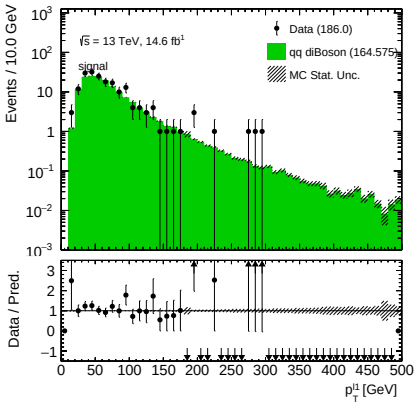

(c)

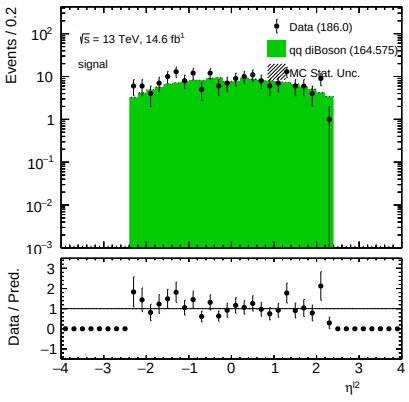

(d)

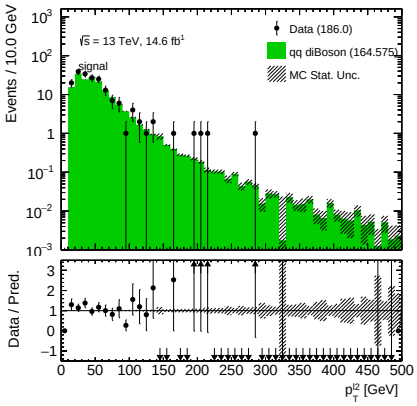

(e)

Figure B.1: Distributions of $p_T^{4\ell}/\sum p_T^{\ell}$ (a), η and p_T of the leading (b-c) and subleading (d-e) leptons. Only the main diboson background MC sample and data are included.

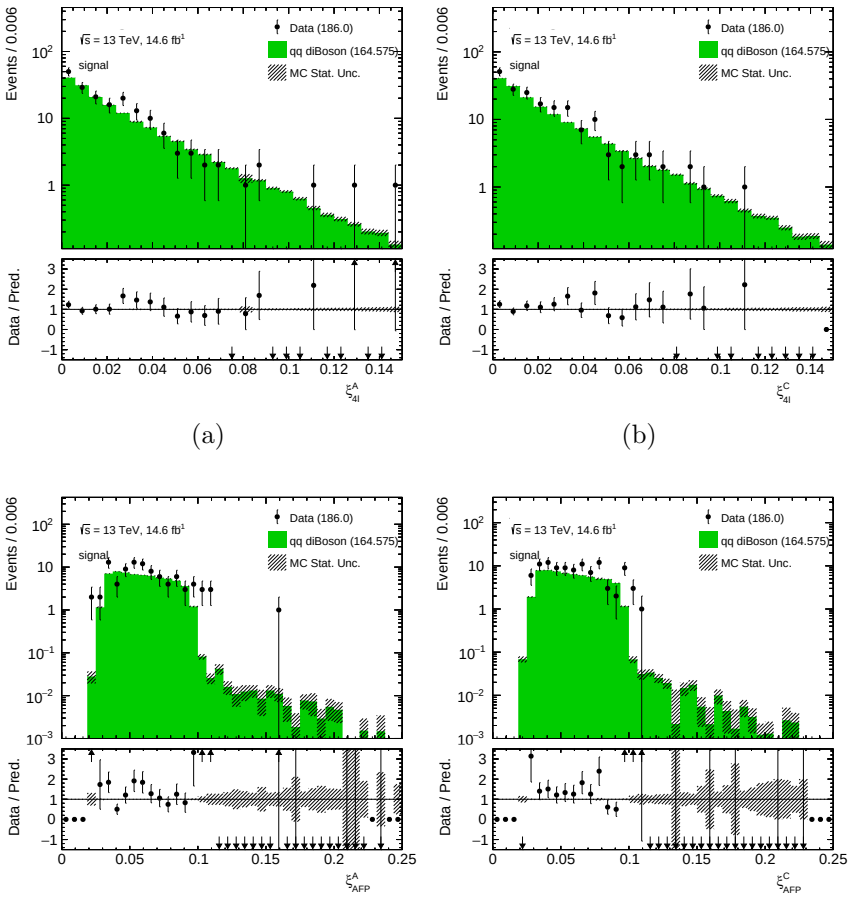

Figure B.2: Distributions of $\xi_{4\ell}^{A}$ and $\xi_{4\ell}^{C}$ (a-b), and ξ_{AFP}^{A} and ξ_{AFP}^{C} (c-d). Only the main diboson background MC sample and data are included.

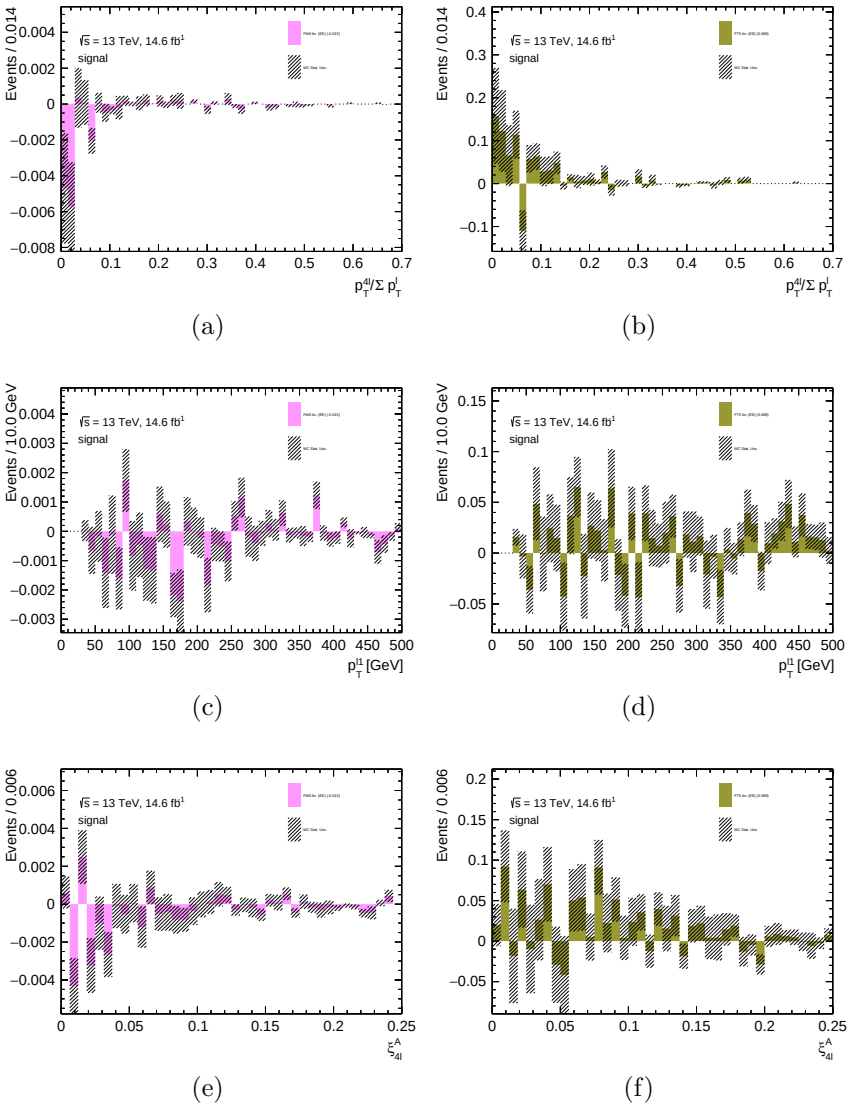

Figure B.3: Distributions of the $p_T^{4\ell}/\sum p_T^{\ell}$ (a-b), p_T of the leading lepton (c-d) and $\xi_{4\ell}$ matching the proton on side A (e-f) for the elastic component of the linear contribution of the $\mathcal{O}_{M0}$ (a-c-e) and $\mathcal{O}_{T5}$ (b-d-f) samples.

Appendix C

Additional results of the clipping scan for all Eboli dimension 8 operators considered in the analysis

This section presents the different clipping scans performed and which are discussed in Section 6.8.2. All figures represent the clipping scan considering all dissociative contributions (a) and only the elastic case (b). The blue (orange) points represents the upper (lower) limits at the 95 % confidence level. The black dashed line represents the theoretical unitarity bound for each operator.

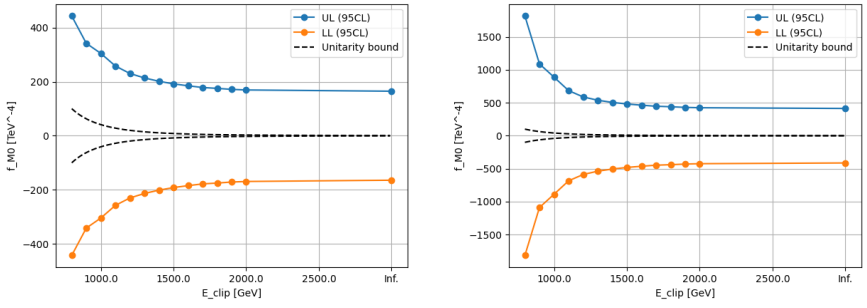

(a) (b)

Figure C.1: Clipping scan for the $\mathcal{O}_{M0}$ operator considering all dissociative contributions (a) and only the elastic case (b).

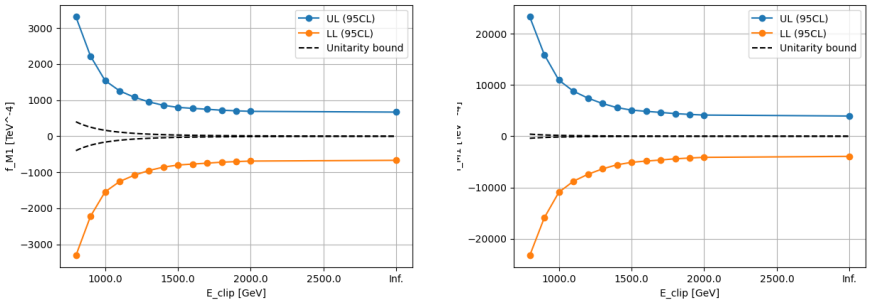

(a) (b)

Figure C.2: Clipping scan for the $\mathcal{O}_{M1}$ operator considering all dissociative contributions (a) and only the elastic case (b).

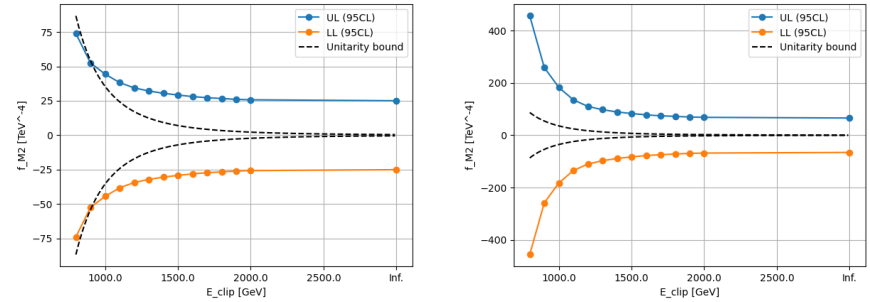

(a) (b)

Figure C.3: Clipping scan for the $\mathcal{O}_{M2}$ operator considering all dissociative contributions (a) and only the elastic case (b).

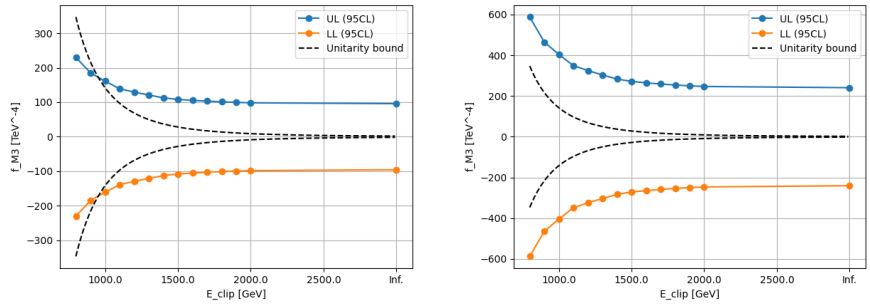

(a) (b)

Figure C.4: Clipping scan for the $\mathcal{O}_{M3}$ operator considering all dissociative contributions (a) and only the elastic case (b).

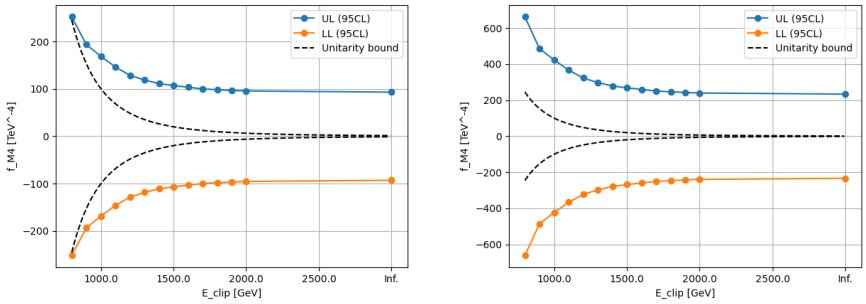

(a) (b)

Figure C.5: Clipping scan for the $\mathcal{O}_{M4}$ operator considering all dissociative contributions (a) and only the elastic case (b).

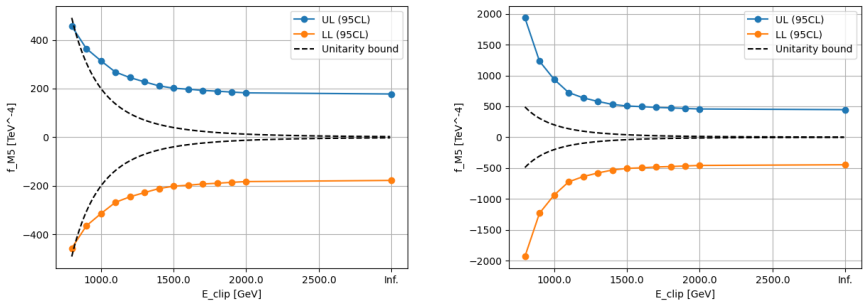

(a) (b)

Figure C.6: Clipping scan for the $\mathcal{O}_{M5}$ operator considering all dissociative contributions (a) and only the elastic case (b).

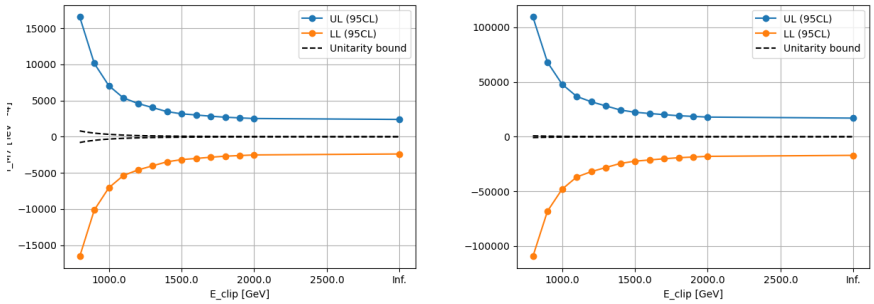

(a) (b)

Figure C.7: Clipping scan for the $\mathcal{O}_{M7}$ operator considering all dissociative contributions (a) and only the elastic case (b).

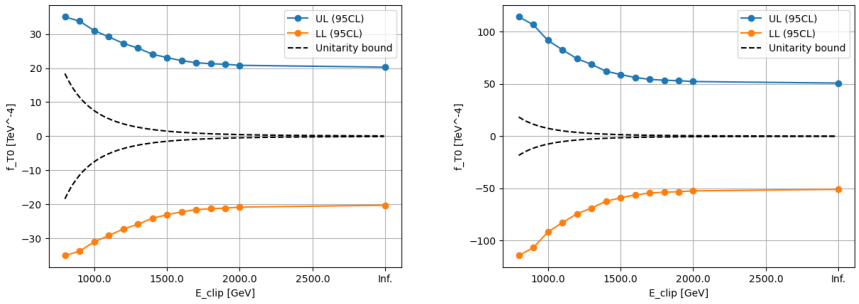

(a) (b)

Figure C.8: Clipping scan for the $\mathcal{O}_{T0}$ operator considering all dissociative contributions (a) and only the elastic case (b).

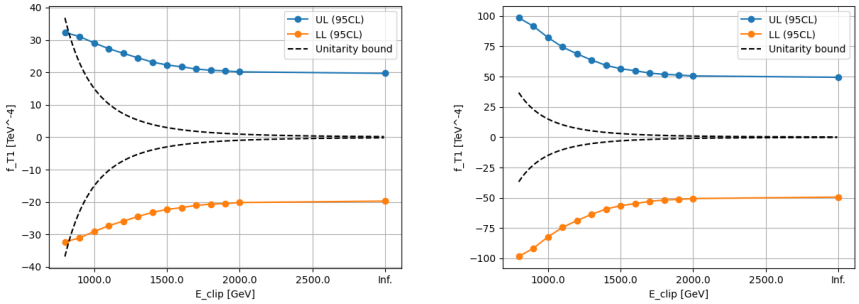

(a) (b)

Figure C.9: Clipping scan for the $\mathcal{O}_{T1}$ operator considering all dissociative contributions (a) and only the elastic case (b).

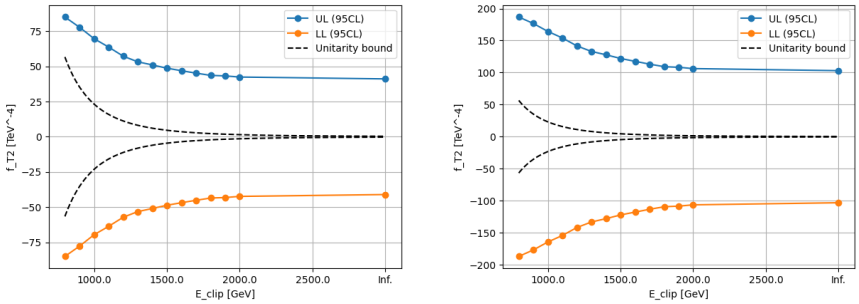

(a) (b)

Figure C.10: Clipping scan for the $\mathcal{O}_{T2}$ operator considering all dissociative contributions (a) and only the elastic case (b).

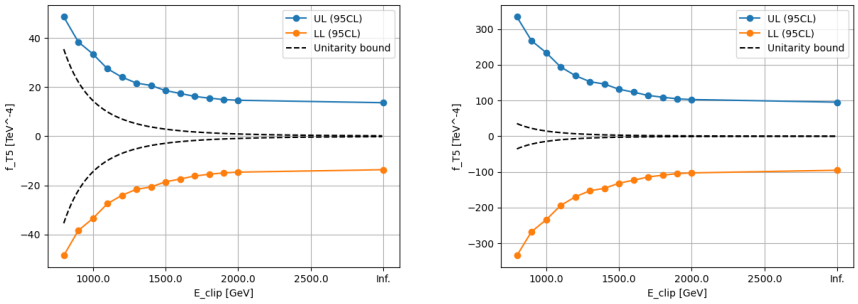

(a) (b)

Figure C.11: Clipping scan for the $\mathcal{O}_{T5}$ operator considering all dissociative contributions (a) and only the elastic case (b).

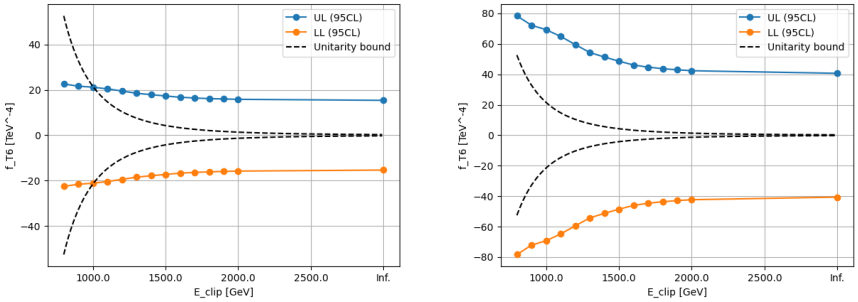

(a) (b)

Figure C.12: Clipping scan for the $\mathcal{O}_{T6}$ operator considering all dissociative contributions (a) and only the elastic case (b).

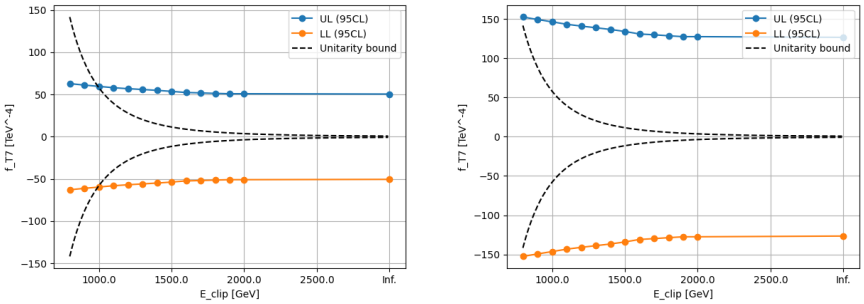

(a) (b)

Figure C.13: Clipping scan for the $\mathcal{O}_{T7}$ operator considering all dissociative contributions (a) and only the elastic case (b).

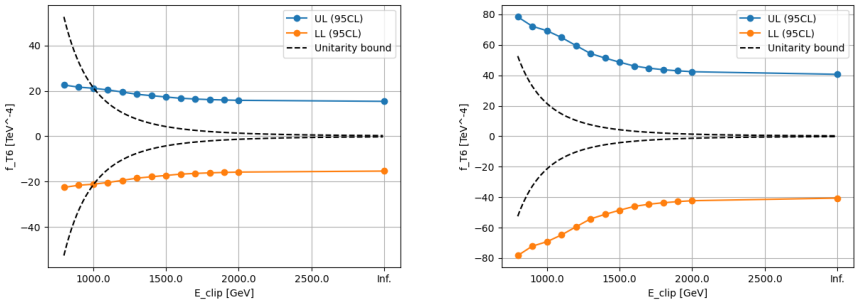

(a) (b)

Figure C.14: Clipping scan for the $\mathcal{O}_{T6}$ operator considering all dissociative contributions (a) and only the elastic case (b).

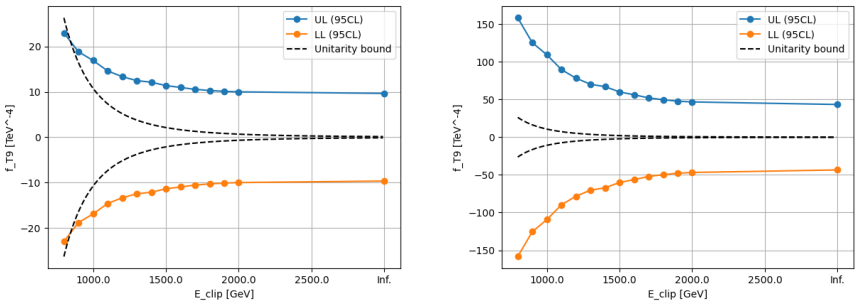

(a) (b)

Figure C.15: Clipping scan for the $\mathcal{O}_{T9}$ operator considering all dissociative contributions (a) and only the elastic case (b).

References

[1] F. Halzen & A. D. Martin; "Quarks and Leptons: An Introductory Course in Modern Particle Physics"; (1984). 2 citations on pages ii and 5

[2] S. E. Clawson; "The light at the end of the tunnel gets weaker: Observation and measurement of photon-induced W^+W^- production at the ATLAS Experiment"; . 10 citations on pages ii, 19, 20, 47, 64, 67, 69, 70, 71, and 76

[3] R. J. Ward; "Searches for Rare and Flavour-Violating Exclusive Decays of the Higgs and Z bosons with the ATLAS Experiment"; . Cited on page ii

[4] J. Kendrick; "Measurements of Single Dissociative Diffraction of Protons in $\sqrt{s} = 13$ TeV Collisions with the ATLAS Experiment"; . Cited on page ii

[5] K. Ciesla; "Studies of Multi-Parton Interactions in Diffractive Processes with the ATLAS Forward Proton Detector"; . 2 citations on pages ii and 64

[6] ATLAS collaboration; "Observation and Measurement of Forward Proton Scattering in Association with Lepton Pairs Produced via the Photon Fusion Mechanism at ATLAS"; Phys. Rev. Lett. **125**, p. 261801 (2020). 17 citations on pages xviii, 19, 56, 74, 82, 83, 84, 85, 86, 87, 88, 90, 97, 98, 110, 134, and 148

[7] S. L. Glashow; "Partial-symmetries of weak interactions"; Nuclear Physics **22**, pp. 579–588 (1961). 2 citations on pages 5 and 7

[8] S. Weinberg; "A Model of Leptons"; Phys. Rev. Lett. **19**, pp. 1264–1266 (1967). Cited on page 5

[9] G. 't Hooft & M. Veltman; "Regularization and renormalization of gauge fields"; Nuclear Physics B **44**, pp. 189–213 (1972). Cited on page 5

[10] P. W. Higgs; "Broken Symmetries and the Masses of Gauge Bosons"; Phys. Rev. Lett. **13**, pp. 508–509 (1964). 2 citations on pages 5 and 9

[11] G. S. Guralnik, C. R. Hagen & T. W. B. Kibble; "Global Conservation Laws and Massless Particles"; Phys. Rev. Lett. **13**, pp. 585–587 (1964). 2 citations on pages 5 and 9

[12] P. W. Higgs; "Spontaneous Symmetry Breakdown without Massless Bosons"; Phys. Rev. **145**, pp. 1156–1163 (1966). 2 citations on pages 5 and 9

[13] T. W. B. Kibble; "Symmetry Breaking in Non-Abelian Gauge Theories"; Phys. Rev. **155**, pp. 1554–1561 (1967). 2 citations on pages 5 and 9

[14] H. Georgi; *Lie algebras in particle physics* (CRC Press, London, England). (2019). Cited on page 6

[15] MissMJ & Cush; "Standard model of elementary particles: the 12 fundamental fermions and 5 fundamental bosons." `https://commons.wikimedia.org/wiki/File:Standard_Model_of_Elementary_Particles.svg`. Cited on page 6

[16] S. Bilenky; "Neutrino. History of a unique particle"; The European Physical Journal H **38**, p. 345–404 (2012). Cited on page 7

[17] E. Fermi; "Versuch einer Theorie der β-Strahlen. I"; Zeitschrift für Physik **88**, pp. 161–177 (1934). Cited on page 7

[18] F. Hasert *et al.*; "Observation of neutrino-like interactions without muon or electron in the gargamelle neutrino experiment"; Physics Letters B **46**, pp. 138–140 (1973). Cited on page 7

[19] UA1 collaboration; "Experimental observation of lepton pairs of invariant mass around 95 GeV/c^2 at the CERN SPS collider"; Physics Letters B **126**, pp. 398–410 (1983). Cited on page 8

[20] UA2 collaboration; "Observation of single isolated electrons of high transverse momentum in events with missing transverse energy at the CERN pp collider"; Physics Letters B **122**, pp. 476–485 (1983). Cited on page 8

[21] LHCb Collaboration; "Observation of the Resonant Character of the $Z(4430)^-$ state"; Phys. Rev. Lett. **112**, p. 222002 (2014). Cited on page 8

[22] LHCb Collaboration; "Observation of $J/\psi p$ Resonances Consistent with Pentaquark States in $\Lambda_b^0 \to J/\psi K^- p$ decays"; Physical Review Letters **115** (2015). Cited on page 8

[23] F. Englert & R. Brout; "Broken Symmetry and the Mass of Gauge Vector Mesons"; Phys. Rev. Lett. **13**, pp. 321–323 (1964). Cited on page 9

[24] P. Higgs; "Broken symmetries, massless particles and gauge fields"; Physics Letters **12**, pp. 132–133 (1964). Cited on page 9

[25] J. Ellis; "Higgs Physics"; (2013); 1312.5672. Cited on page 10

[26] W. M. Yao *et al.*; "Particle Data Group"; Phys. Rev. D **86** (2012). 3 citations on pages 11, 52, and 144

[27] CDF Collaboration; "High-precision measurement of the W boson mass with the CDF II detector"; Science **376**, pp. 170–176 (2022). Cited on page 11

[28] ATLAS collaboration; "Standard Model Summary Plots February 2022"; Technical report; CERN; Geneva (2022). https://cds.cern.ch/record/2804061. Cited on page 12

[29] Y. Fukuda *et al.*; "Evidence for Oscillation of Atmospheric Neutrinos"; Phys. Rev. Lett. **81**, pp. 1562–1567 (1998). Cited on page 12

[30] Q. R. Ahmad *et al.*; "Direct Evidence for Neutrino Flavor Transformation from Neutral-Current Interactions in the Sudbury Neutrino Observatory"; Phys. Rev. Lett. **89**, p. 011301 (2002). Cited on page 12

[31] Planck collaboration; "Planck 2013 results. I. Overview of products and scientific results"; A&A **571**, p. A1 (2014). Cited on page 12

[32] S. M. Carroll; "The Cosmological Constant"; Living Reviews in Relativity **4**, p. 1 (2001). Cited on page 13

[33] E. Fermi; "Tentativo di una Teoria Dei Raggi β"; Il Nuovo Cimento (1924-1942) **11**, pp. 1–19 (1934). Cited on page 13

[34] C. Degrande *et al.*; "Effective field theory: A modern approach to anomalous couplings"; Annals of Physics **335**, pp. 21–32 (2013). Cited on page 14

[35] B. Grzadkowski *et al.*; "Dimension-six terms in the Standard Model Lagrangian"; Journal of High Energy Physics **2010**, p. 85 (2010). Cited on page 15

[36] O. J. P. Éboli & M. C. Gonzalez-Garcia; "Classifying the bosonic quartic couplings"; Phys. Rev. D **93**, p. 093013 (2016). 2 citations on pages 15 and 144

[37] B. E. Lindquist *et al.*; "Recommendations from the Anomalous Gauge Coupling Taskforce"; Technical report; CERN; Geneva (2017). https://cds.cern.ch/record/2261444. Cited on page 16

[38] E. d. S. Almeida, O. Éboli & M. Gonzalez–Garcia; "Unitarity constraints on anomalous quartic couplings"; Physical Review D **101** (2020). 2 citations on pages 16 and 141

[39] J. C. Collins & D. E. Soper; "The Theorems of Perturbative QCD"; Annual Review of Nuclear and Particle Science **37**, pp. 383–409 (1987). Cited on page 17

[40] C. Schmidt, J. Pumplin, D. Stump & C.-P. Yuan; "CT14QED parton distribution functions from isolated photon production in deep inelastic scattering"; Physical Review D **93** (2016). 3 citations on pages 18, 22, and 107

[41] R. D. Ball *et al.*; "Parton distributions with LHC data"; Nuclear Physics B **867**, pp. 244–289 (2013). 2 citations on pages 18 and 107

[42] NNPDF collaboration; "Parton distributions for the LHC run II"; Journal of High Energy Physics **2015**, p. 40 (2015). 2 citations on pages 18 and 107

[43] S. Fichet *et al.*; "Light-by-light scattering with intact protons at the LHC: from standard model to new physics"; Journal of High Energy Physics **2015** (2015). Cited on page 18

[44] L. A. Harland-Lang, V. A. Khoze & M. G. Ryskin; "Exclusive LHC physics with heavy ions: SuperChic 3"; The European Physical Journal C **79** (2019). 2 citations on pages 18 and 19

[45] C. A. Bertulani; "Electromagnetic interaction of ultrarelativistic heavy ions"; Phys. Rev. A **63**, p. 062706 (2001). Cited on page 19

[46] V. Budnev *et al.*; "The two-photon particle production mechanism. Physical problems. Applications. Equivalent photon approximation"; Physics Reports **15**, pp. 181–282 (1975). 2 citations on pages 19 and 22

[47] A. Buckley *et al.*; "General-purpose event generators for LHC physics"; Physics Reports **504**, p. 145–233 (2011). Cited on page 20

[48] B. Andersson *et al.*; "Parton fragmentation and string dynamics"; Physics Reports **97**, pp. 31–145 (1983). Cited on page 21

[49] T. Sjöstrand *et al.*; "An introduction to PYTHIA 8.2"; Computer Physics Communications **191**, pp. 159–177 (2015). 2 citations on pages 21 and 22

[50] M. Bähr, S. Gieseke & M. H. Seymour; "Simulation of multiple partonic interactions in Herwig++"; Journal of High Energy Physics **2008**, p. 076 (2008). Cited on page 21

[51] S. Gieseke, F. Loshaj & P. Kirchgaesser; "Soft and diffractive scattering with the cluster model in Herwig"; The European Physical Journal C **77**, p. 156 (2017). Cited on page 21

[52] B. Webber; "A QCD model for jet fragmentation including soft gluon interference"; Nuclear Physics B **238**, pp. 492–528 (1984). Cited on page 21

[53] M. Bahr *et al.*; "Herwig++ physics and manual"; The European Physical Journal C **58**, pp. 639–707 (2008). 3 citations on pages 21, 22, and 88

[54] J. Bellm *et al.*; "Herwig 7.0/Herwig++ 3.0 release note"; Eur. Phys. J. C **76**, p. 196 (2016). 3 citations on pages 21, 22, and 88

[55] T. Gleisberg *et al.*; "Event generation with SHERPA 1.1"; Journal of High Energy Physics **2009**, p. 007–007 (2009). 3 citations on pages 22, 24, and 107

[56] J. Alwall *et al.*; "The automated computation of tree-level and next-to-leading order differential cross sections, and their matching to parton shower simulations"; Journal of High Energy Physics **2014** (2014). 2 citations on pages 22 and 107

[57] R. Frederix *et al.*; "The automation of next-to-leading order electroweak calculations"; Journal of High Energy Physics **2018** (2018). 2 citations on pages 22 and 107

[58] S. Agostinelli *et al.*; "Geant4—a simulation toolkit"; Nuclear Instruments and Methods in Physics Research Section A: Accelerators, Spectrometers, Detectors and Associated Equipment **506**, pp. 250–303 (2003). Cited on page 23

[59] R. Brun *et al.*; "root-project/root: v6.18/02"; (2020). `https://doi.org/10.5281/zenodo.3895860`. 3 citations on pages 23, 97, and 104

[60] O. S. Bruning *et al.*; *LHC Design Report*; CERN Yellow Reports: Monographs (CERN, Geneva) (2004). Cited on page 25

[61] ATLAS collaboration; "The ATLAS Experiment at the CERN Large Hadron Collider"; Journal of Instrumentation **3**, pp. S08003–S08003 (2008). Cited on page 26

[62] CMS Collaboration; "The CMS experiment at the CERN LHC"; Journal of Instrumentation **3**, p. S08004 (2008). Cited on page 26

[63] LHCb collaboration; *LHCb reoptimized detector design and performance: Technical Design Report*; Technical design report. LHCb (CERN, Geneva). (2003). Cited on page 26

[64] ALICE collaboration; *ALICE: Technical proposal for a Large Ion collider Experiment at the CERN LHC*; LHC technical proposal (CERN, Geneva). (1995). Cited on page 26

[65] J. Haffner; "The CERN accelerator complex. Complexe des accélérateurs du CERN"; (2013). Cited on page 27

[66] W. Herr & B. Muratori; "Concept of luminosity"; (2006). Cited on page 27

[67] CERN; "The HL-LHC project"; `https://hilumilhc.web.cern.ch/content/hl-lhc-project`. Cited on page 29

[68] J. Pequenao; "Computer generated image of the whole ATLAS detector"; (2008). `https://cds.cern.ch/record/1095924`. Cited on page 30

[69] ATLAS Collaboration; "Alignment of the ATLAS Inner Detector in Run-2"; Eur. Phys. J. C **80**, p. 1194 (2020). Cited on page 32

[70] A. Buckley, C. White & M. White; *Practical Collider Physics*; 2053-2563 (IOP Publishing) (2021). Cited on page 33

[71] ATLAS collaboration; *ATLAS inner detector: Technical Design Report, 1*; Technical design report. ATLAS (CERN, Geneva). (1997). 2 citations on pages 33 and 34

[72] M. Capeans *et al.*; "ATLAS Insertable B-Layer Technical Design Report"; Technical report (2010). https://cds.cern.ch/record/1291633. Cited on page 33

[73] K. Potamianos; "The upgraded Pixel detector and the commissioning of the Inner Detector tracking of the ATLAS experiment for Run-2 at the Large Hadron Collider"; (2016); 1608.07850. Cited on page 33

[74] ATLAS collaboration; "Operation and performance of the ATLAS semiconductor tracker"; Journal of Instrumentation **9**, p. P08009–P08009 (2014). Cited on page 33

[75] ATLAS TRT collaboration; "The ATLAS TRT Barrel Detector"; Journal of Instrumentation **3**, p. P02014 (2008). Cited on page 34

[76] ATLAS TRT collaboration; "The ATLAS TRT end-cap detectors"; Journal of Instrumentation **3**, p. P10003 (2008). Cited on page 34

[77] ATLAS TRT collaboration; "The ATLAS Transition Radiation Tracker (TRT) proportional drift tube: design and performance"; Journal of Instrumentation **3**, p. P02013 (2008). Cited on page 34

[78] ATLAS collaboration; *ATLAS central solenoid: Technical Design Report*; Technical design report. ATLAS (CERN, Geneva) (1997). Cited on page 34

[79] ATLAS collaboration; *ATLAS liquid-argon calorimeter: Technical Design Report*; Technical design report. ATLAS (CERN, Geneva) (1996). 3 citations on pages 35, 36, and 37

[80] W. Frass; "Passage of Particles Through Matter"; (2009). https://www2.physics.ox.ac.uk/sites/default/files/Passage.pdf. 2 citations on pages 36 and 39

[81] C. W. Fabjan & F. Gianotti; "Calorimetry for Particle Physics"; Rev. Mod. Phys. **75**, pp. 1243–1286 (2003). Cited on page 36

[82] Z. Meng; "Performance of the ATLAS Liquid Argon Calorimeter"; Technical report; CERN; Geneva (2010). https://cds.cern.ch/record/1304279. Cited on page 36

[83] N. Nikiforou; "Performance of the ATLAS Liquid Argon Calorimeter after three years of LHC operation and plans for a future upgrade"; (2013); 1306.6756. Cited on page 36

[84] M. McKay; "ATLAS LAr calorimeter performance in LHC run 2 and electronics upgrades for next runs"; Nuclear Instruments and Methods in Physics Research Section A: Accelerators, Spectrometers, Detectors and Associated Equipment **958**, p. 162207 (2020). Cited on page 36

[85] ATLAS collaboration; *ATLAS tile calorimeter: Technical Design Report*; Technical design report. ATLAS (CERN, Geneva) (1996). Cited on page 38

[86] J. P. Badiou, J. Beltramelli, J. M. Baze & J. Belorgey; *ATLAS barrel toroid: Technical Design Report*; Technical design report. ATLAS (CERN, Geneva) (1997). Cited on page 39

[87] ATLAS collaboration; *ATLAS end-cap toroids: Technical Design Report*; Technical design report. ATLAS (CERN, Geneva) (1997). Cited on page 40

[88] R. Ruber; "ATLAS Magnet System"; `https://atlas-magnet.web.cern.ch/atlas-magnet/`. Cited on page 40

[89] J. Pequenao; "Computer generated image of the ATLAS Muons subsystem"; (2008). `https://cds.cern.ch/record/1095929`. Cited on page 41

[90] ATLAS collaboration; *ATLAS muon spectrometer: Technical Design Report*; Technical design report. ATLAS (CERN, Geneva). (1997). 2 citations on pages 41 and 42

[91] ATLAS LUCID collaboration; "ATLAS LUCID detector upgrade for LHC Run 2"; Technical report; CERN; Geneva (2015). `https://cds.cern.ch/record/2062038`. Cited on page 42

[92] P. Jenni, M. Nessi & M. Nordberg; "Zero Degree Calorimeters for ATLAS"; Technical report; CERN; Geneva (2007). `https://cds.cern.ch/record/1009649`. Cited on page 42

[93] P. Jenni *et al.*; *ATLAS Forward Detectors for Measurement of Elastic Scattering and Luminosity*; Technical design report. ATLAS (CERN, Geneva) (2008). Cited on page 43

[94] ATLAS Collaboration; "ATLAS Forward Detectors"; (2018). `https://cds.cern.ch/record/2627582`. Cited on page 43

[95] ATLAS collaboration; "Operation of the ATLAS trigger system in Run 2"; Journal of Instrumentation **15**, p. P10004 (2020). Cited on page 44

[96] ATLAS collaboration; *ATLAS level-1 trigger: Technical Design Report*; Technical design report. ATLAS (CERN, Geneva). (1998). Cited on page 44

[97] P. Jenni *et al.*; *ATLAS high-level trigger, data-acquisition and controls: Technical Design Report*; Technical design report. ATLAS (CERN, Geneva). (2003). Cited on page 44

[98] CERN; "Worldwide LHC computing grid"; https://wlcg-public.web.cern.ch/. Cited on page 45

[99] ATLAS collaboration; "ATLAS track tutorial"; https://atlassoftwaredocs.web.cern.ch/trackingTutorial/idoverview/. Cited on page 47

[100] R. Frühwirth; "Application of Kalman filtering to track and vertex fitting"; Nuclear Instruments and Methods in Physics Research Section A: Accelerators, Spectrometers, Detectors and Associated Equipment **262**, pp. 444–450 (1987). Cited on page 46

[101] T. G. Cornelissen *et al.*; "The global χ^2 track fitter in ATLAS"; Journal of Physics: Conference Series **119**, p. 032013 (2008). Cited on page 47

[102] ATLAS collaboration; "Early Inner Detector Tracking Performance in the 2015 data at $\sqrt{s}$ = 13 TeV"; Technical report; CERN; Geneva (2015). https://cds.cern.ch/record/2110140. Cited on page 47

[103] ATLAS collaboration; "Performance of primary vertex reconstruction in proton-proton collisions at $\sqrt{s}$ = 7 TeV in the ATLAS experiment"; Technical report; CERN; Geneva (2010). https://cds.cern.ch/record/1281344. Cited on page 48

[104] ATLAS collaboration; "Vertex Reconstruction Performance of the ATLAS Detector at $\sqrt{s}$ = 13 TeV"; Technical report; CERN; Geneva (2015). https://cds.cern.ch/record/2037717. Cited on page 48

[105] W. Lampl *et al.*; "Calorimeter Clustering Algorithms: Description and Performance"; Technical report; CERN; Geneva (2008). https://cds.cern.ch/record/1099735. Cited on page 49

[106] ATLAS collaboration; "Electron and photon reconstruction and performance in ATLAS using a dynamical, topological cell clustering-based approach"; Technical report; CERN; Geneva (2017). https://cds.cern.ch/record/2298955. Cited on page 49

[107] ATLAS collaboration; "Electron reconstruction and identification in the ATLAS experiment using the 2015 and 2016 LHC proton–proton collision data at $\sqrt{s}$ =13 TeV"; The European Physical Journal C **79** (2019). Cited on page 49

[108] ATLAS collaboration; "Measurement of the photon identification efficiencies with the ATLAS detector using LHC Run 2 data collected in 2015 and 2016"; The European Physical Journal C **79** (2019). Cited on page 49

[109] ATLAS collaboration; "Electron and photon performance measurements with the ATLAS detector using the 2015–2017 LHC proton-proton collision data"; Journal of Instrumentation **14**, p. P12006–P12006 (2019). Cited on page 50

[110] ATLAS collaboration; "Muon reconstruction performance of the ATLAS detector in proton–proton collision data at $\sqrt{s} = 13$ TeV"; The European Physical Journal C **76** (2016). 2 citations on pages 50 and 51

[111] J. Illingworth & J. Kittler; "A survey of the hough transform"; Computer Vision, Graphics, and Image Processing **44**, pp. 87–116 (1988). Cited on page 50

[112] ATLAS collaboration; "Muon reconstruction and identification efficiency in ATLAS using the full Run 2 pp collision data set at $\sqrt{s} = 13$ TeV"; The European Physical Journal C **81**, p. 578 (2021). Cited on page 52

[113] F. Friedrich; "Tau Lepton Reconstruction and Identification at ATLAS"; EPJ Web of Conferences **28**, p. 12007 (2012). Cited on page 52

[114] ATLAS collaboration; "Jet reconstruction and performance using particle flow with the ATLAS Detector"; The European Physical Journal C **77** (2017). Cited on page 52

[115] ATLAS collaboration; "Performance of missing transverse momentum reconstruction with the ATLAS detector using proton–proton collisions at $\sqrt{s} =$ 13 TeV"; The European Physical Journal C **78** (2018). Cited on page 52

[116] ATLAS collaboration; "AFP Figures"; `https://twiki.cern.ch/twiki/bin/view/Atlas/AFP_Figures`. 4 citations on pages 54, 57, 60, and 61

[117] L. Adamczyk *et al.*; "Technical Design Report for the ATLAS Forward Proton Detector"; Technical report; CERN (2015). `https://cds.cern.ch/record/2017378`. 5 citations on pages 55, 56, 58, 61, and 91

[118] ATLAS collaboration; "Search for an axion-like particle with forward proton scattering in association with photon pairs at ATLAS"; Journal of High Energy Physics **2023**, p. 234 (2023). 4 citations on pages 56, 82, 97, and 147

[119] ATLAS IBL collaboration; "Prototype ATLAS IBL modules using the FE-I4A front-end readout chip"; Journal of Instrumentation **7**, p. P11010 (2012). Cited on page 56

[120] V. Zivkovic *et al.*; "The FE-I4 pixel readout system-on-chip resubmission for the insertable B-Layer project"; Journal of Instrumentation **7**, p. C02050 (2012). Cited on page 57

[121] M. Backhaus; "Characterization of the FE-I4B pixel readout chip production run for the ATLAS Insertable B-layer upgrade"; Journal of Instrumentation **8**, p. C03013 (2013). Cited on page 57

[122] J. Lange, E. Cavallaro, S. Grinstein & I. L. Paz; "3D silicon pixel detectors for the ATLAS Forward Physics experiment"; Journal of Instrumentation **10**, p. C03031 (2015). Cited on page 58

[123] ATLAS collaboration; "Performance of the ATLAS Forward Proton Time-of-Flight Detector in 2017"; Technical report; CERN; Geneva (2021). https://cds.cern.ch/record/2749821. 3 citations on pages 61, 77, and 78

[124] J. Lange *et al.*; "Beam tests of an integrated prototype of the ATLAS Forward Proton detector"; Journal of Instrumentation **11**, p. P09005 (2016). Cited on page 63

[125] ATLAS collaboration; "Performance of the ATLAS Forward Proton Spectrometer during High Luminosity 2017 Data Taking"; Technical report; CERN; Geneva (2024). https://cds.cern.ch/record/2890974. 9 citations on pages 66, 67, 68, 72, 73, 74, 76, 79, and 89

[126] M. Trzebiński; "Machine optics studies for the LHC measurements"; in "Photonics Applications in Astronomy, Communications, Industry, and High-Energy Physics Experiments 2014," , edited by R. S. Romaniuk (SPIE) (2014); ISSN 0277-786X. Cited on page 66

[127] G. Valentino *et al.*; "Semiautomatic beam-based LHC collimator alignment"; Phys. Rev. ST Accel. Beams **15**, p. 051002 (2012). Cited on page 73

[128] G. Valentino *et al.*; "Final implementation, commissioning, and performance of embedded collimator beam position monitors in the Large Hadron Collider"; Phys. Rev. Accel. Beams **20**, p. 081002 (2017). Cited on page 73

[129] ATLAS collaboration; "ATLAS Internal Luminosity Plots"; https://atlas.web.cern.ch/Atlas/GROUPS/DATAPREPARATION/DataSummary/2018/gallery.html. Cited on page 75

[130] M. P. Lewicki; "Performance Plots: AFP Special Runs 2017"; Technical report; CERN; Geneva (2021). https://cds.cern.ch/record/2767314. Cited on page 80

[131] B. Esposito & M. Curatolo; "Relative luminosity determination using ATLAS Forward Proton detector"; (2021). Cited on page 81

[132] A. Collaboration; "Athena"; (2019). https://doi.org/10.5281/zenodo.2641997. 5 citations on pages 86, 95, 97, 104, and 149

[133] R. Staszewski & J. K. K. Liu; "AFP alignment"; Technical report; CERN; Geneva (2020). https://cds.cern.ch/record/2723730. Cited on page 89

[134] ATLAS collaboration; "AfpAnalysisToolbox"; https://gitlab.cern.ch/afp/AfpAnalysisToolbox (2018). 2 citations on pages 95 and 97

[135] ATLAS collaboration; "AfpAnalysisToolbox_pileupDB"; https://gitlab.cern.ch/afp/AfpAnalysisToolbox_pileupDB (2021). Cited on page 97

[136] O. J. P. Éboli, M. C. Gonzalez-Garcia & J. K. Mizukoshi; "$pp \to jje^{\pm}\mu^{\pm}\nu\nu$ and $jje^{\pm}\mu^{\mp}\nu\nu$ at $\mathcal{O}(\alpha_{em}^6)$ and $\mathcal{O}(\alpha_{em}^4\alpha_s^2)$ for the study of the quartic electroweak gauge boson vertex at CERN LHC"; Physical Review D **74** (2006). Cited on page 103

[137] ATLAS collaboration; "SusySkimAna"; `https://gitlab.cern.ch/SusySkimAna` (2024). Cited on page 104

[138] G. Van Rossum & F. L. Drake Jr; *Python reference manual* (Centrum voor Wiskunde en Informatica Amsterdam). (1995). Cited on page 104

[139] E. Guiraud, A. Naumann & D. Piparo; "TDataFrame: functional chains for ROOT data analyses"; (2017). `https://doi.org/10.5281/zenodo.260230`. Cited on page 105

[140] J. Carter; "atlasplots python package"; `https://atlas-plots.readthedocs.io/en/latest/index.html`. Cited on page 105

[141] L. Heinrich, M. Feickert & G. Stark; "pyhf: v0.7.6"; `https://doi.org/10.5281/zenodo.1169739`. Cited on page 105

[142] L. Heinrich, M. Feickert, G. Stark & K. Cranmer; "pyhf: pure-Python implementation of HistFactory statistical models"; Journal of Open Source Software **6**, p. 2823 (2021). Cited on page 105

[143] H. Mildner; "EFTfun : EFT Fitter for UNfolded measurements"; `https://gitlab.cern.ch/eft-tools/eft-fun`. Cited on page 105

[144] ATLAS collaboration; "ATLAS data quality operations and performance for 2015–2018 data-taking"; Journal of Instrumentation **15**, p. P04003–P04003 (2020). Cited on page 105

[145] ATLAS collaboration; "Luminosity determination in pp collisions at $\sqrt{s} = 13$ TeV using the ATLAS detector at the LHC"; Technical report; CERN; Geneva (2019). `https://cds.cern.ch/record/2677054`. 2 citations on pages 105 and 132

[146] ATLAS collaboration; "ATLAS Physics Twiki (ATLAS protected)"; `https://twiki.cern.ch/twiki/bin/view/AtlasProtected/AtlasPhysics`. Cited on page 107

[147] Rafał Staszewski; "Toy MC studies of event mixing background methods (ATLAS restricted)"; `https://indico.cern.ch/event/1135761/contributions/4765385/attachments/2402198/4108443/2022.03.04_staszewski.pdf`. Cited on page 116

[148] Aleksandra Dimitrievska; "Private communication with ATLAS photon-induced WW pair production using low-p_T tracking analysis member." . Cited on page 129

[149] Rafał Staszewski; "Towards optics reconstruction (ATLAS restricted)"; https://indico.cern.ch/event/853525/contributions/3589481/attachments/1920715/3177167/2019.09.04_staszewski.pdf.
Cited on page 136

[150] G. Cowan *et al.*; "Asymptotic formulae for likelihood-based tests of new physics"; The European Physical Journal C **71** (2011).
2 citations on pages 138 and 141

[151] I. Asimov; *The short story library: Franchise* (Creative Education). (1989).
Cited on page 141

[152] CMS collaboration; "Search for exclusive $\gamma\gamma \to$ WW and $\gamma\gamma \to$ ZZ production in final states with jets and forward protons"; Technical report; CERN; Geneva (2022). https://cds.cern.ch/record/2803716.
2 citations on pages 144 and 145

[153] CMS-TOTEM Collaboration; "CMS-TOTEM Precision Proton Spectrometer"; Technical report (2014). https://cds.cern.ch/record/1753795.
Cited on page 144